

University of Nottingham
UK | CHINA | MALAYSIA

THE DEVELOPMENT OF A MICRO-SCALE TURBINE-GENERATOR AND ITS POTENTIAL APPLICATION TO DEVELOP A MICRO-SCALE AND COST-EFFECTIVE ORC POWER PLANT

Submitted January 2020, for the award of the degree Doctor of Philosophy

ISAIAS HERNANDEZ-CARRILLO, (B.ENG.; M.ENG.)

Student ID: 4243868

Supervised by Prof. Hao Liu, Dr. Christopher Wood.

Faculty of Engineering

UNIVERSITY OF NOTTINGHAM

I hereby declare that this dissertation is all my own work, except as indicated in the text:

Date: January 2020

I hereby declare that I have all necessary rights and consents to publicly distribute this dissertation via the University of Nottingham's e-dissertation archive.

Public access to this dissertation is restricted until January 2022

To Dafne, Robin and...

Once in a while, **innovation** is totally disruptive, though most of the time, it results from a small and continuous improvement that is almost **imperceptible**.

ACKNOWLEDGMENTS

Agradezco la ayuda incondicional, el apoyo y la motivación que me dieron mis padres Isaias y Norma, mis hermanas Irais y Berenice; así como a todos los demás miembros de mi familia y amigos.

I wish to acknowledge the unconditional help, support and motivation provided throughout these studies by my parents, Norma and Isaias; my sisters, Irais and Berenice, as well as all other members of my family and friends.

I wish to acknowledge the outstanding academic and personal support provided by my supervisors Prof. Hao Liu and Dr. Christopher Wood throughout my PhD studies.

I wish to acknowledge the help provided by the technical staff of the Faculty of Engineering and the Department of Architecture and Built Environment at the University of Nottingham.

I wish to acknowledge the support provided by Sebastian Eyerer, Johannes Kaindl and the Technical University of Munich for performing the laboratory tests for the study of chemical compatibility presented in the section 5.3 of this thesis.

This study was financed by the Mexican Energy Ministry (SENER) and the National Council for Science and Technology (CONACYT) through the Scholarship: CONACYT-SECRETARÍA DE ENERGÍA-SUSTENTABILIDAD ENERGÉTICA 2015-ref.: 240373/409198.

ABSTRACT

In the context of a sustainable future, distributed power will become increasingly relevant to satisfy the demand for heat and power of the domestic sectors, which are energy-intensive and suffer from low efficiency and hence waste heat. Although several technologies are available to convert this waste heat into power, the organic Rankine cycle (ORC) is advantageous in terms of maturity, versatility and simplicity. However, for microscale, it can often be uneconomical, due to the required investment cost of an expander. In this thesis the following research question is proposed: How can the techno-economic performance of a micro-capacity ORC expander be improved?

To address this question, a micro-turbo-generator (MTG) was developed following the product design method. This consisted of four main tasks: an exploration of the need, design, testing and assessment of feasibility.

During the investigation of the need, polymeric structural components, an outer enclosure and a limited expansion control were the three features proposed for addressing key needs of the MTG-ORC.

For the design, two activities were performed: conceptual design and analysis. The conceptual design consisted of the definition of the cycle and the architecture of the MTG-ORC as well as the design/selection of its components (turbine, generator, control and outer enclosure). The analysis is comprised of a simulation of the thermo-aerodynamic performance, an analysis of the fluid-structure interaction and an analysis of the chemical compatibility between materials and working fluids.

The testing involved the fabrication of a prototype, the construction of a test rig and the experimentation of the unit with compressed air as the working fluid. During this test, the performance of polymeric components was assessed and compared with their metal counterparts.

The results shown that, according to the simulations, the unit presents a comparable performance regardless of the working fluid used (idealised-R245fa, real-R245fa and air). This allows the prediction of performance of the unit working with R245fa using two different methods: a performance simulation with real-R245fa and a test with air combined with the dynamic similarity principle. With these two methods, the performance of the unit

working with R245fa at peak thermo-aerodynamic efficiency showed respective results of: efficiency 0.7-0.7, rotational speed 33200[rpm]-30100[rpm], mass flowrate 0.22[kg/s]-0.2[kg/s] and thermo-aerodynamic power 1.3[kW]-1.2[kW]. An examination of these results revealed consistency between the two methods, which proves that dynamic similarity principle is valid for this investigation.

Additionally, the implementation of polymeric components seems feasible in terms of thermo-aerodynamic performance, mechanical strength and chemical compatibility. This became the principal advancement in this investigation. However, a test of these components with refrigerant is yet to be conducted when the resources become available.

The results also indicated that the polymeric components do not show a significant difference on the thermo-aerodynamic performance with respect to their aluminium counterparts with a statistical significance of $p=0.05$; therefore, they can be a solution to reduce the power/weight ratio of the MTG whilst maintaining a competitive performance. Moreover, they can potentially reduce the production cost of components. In contrast, although the outer enclosure and the limited expansion seem to be theoretically feasible, they are yet to be experimentally validated.

The results of this investigation are expected to lay a firm foundation to recommend the implementation of polymeric components into expanders and other elements of small/micro-scale ORC and refrigeration systems in the future.

PUBLICATIONS

- I. Hernandez-Carrillo, C. Wood, H. Liu. Development of a 1000 W organic Rankine cycle micro-turbine-generator using polymeric structural materials and its performance test with compressed air. Energy Conversion and Management. 190 (2019) 105-20.
- I. Hernandez-Carrillo, C.J. Wood, H. Liu. Advanced materials for the impeller in an ORC radial microturbine. Energy Procedia. 129 (2017) 1047-54.

CONTENT

ACKNOWLEDGMENTS **IV**

ABSTRACT **V**

PUBLICATIONS **VII**

CONTENT **VIII**

ACRONYMS **XII**

NOMENCLATURE **XIV**

LIST OF FIGURES **XIX**

LIST OF TABLES **XXI**

CHAPTER 1. INTRODUCTION **1**

1.1. CONTEXT 1
1.2. LOW-GRADE ENERGY RESOURCES 1
1.2.1. Waste heat 2
1.2.2. Renewable energy 3
1.3. DISTRIBUTED POWER SYSTEMS 5
1.4. PROBLEM AND RESEARCH QUESTION 7
1.5. HYPOTHESIS 7
1.6. AIM AND OBJECTIVES 7
1.7. STRUCTURE OF THE THESIS 8

CHAPTER 2. LITERATURE REVIEW **10**

2.1. TECHNOLOGIES FOR THE UTILISATION OF LOW-GRADE HEAT 10
2.2. THE ORGANIC RANKINE CYCLE (ORC) 11
2.2.1. Performance 15
2.3. EXPANDERS 15
2.3.1. Volumetric expanders 16
2.3.2. Micro-turbines 22

CHAPTER 3. THEORY AND METHODS 39

3.1. THEORY 39
3.1.1. Turbines 39
3.1.2. Generator 49
3.1.3. Control 51
3.2. METHODS 53
3.2.1. General development method 53
3.2.2. Exploration of the need 54
3.2.3. Design 56
3.2.4. Analysis 56
3.2.5. Test 57
3.2.6. Presentation of results 58
3.2.7. Health and safety 59

CHAPTER 4. DESIGN 63

4.1. CONCEPTUAL DESIGN 63
4.2. DEFINITION OF THE POWER CYCLE 64
4.3. ARCHITECTURE OF THE MTG 65
4.4. MATERIAL SELECTION 68
4.5. DESIGN OF THE TURBINE 73
4.5.1. Mean-line design 73
4.5.2. Design of the nozzle body 76
4.5.3. Design of the impeller 79
4.5.4. Design of the shaft 81
4.5.5. Selection of the inlet volute 85
4.6. SELECTION OF THE GENERATOR 87
4.7. SELECTION OF THE CONTROL 93
4.8. DESIGN OF THE ENCLOSURE 95

CHAPTER 5. ANALYSIS 100

5.1. PROGRAM FOR SIMULATION OF THE PERFORMANCE 100
5.1.1. Thermo-aerodynamics 101

5.1.2. Mass flow 109
5.1.3. Dimensionless interpretation 109
5.1.4. Validation of the program 110
5.1.5. Results of simulations 113
5.2. FLUID STRUCTURE INTERACTION STUDY 116
5.2.1. Studied scenarios 116
5.2.2. Computational Fluid Dynamics (CFD) 117
5.2.3. Structural Finite Element Analysis (FEA) 120
5.3. CHEMICAL COMPATIBILITY STUDY 125

CHAPTER 6. MANUFACTURE &TEST 130

6.1. FABRICATION 130
6.2. THE TEST RIG 135
6.3. PROCEDURE 137
6.3.1. Experimental determination of the dimensionless parameters 139
6.3.2. Instruments 142
6.4. RESULTS OF THE TEST 143
6.4.1. Performance assessment 143
6.4.2. Results of the air test 144
6.4.3. Enhanced air test 154
6.4.4. Uncertainty and error propagation 164
6.4.5. Structural integrity 167
6.5. COMPARISON WITH ALUMINIUM COMPONENTS 167
6.5.1. The aluminium impeller and nozzle body 168
6.5.2. Results of testing with aluminium components 168
6.5.3. Statistical comparison 173

CHAPTER 7. DISCUSSION 181

7.1. PREDICTION OF THE PERFORMANCE FOR AN ORC 181
7.2. ASSESSMENT OF THE IMPROVEMENT 182
7.2.1. Feasibility of features 182
7.2.2. Technical improvement 186
7.2.3. Economic improvement 187

7.2.4. Structural polymers beyond the MTG-ORC 191
7.3. CONTRIBUTION TO THE KNOWLEDGE RESEARCH IN THE FIELD. 192
7.3.1. Technical relevance 192
7.3.2. Economic relevance 193
7.3.3. Beyond the organic Rankine cycle 193

CHAPTER 8. CONCLUSIONS AND FUTURE WORK 194

8.1. CONCLUSIONS 194
8.2. FUTURE WORK 198

REFERENCES 201

APPENDICES 219

A. SUMMARY OF PROPERTIES OF THE STUDIED POLYMERS 219
B. WEIGHTED SIGNIFICANCE OF PROPERTIES FOR MATERIAL SELECTION 223
C. CODE FOR THE UNCERTAINTY AND ERROR PROPAGATION ANALYSIS. 224
D. RESULTS OF THE DESIGN OF THE NOZZLE BODY. 228

ACRONYMS

Acronym	Description
ABS	Acrylonitrile butadiene styrene
ANSYS	Simulation software
ASME	American Society of Mechanical Engineers
ATM	Atmosphere
BPVC	Boiler and pressure vessels code
CAS	Chemical Abstracts Service
CFD	Computational fluid dynamics
CHP	Combined heat and power
CNC	Computer Numerical Control
COP	Cyclic olefin copolymer
CPVC	Chlorinated polyvinyl chloride
CSP	Concentrated solar power
EOS	Equation(s) of state
ETFE	Ethylene Tetrafluoroethylene
FEA	Finite element analysis
FEP	Fluorinated ethylene–propylene
FI	Flow indicator
FSI	Fluid structure interaction
GF	Glass filled
GWP	Global warming potential
HC	Hydrocarbon
HD	High density
HFC	Hydro-fluoro-carbon
HFO	Hydro-fluoro-olefin
IEA	International Energy Agency
ISO	International Standards Organization
Kevlar 49	poly (p-phenylene terephthalamide)/Kevlar 49
LCOE	Levelised cost of energy
LCP	Liquid crystal line polymer
LE	Leading edge
MTG	Micro-turbine-generator
NA	Not available
NREL	National Renewable Energy Laboratory
ODP	Ozone depletion potential
OFC	Organic flash cycle
ORC	Organic Rankine cycle
PA11	Polyundecanolactam/Nylon 11
PA12	Polylauryllactam/Nylon 12
PA4,6	Poly (hexamethylene succinamide)/Nylon 46
PA6	Poly(caprolactam)/Nylon 6
PA6,10	Poly (hexamethylene sebacamide)/Nylon 610
PA6,12	Poly (hexamethylene dodecanediamide)/Nylon 612
PA6,6	Poly (hexamethylene adipamide)/Nylon 66
PAI	Polyamide imide
PAR	Polyarylate
PAS	Poly (aryl sulfone)

PBT	Poly (butylene terephthalate)
PBT	Polybutilene terephthalate
PC	Polycarbonate
PEC	Prime Energy Consumption
PEEK	Poly (ether ether ketone)
PEI	Polyetherimide
PEK	Poly (ether ketone)
PEKEKK	Poly (ether ketone ether ketone ketone)
PEKK	Poly (ether ketone ketone)
PEN	Poly (ethylene naphthalate)
PES	Poly (ether sulfone)
PET	Poly (ethylene terephthalate)
PFA	Perfluorovinylether–tetrafluoroethylene
PI	Polyimide
PI	Pressure indicator
PK	Aliphatic polyketone
PMMA	Poly (methyl methacrylate)
POM	Polyoxymethylene
PPA	Polyphthalamide
PPE	Poly (phenylene ether)
PPS	Poly (phenylene sulfide)
PR	Pressure ratio
PSU	Polysulfone
PTFE	Poly(tetrafluoroethylene)
PVC	Polyvinyl chloride
PVDF	Polyvinylidene fluoride
Re	Reynolds number
REFPROP	Reference fluid properties
RMSE	Root mean squared error
RS	RS instruments brand
SAN	Styrene acrylonitrile
SKF	Bearing brand
SMA	Styrene maleic anhydride
SPS	Syndiotactic polystyrene
TE	Trailing edge
TG	Turbo-generator
TI	Temperature Indicator
UK	The United Kingdom
UKAS	United Kingdom Accreditation Service
USA	United Sates of America
VISTA RTD™	Design software for radial turbines
WHP	Waste heat to power

NOMENCLATURE

Symbol	Description	Units
ω	Rotational speed	Rad/s
ψ	Loading coefficient	1
ϕ	Flow coefficient	1
ρ	Density	Kg/m^3
$\delta\eta$	Uncertainty of efficiency	1
δx_n	Uncertainty of variable n	-
δx_2	Uncertainty of variable 2	-
δx_1	Uncertainty of variable 1	-
ΔP_{loss}	Drop of pressure due to losses	kPa
Δh_s	Drop of specific enthalpy due to secondary flows	kJ/kg
Δh_{loss}	Drop of specific enthalpy	kJ/kg
Δh_i	Drop of specific enthalpy due to incidence	kJ/kg
Δh_f	Drop of specific enthalpy due to friction	kJ/kg
Δh_e	Drop of specific enthalpy due to exit speed	kJ/kg
Δh_c	Drop of specific enthalpy due to clearances	kJ/kg
Δh_{0s}	Drop of total specific enthalpy, isentropic	kJ/kg
Δh_0	Drop of total specific enthalpy	kJ/kg
β_e	Empirical constant	-
α_e	Empirical constant	-
α_2	Angle with respect of the axis, state 2	º
α_3	Angle with respect of the axis, state 3	º
α	Statistical significance	-
Z	Number of blades	-
Z	Test value normal distribution	-
VR	Volumetric ratio	1
tc	Tip clearance	m
SP	Shape ratio	1
RMSE	Root mean squared error	-
Re	Reynolds number	1
r	radius	m
Q	Volume flowrate	m^3/s
P	Pressure	kPa
Ns	Specific speed	1
n_e	Number of spires	-
n	Size of the sample	-
L	losses	kW
k	Rugosity	m
γ	Adiabatic coefficient	1
FC	Function of cumulative probability	-
f	Frequency	Hz
F	Test value variance	-
e	eccentricity	m
Ds	Specific diameter	1
D	diameter	m
d	Test value	-

BSR	Blade speed ratio	1
B	Magnetic field	T
A	Area	m^2
ω_{max}	Rotational speed, maximum	rad/s
τ_m	Frictional moment	Nm
σ_{max}	Stress, maximum	MPa
ρ_1	Density, state 1	kg/m^3
ρ_2	Density, state 2	kg/m^3
ρ_3	Density, state 3	kg/m^3
$\eta_{thermo-aero}$	Power, thermo-aerodynamic	kW
η_{thermo}	Efficiency, thermodynamic	1
η_T	Efficiency, Thermal	1
η_i^{test}	Efficiency of the test trial *i*	1
η_i^{sim}	Efficiency of simulation trial *i*	1
η_{Ex}	Efficiency, exergy	1
η_{carnot}	Efficiency, Carnot	1
$\eta_{aero}^{real-R245fa}$	Efficiency, aerodynamic with real R245fa	1
$\eta_{aero}^{ideal-R245fa}$	Efficiency, aerodynamic with ideal R245fa	1
η_{aero}^{air}	Efficiency, aerodynamic with air	1
Z_{min}	Min limit test normal distribution	-
Z_{max}	Max limit test normal distribution	-
$\bar{y}$	Mean of normalized error	1
y_i	Normalised error of efficiency	1
x_n	Variable n	-
x_i	Error of efficiency trial *i*	1
x_2	Variable 2	-
x_1	Variable 1	-
W_{out}	Work outlet	kJ
w_j	Weighting vector	-
W_{in}	Work inlet	kJ
w_3	Relative speed, state 3	m/s
w_2	Relative speed, state 2	m/s
$w_{2,u}$	Relative speed state 2, tangential direction	m/s
V_{rms}	Voltage, root mean square	V
v_3	Relative speed, state 3	m/s
v_2	Relative speed, state 2	m/s
u_3	Blade speed, state 3	m/s
u_2	Blade speed, state 2	m/s
u_2	Blade speed state 2	m/s
t_s	Thickness, shell	m
t_n	Thickness, nozzle	m
T_i	Temperature, state *i*	K
T_H	Temperature, heat source	K
t_h	Thickness, head	m
T_C	Temperature, heat sink	K
T_3	Temperature, state 3	K
T_2	Temperature, state 2	K

S_y	Standard deviation of normalized error	1
$S_{y,Poly}^2$	Standard deviation for polymer component	-
$S_{y,Al}^2$	Standard deviation for aluminium component	-
S_{ij}	Score matrix	-
s_i	Ranked score vector	-
$S_{1,1}$	Score matrix, position 1,1	-
R_w	Windings resistance	Ω
r_i	Radio, position *i*	m
r_g	Outer radius of the generator rotor	m
r_c	Radius of curvature	m
r_{cs}	reduction of cost	1
r_2	Radius, state 2	m
$Q_{h,in}$	Heat, inlet	kJ
Q_{in}	Volume flow rate, inlet	m^3
Q_4	Volume flowrate, state 4	m^3/s
Q_1	Volume flowrate, state 1	m^3/s
P_i	Pressure, state *i*	kPa
P_i^f	Future cumulative production per component	-
P_i^0	Current cumulative production per component	-
P_3	Pressure, state 3	kPa
P_2	Pressure, state 2	kPa
P_{0i}	Total pressure, state *i*	kPa
P_{02}	Total specific pressure, nozzle outlet, rotor inlet	kJ/kg
P_{01}	Total specific pressure, nozzle inlet	kJ/kg
P_{01}	Total pressure nozzle inlet	kPa
$P_{0,in}$	Total pressure, inlet	kPa
n_{Poly}	Size of the sample for polymer component	-
n_{Al}	Size of the sample for aluminium component	-
$\dot{m}$	Mass flow rate	kg/s
m_r	Mass of rotor	kg
L_h	Length, hydraulic	m
L_g	Active length of generator rotor	m
I_{rms}	Current, root mean squared	A
I_{rms}^c	Current, root mean square, phase a	A
I_{rms}^b	Current, root mean square, phase a	A
I_{rms}^a	Current, root mean square, phase a	A
I_r	Moment of inertia, respect to the axis	m^5
I_{0r}	Moment of inertia, respect to the centre of mass	m^5
h_i	specific enthalpy, state *i*	kJ/kg
h_6	Specific enthalpy, condenser outlet	kJ/kg
h_5	Specific enthalpy, pump outlet	kJ/kg
h_4	Specific enthalpy, turbine outlet	kJ/kg
h_1	Specific enthalpy, turbine inlet	kJ/kg
h_{0i}	Total specific enthalpy, state *i*	kJ/kg
h_{03s}	Total specific enthalpy, state 3, isentropic	kJ/kg
h_{03}	Total specific enthalpy, state 3	kJ/kg
h_{02}	Total specific enthalpy, state 2	kJ/kg

h_{01}	Total specific enthalpy, nozzle inlet	kJ/kg
FC_0	Theoretical function of cumulative probability	-
F_{min}	Min limit test variance	-
F_{max}	Max limit test variance	-
E_k	Energy, kinetic	kJ
E_j	Join factor	1
D_h	Diameter, hydraulic	m
$d_{critical}$	Critical test value	-
D_2	Diameter state 2	m
C_u	Future direct cost per unit	£
c_p	Heat capacity, constant pressure	kJ/kg K
C_m	Empirical constant	-
c_i	Speed of flow, state *i*	m/s
$c_{i,u}$	Flow speed, position *i*, tangential direction	m/s
C_i^f	Future direct cost per component	£
C_i^0	Current direct cost per component	£
c_f	Coefficient of friction	1
$c_{f,c}$	Coefficient of friction, corrected	1
$c'_{f,c}$	Coefficient of friction, further corrected	1
$c_{f,3}$	Speed of flow, state 3, direction of flow	m/s
$c_{f,2}$	Speed of flow, flow direction	m/s
c_3	Speed of flow, state 3	m/s
c_2	Speed of flow, state 2	m/s
$c_{2,u}$	Speed of flow state 2, tangential direction	m/s
C_0	Spouting speed	m/s
b_Q	Empirical constant	kg/m^4-s
B_m	Magnetic peak flux density	T/m^2
b_L	Empirical constant	kg-m^2/s^2
b_2	Blade height	m
a_Q	Empirical constant	kg/m^7
a_L	Empirical constant	kg-m^2/s
a_i	Constant of elasticity of cost per component	-
A_3	Area, state 3	m^2
A_2	Area, state 2	m^2
$\bar{y}_{Poly}$	Normalized error for polymer component	-
$\bar{y}_{Al}$	Normalized error for aluminium component	-
$\dot{W}_{windage}$	Power windage	kW
$\dot{W}_{thermo}$	Power, thermodynamic	kW
$\dot{W}_m$	Power mechanic	kW
$\dot{W}_{loss}$	Power losses	kW
$\dot{W}_{joule}$	Power Joule effect	kW
$\dot{W}_{electric}$	Power, electric	kW
$\dot{W}_e$	Power electric	kW
$\dot{W}_{core}$	Power losses at the core	kW
$\dot{W}_{bearings}$	Power bearings	kW
$\dot{W}_{bank}$	Power at the bank	kW

$\dot{W}_{aero}$	Power, aerodynamic	kW
$\bar{w}_{2-3}$	Relative speed, average state 2 to 3	m/s

LIST OF FIGURES

Fig. 1.1 Sankey diagram of the potential WHP from available heat in 2016; 3
Fig. 2.1. Schematic of the ORC (simple); 12
Fig. 2.2. Schematic of the ORC (recuperated); 13
Fig. 2.3 Sectioned hermetic scroll compressor; 17
Fig. 2.4 Open twin screw compressor; 19
Fig. 2.5 Sectioned pneumatic vane expander [45]. 20
Fig. 2.6 Sectioned piston compressor for refrigeration [46]. 21
Fig. 2.7 Comparison of R245fa and alternative working fluids; 33
Fig. 3.1 Cross-sectional view of a stage; a) axial flow turbine; b) radial inflow turbine... 41
Fig. 3.2 Turbine type schematic; a) Meridional view; b) Blade to blade view. 42
Fig. 3.3. Velocity triangles for the turbine rotor at off-design conditions; 43
Fig. 3.4 Specific chart (Smith type) axial turbines with 50% reaction; 47
Fig. 3.5 Simulation of a radial turbine rotor; 48
Fig. 3.6 Comparison of the design procedure for high-speed motors and generators; 50
Fig. 3.7 Diagram of the governing loop; 52
Fig. 3.8 Schematic of the development process; 54
Fig. 3.9 Root-cause analysis for improving the overall performance of an MTG-ORC. .. 55
Fig. 3.10 Steps for the conceptual design of the MTG-ORC. 56
Fig. 3.11 Steps of the analysis of the MTG-ORC. 57
Fig. 3.12 Photograph of the burst containment tank; 61
Fig. 4.1 Cross section of the MTG; 67
Fig. 4.2 Schematic of the meridional section of an inflow radial turbine; 74
Fig. 4.3 Work views of the design software for the nozzle body; 78
Fig. 4.4 Work views of the design software for the impeller; 81
Fig. 4.5 Design of the shaft for the MTG-ORC; 82
Fig. 4.6 Static structural finite element analysis of the shaft; 84
Fig. 4.7 Design of the inlet volute for a radial turbine; 86
Fig. 4.8 High-speed motor spindle. 88
Fig. 4.9 Design of the rotor of the generator; 89
Fig. 4.10 Static structural finite element analysis of the magnets sleeve; 91
Fig. 4.11 Schematic of a rectifier-inverter for frequency conversion. 93
Fig. 5.1. Simplified flow-chart of the program for performance prediction; 100
Fig. 5.2 Error of calculation of the specific volume using ideal gas; 103
Fig. 5.3 Error of calculation of the specific enthalpy using ideal gas; 104
Fig. 5.4 Error of calculation of the speed of sound using ideal gas; 105
Fig. 5.5. Cross-sectional view of a radial turbine and model nomenclature; 108
Fig. 5.6 Validation of the results using ANSYS® 16.2 VISTA RTD™. 112
Fig. 5.7 Comparison of the simulated performance; 115
Fig. 5.8 Geometry of the rotational element of fluid; 118
Fig. 5.9 Relative streamlines coloured by total temperature [K]; 120
Fig. 5.10 Finite Element Analysis of the impeller; 122
Fig. 5.11 Stress contours in Pascal for PEEK; 123
Fig. 5.12 Comparison of the results from the fluid-structure interaction study; 124
Fig. 5.13 Specimens of ABS for the chemical compatibility analysis. 127
Fig. 5.14 Results of the chemical compatibility analysis for a) PEEK and b) PET. 129
Fig. 6.1 Fabrication of the impeller made of PEEK-GF30; 131

Fig. 6.2 Comparison of prototype impellers; 132
Fig. 6.3 Assembly of the MTG-ORC; 133
Fig. 6.4 Fabrication of the shaft; 134
Fig. 6.5 Assembly of the MTG; 135
Fig. 6.6. Test rig using compressed air; 136
Fig. 6.7. Parameters of the test presented in a reduced form; 146
Fig. 6.8. Electric output of the MTG; 148
Fig. 6.9. Model for the estimation of mechanical loss; 149
Fig. 6.10. Comparison of the performance of the test for PEEK-GF30; 152
Fig. 6.11 Parameters of the enhanced test presented in a reduced form; 156
Fig. 6.12 Comparison of the performance of the enhanced air test for PEEK-GF30; 159
Fig. 6.13 Enhanced polynomial model for the estimation of losses; 161
Fig. 6.14 Comparison of the performance of the enhanced air test for PEEK-GF30 with the empirical loss model; 163
Fig. 6.15 Comparison of the performance of the enhanced air test for PEEK-GF30 with the empirical loss model and including propagation of error; 166
Fig. 6.16. Impeller and nozzle body made of Aluminium. 168
Fig. 6.17 Parameters of the aluminium test presented in a reduced form; 169
Fig. 6.18 Polynomial model for Aluminium for the estimation of losses; 170
Fig. 6.19 Comparison of the performance of the enhanced air test for Aluminium with the empirical loss model; 172
Fig. 6.20 Histogram of the error, $\boldsymbol{x}$, for the experimental thermodynamic efficiency; 174
Fig. 6.21 Histogram of the normalised error, $\boldsymbol{y}$, for the experimental thermodynamic efficiency; 176
Fig. 6.22 Graphical comparison of the normalised error, $\boldsymbol{y}$, and the normal standard distribution for the Kolmogorov–Smirnov [260] test of normality. 178
Fig. 7.1 Schematic of the proposed speed control with a bypass valve. 185
Fig. 7.2 Prediction of the production cost per unit. 190

LIST OF TABLES

Table 1.1 Classification of capacity rating for distributed generation 6
Table 2.1 Reported results in relevant experimental works using low-capacity ORC radial turbines. 29
Table 2.2 Properties of the studied working fluids. 33
Table 4.1 Definition of desired characteristics for the improvement of the MTG-ORC 63
Table 4.2 Thermodynamic states of the heat and mass balance of the studied ORC. 64
Table 4.3 General performance of the low temperature ORC, simple configuration. 65
Table 4.4 Vector of overall score for the evaluated polymers 71
Table 4.5 Chemical compatibility of polymers and fluids (literature). 72
Table 4.6 Inputs for the preliminary design of the turbine (ideal) 75
Table 4.7 Results of the preliminary design of the turbine 75
Table 4.8 Calculation of thickness for the outer enclosure 97
Table 5.1 Summary of inputs for the performance prediction program 101
Table 5.2 Scenarios for the FSI study 117
Table 5.3. Summary of properties of studied materials. 121
Table 5.4 Limits of change in properties for the chemical compatibility assessment 128
Table 6.1 Convention for numbering for the experimental test. 138
Table 6.2 Experimental parameters 142
Table 6.3 Instruments used for the measurement of the parameters 143
Table 6.4 Certificate of calibration 155
Table 6.5 Values of the constants for the regression of inlet pressure drop, $\boldsymbol{\Delta P}$. 157
Table 6.6 Values of the constants for the polynomial regression of the losses. 160
Table 6.7 Summary of the results of the analysis of propagation of error 167
Table 6.8 Descriptive statistics of the normalised error of the two samples 177
Table 6.9 Results of the K-S test of normality for the samples 178
Table 6.10 Results of the statistical comparison 180
Table 8.1 Summary of the properties of the evaluated polymers. 219
Table 8.2 Weighted significance of properties for material selection 223

CHAPTER 1. INTRODUCTION

This introduction provides an overview of the context of the research, the gap of knowledge and the research questions that motivate this work alongside its aim and objectives. An overview of the structure of the thesis is given to facilitate the navigation in the document to the reader.

1.1. CONTEXT

The sustainable development goals are a plan of action defined by the leaders of the world at the United Nations; this plan was conceived to be followed by nations and individuals to pursue the ultimate goal of eradicating poverty in the world, in all its dimensions, by 2030. A total of seventeen goals and 169 specific targets were set where energy has an important role. For instance, the 7th goal is dedicated to address the energy needs and has the purpose of *"ensuring affordable, reliable, sustainable and modern energy for all the human beings"*.The specific goal 7.2 has the intention of substantially increasing the contribution of renewable sources in the world's energy portfolio. Goal 7.3 expresses the intention of doubling the global rate of improvement in energy efficiency. In this context, the scarcity of energy resources is of great importance.

Conventionally, energy conversion seeks efficiency and, in a power cycle, efficiency is a function of the temperature of the hot source. Thus, energy resources of high-temperature are greatly valued. However, these resources are scarce in nature and, conversely, the energy resources of low temperature are much more abundant. Unfortunately, the utilization of low-temperature resources represents a challenge from the technical and economical points of view and these resources are frequently underutilised. Nevertheless, if these low-temperature resources are harvested and converted into power, they can satisfy a considerable fraction of the electric demand of nations and even with a low efficiency the benefits of this conversion is worthwhile.

1.2. LOW-GRADE ENERGY RESOURCES

The heat sources of low temperature, also known as low-grade resources, can be classified into waste heat and renewable energy, depending on their origin, as explained below.

1.2.1. Waste heat

For the purpose of this work, waste heat is understood as the thermal energy exiting a process that is not further utilised. The sources of waste heat are diverse, though the most interesting are those whose prime source is a fossil fuel. Therefore, special attention is given to flue gases from combustion processes such as internal combustion engines, ovens, boilers and other furnaces.

An accurate estimation of waste heat in the world is extremely challenging but efforts has been made to quantify this resource. Clemens et.al [1] performed a simplified estimation of the end-use energy efficiency in the world in 2012. They reported an average end-use energy efficiency of 28%, which means that around 72% of the consumed energy is wasted.

In this study, the contribution of the different productive sectors into this is not uniform. The end-use efficiency in the residential sector was reportedly 51%, in the commercial sector 40%, in the transportation sector 19% and in the industrial sector 49%. According to a similar study conducted by the Lawrence Livermore National Laboratory [2], the energy efficiency does not seem considerably higher in developed countries compared to developing countries. Therefore, arguably, the problem of waste heat is accentuated in developed economies because they are the largest consumers.

The above-mentioned scenario evidences that a great deal of energy is being wasted which could have been harvested and converted into useful power. However, as the study of Clemens et al. [1] also highlighted, around 63% is of low temperature ($T \leq 373[K]$) and hence difficult to harvest. Based on the aforementioned study, the world´s availability of waste heat and its potential for power conversion is illustrated in Fig. 1.1. In this figure it can be seen that up to 5% of the world energy consumption can be satisfied if waste heat is converted into power with 0.1 conversion efficiency for high-temperature waste heat and 0.05 for low-temperature waste heat.

To put the economic significance of this into a perspective, this power would be worth +/-500billion[£/year] assuming a levelised cost of energy (LCoE) of 100[£/MWh]. In this estimation, the residential, commercial and transportation sectors represent a major fraction. At this point, the necessity of utilising waste heat to power

(WHP) systems of micro-capacity becomes evident. Unfortunately, these systems are still under development [3-5] and hence this may be considered an unattended problem that supposes a high cost of opportunity.

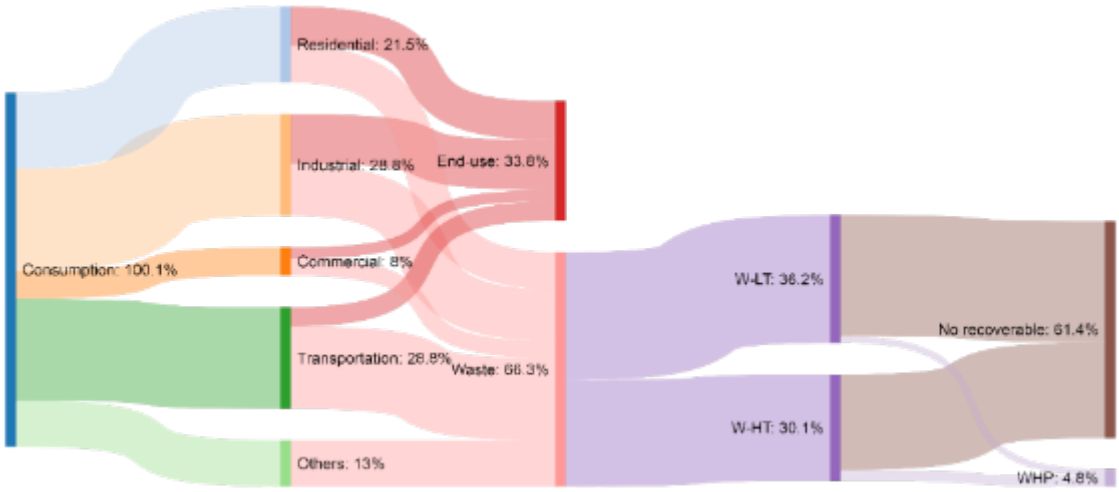


Fig. 1.1 Sankey diagram of the potential WHP from available heat in 2016; round error of 0.1%; updated from Clemens et al. [1].

1.2.2. Renewable energy

The world´s potential of low temperature heat from geothermal and solar resources is also vast. Nonetheless, the exploitation of these resources in utilities of large capacity is often not feasible. In these cases, distributed generation can be a reliable, affordable, and environment friendly option for the utilisation of these resources that can satisfy wholly or a fraction of local energy demand in remote areas.

In the category of renewable energy, the ORC [6, 7] can be applied to convert power from: low-enthalpy geothermal resources, solar thermal energy, ocean thermal gradients, and heat from the chemical conversion of biomass. However, the geothermal and solar energies are, for the purposes of this work, the most suitable for domestic application as they are combustion-free and can be available locally to consumption spots.

Geothermal

Geothermal energy is the heat contained in the earth, which can be classified as high-temperature, mid-temperature, and low-temperature resources [8]. The high-temperature resources have reservoir temperatures $T_r \geq 423[\mathrm{K}]$, the mid-temperature

resources have a reservoir temperatures $363[\mathrm{K}] \leq T_r < 423[\mathrm{K}]$ and the low-temperature resources have a reservoir temperatures $298[\mathrm{K}] \leq T_r < 363[\mathrm{K}]$.

The power conversion of high-temperature and mid-temperature resources is conventional; however, the conversion of low-temperature resources is less common because it presents significant techno-economic challenges. Worldwide, the geothermal potential is vast and the availability of resources seems to increase exponentially as the temperature decreases. Low-temperature resources may account for the majority of the useful geothermal energy [9]. The global availability of useful geothermal energy has been estimated by Stefansson [9] of around 210[EJ/year], of which 32% are resources of temperature higher than $403[\mathrm{K}]$, and the remining 68% are resources with a temperature equal or lower than $403[\mathrm{K}]$.

The geothermal heat can be extracted and converted into useful power with state-of-the-art technology, though its conversion is sometimes costly. This often results in it being economically unfeasible. Nevertheless, a fraction of the geothermal resource can be reached with shallow wells that are affordable. For example, Waring et al. [10] presented a compilation of more than 5000 areas with surface hydrothermal manifestations around the world where distributed power generation can take place. These areas have together a vast quantity of hot springs, which may suggest that sites with a shallow geothermal resource suitable for distributed generation are not infrequent.

Despite their potential, most of the aforementioned hot springs are not utilized for power generation of large capacity because it is uneconomical; therefore they are mostly limited to direct uses. However, these resources can be utilised for distributed generation and/or cogeneration for the neighbouring villages.

Solar

Solar energy is defined as the radiation of the sun falling upon the surface of the earth (irradiation). Irradiation comprises a wide range of wave lengths and can be manifested as light, heat or both. A fraction of this irradiation is naturally absorbed by clouds, land and water bodies while the remaining is reflected into space; therefore, the irradiance on the surface of the earth is variable and depends on the geography and

climatology, though in general, it may be fairly constant throughout the years; therefore, the world potential of solar energy can be estimated with a reasonable accuracy. For instance, the National Renewable Energy Laboratory in the United States (NREL) estimated in 2014 [11] that the total solar potential in the world is around *SE*=1430[EJ/year], if this energy was converted with an efficiency of $\eta_{conv} = 0.05$, typical of low temperature ORC systems, the world potential of solar to power conversion is around *SEP*=72[J/year].

Nevertheless, the techno-economic feasibility of large utilities is very sensitive to the distance of the plant from the consumption spot, which often results in large utilities not being feasible. In such cases, distributed solar to power conversion is an outstanding alternative. In this niche, the use of concentrated solar plants (CSP) based on the ORC can be and attractive technology if they are demonstrated to be economically viable.

1.3. DISTRIBUTED POWER SYSTEMS

Distributed power systems are needed for utilizing the above-mentioned low-temperature energy resources but, they can also enhance the energy systems by allowing them to satisfy the *in situ* demand of electricity and heat. Furthermore, they can make the utilisation of fossil fuels cleaner by enhancing the efficiency of their utilization. Depending on the technology, they can also enable the integration of fossil and renewable sources. They allow the agile addition of capacity, reduce the necessity for large stand-by plants, and minimise the distortion of the electric system whilst matching the demand-generation curve.

Power systems refer electricity generation from the conversion of a source of prime energy. Cogeneration, is a term referring to the process of simultaneously converting heat and electricity from a single source of prime energy. Cogeneration can be classified into combined heat and power (CHP) and waste heat to power conversion (WHP). CHP produces integrated heat and electricity from a single prime energy source, with electricity being the primary product and heat a used by-product; WHP produces heat as the main product and electricity as a useable by-product from the conversion of the surplus heat that otherwise would be wasted (waste heat).

Table 1.1 Classification of capacity rating for distributed generation

Classification	Capacity [kW]
Micro	1 to 5
Small	5 to 5000
Medium	5000 to 50000
Large	50000 to 300000

The term 'distributed' is more difficult to precisely define as there is no consensus in literature about its definition [12, 13]. Consequently, for the purposes of this work, the definition of Ackermann et al. [13] is followed, which defines distributed generation as a power generation system directly connected to the distribution network of the consumer, regardless of the capacity. However, Ackermann et al. [13] also found handy to extend their definition by giving a classification based on capacity ratings, which is presented in Table 1.1. According to this classification and considering that the application in this investigation is domestic, the term micro-generation and micro-cogeneration are used throughout this document.

The above-described power systems are of a few kilowatts capacity, also called micro-capacity [14], which are still under research and so they present limited commercial availability. Although several technological options are suitable for domestic cogeneration, the organic Rankine cycle (ORC) stands out due to its numerous advantages, including, simplicity, maturity, scalability and versatility. This latest characteristic makes it able to utilise waste heat or renewable energy resources.

The ORC is an advanced power cycle that was originally conceived for exploiting low-temperature sources. Although this power cycle is an attractive option for distributed power, it is not currently broadly accepted due to its high capital cost, which has resulted in only a modest use of the technology. This problem is accentuated in systems of micro-capacity where the capacity factor is typically low, which results in long payback periods. The expander, as the core of the ORC power system, is a major contributor to the problem of high cost since it can represent 40%-70% [15-18] of the upfront cost. Moreover, the expander is also a critical component in terms of reliability, operation, and safety. For these reasons, intensive research has been recently conducted to improve their efficiency, which may have allowed them to approach its practical maximum efficiency but their economy seems to be still an unaddressed topic.

1.4. PROBLEM AND RESEARCH QUESTION

In summary, the problem to be focused on is the poor techno-economic performance of micro-capacity ORC expanders. Consequently, the research question to address in this work is:

How can the overall performance of a micro-capacity ORC expander be improved?

1.5. HYPOTHESIS

This question is broad and can have several possible answers; thus, two hypotheses are formulated to address such a question. The second of these hypotheses has several sub-hypotheses as stated below.

Hypothesis 1: A techno-economically enhanced micro-turbine-generator (MTG) for an ORC (MTG-ORC) is feasible as expander.

Hypothesis 2: The techno-economic performance of an MTG-ORC can be improved if:

- 2.1 Components made of structural polymers can be used in an MTG-ORC.
- 2.2 The technical performance of polymeric elements of an MTG-ORC can be comparable with their metal counterpart.
- 2.3 The economic performance of polymeric elements of an MTG-ORC can be better than their metal counterpart
- 2.4 The rotational speed of an MTG-ORC can be passively controlled.
- 2.5 An MTG-ORC can be reliably operated with an outer hermetic enclosure.

1.6. AIM AND OBJECTIVES

The aim of this work is to develop and evaluate the technical and economic feasibility of an enhanced MTG-ORC. A specific goal of this work is to perform enhancements to an MTC-ORC to improve its overall performance. The specific objectives of this research are thus:

I. To assess the use of a micro-turbine as expander for a micro-capacity ORC
II. To develop a simplified MTG-ORC
III. To assess the technical and economic performance of structural polymers in elements of an MTG-ORC

The replacement of metals with polymers may represent a potential reduction of the production cost of components. This has driven a reduction in the production cost of parts of 20%-50%in several industries [19] which can be associated to savings of time, labour and energy. Therefore, the feasibility of the adoption of polymers in this field is worthwhile investigating in depth.

This work creates awareness of the potential that polymers represent as metal replacements for elements not only in an MTG-ORC but also for a broad range of other low-temperature elements and applications in the refrigeration and distributed power industries.

1.7. STRUCTURE OF THE THESIS

In this work, the development and preliminary test of a simplified micro-turbine generator intended for an organic Rankine cycle (MTG-ORC) is presented. The development includes the design and fabrication of a variable MTG that adopts several components made of structural polymers. Two critical elements are specifically studied: a nozzle body and an impeller; both components are fabricated with polymeric materials.

The work is comprised of eight chapters. In the first chapter, a brief introduction of the work is given to provide a context of the development, state the aims and objectives and provide an early insight of the structure and relevance and pertinence of the work.

In the second chapter, a review of the literature is presented. This review provides some fundamental knowledge on distributed power systems, and a review of the technological background of low capacity power systems, the organic Rankine cycle and expander technologies, with special focus on micro-turbines.

In the third chapter, the theory and methods adopted by this investigation are presented. The methods include a general development method and its complementary specific methods for designing, analysing and testing the MTG-ORC.

In the fourth chapter, the design of the MTG-ORC is presented, where the contribution of conceptual design and analysis (embodiment design) are detailed.

I the fifth chapter, the preliminary analysis of the aforementioned designed is presented. In this section, the analysis that were conducted to validate the design before experimentation are introduced.

In the sixth chapter, the procedures of manufacturing and testing are presented, where the fabrication of the prototype is described and the experimental methods are explained.

In the seventh chapter, the major findings of the investigation are presented and their implications discussed.

Finally, in the eighth chapter, conclusions and future work, the major findings of the research are highlighted and the contribution of these finding in addressing the research question are summarised.

CHAPTER 2. LITERATURE REVIEW

In this section the literature review is presented, which includes the relevant works on unconventional technologies for power conversion and, more specifically, a comprehensive exploration of the ORC. The technological options on the field of expanders for ORC are also reviewed with special focus on turbines, which is the type of expander selected in this work. Finally, the available options of working fluids and a variety of polymers that can be potentially used for structural elements in expanders are also reviewed for being of relevance in this work. This review provided a foundation to conduct the research and helped to find the knowledge gaps in this field.

2.1. TECHNOLOGIES FOR THE UTILISATION OF LOW-GRADE HEAT

The steam Rankine cycle is a traditional cycle to convert heat into power. However, for low temperature heat, the Stirling engine, the Kalina cycle and the organic Rankine cycle (ORC) are technologies that can suit better the heat to power conversion.

The Stirling engine [20, 21] is a heat engine that operates by compressing and expanding a gas (working fluid) in a confined space at different temperature levels; it is, thus, a constant volume heat engine. The Stirling engine can use air, helium, hydrogen or nitrogen as working fluid, though any gas with high specific heat capacity, high thermal conductivity, low viscosity and low density can be used. In low-temperature applications, the Stirling engine has demonstrated an energy efficiency of up to 0.15, though typical efficiencies usually remain under 0.1. This engine has two major advantages: quiet operation (does not experience internal explosions) and heat source flexibility (heat is supplied externally). However, shortcomings include complexity, high capital cost and friction.

The Kalina cycle [22, 23] is an advanced power cycle that uses a mixture of ammonia and water as the working fluid. This cycle uses evaporation to experience a temperature glide (occurs at a non-constant temperature) unlike the traditional steam Rankine cycle. Consequently, the cooling of the heat source matches better with the heating of the working fluid in the boiler. A great advantage of this cycle is an enhanced efficiency that can be higher than that of a traditional steam Rankine cycle. However, in low-temperature applications, the energy efficiency of the Kalina cycle typically

remains under 0.1. The shortcomings of a Kalina cycle are greater complexity and high precision machining requirements, which results in increased upfront and operational costs.

2.2. THE ORGANIC RANKINE CYCLE (ORC)

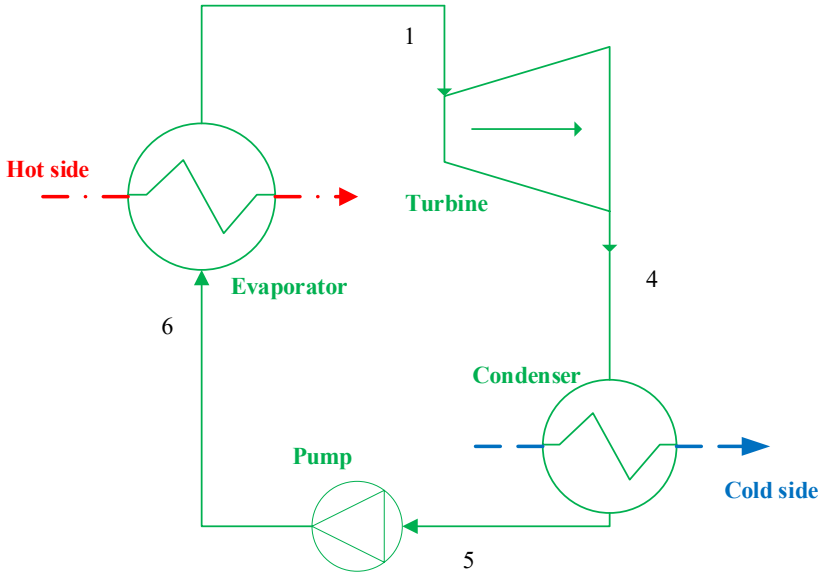
The organic Rankine cycle (ORC) is an option that stands out due to its simplicity, versatility and maturity; therefore, such a technology has been selected for this research. The ORC is a variation of the steam Rankine cycle but, unlike the steam cycle that uses water as the working fluid, the ORC uses a substance with high molecular weight and low normal boiling point as the working fluid. In the early beginnings of the ORC, documented in the 19th century [24], Naphtha replaced steam as the working fluid in engines for the propulsion of boats. However, the ORC in its modern conception is attributed to Professor D'Amelio who in 1936 [24] performed studies of an ORC-based solar thermal plant that used mono-chloro-ethane as the working fluid.

The ORC, on its simplest configuration, comprises four elements: an evaporator, an expander, a condenser and a pump. An additional boosting pump and a storage vessel for the working fluid are often included but do not have an active role. In an ORC, the working fluid experiences four thermodynamic processes: an isobaric heating (evaporation), a near-isentropic expansion, an isobaric cooling (condensing) and near-isentropic pumping. As the process is a cycle, it flows along a closed loop that can start and end at any given state, for example the inlet of the turbine.

A schematic of the simple organic Rankine cycle and its associated thermodynamic diagram are presented in Fig. 2.1a-b. For convenience, the thermodynamic diagram is presented in a temperature, T, versus specific entropy, s, chart. In this figure, the cycle starts on the thermodynamic state 1, located at the inlet of the turbine. From that point, the fluid experiences an expansion through an expander, where the thermal energy is converted into mechanical energy. At point 4 is located at the inlet of the condenser, where the working fluid can be either a low-pressure gas or two-phase mixture that is then condensed into a heat exchanger (condenser). At point 5, at the inlet of the pump, the fluid is a saturated liquid at low pressure and low temperature; from this point, the fluid is pumped to point 6 at the inlet of the boiler. There, the fluid is a pressurised subcooled liquid that is heated and evaporated across another heat exchanger

(evaporator). From this point, the cycle goes back to state 2, which is located at the outlet of the boiler and the inlet of the expander; at this point, the fluid is a saturated vapor at high pressure and the cycle is restarted.

a)



b)

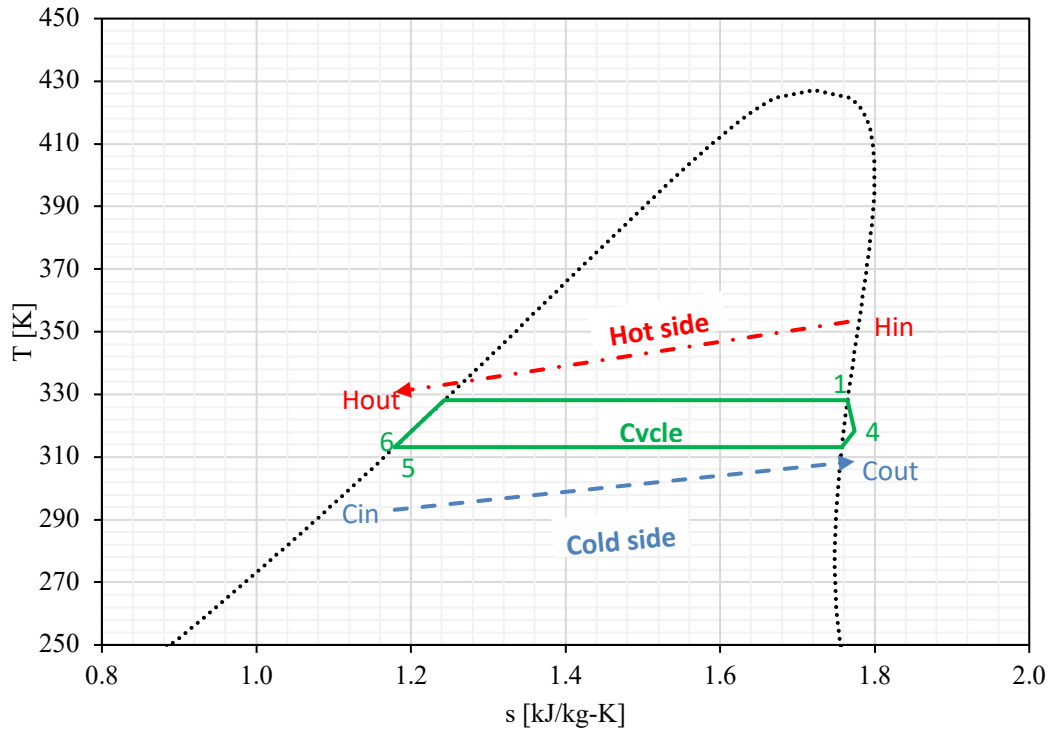
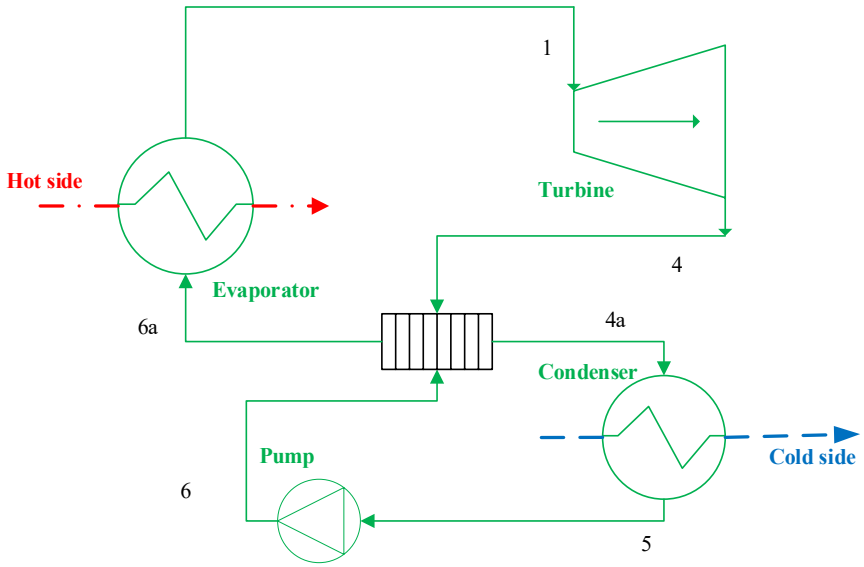


Fig. 2.1. Schematic of the ORC (simple);
a) architecture; b) Temperature–specific entropy diagram); figure adapted from Hernandez-Carrillo et al. [25].

An enhanced configuration of the simple ORC, which is only possible when dry fluids are used, is the recuperated ORC [26] shown in Fig. 2.2a-b. In this array, the state 4 of Fig. 2.1 is always super-heated; thus, some energy needs to be dissipated to bring the expanded gases to the condensing temperature. This energy can be recuperated and used to preheat the working fluid after pumping, which increases the thermal efficiency of the cycle, but makes the architecture more complex and costly as an additional heat exchanger is needed.

a)



b)

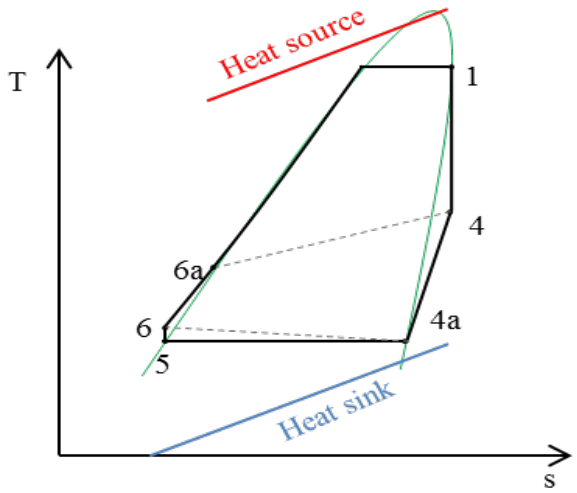


Fig. 2.2. Schematic of the ORC (recuperated);
a) architecture; b) Temperature–specific entropy diagram;

The organic flash cycle (OFC) [27-29] is another modification in the configuration of the simple ORC. In this modification, the evaporation takes place through a flash

evaporation process, which includes high-pressure isobaric heating and flash evaporation produced by an abrupt reduction of the pressure. In the OFC, the temperature profile of heating matches the cooling of the heat source; this reduces irreversibility and thus, may enhance the exergy efficiency. However, the large irreversibility produced by the expansion valve may neutralise such an enhancement.

Another enhancement of the ORC is the supercritical ORC [30-32] or S-ORC, which is a modification of the operational conditions rather than a modification of the configuration. In the supercritical ORC, the evaporation takes place at the supercritical region of the working fluid; thus, the efficiency increases due to a greater differential temperature between the evaporator and the condenser. A better matching of the temperature profiles of the heat source and the working fluid is achieved in the evaporator, which reduces irreversibility. Although the enhancement of the efficiency with the supercritical ORC is attractive, major technical challenges arise from its adoption. For example, the structural integrity of elements becomes more critical due to the greater pressures and temperatures involved, also, the abrupt changes of thermophysical properties require a sophisticated analysis of the fluid dynamics. This latest issue has enormous implications on the design and performance of major elements of the ORC in terms of real gas expansion [33].

The ORC and its variants are nowadays a promising technology with a great potential for exploiting a wide range of low-grade heat sources; thus, the industrial and academic interest on the ORC is lately having a remarkable growth. For example, from an academically-oriented point of view [34], the research can be categorised into six major research trends: applications of the ORC, research on working fluids, expander technology, cycle configurations and architecture, design and optimisation of the thermodynamics and dynamics-control. However, with a specific focus on the applications of low-capacity, the trend seems to point towards an adoption of the ORC for the recovery of domestic waste heat [24, 35], the deployment of concentrated solar power and, in some visionary applications, for the application on the aerospace industry for powering satellites [36].

2.2.1. Performance

The performance of the ORC is a topic that has been extensively studied and reported in literature, where the aforementioned configurations have been extensively analysed. Yet, in order to exemplify the analysis of the performance (the energy and exergy efficiencies), the modelling of a case study of an ORC with the simple configuration is given in this work. The thermal efficiency, η_T, is the ratio of output power over the heat supplied, shown in Eqn.(2.1), where W is the work, Q_h is the heat and the subscripts in and out indicate the direction of such work and/or heat. For an ideal analysis and neglecting losses, this equation can be rearranged in Eqn.(2.2), where h is the specific enthalpy of the state and the subscripts correspond to the thermodynamic states defined in Fig. 2.1.

$$\eta_T = \frac{W_{out} - W_{in}}{Q_{h,in}} \tag{2.1}$$

$$\eta_T = \frac{(h_1 - h_4) - (h_6 - h_5)}{(h_1 - h_6)} \tag{2.2}$$

The energy efficiency, η_{Ex}, is the ratio of the thermal efficiency and the Carnot efficiency, as shown in Eqn.(2.3); where the Carnot efficiency, η_{carnot}, is the maximum theoretical efficiency given by Eqn.(2.4). In this equation, T_C is cold sink temperature and T_H is the hot source temperature.

$$\eta_{Ex} = \frac{\eta_T}{\eta_{carnot}} \tag{2.3}$$

$$\eta_{carnot} = 1 - \frac{T_C}{T_H} \tag{2.4}$$

2.3. EXPANDERS

From the technical and economic standpoints, the expander is the most important element of an ORC because it is the power core . Thus, it has a huge impact on the

reliability, efficiency, safety and cost of the whole system. Therefore, research on expanders is worthwhile to enhance the technical and economic performance of ORCs, especially of low capacity, where the importance of the expander is critical. Few research works dedicated to this narrow topic were found in literature [37] and, consequently, this section is dedicated to a comprehensive examination of the literature of low capacity expanders for ORC systems.

The variety of expansion devices is wide [35, 38, 39], though they can be classified into volumetric expanders (pistons, scrolls, screws, and vanes) and turbo-expanders (turbines). The main characteristics of each of these categories are discussed below.

2.3.1. Volumetric expanders

Scroll Expanders

Scroll expanders are typically scroll compressors, like the one shown in Fig. 2.3, that are adapted from the refrigeration industry to run in reverse. Scroll expanders are comprised of two spiral-shaped vanes that compress the fluid located in the interspace in-between them. One of these vanes is fixed and the other orbits eccentrically, which creates a variable gap. This gap receives a finite mass of fluid at the centre of the scroll, which is then pushed outwards to the periphery of the scroll whilst increasing its volume; this movement allows the expansion of the fluid.



Fig. 2.3 Sectioned hermetic scroll compressor;
left static scroll, right orbiting scroll [40].

Depending on their packing method, scroll compressors and expanders can be categorised into three types [41]: hermetic, semi hermetic, and open drive. In hermetic scrolls all the components, including the scrolls and the drive are enclosed in a permanently closed envelope that avoids leaks, though limits maintenance. In semi-hermetic scrolls, all the components are also enclosed; however, the envelope is not sealed and can be opened for inspection and maintenance but some leaks may occur. In open drive scrolls, the scroll is enclosed and the drive is exposed; this provides flexibility, easy maintenance and a simpler coupling scroll-electrical drive, though leaking may be extensive leading to lower efficiencies.

Scroll expanders are often acknowledged for being an economic, simple, compact, and reliable option for ORC in low capacity. However, they present several shortcomings such as noisy operation, vibration and wear [38], which may make them unsuitable for domestic environments. In terms of performance, they present several technical issues [41]; for example, the suction losses and pressure pulsation deteriorate their power capacity and reliability, which may be a severe issue in the long term. Scroll

expanders operate efficiently, though an acceptable efficiency may be limited to a narrow range of operational conditions. For example, when a scroll expander is operated outside of its design expansion ratio, over or under expansion occur. An under-expansion deteriorates the power capacity and efficiency of the expander whereas an over-expansion produces undesirable backflow. Additionally, a great friction between the scroll vanes causes wear.

In any case, scroll expanders are an attractive for micro-capacity ORC and the experimental research on scroll expanders is very dynamic [42]. The range of power capacities varies from a few watts to up to 12[kW] and the reported isentropic efficiency varies from 0.07 to 0.85, though the average efficiency may be 0.66 considering several studies [42]. This value can be considered the benchmark of efficiency for ORC scroll expanders of micro-capacity.

Screw Expanders

Like scroll expanders, screw expanders are usually compressors adapted to work in reverse, as shown in Fig. 2.4. Screw expanders are comprised of two helical bodies (a male and a female) that are coupled to have a variable interspace in-between them that contains the working fluid; the rotation of the helical bodies causes the volume of the interspace to increase progressively allowing the expansion of the working fluid to happen. Both helical bodies rotate, therefore, screw expanders have two rotors. These rotors are enclosed in a casing that demands very tight tolerances to avoid leaks [42, 43]. Consequently, screw expanders are usually costly, complex and maintenance demanding.

Screw expanders are suitable for a wide range of capacities, though they are more appropriate for applications of tens of kilowatts capacity because they may be too costly and/or complex for micro-scale applications. Screw expanders are well known for having a simple structure, moderate noise levels during operation, moderate leaking and the ability to handle two-phase fluid. Nevertheless, the need of continuous and abundant lubrication to avoid wear in the rotors is a major disadvantage that makes them even more expensive and more complex.



Fig. 2.4 Open twin screw compressor;
left helical rotors, right casing [44].

The research in screw expanders for low-capacity ORC is minimal [42] and tends to be more dynamic for the application on capacities in the range of 1.1[kW] to 800[kW]. The reported isentropic efficiency varies from 0.12 to 0.88; however, the average efficiency may be around 0.66 considering several studies [42]. This can be considered the benchmark of efficiency for ORC screw expanders.

Rotary Vane Expanders

Rotary vane expanders are usually pneumatic motors, like the one shown in Fig. 2.5, adapted to work with refrigerants. They are comprised by a fixed casing and a rotor that spins eccentrically with respect to such a casing. The rotor contains several sliding vanes that delimit separate compartments whose volume increases as the rotor spins; this allows the expansion of the working fluid. Each of the sliding vanes is equipped with a spring that push it against the casing to keep the separation between compartments and to avoid cross flow in-between them.



Fig. 2.5 Sectioned pneumatic vane expander [45].

Rotary vane expanders are well-known for having a very simple structure, low cost, high torque, high volumetric efficiency and a wide range of operation conditions [38, 42]. However, leaking is very difficult to prevent. Additionally, wear in the sliding vanes may worsen the leaking problems, and can increase the operation and maintenance requirements and reduce their lifespan.

Although rotary vane expanders are suitable for micro-capacity ORC systems, the experimental research on vane expanders for such an application is not extensive [42]. The range of power capacities studied varies from a few watts to up to 2.2[kW] and the reported isentropic efficiencies vary from 0.15 to 0.71. However, the average of efficiency may be around 0.49 considering several studies [38, 42], which can be considered the benchmark of efficiency for ORC rotary vane expanders of micro-capacity.

Piston Expanders

Piston type expanders are typically compressors adopted from the refrigeration industry, which are normally hermetic, as shown in Fig. 2.6. These expanders consist of a reciprocating piston driven by a crankshaft that is coupled to the drive. The piston is enclosed in an expansion chamber whose volume varies with the stroke of the piston. The working fluid enters the chamber and pushes the piston, which increases the volume

of the cavity and allows the expansion of the fluid to happen and then, the piston returns to the original position whilst pushing the fluid out. Two check valves are needed at the inlet and outlet to keep the fluid into the chamber whilst the expansion is happening.



Fig. 2.6 Sectioned piston compressor for refrigeration [46].

The great adoption of piston compressors in the refrigeration industry makes them inexpensive and, they are well-known for being particularly suitable for high expansion ratios and low volume flowrates. However, the check valves needed make them complex, inefficient and with a limited operation range.

Although piston expanders are suitable for micro-capacity ORC, the experimental research on them for micro-capacity ORC has been moderate [42]. The range of power capacities varies from a few watts to up to 18.6[kW] and the reported isentropic efficiency varies from 0.1 to 0.76. However, the average efficiency may be around 0.49 considering several studies [42] , which can be considered the benchmark of efficiency for ORC rotary vane expanders of micro-capacity.

2.3.2. Micro-turbines

Since the early ORC systems were developed, axial turbines became the standard choice for large and medium capacity [47, 48], although for small capacity systems radial turbines are more convenient [49]. In micro-capacity systems , volumetric expanders are usually preferred. [35, 39, 50] despite exhibiting important limitations such as a complexity, short lifespan, wear and noisy operation. Micro-capacity, turbines are often overlooked because they are considered costly and complex, and are a very mature and reliable technology is often overlooked. In fact, turbines have been adopted for micro-capacity applications in several industries such as automotive [51], aerospace [52], energy [53], dental [54] and home appliances [55]. In those industries, simplification strategies were successfully implemented to make turbines suitable for the intended purpose. For these reasons, the author considers that a turbine can be a valid option and is selected as the expander for the low-capacity ORC studied in this work.

The reduction of capacity of an ORC results in two requirements for the turbine: a reduced flow rate or a reduced expansion ratio. A small flow rate requires a small flow area, which can be satisfied with a small flow path. This can be achieved with a short span of the blades, a small rotor diameter or, when suitable, partial admission. Partial admission presents some inconveniences including an incompatibility with reaction turbines, increased friction losses, and increased likelihood of fatigue [56, 57]. Therefore, a compromise of short blades, a practically small rotor and manufacturability is aimed to reduce the capacity of turbines. Nevertheless, to achieve a reasonable efficiency, a reduction of the rotor diameter results in a high rotational speed, which demands sophisticated bearings [38] and increases the centrifugal forces on the blades. Additionally, the ability of low-capacity turbines to handle large enthalpy drops is limited.

The use of ORC normally involves small enthalpy drops; thus, turbines typically require a small number of stages, rarely more than two. However, depending on the working fluid, even a small enthalpy drop may produce supersonic flow, meaning the friction losses can be dramatically increased and shockwaves may appear [58] if supersonic flow is achieved, which is undesirable. Although a degree of supersonic flow

is well handled by single stage turbines, multiple staging may be an required to avoid them. However, the use of multiple stages would increase the overall dimensions of the turbine, which may make it bulky and inadequate for a domestic application. Furthermore, compared with higher capacity turbines, micro-turbines tend to have a lower efficiency that results from greater relative clearances, greater secondary flows, relative higher friction loses from narrow passages and heat loses [38, 57].

Presented below are the most relevant works in literature regarding microturbines for ORC application. The studies reviewed in this section are categorized into: general, analytic, numerical, design, experimental, special focused, working fluids and the use of polymers.

General Studies

Microturbines have the potential of being implemented for ORC turbines with capacity of 3kW or lower as concluded by several authors, for example, Weiß [59] and Zywica et al.[38]. These studies show the suitability of downsized turbines for ORC and discussed how they perform against volumetric expanders. Conversely, Qiu et al. [39] Bao-Zhao [50], Imran et al. [42] and Rahbar et al. [35] performed similar comparative studies where turbines were disregarded as a practical option of expander for capacities lower than 3[kW]. These studies highlight that the major shortcoming of turbines is their complexity, lack of commercial availability and high costs.

In fact, down sized turbines, require precise manufacturing and high-speed operation [59], which are disadvantageous as they increase cost, but they are a mature technology that offer very high specific power, operational flexibility, fast response, high reliability, safe operation, and competitive efficiency. These characteristics make small turbines attractive, and therefore they have the potential to become the standard choice of expander if effectively adopted.

Analytic Studies

The mean-line design is a topic extensively studied because it can make the generalisation of designs of greater capacity into microturbines possible.

For axial turbines, Da Lio et al. [60, 61] proposed empirical correlations for efficiency prediction of single stage axial turbines whereas Klonowicz et al. [62] presented a mean-line design procedure. Astolfi-Macchi [63] proposed a new loss model based on a combination of two previously existing models. Klonowicz et.al [58] performed a comparison of loss models, concluding that the divergence among them, for efficiency prediction, is 5% to 15%; according with their conclusion, the Craig–Cox [64] model seems to be the most accurate for predicting subsonic but none is acceptable to study supersonic flows.

For radial turbines, the study with the mean-line approach is popular. Uusitalo et al. [65], performed mean-line design for low scale radial turbines. Capata-Hernandez [66, 67], performed design and thermo-structural analysis of 2[kW] to 15[kW] radial turbines. Lopez [68] performed design of a 3.5[kW] turbine. Ssebabi et al. [69] developed a computational tool to perform the mean-line design of a low-capacity unit. Arifin-Pasek [70] presented a mean-line design procedure for down-sized units. Demierre et al. [71] performed the mean-line design of 2[kW], 200000 [rpm] turbine. Rahbar et al. [72, 73] presented a new correlation for efficiency prediction low capacity units. White-Sayma [74] presented a methodology and a tool for microturbine mean-line design. Although the Suhrman et al. [75] model is dedicated for low capacity turbines it is only followed by Li-Ren [76], with most of the other authors following the Baines [77] or Rohlik [78] models. Al Jubori et al. [79] presented a revised mean-line procedure for selecting microturbines of radial and axial configurations, which is essentially a compilation of design methods. Song et al. [80, 81] presented a mean-line model to assess the performance of Tesla turbines where a group of dimensionless parameters, exclusive for Tesla turbines, are introduced.

Specific charts are a simple way to present the mean-line analysis; therefore, Da Lio et al. [60, 61] and Astolfi-Macchi [63] complemented their works creating specific charts for axial turbines whereas Rahbar et al. [72] and White-Sayma [74] created specific charts for radial turbines.

Finally, optimisation of the mean-line design has been proposed by White-Sayma [74], who proposed multiple-objective optimization of the efficiency; and Rahbar et al.

[82], who proposed the efficiency optimisation through genetic algorithms. However, the economical optimisation is yet to be studied.

Numerical Studies

The study of turbomachinery based on CFD is popular because such a technique can assist in the design of turbines with an exhaustive three-dimensional analysis. Additionally, CFD can give accurate results for complex situations where the mean line approach is not accurate, for example, supersonic flows, prediction of the performance with partial admission and fluid-structure interaction analyses.

Kosowski et al. [83] performed the CFD-aided design of an axial multi-stage microturbine of 3[kW] capacity with partial admission, which is reported to be in agreement with the experimental validation. Li et al. [56] analysed the aerodynamic performance of a partial admission low-capacity radial turbine and reported an adverse affectation of the unit under intermittent flow. Harinck et al.[84] analysed supersonic flows in radial inflow turbines and provided conclusive remarks based on a qualitative analysis of the shocked flow patterns. Capata-Hernandez [66, 67] used CFD simulations to assess the performance of several radial turbines ranging on 2[kW] to 15[kW]. Rahbar et al. [73] proposed a combination of mean-line and CFD methods to perform downsized radial turbines design. Hernandez-Carrillo et al. [25] validated, through CFD simulation, the mean-line design of a 1[kW] radial turbine rotor and assessed the structural affectation due to centrifugal force and blade loading.

Design oriented studies

In terms of specific designs, Cho et al. [85] presented the design of a 3[kW] single-stage axial turbine having supersonic nozzles, 8mm height blades and 16.7% admission. The rotor was 81mm tip diameter having 29 blades with 11500 [rpm] rotational speed. Kosowski et al. [83] and Kaczmarczyk et al. [86] presented the design of a 3[kW] five-stage axial turbine having partial admission (5% to 40%).It had identical blade discs of 100mm diameter with 8000 [rpm] to 12000[rpm] rotational speed, 10mm blade height, 12bar inlet pressure, 70% target efficiency. Klonowicz et al. [87] presented a comparative design of single-stage axial turbines of 1.5[kW] to 2.25[kW] capacity having partial admission 14% to 100%, diamter 17mm to 110mm and rotational speed

30000[rpm] to 200000[rpm]. Schubert [36] proposed a micro-scale radial turbine of 28W capacity, 160000[rpm] with a target efficiency of 18.4%. Yamamoto et al. [88] designed a 12[kW] radial turbine made of Aluminium having 30mm diameter and 35000[rpm] rotational speed.

Capata-Hernandez [66, 67], performed a comparative design of three radial turbines; the main characteristics investigated were working fluids,(water, R1345a, R245fa), capacity, (2[kW], 3.3, 4.5[kW]; ratational speed, 84000[rpm], 42.5000[rpm], 30000[rpm]) and diameter, (58m, 41mm, 73mm).

Demierre et al. [71] designed a 2.4[kW] radial turbine of 18mm diameter, made of steel alloy and tip clearances of up to 20% of the blade span, and designed to run at up to 200000[rpm]. Li et al. [57] and Pei et al. [89]presented the design of a 3.3[kW] radial inflow turbine targeting an efficiency of 0.71, having an overall diameter of 138mm and rotational speed of 60000[rpm]. Zywica et al. [90, 91] reported the design of a 2.7[kW], 24000[rpm] radial turbine with a four-stage configuration, combining outflow and inflow stages. Wong et al. [92] proposed a 1[kW] a radial turbine from converting a conventional turbocharger of 22mm impeller diameter with a specially-designed housing to prevent leaks. Deligant et al. [93] proposed the design of a 3[kW] radial turbine, adapted from a standard turbocharger, having 42mm diameter, 2.5mm blade height and 58600[rpm] rotational speed and 0.75-0.80 target efficiency. Shao et al. [94-96] presented the design of an inflow radial turbine having 2.8[kW] capacity, 50mm impeller diameter, 1.8mm blade height, 54000[rpm]. Hernandez-Carrillo et al. [25] presented the design of a 1.5[kW] composite-made radial turbine having a 49mm diameter, 36000[rpm] speed and target efficiency of 0.7.

From the review it can be seen that in axial turbines partial admission is a common characteristic [62, 85, 97-99], which makes evident its practicality to lower the capacity whilst preserving practical dimensions. Therefore, variable partial admission has been proposed [100] to enhance the performance under off-design conditions. However, partial admission is only suitable for impulse turbines because reaction causes uneven cyclic loading of the rotor and fatigue in the components as a consequence [56]. Additionally, partial admission limits the expansion ratio unless supersonic conditions [85, 100] or multiple staging are allowed.

A characteristic high rotational speed of microturbines is found in the above-presented designs, with velocities ranging from 8000[rpm], in multi-staged designs, to 200000[rpm], in highly loaded single stage designs. This supposes an important effort on the development of appropriate bearing systems capable to withstand such high speeds.

Small diameter turbines are also found as a common characteristic, ranging from 17mm to 138mm. However, the 22mm to 50mm diameter range appears to be more practical, especially if the adoption of hardware from small commercial gas turbines is intended, as proposed by Wong et al. [92], Guillaume et al. [101] and Deligant et al. [93]. Indeed, the adoption of hardware and design experience of low-capacity units in the turbocharger industry may be important for downsized ORC turbines since turbochargers are broadly used to boost combustion engines and the hardware is commercially available. However the commercially available turbines have several disadvantages including working fluid leaks and oil-fluid contamination which will inhibit their effectiveness.

Experimental Studies

The literature review on experimental work of ORC micro-turbines revealed that they can be an efficient and reliable option despite of the high speed, which is their most criticised characteristic. Shao et al. [94, 95], for example, developed a mini ORC, containing a radial micro-turbine with a rotational speed of 53500[rpm] and power output 3.4[kW], which achieved an isentropic efficiency of 0.75-0.83.

Li et al. [102] studied an ORC employing a high speed turboexpander, which achieved a power output of about 0.7[kW] with an isentropic efficiency of around 0.35. Pu et.al [103] tested an ORC containing a high-speed axial micro-turbine with a rotational speed of 18000[rpm] and 2[kW] power; the unit achieved an isentropic efficiency of 0.59. Pei et al. [89] studied a radial turbine with a rotational speed 60000[rpm] and 3.3[kW] power, whose isentropic efficiency was 0.65. Yagoub et al. [104] tested an MTG rated at power 1.5[kW] and rotational speed 60000[rpm], which achieved an isentropic efficiency of 0.85. Yamamoto et al. [88] studied an inflow radial micro-turbine, rated at 45000[rpm] rotational speed and 0.15[kW] power, which achieved an efficiency of around 0.5.

As shown by the above review, the successful experimentation suggests that the benchmark efficiency of ORC micro-capacity turbines can be in the range 0.65-0.7, which is comparable with the aforementioned benchmark efficiency for volumetric expanders; however, the problem of high capital cost seems still to be unaddressed and so it is beneficial to study it.

In a collaborative project led by the Gyeongsang National University in Korea, Cho et al. [85] experimented with a 3[kW] partially admitted axial single-stage turbine reporting an actual power in the range of 0.5[kW] to 2.5[kW], overall cycle efficiency of 0.014 to 0.026, rotational speed of 5000[rpm] to 10000[rpm], mass flowrate of 0.2kg/s to 0.6kg/s and partial admission of 16.5%.

Pu et al. [103] experimented with a 3[kW] single-stage axial turbine provided by a commercial partner [105]; the unit was reportedly achieved 0.5[kW] to 2[kW], 0.60 efficiency of the turbine, 0.04 efficiency of the cycle and 12000[rpm] as maximum rotational speed.

Kaczmarczyk et al. [86] experimented with a 3[kW] five-stage axial turbine reporting a maximum power of 0.75[kW], 10000[rpm] rotational speed and 0.17 kg/s flow rate.

Kosowski et al. [83] experimented, with a five-stage axial turbine and proved its capability to deliver about 0.7[kW] to 2.6[kW] with relatively low rotational speed (8000[rpm] to 9000[rpm]). The unit was reported to have an efficiency slightly below 0.70 initially and up to 0.74 after improvements, 3Bar to 6.6Bar inlet pressure.

As a summary of the reviewed work shows that radial inflow turbines are more common than axial turbines in experimental works. Also, experimentally, the efficiency can be expected of around 0.70. Rotational speeds of up to 200000[rpm] have been demonstrated in experimental work, which suggests that state of the art high-speed bearing systems can be successful in this application. However, the lifespan and economy of these systems is not reported and thus, the commercial suitability of high speed bearings in domestic cogeneration systems may still be questionable. Table 2.1presents a summary of the reviewed work showing the main factors.

Table 2.1 Reported results in relevant experimental works using low-capacity ORC radial turbines.

$\dot{W}$ [kW]	η_{max}	ω[rpm]	Institution	Country	Ref
0-1.2	0.7	8000	Nagoya University	Japan	[88]
1.5	0.5	65000	University of Nottingham	UK	[106]
1.5	0.85	60000	University of Nottingham	UK	[104]
0.76-1.4	0.68	48000	University of Science and Technology of China	China	[57, 89, 107]
0-12	0.75	50000	University of Canterbury	New Zealand	[92]
0-2	0.52	18000	Polish Academy of Science	Poland	[90, 91, 108, 109] [110]
1.3-2.4	0.74	206000	Ecole Polytechnique Federale de Lausanne	Switzerland	[71]
0-2.8	0.75	68000	University of Liege	Belgium	[101]
0.7	0.35	-	Brunel University	UK	[80, 102]
1.5-3.5	0.85	54000	Zhengzhou University	China	[94-96]

Studies with special focus on subsystems

Bearings

Hydrodynamic bearings use a thin film of liquid lubricant, oil or working fluid, to support the rotating shaft. They are the most conventional bearings [92, 101, 111] as they represent a simple and economic solution but they are not always the right solution because they need a lubrication medium, which promotes working fluid contamination, demands additional hardware, and has speed limitations. As a result unconventional bearings, e.g. ceramic roller [94, 112], aerodynamic [71, 90, 91, 108, 111] or magnetic [113], are attractive alternatives.

Ceramic rollers use ceramic rather than metal balls to support the shaft. This feature alongside tight fabrication and runout tolerances allow this type of bearing to reach high speeds with low friction; however, their lifespan is short.

Aerodynamic bearings also use a thin film of fluid to support the spinning shaft, but, unlike hydrodynamic bearings, the lubricating media is gas, normally air or working

fluid vapour. This reduces friction considerably allowing very high speeds; however, aerodynamic bearings demand sophisticated hardware and control systems.

Magnetic bearings rely on magnetic levitation to support the shaft; they can be passive, which use permanent magnets; and active, which use electromagnets, however, passive magnet bearings are not stable and active magnet bearings are more common. Magnetic bearings reduce friction and, consequently, the attainable speeds increase tremendously though, they require a complex electronic control and expensive hardware. Unconventional bearings are attractive alternatives because they resolve some of the problems of conventional bearings, but they still present limitations that must be addressed for them to become feasible.

The common types of bearings used in low-capacity ORC turbines are unclear since different methods are applied. Hydrodynamic bearings are implemented with oil [114] and working fluid [115] as lubricant and also ceramic roller [57, 89, 92, 100, 116], magnetic [117, 118] and aerodynamic [71, 90, 101, 108, 110, 119] bearings are proposed. However, for practical convenience, the ceramic roller bearings are selected for this work, as they are oil-free and do not require additional hardware to work.

Coupling

The generator-turbine coupling is important in terms of efficiency and reliability, but it can also influence the selection of bearings and sealing. Three main coupling methods can be found; direct coupling, transmission coupling and magnetic coupling.

Direct coupling, which is the simplest and the most common, attaches turbine and generator in a single shaft; thus, no frictional losses are present, and the rotational speeds of turbine and generator are the same. If the generator frequency is different from the consumption frequency, a signal conditioner must be used. Direct coupling may demand high speed but eases the implementation of hermetic sealing. However, transmission coupling attaches the turbine and generator shafts through a mechanical transmission, e.g. gearbox, belt, or chain; thus, some friction losses are expected. Transmission coupling allows an independent development of turbine and generator, which gives flexibility, and permits stacking several stages in parallel [120], though it adds complexity and cost. Finally, magnetic coupling is an unconventional method that

transfers mechanical power through magnetic forces, hence, no contact exists. This reduces mechanical loses and enables the implementation of sealing membranes; however, it may also add complexity and cost.

In low-capacity ORC turbines, the tendency is to implement direct coupling, with most of the reviewed manufacturers and experimental works adopting it. Transmission coupling is a rare practice with no manufacturers and only a few experimental works [57, 89, 94, 107], implementing this method. Magnetic coupling is also rare, and only Wong [92] proposed it. This leaves a big opportunity if magnetic coupling is adopted for low-capacity ORC turbines as the effectiveness of this coupling method is broadly known in industries like chemical and submarine propulsion, where aggressive fluids are present.

Enclosure

ORC demands a sophisticated enclosure to avoid leaking of working fluids, which are greenhouse gases. There are three options: seal packed, hermetic and semi-hermetic enclosures.

Adopted from the gas turbine industry, seal packed is a traditional enclosing method that keeps the fluid within the casing applying seals (carbon, labyrinth, brush, honeycomb, mechanical, etc.) between static and dynamic parts. However this method will inevitably allow a small volume of fluid leakage trough the seals, even in advanced seals, which is a severe shortcoming. Seal packing is found some experimental works [71, 98, 100]. In contrast, a hermetic enclosure [71, 90, 91, 108] permanently envelopes the turbine and, often, the generator. This prevents the working fluid of leaking but makes inspection and servicing difficult tasks. Hermetic enclosure were adopted by commercial providers and most of the experimental works studied in this review. Finally, the semi-hermetic enclosure is a transitional method that seeks to envelope the turbine-generator group in a single hermetic pack but still grants easy access by adopting gasket-sealed openings. This option represents a good balance between fluid leaking and ease of maintenance; nevertheless, none of the reviewed used a semi hermetic enclosure method.

Working fluid oriented studies

The use of substances with high molecular weight as the working fluid has been proposed in various studies [24, 48, 121, 122]. These include a broad range of substances [50, 123-126] but only a few of them have been experimentally proven [24, 38, 47, 62, 74, 76, 90, 126-130] and the most popular are iso-pentane, R245fa, R134a, R123, R227ea and HFE7100. The technical implications of using these fluids and its selection is also a topic that has been extensively discussed in literature [47, 123, 124, 126-128, 131-133]; thus, the review in this section will be limited to the implications of using those substances in micro-turbines.

Although the selection of the working fluid is critical, the literature review revealed a lack of agreement regarding the most suitable method for working fluid selection. Pezzuolo et al. [124], for example, claimed that a unique optimum working fluid might not exist because the fluid selection is a tailored process that depended on a variety of aspects, namely, the application, the ORC configuration, the operating conditions, the environmental restrictions, and the optimization. Nevertheless, a few methods, rules and tools [124, 134] have been proposed aiming to help the scientific community to conduct this critical task in an efficient and structured manner.

The aim of this investigation does not consider an exhaustive study of the working fluid and the R45fa was selected *a priori*. This substance was selected because it is a popular choice of working fluid in experimental investigations [135], and seems to be adequate for the operational conditions studied in this work, presented in section 4.2. Its chemical compatibility with a few structural polymers is explained in section 5.3. Nevertheless, the review of a shortlist of alternative working fluids is considered useful to give alternatives to replace R245fa in applications where the use of such a fluid is not convenient.

If the working fluid is replaced, a complete revision of this work would be mandatory to ensure suitability of the new working fluid. The reviewed fluids include two hydrofluorocarbons (HFC) widely used in refrigeration and ORC systems: R245fa and R134a; and four hydro-fluoro-olefins (HFO), which are working fluids of a new generation: R1224yd, R1233zd, R1234yf and R1234ze. The major properties of these fluids are summarised in Table 2.2 while a comparison of their saturation curve in a

temperature-specific entropy chart is presented in Fig. 2.7. It can be seen that R1224yd, R245fa and R1233yd have a similar saturation curve with a higher working temperature whereas R1234yf, R134a and R1234ze all have lower working temperatures.

Table 2.2 Properties of the studied working fluids.

Fluid	**R245fa**	**R1224yd**	**R1233zd**	**R134a**	**R1234yf**	**R1234ze**
Type	HC	HFO	HFO	HC	HFO	HFO
CAS	460-73-1	111512-60-8	102687-65-0	811-97-2	754-12-1	29118-24-9
ODP	-	23000	0	0	0	0
GWP	1030	0.88	1	1200	4	<1
Flammability	No	No	No	No	Mild	Mild
Formula	$C_3H_5F_5$	C_3HClF_4	$C_3H_2ClF_3$	$C_2H_2F_4$	$C_3H_2F_4$	$C_3H_2F_4$
MW[kg/kmol]	134.04	148.5	130.5	102.03	114	114
T_{crit}[K]	427.2	428.7	438.75	374.2	367.85	382.6
P_{crit}[MPa]	3.64	3.34	3.57	4.06	3.38	3.64
ρ_{crit}[kg/m^3]	517	527	478.92	511	475	489
T_{bn} [K]	288.05	288.2	291.4	247.1	243.65	254.2
References	[136-139]	[140]	[141, 142]	[136, 143]	[144, 145]	[146]

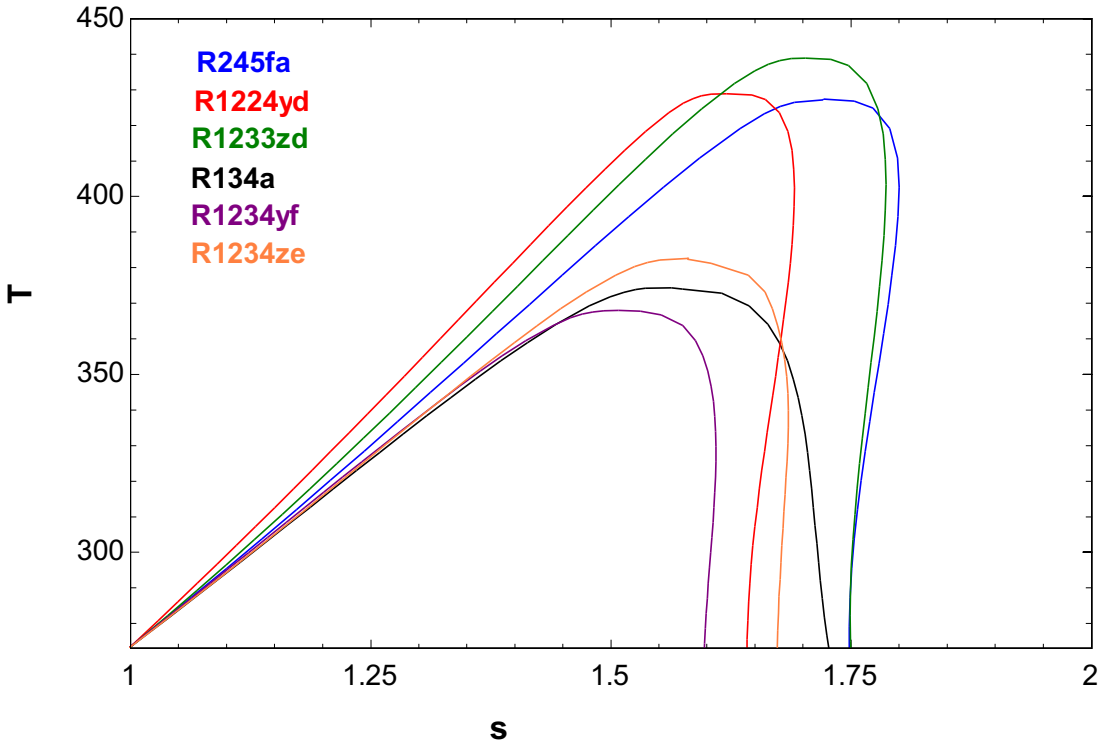


Fig. 2.7 Comparison of R245fa and alternative working fluids;
Temperature (T)-specific entropy (s) diagram of the saturation curve of the fluids.

R245fa: This refrigerant is a hydrocarbon with the chemical name 1,1,1,3,3-Pentafluoropropane. It has a low toxicity, is non-flammable, has shown chemical

stability at temperatures of up to 533[K] and has proven satisfactory compatibility with several polymers such as Polyethylene, Polypropylene, Polytetrafluoroethylene (PTFE), Polyvinylidene fluoride (PVDF) and polyamide (PA). This fluid is commonly used in refrigeration and ORC, though its major application is in the production of insulating foam [136-139]. This refrigerant is harmful to the environment.

R1224yd: This refrigerant is a hydro-fluor-olefin with the chemical name (Z)-1-Chloro-2,3,3,3-Tetrafluoropropane. It is non-flammable and is chemically stable at temperatures of up to 448[K]. It has demonstrated compatibility with several polymers such as Polyvinyl chloride (PVC), Polycarbonate, Phenolic resin, Epoxy resin, PTFE, Polypropylene, Polystyrene, Acrylic, Polyphenylene oxide, Acrylonitrile butadiene styrene (ABS) and PA-66. The R1224yd is an environmentally alternative for the R245fa and is being adopted for refrigeration, ORC systems, heat pumps and foam blowing [140].

R1233zd: This refrigerant is a hydro-fluor-olefin with the chemical name trans-1-chloro-3,3,3-trifluoropropene. It is non-flammable and is chemically stable at up to 373 K. It has demonstrated compatibility with several polymers such as Polybutylene terephthalate (PBT), PTFE, PVC, and PA-6. The R12333yd is used as a blowing agent in the production of foams [141, 142]. This product is not environmentally friendly.

R134a: This refrigerant is a hydrocarbon with the chemical name 1,1,1,2-Tetrafluoroethane or Norflurane. It is non-flammable and is stable at temperatures of up to 448[K], though it may decompose when exposed to higher temperatures, and has demonstrated compatibility with several polymers such as ABS, Acetal, Epoxy resin, PTFE, Ethylene tetrafluoroethylene (ETFE), PVDF, PA-6, Polycarbonate, Polyethylene terephthalate (PET), high density Polyethylene, Polyphenylene Sulfide, Polypropylene, Polystyrene, Polysulfone, PVC and Chlorinated polyvinyl chloride (CPVC). The refrigerant R134a is an environmentally friendly alternative to the refrigerant R12, which is widely applied for refrigeration, foam blowing and aerosols [136, 143].

R1234yf: This refrigerant is a hydro-fluor-olefin with the chemical name 2,3,3,3-Tetrafluoroprop-1-ene. It is mildly flammable and has demonstrated compatibility with

several polymers such as Polyester, PA, Epoxy resin and PET. The R1234yf was conceived as a replacement for R134a for refrigeration applications [144, 145].

R1234ze: This refrigerant is a hydro-fluor-olefin with the chemical name trans-1,3,3,3-Tetrafluoroprop-1-ene. It is mildly flammable and has demonstrated compatibility with the polymeric materials: ABS, Acetal, high density Polyethylene, PA-66, Polyetherimide, PTFE, Polystyrene, PVC and PET. The R1234ze is a replacement for traditional mid-temperature refrigerants in applications such as foam production and refrigeration [146].

A heavy weight substance has a great density, which means a small flow area for a given mass flowrate. Their characteristically small adiabatic index cause most of these fluids to have a low speed of sound. As a consequence, the expansion ratio [76], the number of stages and the rotational speed are reduced for a given Mach number. Organic fluids are also characterised for having a low normal boiling point, allowing turbines to work at super-atmospheric pressure; this fact simplifies their configuration, because no vacuum is needed, and minimises fluid contamination.

Carbon dioxide (CO_2) is of increasing interest as a working fluid due to its numerous advantages, namely, vast availability in nature, non-flammability, low reactivity with polymers, low environmental impact (compared to hydrocarbons) and low cost. CO_2 can be used into the Rankine cycle, often know as trans-critical CO_2 cycle, as shown by Ge et al. [147]. The trans-critical CO_2 cycle is a modern version of the Rankine cycle that is more compact and has better performance for exploiting low-grade heat sources. However, it demands very high pressures during operation because of the required supercritical conditions.

Real Gas Expansion

During the expansion, the behaviour of an organic substance is, in general, different [68, 148] than the behaviour of an ideal gas. The traditional methods for the study of turbines are based on the ideal gas equation of estate [61]. Therefore, the design of ORC turbines with these methods can be imprecise and unoptimized, although these methods can still be used for preliminary designs, where an optimal efficiency is not a strong

requirement or for a narrow operation range where the fluid can be idealized. However, if that is not the case, real gas modelling should be used to achieve optimum results.

Several analytic real gas models may be used for this purpose, namely, Van der Waals, Redlich–Kwong [149], Aungier–Redlich–Kwong [150], and Peng–Robinson [151]. Such models predict the real gas behaviour with more precision than ideal gas formulation and do not represent an important increment in computing time; however, they are still insufficient when superior precision is needed. In that case, the multiparameter Helmholtz energy explicit formulations must be used, which are available nowadays within a user friendly software interface containing databases with a variety of pure and mixed substances. The most popular databases for such a purpose are REFPROP [152], COOLPROP [153] and FLUIDPROP [154]. In research, a great deal of effort is paid to integrate real-gas behaviour into the analysis of turbines. Several studies [60, 61, 72-74, 76, 82, 155-158] intended to include real-gas EoS and updated loss models into the mean-line approach. These actualizations should enhance the confidence on the mean-line study of ORC turbines. Additionally, recent CFD studies also take in account the effect of real-gas behaviour. This allows exhaustive optimization on the design of nozzles [148, 159-164] and rotor blades to be performed [70, 165] as well as targeted studies, for example on rotor-stator interactions [62, 68, 84, 166-170]. It would not be possible to perform these studies without these powerful computational tools.

Polymers for structural elements

The low temperature characteristic of the ORC, can make the implementation of structural polymers in micro-turbines feasible, representing an important advancement in terms of weight and manufacturability. The replacement of metals by structural polymers can be an option to reduce weight and production cost in components such as blades, wheels, volutes and bearings amongst others. This modification can help to reduce the manufacturing effort whilst reducing the fabrication cost of components, which in turn can reduce the cost of the turbine and the entire ORC. Furthermore, this improvement can promote a better adoption of ORC systems in micro-capacity applications such as combined heat and power (CHP) and waste heat to power (WHP).

A review of the literature revealed that only a few research groups have been conducting academic research on the adoption of structural polymers into ORC expanders, though the scientific community has recently gained interest in this topic.

Rahbar et al. [171] presented the design, analysis and preliminary experiment of a turbine fabricated with additive layering manufacturing (Stereolithography) using the material FullCure720. The unit was run at up to 20000[rpm] to validate their CFD model at off-design conditions. They found that polymeric materials and additive manufacturing are advantageous to create functional prototypes of microturbines for various applications, including ORC.

Hernandez-Carrillo et al. [25] proposed the utilization of polymers such as polyether ether ketone (PEEK) and Acrylonitrile butadiene styrene (ABS) for components of an ORC turbine. With an analysis of the fluid-structure interaction, they concluded thatseveral polymers can be adopted for a number of components such as blades, casings and bearings.

Novotny et al. [172] proposed the adoption of polymeric components in expanders, aiming to reduce the cost. They fabricated a several models of turbine components through additive layer manufacturing (metal laser sintering, stereo-lithography and fused deposition of polymers), and concluded that the metal laser deposition is adequate when operation conditions of the prototype are extreme. However, for less-demanding conditions, such as low temperature and power, stereo-lithography and fused deposition of polymers could give satisfactory results for functional prototypes and small production.

Zywica et al. [173] performed a comprehensive assessment on the implementation of polymers for the construction of ORC expanders. They suggested that the upper practical limits of temperature and pressure are 423[K] and 1[MPa] respectively. Their assessment of the mechanical integrity and the chemical compatibility suggest that the material they selected may be suitable for fabricating some subassemblies of turbines, which has a tremendous impact in the fast development of turbine units.

Hernandez Carrillo et al. [174] developed an MTG of 1[kW] nominal power capacity and 36000[rpm] rotational speed; this unit was equipped with polymer

components and used air as the experimental working fluid. They concluded that these components can withstand rotational speeds of up to 40000[rpm] and suggest that those components can achieve efficiencies comparable with standard components.

Novotny et al. [175] conducted an overview of the potentials of additive manufacturing and polymers for the fabrication of turbomachinery components. They presented worldwide efforts to adopt various additive manufacturing methods to produce turbomachinery components. As they explain, the techniques that have produced functional components include stereolithography (SLA), plastic laser sintering (PLS) and fused deposition modeling (FDM).

Weiß et al. [176] developed a construction kit for MTGs with capacities ranging 1[kW]-200[kW] and provided an outlook on the possibilities of additive manufacturing to fabricate components such as turbine wheels. They concluded that the adoption of additive manufacturing and polymeric materials in components of ORC turbines can drive an improvement of the competitiveness of such devices.

Zywica et al. [177] implemented modern polymers for the fabrication of an ORC microturbine with a power capacity of 1[kW] and a rated rotational speed of 120000[rpm]. After having conducted the material selection with mechanical and chemical analyses, they concluded that polyether-ether-ketone (PEEK) and Polyphenylene sulfide (PPS) can potentially be used for the fabrication of components and these materials provide important improvements in terms of ease of manufacturability.

The above review suggest that, polymer components can be a valid option to enhance the technical and economic performance of ORC microturbines; however, the thermo-aerodynamic properties of polymer components to replace standard components is yet to be studied and, therefore, is a topic addressed in this work.

CHAPTER 3. THEORY AND METHODS

In this section, the theory and methods used in this investigation are given. First, the basic theory of turbines, generators and other major components is overviewed to provide a baseline for the development, then the methods are presented, which are comprised of a general method and several specific methods. All of them needed to conduct this research.

3.1. THEORY

3.1.1. Turbines

ORC turbines are aerodynamic machines that convert fluid power into mechanical power. Their principle of operation is similar to that of steam or gas turbines. The process can be separated into two steps: an expansion of fluid and a mechanical conversion of kinetic energy, however, in reality, these two steps can happen simultaneously. The expansion of fluid converts the thermal energy of the fluid into kinetic energy, which is a near-isentropic process that takes place through a set of nozzles and accelerates the working fluid into a jet stream. Then the kinetic energy of the jet stream is converted into useful mechanical power by a number of rows of blades, which are attached to a shaft. This rotative component is known as rotor.

Depending on the flow orientation with respect to the axis of rotation, turbines can be classified into axial and radial; both types are suitable for ORC. Axial turbines are preferred for high flowrates and large capacities due to their ability of multiple staging, which allows high expansion ratios. Thus, axial multistate turbines tend to be the standard choice, though single stage axial turbines are a valid option for applications of low-capacity because they are simpler and inexpensive [178]. Radial turbines are preferred for medium to low capacities since they are adequate for handling moderate flowrates with moderate expansion ratios. Compared to axial turbines, radial turbines are limited to a smaller volume flowrate; however, they can handle a larger expansion ratio per stage (for a given limitation of flow speed). This becomes a considerable advantage when supersonic conditions and/or multiple staging are not desirable.

Typology

Turbines can be sub-classified into single-stage and multi-stage. Single-stage configuration is a simple configuration that is appropriate for low capacities [58] but presents a modest performance and requires high flow and rotational speeds. Conversely, the multi-stage configuration lowers the speed by splitting the expansion ratio [179, 180] in several stages but it can be very complex for low capacity turbines. Because of this ORC rarely require more than two stages [47, 179, 181, 182].

Depending on the flow direction with respect to the axis of rotation, turbines can also be classified in axial and radial as illustrated in Fig. 3.1. Axial turbines are, in general, the most popular due to its numerous advantages: large capacity capability, wetness handling, high reliability, and structural stability. However, complexity and high production cost are major inconveniences. In axial turbines, streamlines face a constant speed of blade, and hence the third term in Eqn.(**3**.**5**) is null, having no contribution to the specific work. Furthermore, impulse (zero reaction) turbines have no change in relative speed of streamlines and the second term of Eqn.(**3**.**5**) is null. On the other hand, radial turbines present advantages that may complement axial turbines, namely, compactness, simple structure [157], light weight and flexibility [47, 60, 72].

Radial turbines can be subcategorised, depending on the flow orientation, of inflow and outflow. Inflow turbines are popular for low capacity because they can handle high expansion ratios with low flowrates in a single-stage; therefore, in low capacity, multi-staging is uncommon. Despite their numerous advantages, the inability of radial turbines to handle wetness in gasses is an important shortcoming and so outflow turbines are preferred for large capacities. Their characteristic centrifugal flow increases the area stream-wise, which helps increasing the expansion ratio [58, 59, 183] and simplifies multi-staging. In radial turbines the three terms of Eqn.(**3**.**5**) have an influence on the specific work; however, the influence of the third term is positive for radial inflow turbines and negative for radial outflow turbines. This means that radial outflow turbines consume a fraction of the available fluid power, which is not desirable because is inneficient.

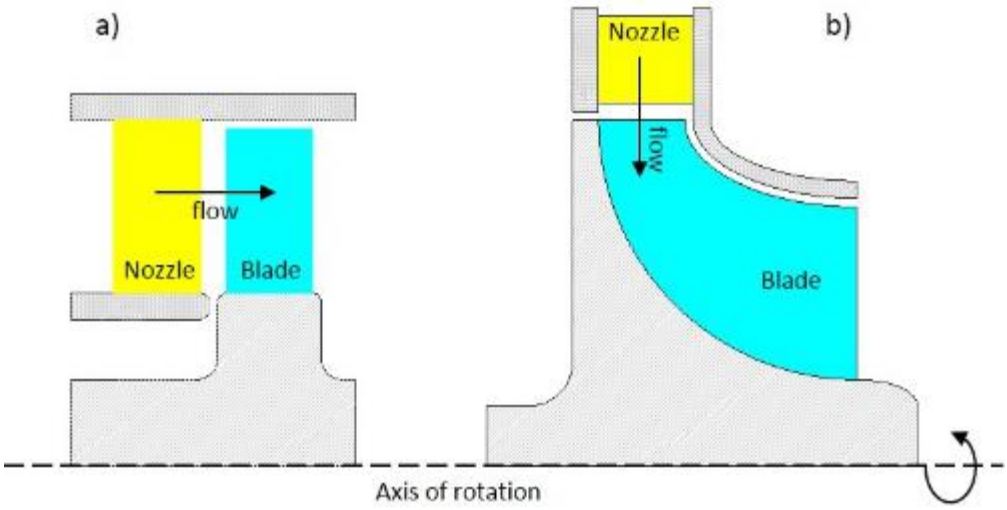


Fig. 3.1 Cross-sectional view of a stage; a) axial flow turbine; b) radial inflow turbine.

Finally, the boundary layer turbine, also named Tesla turbine [184], is an unconventional type of inflow radial turbine that is bladeless. This turbine contains a rotor formed by parallel discs with gaps among them. Tangential nozzles produce an inwards radial (spiral pattern) through these gaps and the drag forces in the wall make the rotor spin. This turbine is characterised by having a very low torque and a high rotational speed to achieve a barely competitive efficiency. However, its simplicity may offset these disadvantages and make it an interesting alternative for applications where the economic effectiveness is critical.

Thermo-aerodynamics

In the expander, the expansion of a confined fluid (working fluid) converts its thermal energy into mechanical work. In expanders of the turbine type, this conversion is driven by a thermo-aerodynamic interaction between the flow stream and a set of nozzles and moving blades (stage), as illustrated in Fig. 3.2, where the main parts of a turbine are exemplified. The analysis of turbines typically starts with the definition of boundaries, and then, the aerodynamic interaction is manipulated to obtain a desired performance.

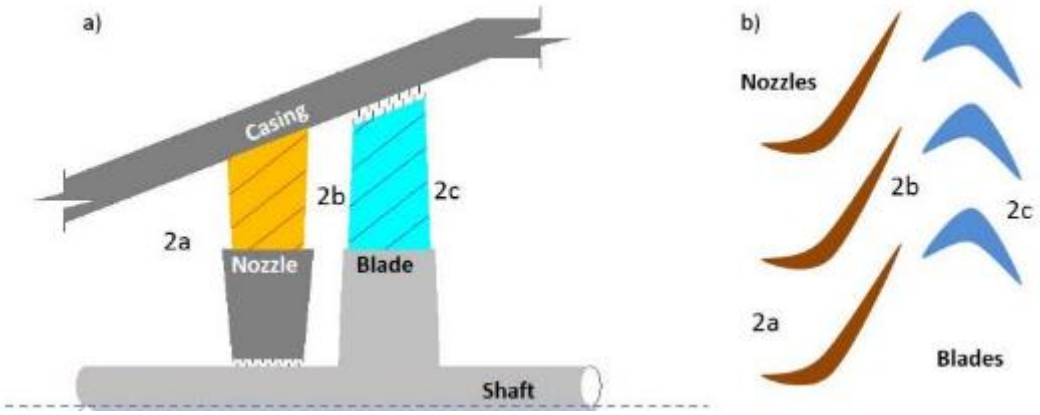


Fig. 3.2 Turbine type schematic; a) Meridional view; b) Blade to blade view.

Across the nozzle, the total specific enthalpy is considered constant as shown in Eqn.(3.1) and the change of total pressure is given by Eqn.(3.2). The total pressure and temperature for any give state, i, can be obtained with their corresponding static properties and their relationships shown in Eqn.(3.3) and Eqn.(3.4) respectively.

$$h_{01} = h_{02} \tag{3.1}$$

$$P_{02} = P_{01} - \Delta P_{loss} \tag{3.2}$$

$$h_{0i} = h_i + \frac{1}{2} c_i^2 \tag{3.3}$$

$$P_{0i} = P_i + \frac{1}{2} \rho_i c_i^2 \tag{3.4}$$

Aerodynamics

The change of total enthalpy across the rotor is governed by the Euler equation for turbines and pumps [185], presented in Eqn.(3.5), which predicts the ideal specific work of a turbomachine in terms of total enthalpy drop. This equation makes evident that the specific work is a sum of three terms, which are the difference (from the inlet to the outlet) of the square speed of the blade, u, the square absolute speed of the fluid, c, and the square relative speed of the fluid respect to the blade, w. This equation has enormous

relevance in turbomachinery since is the foundation for performance prediction and has major implications on the turbine topology.

$$\Delta h_0 = \frac{1}{2}\left[\left(c_2^2 - c_3^2\right) - \left(v_2^2 - v_3^2\right) + \left(u_2^2 - u_3^2\right)\right] \tag{3.5}$$

The velocity triangles presented in Fig. 3.3 are determined using a combination of the equation of continuity, the thermodynamic equations, the nozzle geometry and the rotor geometry. These triangles show the relationship of the aforementioned absolute velocity, c, relative velocity, w, and the blade velocity, u, at the inlet and outlet of the rotor. The rotor-inlet is denoted with the subscript 2 and the rotor-outlet is denoted with a subscript 3. The components on the flow direction are denoted with the subscript f whereas the components on the tangential direction (movement of the blade) are denoted with the subscript u.

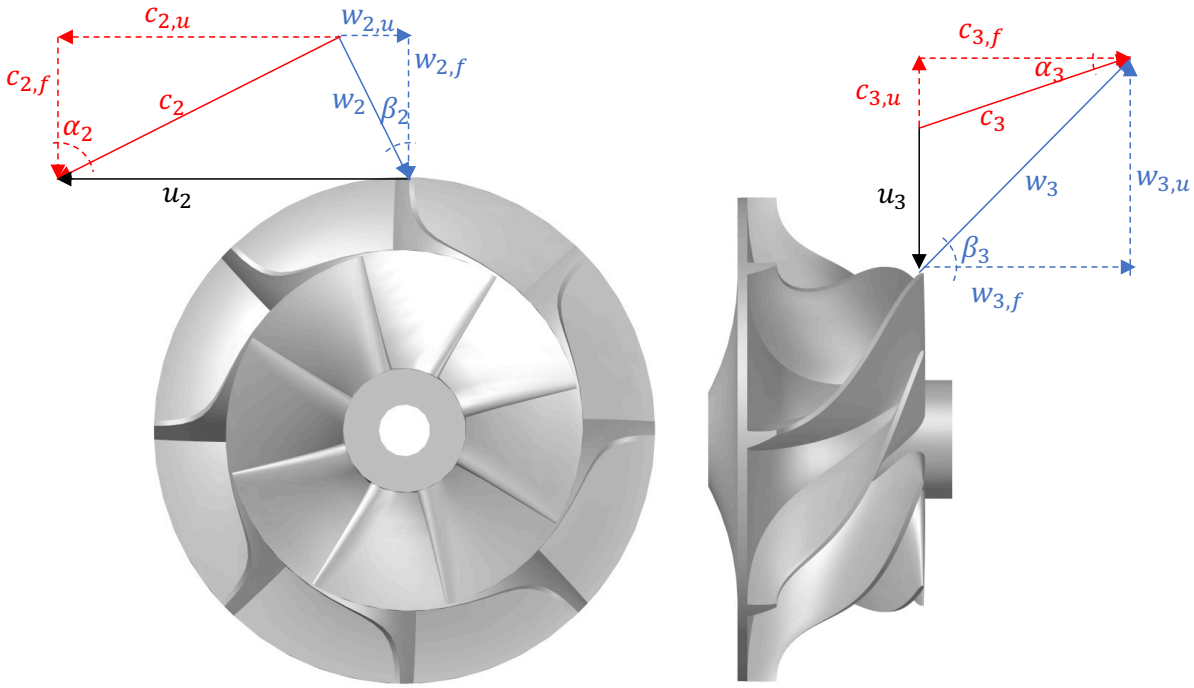


Fig. 3.3. Velocity triangles for the turbine rotor at off-design conditions;
c: absolute flow speed, u: blade speed; w: relative flow speed; α: absolute angle of the flow with respect to the flow direction; β: relative angle of the flow with respect to the movement direction; 2: impeller inlet conditions; 3: impeller outlet conditions; sub index u: in tangential direction; sub index f: in the flow direction.

Efficiency and power

Thermodynamically, the actual power can be predicted with Eqn.(3.6) and the thermodynamic efficiency can be obtained with Eqn.(3.7).

$$\dot{W}_{thermo} = \dot{m}\Delta h_0 = \dot{m}\Delta h_{0s}\eta_{thermo} \tag{3.6}$$

$$\eta_{thermo} = \frac{\Delta h_0}{\Delta h_{0s}} \tag{3.7}$$

If the adiabatic condition is met, the aerodynamic power should be equal to the thermodynamic power as shown in Eqn.(3.8); consequently, the aerodynamic efficiency should also be equal to the thermodynamic efficiency as shown in Eqn.(3.9).

$$\dot{W}_{thermo} = \dot{W}_{aero} \tag{3.8}$$

$$\eta_{thermo} = \eta_{aero} = \eta_{thermo-aero} \tag{3.9}$$

Mass flow

The mass flow can be iteratively obtained by simultaneously solving all the above equations and the equation of continuity for a volume of control shown in Eqn.(3.10).

$$\dot{m} = \rho_2 A_2 c_{f,2} = \rho_3 A_3 c_{f,3} \tag{3.10}$$

Mean-line analysis and loss models

Although Eqn. (3.5) is a simple model to predict the behaviour of turbines, it does represent a single stream line of flow. When a single stream line that represents the average behaviour of the transversal section is used, the method is named mean-line modelling or one-dimensional modelling. Mean-line modelling is usually the first step in the design and study of turbines, because it can provide an accurate prediction of the performance in a fast manner with minimal resources. The use of the mean line method

enables the possibility of using stochastic optimisation using genetic algorithms [72, 156, 157] or Monte Carlo simulations. Additionally, mean-line modelling also permits the generalisation of results if dimensional similarity is achieved, which significantly reduces the effort in the design and study of turbines.

The main-line analysis can provide a close prediction of the real performance if inefficiencies are taken into account. This is possible with loss models, which are a set of empirical coefficients that affect the mean-line theoretical modelling to account for losses of different types. Generally, loss models include power reduction due to exiting kinetic energy, profile friction, windage, incidence flow disturbances, secondary flows, partial admission, clearance leaks, and shock waves [58, 61, 186].Exiting kinetic energy and profile friction are often the most dominant loss mechanisms in subsonic flows whereas shockwave losses become substantial in supersonic flows[156]. Diverse empirical loss models exist, but none of them have proven general applicability; for that reason, they are categorised according to turbine typology. For Axial turbines the most popular loss models are: Soderberg [185, 187], Ainley-Mathienson [188], Balje-Binsley [189], Traupel [190], Denton [191], Dunham-Came [192], Kacker-Okapuu [193], Craig-Cox [64] and Aungier [150]; whereas for radial turbines are: Rohlik [78], Baines et al. [77, 194], Suhrmann et al. [75] and Aungier [150]. An important point to highlight is that these models were conceived for the modelling of gas turbines, hence they consider the ideal gas equation. For this reason, their applicability in the study of ORC turbines can be questionable as highlighted by White-Sayma [74], who concluded that the mean-line analysis is not sufficiently validated for organic working fluids and may not be accurate enough especially to model supersonic flows. However, if the working fluid can be considered as an ideal gas in the range of operational conditions, these models can provide an accurate prediction.

Dimensional similarity

The performance of turbines depends on several parameters and hence is graphically difficult to represent. However, as stated by Dixon-Hall [185], the performance of turbines can be described with a reduced number of dimensionless independent parameters. For example, geometrically similar turbines working with a single fluid can be modelled with only four parameters [195], although this is still difficult to represent

graphically. Nevertheless, families of turbines can be derived when the effect of some parameters is fixed or neglected e.g. degree of reaction or Reynolds number. In that case, the performance can be predicted with two parameters only, which is easy to represent in specific charts. Often, the flow coefficient, ϕ, and the loading coefficient, φ, are paired together to represent the performance of existing turbines while the specific speed, Ns, and specific diameter, Ds, are paired for design purposes. Nevertheless, Rahbar et al. [72] and Da Lio et al. [61] consider that the volume ratio, VR, and the size parameter, SP, may be more appropriate for representing ORC turbines. The definition of the above-mentioned parameters is presented in Eqn.(3.11)-(3.16).

$$\boldsymbol{\phi} = \frac{\boldsymbol{c_{f,2}}}{\boldsymbol{u_2}} \tag{3.11}$$

$$\boldsymbol{\psi} = \frac{\boldsymbol{\Delta h_{0S}}}{\boldsymbol{u_2^2}} \tag{3.12}$$

$$\boldsymbol{Ns} = \boldsymbol{\omega}\frac{\boldsymbol{Q^{1/4}}}{\boldsymbol{\Delta h_{0s}}^{\boldsymbol{3/4}}} \tag{3.13}$$

$$\boldsymbol{Ds} = \mathbf{D}\frac{\boldsymbol{\Delta h_{0s}}^{\boldsymbol{1/4}}}{\boldsymbol{Q^{1/2}}} \tag{3.14}$$

$$\boldsymbol{VR} = \frac{\boldsymbol{Q_1}}{\boldsymbol{Q_4}} \tag{3.15}$$

$$\boldsymbol{SP} = \frac{\sqrt{\boldsymbol{Q_4}}}{\boldsymbol{\Delta h_{0s}}} \tag{3.16}$$

Dimensional similarity allows the prediction of performance of a certain turbine based on experimentation of any other similar turbine or condition. In other words, comparable performance is expected from different members of the same family of

dimensionally similar turbines. Analogously, comparable performance is expected from a given turbine if operated in different but dimensionally similar conditions e. g. different working fluid [185, 196-199]. More generally, the analysis of a specific case can be analogous to any other if the dimensionless parameters are common [63]; although negligible differences are still to be expected because the complexity of matching all the dimensional numbers. The dimensional similarity principle is highly reliable and widely used to predict the behaviour of turbines in a great range of situations.

Specific charts

Specific charts are a convenient manner for presenting the performance of a family of turbomachines. A Smith type chart [200] for axial turbines of 50% degree of reaction is shown in Fig. 3.4; in this figure, the efficiency can be easily predicted by giving values of the loading and flow coefficients. Similarly, in a Balje-Binsley type chart [189], the efficiency and basic design can be predicted by giving values for the specific speed and diameter. As these charts are derived from the mean-line analysis, their applicability to be used in ORC turbines may be questionable [72], as warned by Da Lio et al. [61] who questioned the suitability of Balje-Binsley type charts [189] for designing micro ORC turbines.

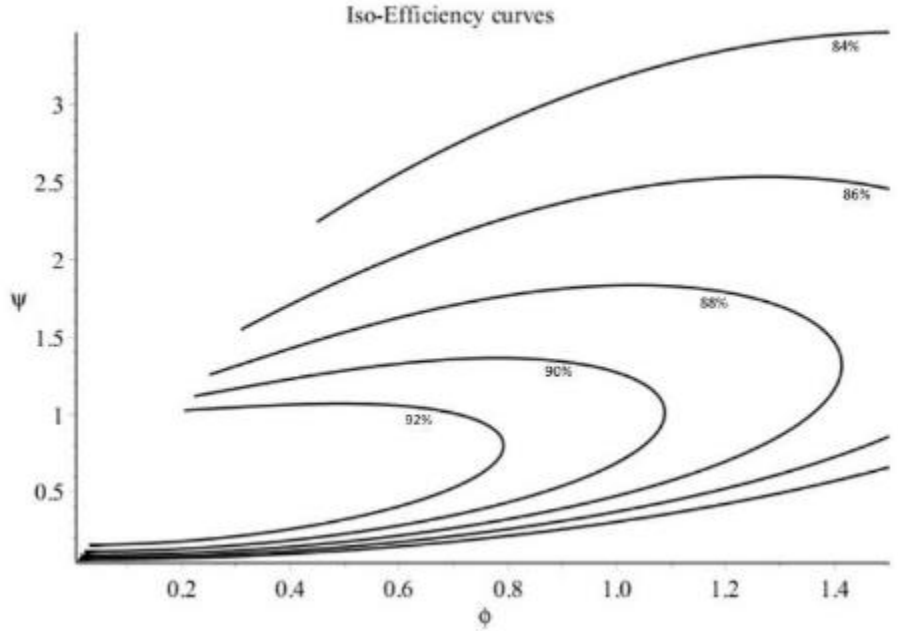


Fig. 3.4 Specific chart (Smith type) axial turbines with 50% reaction; loading coefficient (ψ) and flow coefficients (ϕ), adapted from Dixon-Hall [185].

Computational Fluid Dynamics

When studies with more detail are pursued, the computational fluid dynamic (CFD) analysis is a powerful tool that allows a three-dimensional study of turbines. CFD analysis is fed with the boundary conditions, and then the problem is solved by dividing the volume of control in elements where the fundamental equations (e.g. Navier-Stokes) are linearized and solved. This method can accurately account for friction losses since it allows for turbulence models [56, 66-68, 70, 73, 167], which quantify the head losses caused by turbulence. CFD modelling predicts the flow behaviour with high accuracy but demands large computational resources. An alternative method to the traditional CFD is the throughflow modelling [201]; this method is said to give sufficiently accurate results for a fraction of the computational cost. The method assumes averaged axisymmetric flow in the path and solves the problem for the meridional plane. In other words, the method provides a two-dimensional solution for a complex three-dimensional problem. Although is not as accurate as traditional CFD, the throughflow analysis can be considered as a balance between mean-line analysis and CFD modelling. An illustrative comparison of both methods is presented in Fig. 3.5.

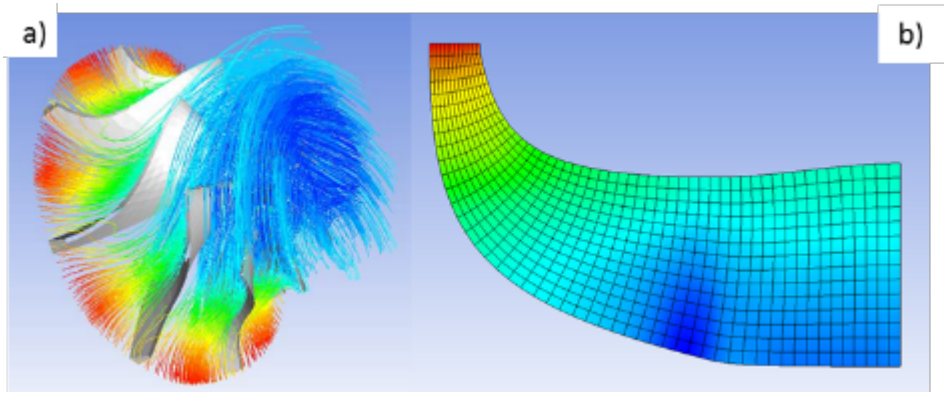


Fig. 3.5 Simulation of a radial turbine rotor;
a) three-dimensional view of a traditional computational fluid dynamics (CFD); b) meridional view of a turbomachinery throughflow model.

Low Capacity

Turbines of low capacity demand low flowrate and, consequently, reduced flow area. Implementing, short blades, a reduced diameter and partial admission can promote reduction in capacity. Partial admission is only suitable for impulse turbines as it increases friction losses, produces fatigue [56, 57] and large overall dimensions. In

contrast short blades have a practical limit due to manufacturing limits. Therefore, reduction of the mean diameter is a common practice, which allows compactness, practical height of blades and full admission. In contrast, the resulting high rotational speed of reduced diameter turbines requires sophisticated bearings [38] and attachment of blades [202].

A high rotational speed is a characteristic of downsized turbines. This feature is derived from the loading and flow coefficients which, for maximum efficiency, are constant for a family of turbines. Therefore, a given enthalpy drop leads to a constant speed of the blade regardless of the capacity if maximum efficiency is pursued and consequently, small diameter turbines need high rotational speeds to be efficient.

ORC is especially suitable to work with low enthalpy drops, hence, single stage turbines are the natural selection because they allow simplicity and cost effectiveness. If large enthalpy drops are involved, supersonic flow may become present increasing passage and shockwave losses [58]. Shockwave losses can be accommodated [76] in single stage turbines but multiple staging may be an adequate alternative.

Relative clearances in microturbines are more substantial [58] than in conventional turbines; causing a larger fraction of leaking fluid. Additionally, the frictional loses are proportionally higher in narrow passages, especially if the material surface is not smooth. Thus, clearance, windage and friction losses are more significant. Furthermore, around 0.03 of inefficiency is expected due to heat losses [57]. As a consequence, the efficiency of microturbines rarely exceeds 0.8 [38], and a reasonable target may be around 0.7 [38, 58].

3.1.2. Generator

A basic design of a high-speed brush-less permanent magnet generator can be conducted following the method proposed by Arkkio et al. [203]. Although this method was conceived for the design of electric motors, it can be adopted to design electric generators because they are analogous machines. Using this method, a simple design of a high-speed motor can be accomplished with a series of seven consecutive-iterative steps: definition of the driven machine, structural design, design of the bearings, electromagnetic design, thermal design and definition of the power supply. As motors

and generators are reversible, the design of a high-speed generator would have seven corresponding steps: design of the driving machine, structural design, design of the bearings, electromagnetic design, thermal design and definition of the power consumption. A comparative schematic of these procedures is presented in Fig. 3.6.

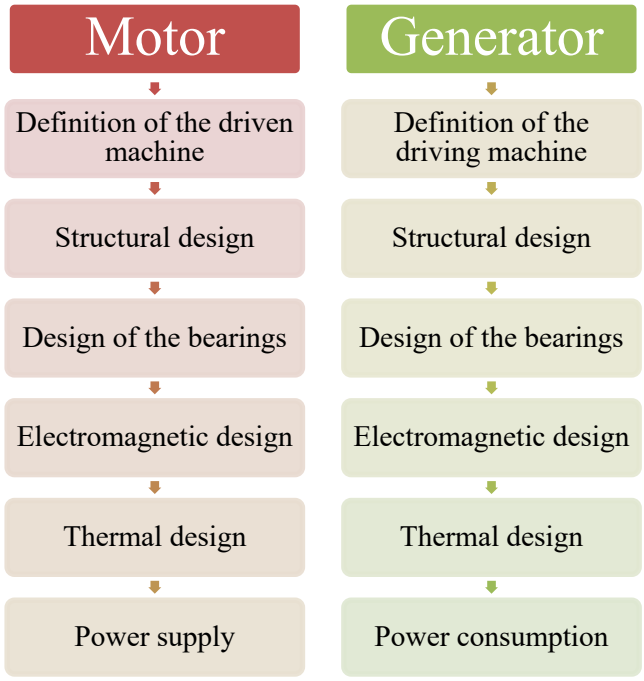


Fig. 3.6 Comparison of the design procedure for high-speed motors and generators;
figure adapted from Arkkio et al. [203].

For the definition of the driving machine, the power and speed requirements are essentially set. In the structural design, the integrity of the rotor is investigated. The generator rotor is usually made of a solid metal rod in which permanent magnets are mounted and fastened with an outer sleeve that holds them in place against the centrifugal force. As a practical rule [203], the active length of the rotor is recommended to be 2.5 times the bore of the stator to ensure the rotor has a critical speed considerably above its rotational speed, though the critical speed of the entire rotor-bearing system might actually be lower than the rotational speed. For the design of the bearings, the structural static and dynamic responses of the rotor-bearing system should be considered. For the electromagnetic design, the calculation of the magnetic field is investigated. This task is usually performed into a finite element electromagnetic software, though a preliminary design can be achieved with analytic calculations based on the specialised literature. For the thermal design, the heat transfer of the generator,

for cooling the rotor and stator, is investigated. This analysis can be done using a thermal network model [203]. In this analysis, the temperature rise, which is a constraint, can be determined as a function of the power losses in the stator (windings, slots and core) as well as the power loss due to friction (bearings and winding). Lastly, the type of the power consumption has to be defined where the rectification and inversion of the generator output signal, as required, must be considered to transform the generator output into a standard power signal, either alternating or direct current.

3.1.3. Control

The control of vapour turbo-generators (TG) consists of controlling the rotational speed and the output power. In conventional power generation, the rotational speed is kept constant to ensure a match between the power output and the frequency of the distribution/consumption network while the power has to be controlled to satisfy the load. These two parameters are typically controlled through variations of the mass flowrate supplied to the TG so that the unit can keep a constant speed whilst supplying the required power; this process is known as governing. Three methods and/or combinations of them are commonly used for governing a TG [204]: throttling, nozzle controlled governing, and bypassing.

Throttling varies the mass flow rate by opening or closing an inlet control valve and, as a consequence, the pressure into the turbine changes, which results in variations of the power. Throttling is the simplest method of governing, though it produces a poor performance of the unit in off-design conditions. Nozzle controlled governing, independently opens or closes individual nozzles or clusters of nozzles. This produces a variation of the mass flowrate only in one nozzle or one cluster of nozzles without disturbing others, which allows the control of the unit with an enhanced off-design performance. However, this type of governing is more complex, expensive and requires multiple valves and actuators. The bypass governing diverts the flowrate of working fluid either to a later stage of the turbine or to the exhaust. This governing type can increase or decrease the power, depending where the bypass is connected to. Although a bypass has the advantage of keeping the upstream conditions relatively constant, it has the shortcoming of reducing the efficiency as the bypassed fluid does not produce power.

The aforementioned controls vary the inlet mass flow with a valve, integrated to the governing loop, that responds to changes of the load whilst keeping the rotational speed constant. In the case of a conventional TG, for example, the rotational speed is measured and compared with a reference speed; if a difference is found, the valve opens or closes to reduce such a difference as illustrated in Fig. 3.7a. In contrast, in a variable frequency TG, the rotational speed does not need to be constant, though the flow rate still needs to respond to changes of the load. Thus, in the governing system for a variable frequency TG, the control valve can be governed with the frequency or, alternatively, the voltage and/or current as illustrated in Fig. 3.7b. This type of governor is common for governing high-speed variable frequency gas microturbines [205] and low-capacity ORC turbines [116, 117].

Additionally, the control valve can be operated with diverse types of actuators; this includes mechanic, hydraulic, pneumatic, electric, electronic or a combination of them. Conventionally for a high-speed TG the actuation is electro-mechanic or pneumatic, which is accurate and reliable, though consumes some of the output power, requires additional hardware and makes the control complex and expensive.

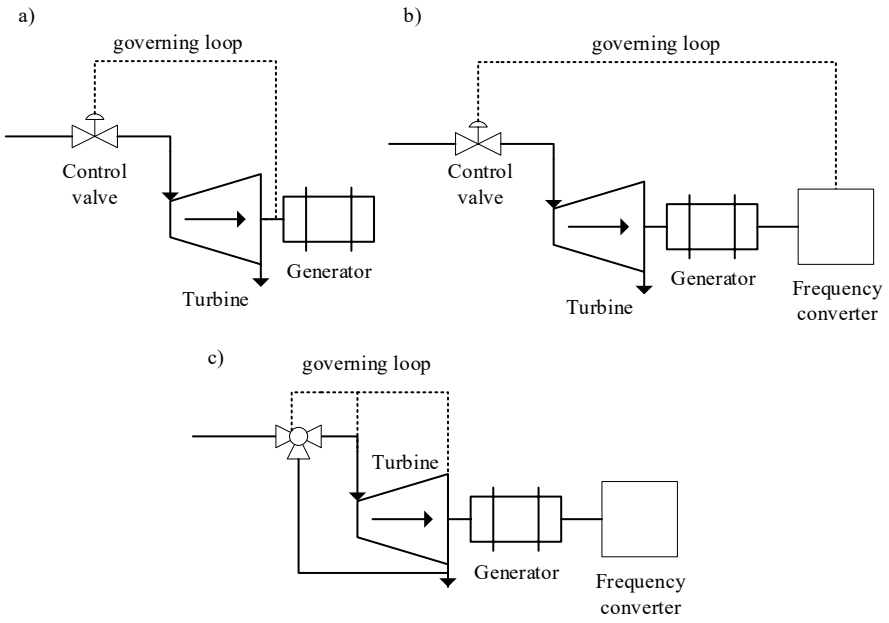


Fig. 3.7 Diagram of the governing loop;
a) conventional turbine-generators; b) variable frequency turbo generators.

3.2. METHODS

3.2.1. General development method

To accomplish the development of the MTG-ORC, the product design method [206, 207] was selected. This method was chosen because the MTG-ORC has the potential of becoming a product, or part of a commercial system if the feasibility is proven. As shown by Dieter and Schmidt [206], the product design method is analogous to the scientific method in terms of the logical procedure. However, fundamental differences exist in terms of their philosophy as the scientific method is dedicated to studying natural phenomena while the design method is dedicated to studying human-made artefacts.

The product development process comprises five stages that end with the production of a product or service; such a process is illustrated in Fig. 3.8, where the main activities can be seen. The first stage in this process is a systematic exploration of the need, which is normally a problem to be solved or an unaddressed opportunity. Then, two critical stages follow: design and testing. These two stages are vital for the evolution of the product/service because this is where the transition from an idea to a solution [206]. Design encompasses three major tasks: conceptual design, also known as concept development; embodiment design and detailed design. Testing usually involves the fabrication of a prototype, a production of small batch of the product or a pilot run of the service, which are then put into the test in a real or a simulated environment. In the fourth stage, an exhaustive assessment of the ability of the product/service to solving the need/problem is conducted. Finally, if the product/service seems to be adequate, a full production takes place. Although the product development process seems to be continuous and consecutive, in reality, it is an iterative and discrete process that requires frequent stopping and revision of the upstream activities when downstream requirements are not met.

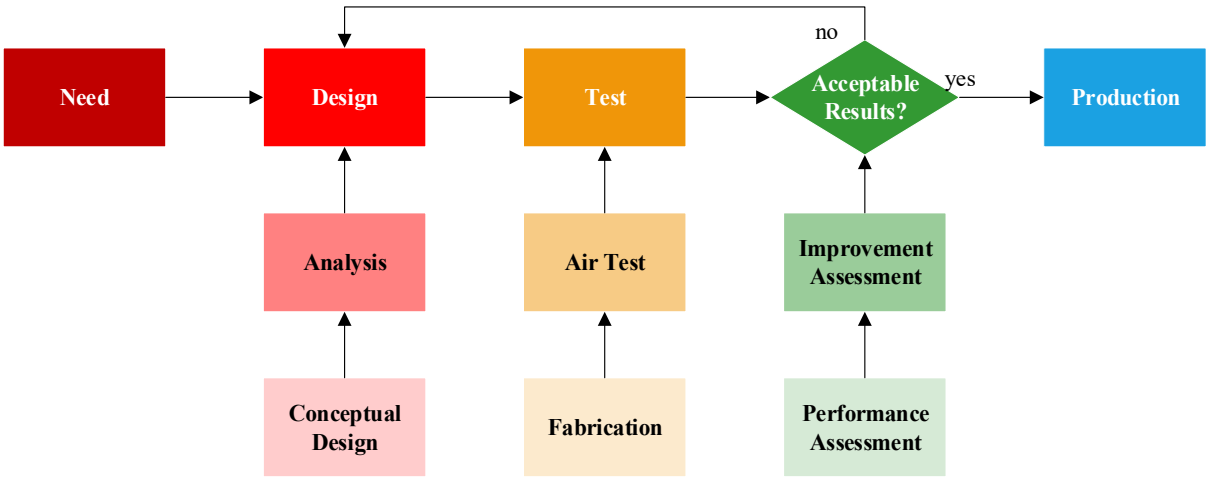


Fig. 3.8 Schematic of the development process;
adapted from Dieter and Schmidt [206].

3.2.2. Exploration of the need

The first step is exploring a need to be addressed. Then, as explained in Chapter 1. , the need driving this research is the enhancement of the techno-economic performance of an MTG-ORC. Thus, a simplified root-cause analysis was performed to identify characteristics that could potentially improve its performance and this analysis is used to make the conceptual design of the unit in section 4.1. A summary of such a root cause analysis is presented in Fig. 3.9, where three major categories of improvement can be seen: health and safety, function and cost.

The category of health and safety was divided into two subcategories: environmental impact and health and safety risks to the final user. In the environmental impact subcategory, emissions are clearly a major area of improvement as the MTG-ORC will eventually use a potentially harmful fluid that can leak. The emission of noise is another area of improvement since a quiet operation is a requirement in the domestic environment. In the safety subcategory, bursting of the MTG-ORC case leading to a release of harmful gas was identified as the principal risk that must be avoided in a domestic application.

The category of function was divided in three subcategories: efficiency, reliability and compactness. The efficiency is one of the most important aspects overall; thus, it is important to maintain it as high as possible. However, the practical limit of efficiency of ORC micro-turbines may have been reached already and so the MTG-ORC must

ensure at least an efficiency comparable to current models. The efficiency is affected by losses, which are primarily aerodynamic, mechanic and electric. Reliability is another important aspect of the MTG-ORC that can be improved by reducing the failure rate and extending the lifespan. Finally, compactness is a desired feature particularly sought for domestic and portable systems, where the available space is scarce.

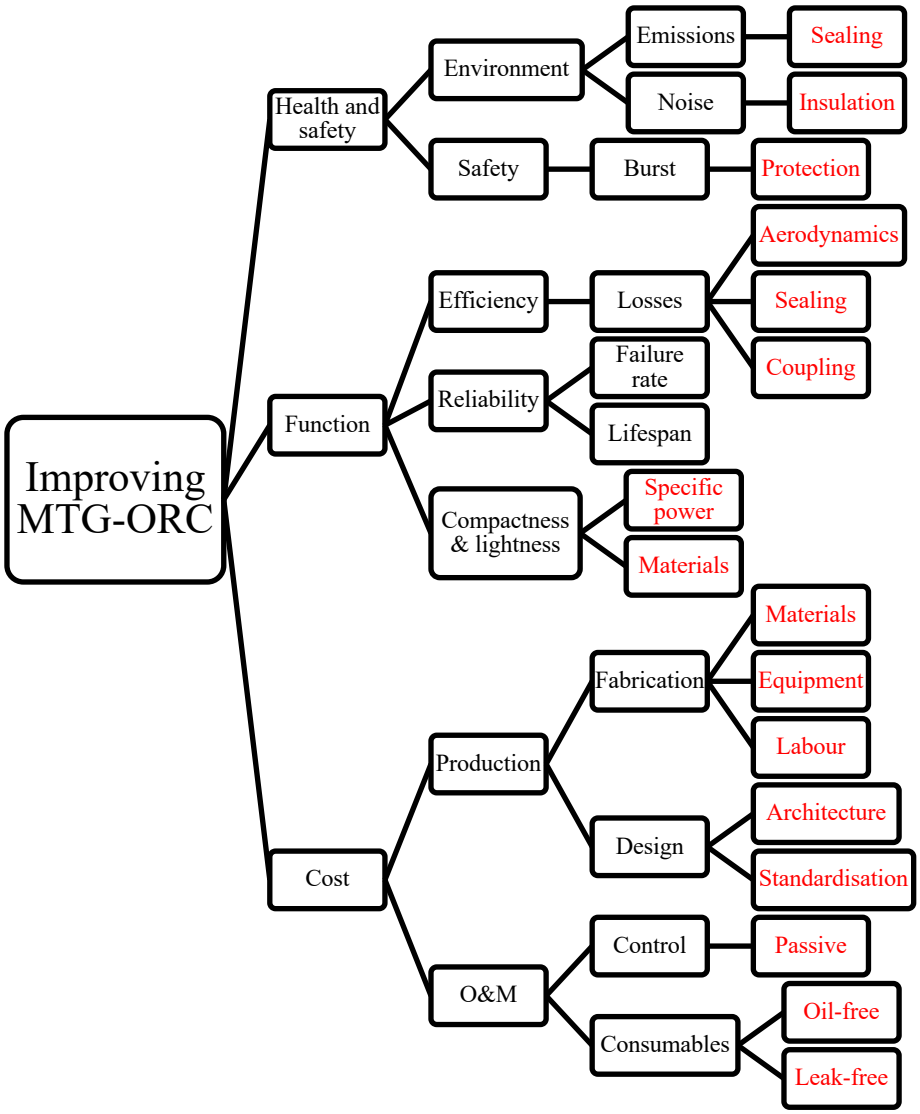


Fig. 3.9 Root-cause analysis for improving the overall performance of an MTG-ORC.

The category of cost is divided into two subcategories: production and operation and maintenance (O&M). The production cost can be enhanced with modifications of the design and/or the fabrication methods whereas the O&M can be improved with modifications of the control and/or reduction of the consumables.

3.2.3. Design

In the conceptual design, the boundary conditions are set and the desirable features are given to the MTG-ORC. Therefore, the architecture of the unit is defined and further developed throughout this process, which is comprised by the six tasks shown in Fig. 3.10 and explained below.

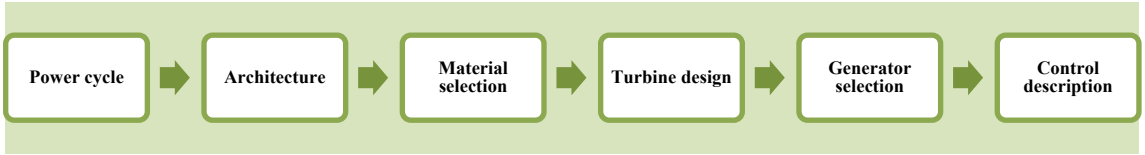


Fig. 3.10 Steps for the conceptual design of the MTG-ORC.

The first task is the definition of the power cycle, where the specific application and the working conditions are defined. The method followed for this task is reported by Hernandez-Carrillo et al. [25] and given in section 4.2. The second task is the definition of the architecture, where the typology of the turbine, the generator and the coupling method are defined alongside the general configuration of the MTG-ORC. The procedures followed to complete this task is presented in section 4.3, which consist in giving a number of proposed features to address the opportunities identified in the aforementioned root cause analysis. The third task is the material selection, where a selection of the materials is made and a review of their relevant properties and characteristics is given and presented in section 4.4. The fourth task is the design of the turbine, which includes the mean-line design, the geometry definition and the selection of major elements (nozzle body, impeller, shaft and scroll); the methods used to complete this task are described in section 4.5. The fifth task is the generator design, where the design and/or selection of the main components of the generator is made. The selection of the generator and the theory for selection are explained in section 4.6. Finally, the control and the principle of operation are explained in 4.7.

3.2.4. Analysis

The second step of the design is the analysis, where a number of studies are conducted to predict the performance of the unit before putting it into a test. The aim of this step is an early assessment of the behaviour of the unit to avoid malfunctioning, unnecessary rework and/or health and safety risks in later stages of this research. The analysis is divided into three tasks: a simulation of the thermo-aerodynamic

performance, a study of fluid-structure interaction and a study of chemical compatibility. The flow diagram given in Fig. 3.11 represents the sequence in which tasks are planned, though that is not necessarily the actual sequence followed during this work.

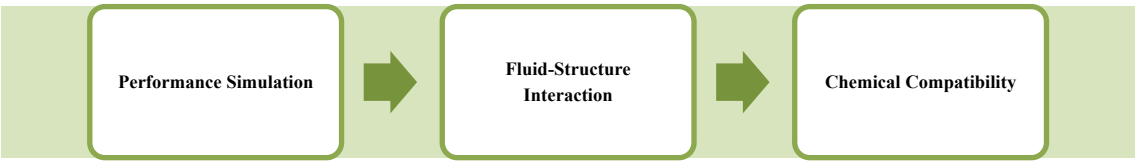


Fig. 3.11 Steps of the analysis of the MTG-ORC.

For the first task, a program for the simulation of the thermo-aerodynamical performance was developed; the procedure to develop such a program is presented in section 5.1 and the results are given in section 5.1.5. This program assesses the unit at off-design conditions working with different working fluids and provides the results in a dimensionless interpretation. This allows predicting the performance of the unit either in real or simulated conditions with comparable results, which considerably simplified the experimental test. For the second task, a study of the interaction fluid-structure is given in section 5.1.5. In this study, a structural assessment of the turbine blades is performed to assessing the effect of the flow pattern and the operating conditions onto the turbine impeller. The aim of this study is providing an early diagnosis of the mechanical integrity of the rotor under a real gas expansion and high rotational speed operation. Finally, the third task consisted of a chemical compatibility study, presented in section 5.3, where a chemical assessment of the interaction between selected polymers and working fluids is made. The aim of this study is to provide awareness of the resilience of polymers into a refrigerant environment.

3.2.5. Test

The next stage of the product design process, according to Fig. 3.8, is testing. The MTG-ORC with the proposed features is tested to validate the simulation program, predicting the thermo-aerodynamic performance, understanding its dynamic behaviour and assessing the reliability and mechanical integrity of the new proposed components. To achieve this, a prototype of the MTG-ORC needs to be fabricated and tested at the laboratory.

Fabrication

A prototype of the MTG-ORC is fabricated in accordance with the developed design and using the techniques described in section 6.1. Essentially, the unit is built using a few custom-made components, several standard elements and diverse manufacturing methods such as machining, assembling and additive layer manufacturing (3D printing). The standard elements are adapted from turbochargers and high-speed electric motors whereas the customised components are designed and fabricated in purpose.

Test with air

The prototype is tested under dynamic similarity using the rig described in 6.2 and the procedure proposed in section 6.3. This means that the test is made using air as the working fluid, instead of the refrigerant, and dynamic similarity of the flow is assured. With this technique, the dimensionless results of the test can be compared with the dimensionless results of the simulations and the aerodynamic performance of the MTG-ORC can be predicted with reference to the dynamic similarity principle.

3.2.6. Presentation of results

Performance assessment

An assessment of the performance of the MTG-ORC with air is made separately with the results of the program simulations, section 5.1.5; the air test, section 6.4.2; and the enhanced air test, section 6.4.3. Additionally, a prediction of the actual performance with refrigerant as the working fluid is done using the principle of dynamic similarity and is presented in section 7.1. Afterwards, an assessment of the performance of the unit from the mechanical, electrical and chemical point of view is presented in section 6.4.5. Lastly, the thermo-aerodynamic performance of the MTG-ORC with polymer components is compared with the performance of an state-of-the-art micro-turbine and presented in section 6.5.

Improvement

A discussion of the improvement is given in section 7.2, where a reflective assessment of the potential improvement to the MTG-ORC derived from this work is

given. Such an analysis is comprised by an evaluation of the feasibility of the proposed features, an assessment of the technical and economic impact that these features could produce into ORC systems and an outlook of the impact onto other industries beyond the ORC

3.2.7. Health and safety

A risk assessment was performed to identify critical hazards during the test. Four main hazards were identified: rotating equipment, pressurised air, noise and electricity. A description of these hazards and the measures to mitigate their effects to the personnel are presented below.

I. Rotating equipment

As exposed in section 4.8, failure of the MTG-ORC could happen leading to ejection of debris. The consequence measures to avoid rotor runaway and/or mitigating the effect of ejected debris, in case of occurrence, must be implemented during the experimental test. Additionally, in rotating equipment, an anticipated diagnose of failure can be done through the monitoring and analysis of its vibrations; therefore, the methods to monitor the vibration have also to be implemented to promote an early identification of failure.

The measures to minimise the occurrence of over-speed during the test were:

- The rotational speed was continuously monitored
- The rotational speed was kept under the allowed limits by controlling the expansion ratio
- The test is performed with small changes of load and sudden total unloading is avoided
- The vibration is monitored

The vibration of the unit was monitored and the works stopped immediately when excessive vibration occurred. The recommended method to monitor the vibration is described in the standard “ISO 20816: Mechanical vibration—Measurement and evaluation of machine vibration” [208]. In this standard, the maximum allowable level of vibration is defined, which, for micro-turbines (1.5[kW] capacity or lower) is 4.5[mm/s]; thus, if a higher vibration level is experienced the experiment must stop. In

this method, vibration transducers are used, which measure acceleration, velocity or displacement of structural static elements of the rotating machine. This signal is later processed to determine the level of vibration. As a result, the monitoring of vibration demands sophisticated and expensive equipment, which is not currently available for this research. Thus, a qualitative assessment of the vibration is made with the "balanced coin" technique described below.

The balanced coin technique is a qualitative method to assess the level of vibration of a machine. Although this is not a standard method, it is widely used in the practical application of turbomachinery. The method consists of a metal coin with approximate dimensions of 25[mm] to 28[mm] diameter and 1.5[mm] to 2[mm] thickness, which is balanced on a horizontal flat surface of the machine while running. If the coin remains balanced, the unit may be considered under acceptable vibration level; if the coin falls down, excessive vibration is occurring, the experiments must stop and an exhaustive vibrational diagnosis is needed. This method was used for assessing the vibration condition during the test and the test was stopped every time the coin felt down.

Additionally, the measures to mitigate damage and personnel injury due to ejected debris during the test were:

- The transit across the working area and the surroundings was limited with cordoning tape
- An outer enclosure with internal deflection baffles was used to contain ejected debris

The outer enclosure shown in Fig. 3.12 was fabricated, according to the specification of section 4.8, to contain ejected debris regardless the origin. This tank encloses the entire MTG-ORC to prevent injury to the personnel in case of burst. However, unlike the enclosure described in section 4.8, for practicality, the enclosure employed in the test is a previously existing tank that is not hermetic and hence cannot prevent leaking. Nevertheless, as the working fluid is air, the lack of hermeticity was not considered an issue for the purposes of this test.

a) b)

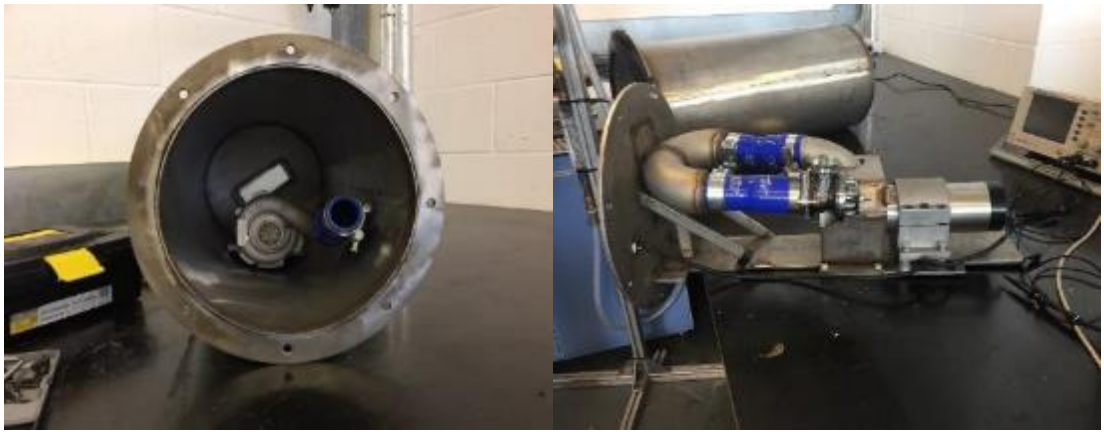


Fig. 3.12 Photograph of the burst containment tank;
a) micro-turbine fitting inside; b) microturbine mounted in a skid on the tank cover.

II. Pressurised air

The compressed air can have high pressure, which can produce a high-speed jet. If the pressure exceeds the rating of the used pipes, the pipes can burst. If the speed of a jet is too high it can cause localised erosion and/or an intense noise. These two issues can cause body injuries to personnel; therefore, the university guideline "Piped compressed gas systems attached to gas cylinders and stand-alone compressed gas cylinder installations" [209] was followed to assure a safe operation and special observance was given to the below measures:

- All piping and fittings are adequate to withstand the pressure and temperature of the experiment
- Monitor and control the inlet pressure, with a pressure regulator, to keep it under safe levels (maximum 200[kPa] gauge).
- Check the fittings and joints continuously
- Wear ear defenders

III. Electricity

Electricity can cause electric shock and other injuries related to electrocution. In the test rig, the high-frequency and voltage can go up to 760[Hz] and 300[VAC], which is sufficient to produce serious injury. Consequently, the "University code of practise for electrical safety" [210] is followed and special observance of the below measures is given:

- All connections are electrically insulated, protections are given, and earthing is assured.
- Pre-use electric checks are performed
- The frequency, voltage and current are continuously monitored

CHAPTER 4. DESIGN

As described in the general development method of the previous section, the design of the MTG-ORC is split into two major tasks: conceptual design and analysis; both tasks are comprised by a number of activities that, due to the convenience of logistics, were not necessarily executed consecutively. However, they are presented in a sequence for the sake of understanding as described below.

4.1. CONCEPTUAL DESIGN

In the conceptual design, the architecture of the unit was defined to fulfil the specific needs of the studied application. Therefore, a summary of the needs, identified in section 3.2.2, is given in Table 4.1. A number of wanted functionalities of the MTG-ORC and the features that can address them are givenincluding: an outer enclosure, the use of polymeric materials and the implementation of a passive control through a limited expansion are innovative features that might enhance the techno-economic performance of the MTG-ORC.

Table 4.1 Definition of desired characteristics for the improvement of the MTG-ORC

Concept to be improved	Wanted functionality	Feature given to the prototype
Emissions	Hermetic sealing	Outer enclosure
Noise	Noise insulation	Outer enclosure
Burst	Burst protection	Outer enclosure
Loses	Aerodynamic loss reduction	Tailored design
	Leak reduction	Outer enclosure
	Mechanical loss reduction	Direct coupling turbine-generator
Failure rate	Long mean time between failures	NA
Lifespan	Long lifespan	NA
Compactness & Lightness	Specific power	Small diameter, high speed
Fabrication	Materials	Polymers
	Equipment	Moulding/Additive manufacturing
	Labour	Moulding
Design	Passive	Controlled expansion
Control	Oil-free	Oil-free bearings
Consumables	Leak-free	Outer enclosure

4.2. DEFINITION OF THE POWER CYCLE

The next step in the process is the definition of the power cycle. Thus, a model of a simple ORC was made, where for the sake of simplicity, only inefficiencies associated with the turbine and pump are considered. The heat source is assumed as a stream of hot water and the heat sink is assumed as a stream of ambient air; however, other single-phase heat sources and/or sinks can be assumed with minimal differences on such a thermodynamic model. The temperatures of the evaporator and the condenser are defined to allow a temperature difference of 5[K] for the pinch point. Penta-fluoro-propane (R45fa) is selected as working fluid and its thermo-physical properties are obtained using the REFPROP [152] real gas equations of state (EoS). The efficiency of the feed pump is assumed to be 0.7, the isentropic efficiency and the gross power of the turbine are assumed to be 0.7 and 1.45[kW] respectively. Table 4.2 and Table 4.3 show the results of the heat and mass balance of the cycle. It can be seen that the turbine inlet temperature is T_1=328[K], the inlet pressure P_1=400[kPa], the actual turbine outlet temperature is T_{4r}=318[K] and the actual outlet pressure is P_{4r}=250[kPa]. The mass flow of the heat source is $\dot{m}_h$=0.54[kg/s], the mass flow of the cooling air is $\dot{m}_c$=3.16[kg/s] and the mass flow of working fluid is $\dot{m}_f$=0.26[kg/s]. The ideal isentropic enthalpy drop is Δh_0=8.4[kJ/kg], and the cycle thermal efficiency is η_{th}=0.03. Although the efficiency of this specific case is slightly low compared with the projects of the same nature [16, 97], the study case is accepted for demonstrating the concept and further optimisation can be done following the principles presented in section 2.2.1 for future investigations.

Table 4.2 Thermodynamic states of the heat and mass balance of the studied ORC.

Side	**Hot**		**Cycle**					**Cold**	
State	H_{in}	H_{out}	1	4s	4r	5	6	C_{in}	C_{out}
Fluid	Water	Water	R245fa	R245fa	R245fa	R245fa	R245fa	Air	Air
T[K]	353	331	328	315	318	313	313	293	309
P[kPa]	-	-	400	250	250	250	400	-	-
X	-	-	1	1	1	0	0	-	-
h[kJ/kg]	-	-	444	436	439	253	253	-	-
s[kJ/kgK]	-	-	1.76	1.76	1.77	1.18	1.18	-	-
ρ[kg/m^3]	1000	1000	22	14	14	1.29	1.29	1	1
$\dot{m}$ [kg/s]	0.54	0.54	0.26	0.26	0.26	0.26	0.26	3.16	3.16

Table 4.3 General performance of the low temperature ORC, simple configuration.

Parameter	Symbol	Value
Heat input	$\dot{Q}_{in}$[kW]	50.4
Heat output	$\dot{Q}_{out}$[kW]	49
Specific enthalpy drop across turbine, ideal	Δh_s[kJ/kg]	8.42
Specific enthalpy drop across turbine, real	Δh[J/kg]	5.55
Efficiency of pump	η_{pump}	0.7
Power of pump	$\dot{W}_{pump}$ [kW]	0.043
Efficiency of MTG-ORC	η_{MTG}	0.66
Power of MTG-ORC	$\dot{W}_{MTG}$ [kW]	1.46
Net power of the cycle	$\dot{W}_{\text{net}}$ [kW]	1.42
Thermal efficiency of the cycle	η_{th}	0.03
Exergy Efficiency of the cycle	η_{ex}	0.01
Imbalance of the calculation	Im	0%

4.3. ARCHITECTURE OF THE MTG

The next step is designing an expander that fulfils the conditions defined above. This task can start with the selection of a type of expander that best suits the application.

As reviewed in section 2.3, volumetric expanders are often reversed refrigeration or air compressors. Consequently, they are widely available in the marketplace, which makes them affordable and convenient and, for these reasons, they are usually preferred in low-capacity ORC systems [39, 43, 50]. However, they also present considerable technical shortcomings such as low efficiency, limited operational flexibility, wear, short lifespan and noisy operation; which may make their appropriateness questionable. Conversely, micro-turbines are barely considered due to the perception that they are costly and complex and the numerous advantages of micro-turbines are often overlooked. Moreover, a few recent studies [38, 59] conclude that micro-turbines can be a valid option of expander for downsized ORC systems due to its compactness and operational flexibility, which are two characteristics greatly valued in distributed power systems. Compactness reduces the footprint of the plant whereas operational flexibility allows customization for a broad range of applications without major hardware modifications. Micro-turbines, thus, might not be having the attention they deserve as an option of expander in downsized ORC systems and, for that reason, they are selected as the type of expander in this investigation.

The type of turbine can be chosen based on their thermo-aerodynamic performance. According to the Euler's pump and turbine equation, presented in Eqn.(**3.5**), the ideal specific work in a turbine stage is the sum of three terms: the difference of the squared speed of the blade, $u_2^2 - u_3^2$; the difference of squared absolute speed of the flow, $c_2^2 - c_3^2$, and the difference of the squared relative speed of the flow, $w_2^2 - w_3^2$. In an axial impulse turbine, for example, the speed of the blade, u, and the relative speed of the flow, w, are constant across a stage; thus, only the term $c_2^2 - c_3^2$ contributes to the specific work. In an axial reaction turbine, only the speed of the blade is constant across a stage; thus, $w_2^2 - w_3^2$ and $c_2^2 - c_3^2$ contribute to the specific work. In contrast, in a radial turbine, none of the aforementioned speeds is constant across a stage; therefore, the three terms contribute to the specific work. Nevertheless, it should be highlighted that the term $u_2^2 - u_3^2$ is positive in radial-inflow turbines, which contributes positively to the specific work, and becomes negative in radial-outflow turbines, which reduces the specific work. Consequently, radial-inflow turbines can provide the largest specific work per stage for a given limit of flow speed while radial outflow turbines consume a fraction of the power to achieve an outward flow. Moreover, radial inflow turbines present the additional advantages of compactness and a feasible nozzle-less configuration, which make them an attractive option. Therefore, radial-inflow type is selected for the turbine.

Multiple staging is convenient for handling a high expansion ratio because the expansion can be distributed throughout the number of stages whilst keeping the efficiency high and the rotational speed low, which is convenient. Nevertheless, due to its characteristic low temperature, ORC turbines rarely require more than two stages [47, 179, 181, 182] and the great advantages of single staging overtake the shortcomings and consequently, a single stage configuration is selected in this study.

An MTG-ORC is then specified and its architecture is presented in Fig. 4.1. The MTG-ORC is a device that converts fluid power into mechanical power, inside a turbine, and then transform it into electrical power, into a generator. Then, the MTG-ORC consist of two major subsystems that are integrated in a common shaft: the turbine and the generator. These two elements are integrated and mounted together; therefore, two major subassemblies can be identified: the rotor and the stator. The rotor comprises

a shaft (A4), two high-speed ball bearings located at the front (A9) and rear (A10) ends of the shaft, two retaining nuts (A13, A15) for the bearings, a dipole of neodymium permanent magnets (A5), a magnet retainer sleeve, an impeller (A3) and a retaining nut (A16) for the impeller. The stator is comprised of a volute (A2), a volute baseplate (A12), two housings for the bearings at the front (A11) and rear (A14), a body (A7) for the generator windings and a rear generator cap. The working fluid enters the MTG-ORC from the inlet (A1) and is distributed through the volute to the periphery of the impeller. The working fluid passes through the impeller, which transforms the fluid power into mechanical power in the shaft. The movement of the magnets creates a dynamic magnetic field in the windings, which produces the electrical output at the generator terminals (A8). The rotor is supported by the front and the rear bearings, the front bearing is kept in place with the front nut and allocated into the front bearing housing, the rear bearing is kept in place with the rear nut and allocated into the rear bearing housing and the impeller is hold with the impeller nut. The volute is fastened to the volute baseplate, which in turn, is fastened to the front bearing housing.

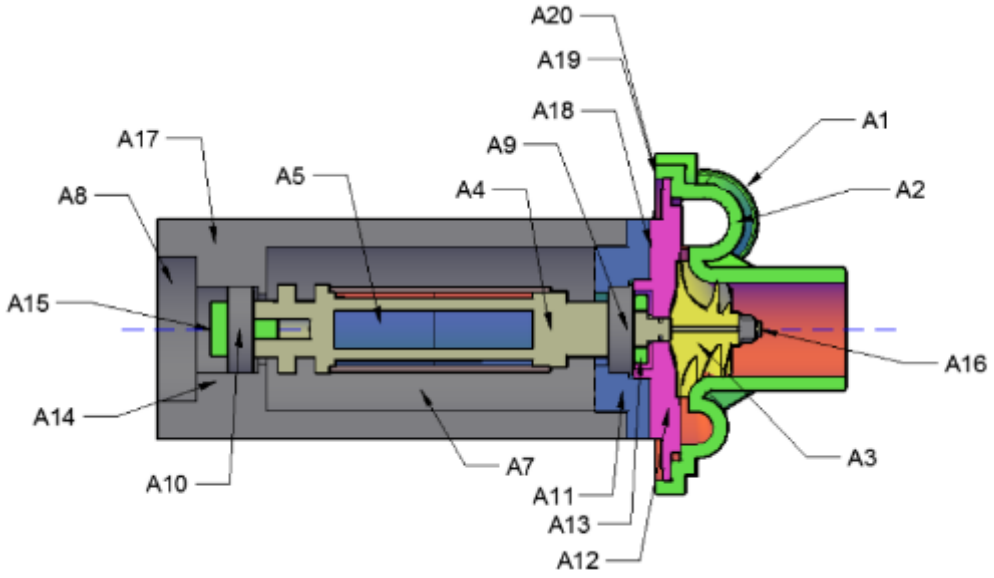


Fig. 4.1 Cross section of the MTG;
A1: turbine casing, A2: Volute, A3: Impeller, A4: Shaft, A5: Magnets, A6: NA, A7: Generator body, A8: Back seal, A9: Front bearing (FB), A10: Rear bearing (RB), A11: FB housing, A12: Baseplate, A13: FB nut, A14: RB housing, A15 RB nut, A16: Impeller nut, A17: Generator Body, A18: Seal, A19: Seal, A20: Seal

The generator and the turbine are mounted on a common shaft to avoid the need of a mechanical transmission; this gives to the MTG a compact size, which in turn makes it suitable to fit into a hermetic enclosure, as explained in section 4.8. The bearings used

are high-speed roller bearings that operate with grease, avoiding the need of an oil system for lubrication. The control of the turbine is detailed in section 4.7. The MTG-ORC is designed to allocate several polymer components, though for practicality, only two components made of polymer are implemented for the time being: the nozzle body and the impeller.

4.4. MATERIAL SELECTION

For the selection of the materials being used in this research, the ranking of candidate materials given in the Table 4.4 was used alongside a review of the market availability of polymers and an assessment of the techniques available at the university for fabricating the required components. As a result, PEEK-GF30 was selected for making the impeller and PET-G for the nozzle body. PEEK is a polymer in the 1st quartile and PET is in the second quartile in the ranking of candidate materials. Although these materials might not be the techno-economical optimum because optimization is yet to be done in future investigations, they can be used for proving the concept and further optimization can be conducted in later investigations. A review of these two materials is given as follows.

PEEK. Polyether-ether-ketone is a general-purpose polymer from the family of Polyketones that has very good tribological properties and hence good resistance to wear. This polymer also has a low flammability, hence low risk of fire or explosion, and a low absorption of water [211]. Its production is complex process that can be accomplished through diverse procedures, though, in the conventional method, PEEK is derived from the reaction of bisphenolate and difluoro-benzophenone [212]. The chemical formula of PEEK is $(C_{19}H_{12}O_3)_n$ and its main properties [211] are: specific volume ν=7.6×10^{-4}[m^3/kg], ultimate tensile strength S_t=110[MPa], tensile modulus of elasticity M_t=4.3[GPa], ultimate flexural strength S_f=170[MPa], flexural modulus of elasticity M_f=4.1[GPa], glass transition temperature T_g=425[K], maximum service temperature T_s=522[K] and deflection temperature at 1.8[MPa], T_d=433[K]. This polymer is compatible with a great deal of substances because it is almost insoluble in most ordinary solvents, including, ammonia, aromatic hydrocarbons and carbon dioxide. However, sulfuric acid and a few other substances can dissolve PEEK at high temperatures. This polymer is compatible with many other polymers of the same family

[213] and is well-matched with glass and carbon fibres, for that reason, it is often used to form composites. PEEK is widely used for high-performance applications such as high-pressure piping, bearings, pumps, valves and, in the field of turbomachinery, it has been used for compressor seals [214] and impellers for high-speed turbomachines [215]. The high-performance of PEEK makes it a very valuable polymer and so it is often recycled. Common techniques for recycling this polymer include the chemical recovery using a dissolvent (sulfuric acid) and then mechanical re-processing [216].

PET. Polyethylene terephthalate is a commodity plastic from the family of polyesters that can be found in amorphous or semi-crystalline morphologies. This material is a very resilient plastic that is well-known for its strength, hardness, stiffness, tribological properties and resistance to several hydrocarbons, including refrigerants, solvents and oils. Moreover, PET presents good dimensional stability at temperatures of up to 373[K]. The chemical formula of PET is $(C_{10}H_8O_4)_n$ and it can be produced through a two-step polymerization from the raw materials: mono-ethylene glycol and terephthalic acid [217]. The main properties of PET are: specific volume v=7.1×10^{-4} [m^3/kg], ultimate tensile strength S_t=86[MPa], tensile modulus of elasticity M_t=3.2[GPa], ultimate flexural strength S_f=120[MPa], flexural modulus of elasticity M_f=3.4[GPa], glass transition temperature T_g=365[K], maximum service temperature T_s=372[K] and deflection temperature at 1.8[MPa], T_d=433[K]. PET is one of the most widely used polymers in the world and, although it is famous for its application in beverage containers and plastic films, its major application seems to be in textiles [217]. In specific applications, this plastic can be used for replacing metals [211], with reinforced PET conventionally used in turbomachinery for making pumps and impellers [218]. From the economic and environmental standpoints, the popularity of PET make its recycling a necessity; thus, techniques for the mechanical and chemical recycling are well developed [217] reducing environmental impacts of the ORC at the end of the lifetime. In the mechanical recycling, recycled PET is milled and reprocessed and, in the chemical recycling, the material is depolymerised into monomers, purified and repolymerised for further utilization.

Polymers

In this section, a review of polymers is conducted to identify potential candidate materials with a quantitative approach. The reviewed polymers were taken from a shortlist of plastics commonly used for engineering applications [219] and an evaluation was done with a multi criteria decision making analysis using the weighted sum method [220]. In this method, a vector, s_i, containing a ranked score of the materials is obtained with Eqn.(4.1), which is a function of a matrix of specific scores S_{ij} and a weighting vector w_j. The matrix of specific scores contains the score of each material, i, for a number of evaluated properties, j, whereas the weight vector contains a quantitative importance of such properties. As a result, the most suitable material would have the highest rank in the vector, s_i, and therefore, should be selected for the intended application.

$$s_i = S_{ij} w_j \tag{4.1}$$

For this evaluation, 39 polymers were considered [219]. From these polymers, ten properties were considered, seven mechanical properties and three thermal properties. This analysis is limited to mechanical and thermal properties because the centrifugal force and the temperature are the principal mechanical loading for the studied elements. The mechanical properties are specific volume, v, ultimate tensile strength, S_t, yield tensile strength, S_{ty}, tensile modulus, M_T, ultimate flexural strength, S_f, yield flexural strength, S_{fy}, and flexural modulus, M_f. The thermal properties are glass transition temperature, T_g, maximum service temperature, T_s, and deflection temperature at 1.8[MPa], T_d. These properties were obtained from the MatWeb database [221]. The scores of the matrix were obtained by comparing the value for a given property, for a given material, with respect of the maximum and minimum values of such a property amongst all the materials; this allowed the scores to be a fraction of the unity. The intention of the score for material $i = 1$ and the property $j = 1$ is given in Eqn.(4.2) as an example while the scores for the remaining materials and properties are calculated analogously.

$$S_{1,1} = \frac{v_{1,1} - min(v_{i,1})}{max(v_{i,1}) - min(v_{i,1})} \quad (4.2)$$

The matrix S_{ij} and the weight vector w_j are given in the A and the B respectively; while the resulting vector s_i containing the ranked score of the materials is given in Table 4.4. This table suggests that Polyimide may be the material with the highest suitability for being adopted into the MTG-ORC whereas FEP would be the material with the lowest suitability, considering the thermal and mechanical loadings. However, additional factors such as chemical compatibility, commercial availability and price and must also be considered for the actual selection.

Table 4.4 Vector of overall score for the evaluated polymers

#	Name	Acronym	Final score
1	Polyimide	PI	0.44
2	Poly (ether ketone ether ketone ketone)	PEKEKK	0.43
3	Poly (ether ketone)	PEK	0.41
4	Poly (ether ketone ketone)	PEKK	0.39
5	Poly (ether ether ketone)	PEEK	0.37
6	Polyetherimide	PEI	0.30
7	Poly (hexamethylene succinamide)/Nylon 46	PA4,6	0.29
8	poly (p-phenylene terephthalamide)/Kevlar 49	Kevlar 49	0.29
9	Poly (phenylene ether)	PPE	0.29
10	Polysulfone	PSU	0.28
11	Polycarbonate	PC	0.27
12	Liquid crystal line polymer	LCP	0.27
13	Poly (hexamethylene adipamide)/Nylon 66	PA6,6	0.27
14	Poly(caprolactam)/Nylon 6	PA6	0.27
15	Cyclic olefin copolymer	COP	0.25
16	Styrene maleic anhydride	SMA	0.24
17	Poly (ethylene terephthalate)	PET	0.24
18	Poly (ether sulfone)	PES	0.24
19	Styrene acrylonitrile	SAN	0.24
20	Poly (methyl methacrylate)	PMMA	0.23
21	Poly (hexamethylene sebacamide)/Nylon 610	PA6,10	0.22
22	Polyundecanolactam/Nylon 11	PA11	0.22
23	Polyoxymethylene	POM	0.22
24	Poly (aryl sulfone)	PAS	0.21
25	Polyarylate	PAR	0.21

26	Polylauryllactam/Nylon 12	PA12	0.21
27	Poly (hexamethylene dodecanediamide)/Nylon 612	PA6,12	0.20
28	Poly (ethylene naphthalate)	PEN	0.19
29	Polyamide imide	PAI	0.19
30	Syndiotactic polystyrene	SPS	0.19
31	Poly (phenylene sulfide)	PPS	0.18
32	Acrylonitrile butadiene styrene	ABS	0.18
33	Poly(tetrafluoroethylene)	PTFE	0.17
34	Aliphatic polyketone	PK	0.16
35	Polyphthalamide	PPA	0.15
36	Ethylene–tetrafluoroethylene	ETFE	0.15
37	Perfluorovinylether–tetrafluoroethylene	PFA	0.14
38	Poly (butylene terephthalate)	PBT	0.11
39	Fluorinated ethylene–propylene	FEP	0.10

In Table 4.5, the chemical compatibility of a few of the above-mentioned polymers with the working fluids presented in the previous section is summarised. It can be seen that Polyamide, is well ranked in terms of mechanical loading but its chemical compatibility is only reported for the R1234yf, which may question its actual convenience for a broader application. Therefore, Table 4.4 is not conclusive alone and more integral criteria should be considered. Additionally, in Table 4.5, only a few of the considered materials can be found due to lack of information in literature; nevertheless, the absence of the other materials does not necessarily mean they are not compatible but might simply suggest they have not been evaluated yet. Thus, a dedicated chemical compatibility study of any specifically proposed material-fluid combination should be performed when resources become available.

Table 4.5 Chemical compatibility of polymers and fluids (literature). *compatible

Polymer/fluid	R245fa	R134a	R1224yd	R1233zd	R1234yf	R1234ze
ABS		*	*			*
Acetal		*				*
Acrylic			*			
CPVC		*				
Epoxy resin		*	*		*	
ETFE		*				
Polyethylene-HD	*					*
Nylon	*	*	*	*	*	*
PBT				*		
PET		*			*	*
PFA	*					

Phenolic resin			*			
Polyamide					*	
Polycarbonate		*	*			
Polyester					*	
Polyetherimide						*
Polyethylene	*					
Polyphenylene Sulfide		*				
Polyphenyleneoxide			*			
Polypropylene	*	*	*			
Polystyrene		*	*			*
Polysulfone		*				
PTFE	*	*	*	*		*
PVC		*	*	*		*
PVDF	*	*				

4.5. DESIGN OF THE TURBINE

4.5.1. Mean-line design

The mean-line design is usually the first step in the design of turbines, because it allows performing a preliminary design in a fast manner with small resources. This method represents the average behaviour of the flow through the transverse section along the gas path [158]. In this work, the software ANSYS® 16.2 VISTA RTD^{TM} is used to perform the mean-line design. The Suhrmann [75] method, explained in section 5.1, is selected for efficiency prediction because is appropriate for micro-capacity turbines and the boundary conditions are imported from section 4.2. The software ANSYS® 16.2 VISTA RTD^{TM} relies on the ideal gas law for determining the thermophysical properties of the fluid; thus, the gas properties of R245fa were idealised within the interval 400[kPa] to 250[kPa],. The gas idealised properties of R245fa in the interval of interest are Cp=1360[J/kg-K] and R=55.8[J/kg-K].

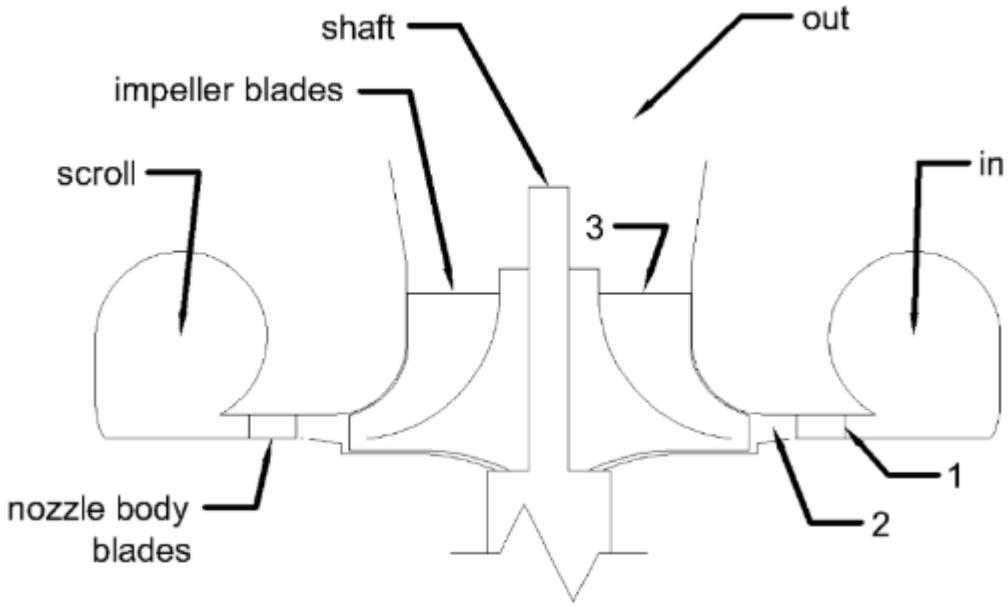


Fig. 4.2 Schematic of the meridional section of an inflow radial turbine;
1: nozzle inlet, 2: rotor inlet, 3: rotor exit.

First a preliminary radial turbine is designed, following the nomenclature of Fig. 4.2, to match the geometry of the volute of the selected turbocharger described in section 4.5.5. An unoptimised design of the radial turbine is made to facilitate the process. Moreover, as the turbine is to have the simplest possible geometry, the blades are designed straight in the radial direction. This should make the impeller simple to fabricate and the centrifugal stress in the blades may be reduced, though the aerodynamic efficiency is yet to be evaluated. The nozzle exit angle is set to α_2=20[°], which can provide a reasonable compromise between manufacturability and aerodynamic efficiency. The exit absolute flow angle is set to α_3=0[°], following the non-whirl criterion. For the preliminary design, the aerodynamic losses are neglected. The wheel trim is set to 0.54 and the blade height is set to 3[mm] to make the impeller compatible with the selected volute. The shroud clearance is set to 0.2[mm], which can be reasonably achieved with a standard milling machine. The selected number of blades is 8, which is one blade extra than the number of blades in the turbocharger compressor to reduce secondary losses. A summary of the inputs for this design is presented in Table 4.6.

Table 4.6 Inputs for the preliminary design of the turbine (ideal)

Input	Value	Input	Value
T_{0in}[K]	328	α_2[°]	70
P_{0in}[kPa]	400	α_3[°]	0
$\dot{m}_f$[kg/s]	0.262	b[mm]	3
PR	1.597	Z	8
Cp[J/kg K]	1360	$r_{3,sh}/r_2$	0.71
R[J/kg K]	55.8	$r_{3,hu}/r_2$	0.245
ω [rpm]	36000	tc [mm]	0.2
BSR	0.71	$L_{impeller}/D_2$	0.35
η_{nozzle}	1	Roughness	Machined
Loss model	1	Spanwise distribution	Radial

The results of the preliminary design are summarised in Table 4.7. It can be seen that the ideal aerodynamic power of the turbine would be 2.2[kW] with the conditions given in cycle. To achieve this, the required impeller would have a rotational speed of 36000[rpm], a diameter of 49[mm] and a blade height of 3[mm]; these dimensions are compatible with the dimensions of the volute; thus, the geometry is accepted.

Table 4.7 Results of the preliminary design of the turbine

Outputs	Value
$\dot{W}_{aero}$[kW]	2.2
η_{aero}	1
$\eta_{impeller}$	1
u_2 [m/s]	92.5
c_2 [m/s]	97.63
w_2 [m/s]	33.4
D_2 [mm]	49.1
b_2 [mm]	3
β_2 [°]	-1.29
β_{3rms} [°]	-65.2

The Mach number seems to be lower than 0.6, which suggest that a greater enthalpy drop across the turbine stage can take place. However, a greater enthalpy drop produces a greater flow speed, which may cause much greater erosion because the erosion is governed by the speed of flow and the density of the fluid [222]. The lifespan of the studied materials must be first evaluated with these less demanding conditions before proceeding to more demanding ones.

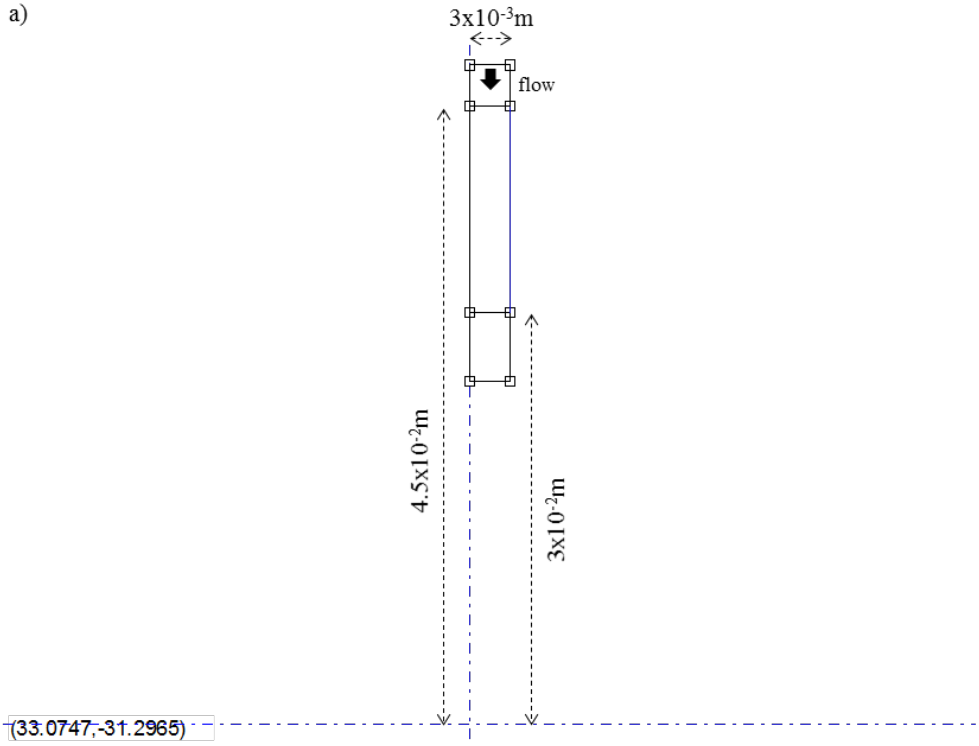
4.5.2. Design of the nozzle body

The nozzle body, also known as guide vanes, is designed with the results of the mean-line design and using the software ANSYS® 16.2 BladeModeler™. First, the following preferences were selected within the software to generate the geometry: diffuser component, radial type, negative rotation, units in millimetres, angle-thickness definition, geometric spanwise calculation, axial beta angle definition, data angle direction from leading edge to trailing edge and maximum curve cord error of 0.02. Guidance on the definition of these options can be found in the Turbo Systems user's guide, which is documentation of the software ANSYS® [223].

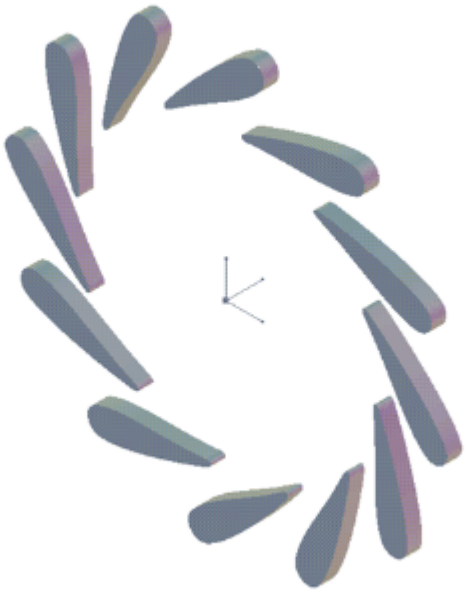
Then the nozzle body is defined with 12 blades, a uniform section along the span, no cutting-off nor extension of the blade edges and plain ends of the hub and shroud. The leading edge is of an elliptical type with a ratio of 1 at the hub and the shroud, whereas the trailing edge, whilst still being of the elliptic type, has a ratio of 2 at the hub and the shroud. The angle of spanwise distribution and the thickness distribution are both general. Only two layers were used to define the blade profile, one at span 0, corresponding to the hub of the nozzle body, and the other at span 1, corresponding to the shroud of the nozzle body.

The inlet radius of the nozzle body was set r_1=45[mm], the outlet radius of the nozzle body was set $r_{2,nozzle}$=30[mm], and the height of the blades was set $b_1 = b_{2nozzle}$=3[mm]. The work views of ANSYS® 16.2 BladeModeler™ used for designing the design of the nozzle body are presented in Fig. 4.3. The meridional view of the nozzle body in an axial-radial plane is shown in Fig. 4.3a and the three-dimensional view of the blades is shown, Fig. 4.3b. additionally, the blade angle distribution along the chord, from the leading edge (LE) to the trailing edge (TE), is shown in Fig. 4.3c, where β is the angle of the camber line with respect to the axial direction. Lastly, the blade thickness distributions along the chord is shown in Fig. 4.3d, where the aerodynamic profile with a maximum thickness of 6[mm] at 15% of the cord can be seen. Although the span of the blade was set as b_2=3[mm], it was later adjusted to b_2=2.5[mm] to compensate tolerances, gasketing and compatibility with the geometry of the volute.

a)



b)



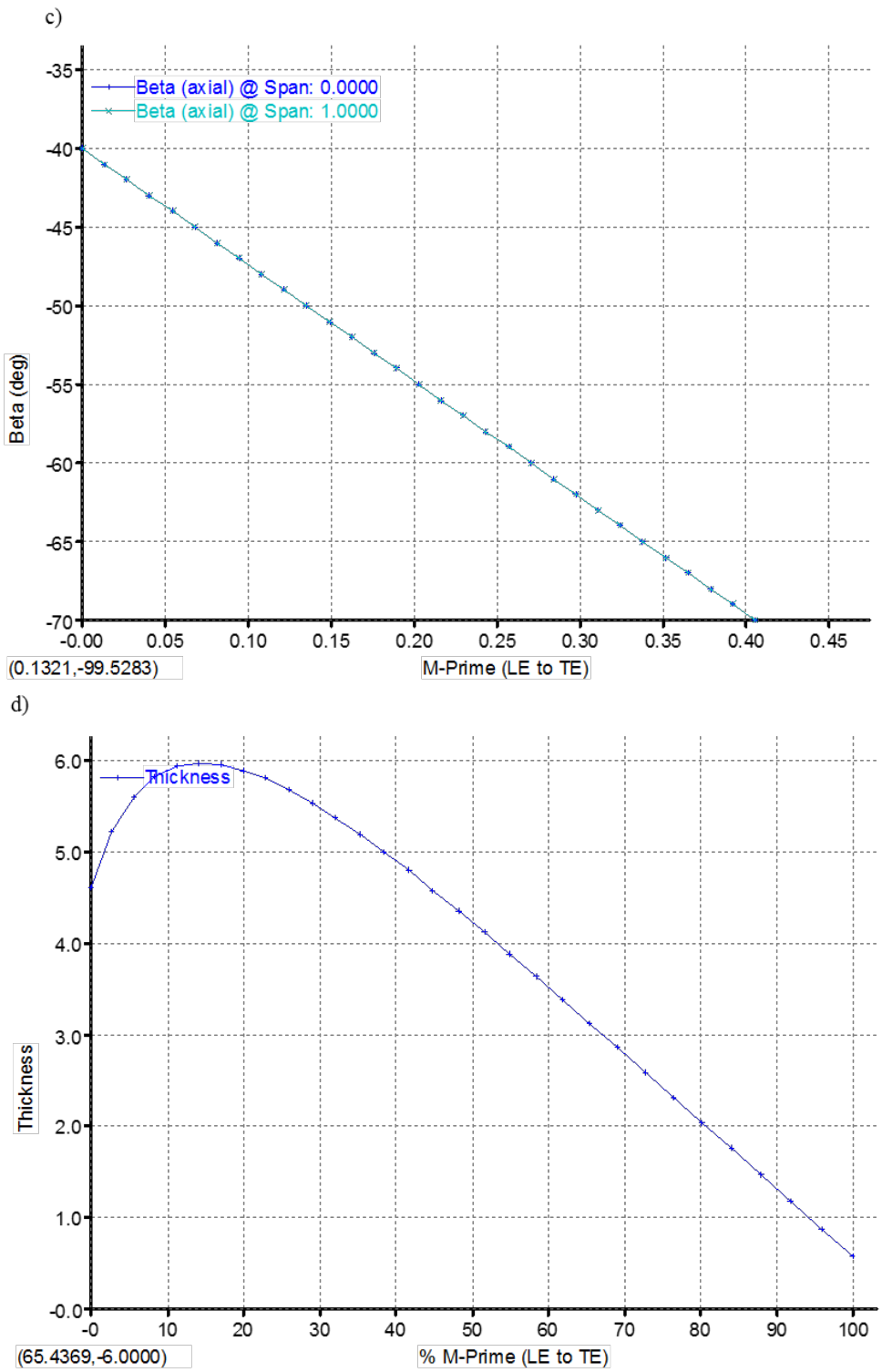
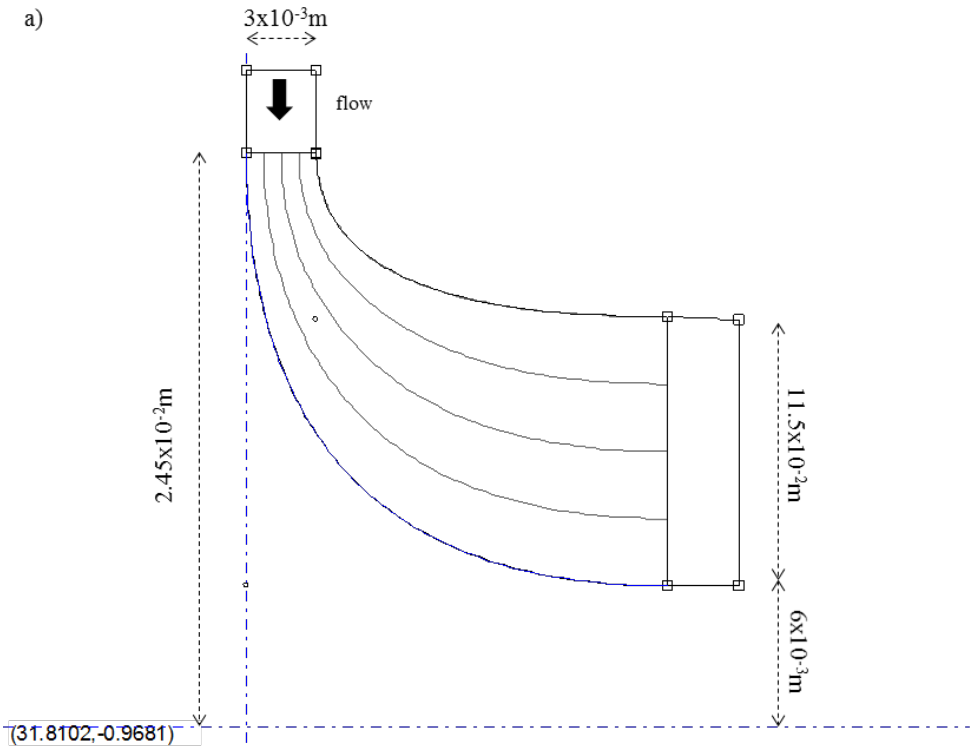


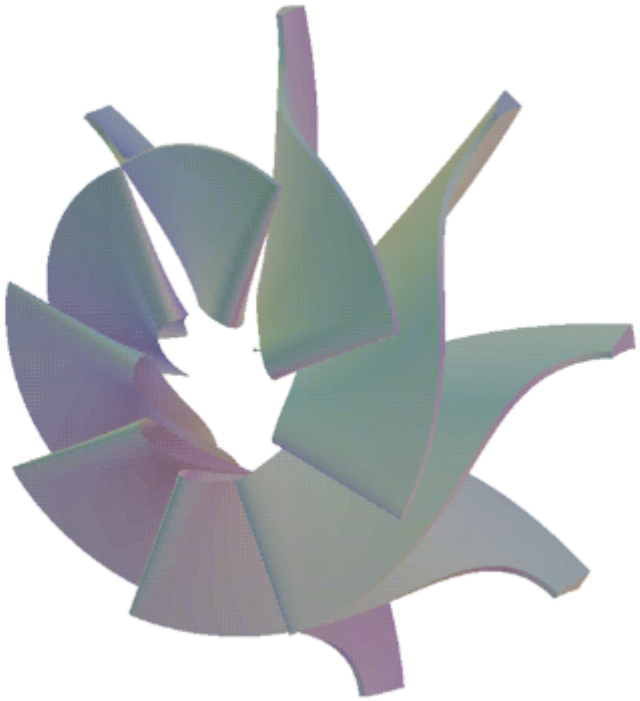
Fig. 4.3 Work views of the design software for the nozzle body;
a) meridional view; b) Three-dimensional view, c) blade angle graph; d) blade thickness graph; adapted from ANSYS® 16.2 BladeModeler™.

4.5.3. Design of the impeller

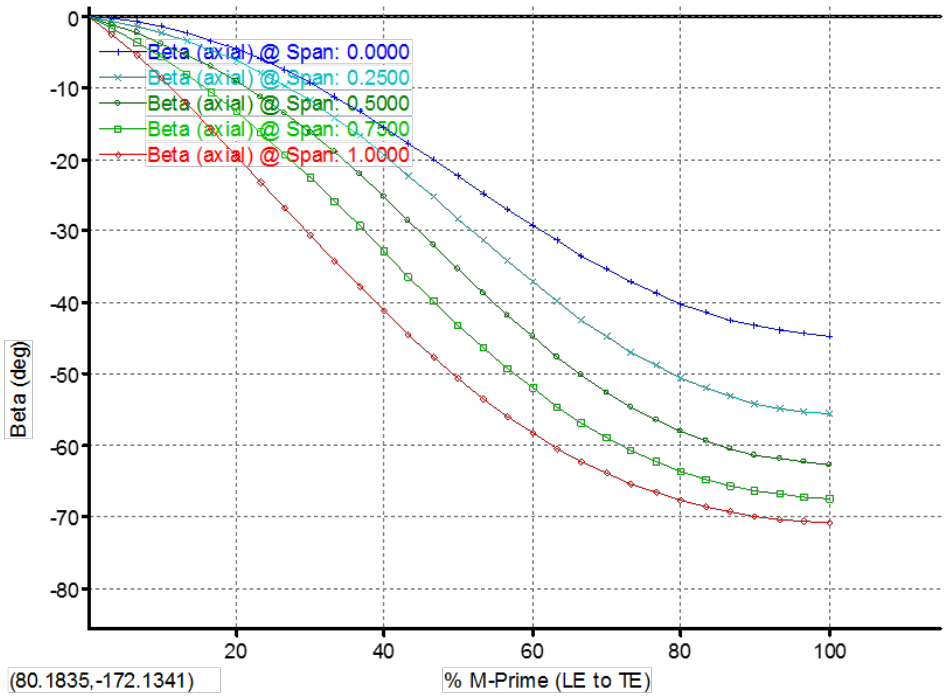
The impeller was also designed based on the mean-line design and using the software ANSYS® 16.2 BladeModeler™. The following preferences were selected: turbine component, radial configuration, negative rotation, units in millimetres, angle-thickness definition, geometric spanwise calculation, axial beta angle definition, data angle direction from leading edge to trailing edge, and maximum curve cord error of 0.01. Then, an impeller with 8 blades was designed using a variable section of the blade along the span, no cutting-off nor extension of the blade edges and flat ends of the hub and shroud. The leading edge is cut-off type whereas the trailing edge is of elliptic type with a ratio of 2 at the hub and 4 at the shroud. The angle of spanwise distribution type is of a radial element and the thickness distribution type is general. Five layers were used to define the blade profile, at span 0, 0.2, 0.4, 0.6, 0.8 and 1; span 0 corresponds to the hub and span 1 corresponds the shroud of the impeller. The inlet radius of the impeller was set $r_{2,impeller}$=24.5[mm], the exit hub radius of the impeller was set $r_{3,hub}$=6[mm], the inlet height of the blades was set $b_{2,impeller}$=3[mm] and the outlet height of the blades was set b_3=11.5[mm]; Bezier curves are used for the meridional shroud and hub definition.



b)



c)


Beta (axial) @ Span: 0.0000
Beta (axial) @ Span: 0.2500
Beta (axial) @ Span: 0.5000
Beta (axial) @ Span: 0.7500
Beta (axial) @ Span: 1.0000
0
-10
-20
-30
-40
-50
-60
-70
-80
Beta (deg)
20
40
60
80
100
% M-Prime (LE to TE)
(80.1835,-172.1341)

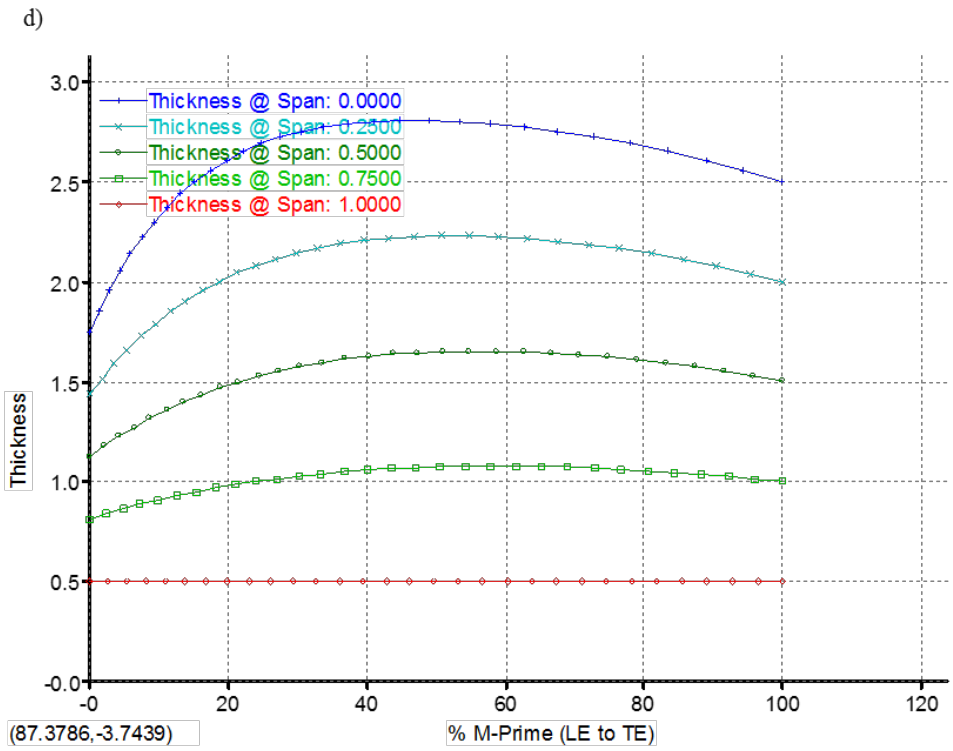


Fig. 4.4 Work views of the design software for the impeller;
a) meridional view; b) Three-dimensional view, c) blade angle graph; d) blade thickness graph; adapted from ANSYS® 16.2 BladeModeler™.

The work views of ANSYS® 16.2 BladeModeler™ used for designing the impeller are presented in Fig. 4.4. The meridional view of the impeller can be seen in Fig. 4.4a and the three-dimensional view of the impeller can be seen in Fig. 4.4b. Additionally, the distribution of the blade angle along the chord, from the leading edge (LE) to the trailing edge (TE), can be seen in Fig. 4.4c, where β is defined with respect of the axial direction. Lastly, the distributions of the blade thickness along the chord can be seen in Fig. 4.4d, where the thickness for the profiles defined for each of the layers can be observed.

4.5.4. Design of the shaft

A single custom-made shaft is designed to mount the turbine and the generator of the MTG-ORC. This design consisted in merging the geometry of the shaft of a high-speed motor, described in section 4.6, and the geometry of the shaft of a turbocharger model GT1549s. The resulting geometry is shown in the drawing of Fig. 4.5. As can be seen in the drawing, the rear end (left) corresponds to the generator and the front end (right) corresponds to the turbine. The greatest diameter of the resulting shaft is 27.2[m], the smaller diameter is 5[mm] and the total length is 193[mm].

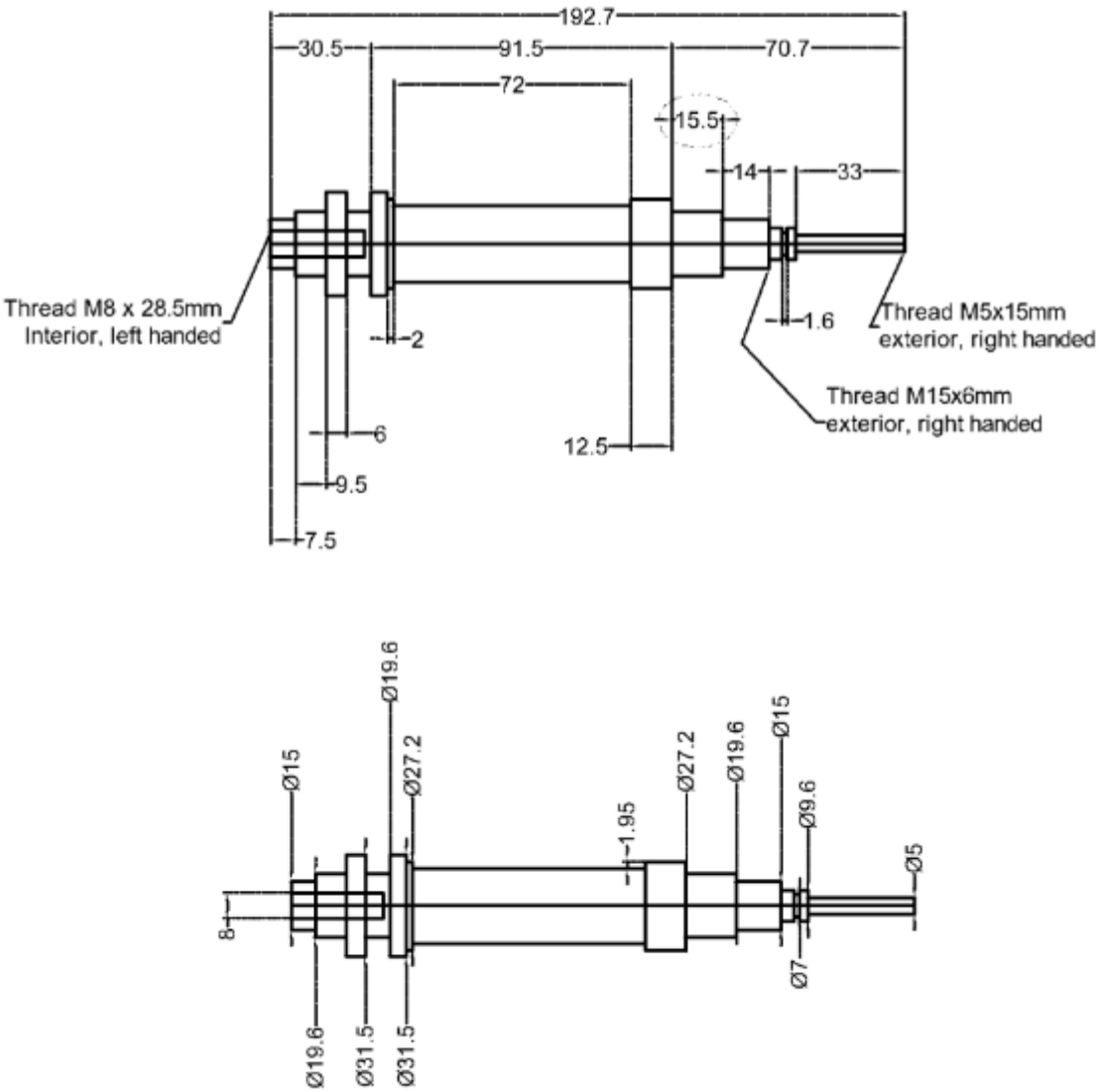


Fig. 4.5 Design of the shaft for the MTG-ORC;
dimensions in millimetres.

The dimensions of the turbine and generator shafts were unchanged, the supporting points of the shaft remained in the same axial positions as in the nominal application of both components; thus, the above-described design should be suitable for operating at conditions comparable with the nominal application if equivalent materials, fabrication methods and tolerance levels are used.

In its nominal application, the motor is equipped with four high speed angular bearings, designation 7002, into a paired face to face array, two at the rear and two at the front. The rear bearings are located at 17[mm] from the rear end and the front bearings at 122[mm] from the rear end. Additionally, the diameter of the motor shaft in

between the bearings is 31.5[mm]. For this investigation, the location of the bearings and the diameter of the shaft in between the bearings remained unchanged as can be seen in Fig. 4.5. Although the face to face array of the bearings was kept, only one bearing was left in each side because the shaft is expected to experience much less axial and radial forces than in the nominal application. Nevertheless, the designation of the bearings was tailored to withstand a considerably higher speed (up to 68000[rpm]), which is considerably higher than the nominal speed of the motor (24000[rpm]).

In its nominal application, the compressor of the turbocharger was supported in cantilever with two journal bearings and one axial bearing. The rear journal bearing is located at 80[mm] from the front end, the front journal bearing was located at 55[mm] from the front end and the axial bearing was located at 50[mm] from the front end. The diameter of the shaft at the journal bearings was 7.8[mm] while the diameter of the shaft where the impeller is allocated was 5[mm]. For this investigation, the front bearing of the custom-made shaft is located at 55[mm] from the front end, which agrees with the generator front bearing mentioned above and the rear bearing is located considerably further backwards, which should benefit the alignment of the shaft. Additionally, the diameter of the shaft, where the impeller is allocated, is 5[mm], which also agrees with the nominal application.

As mentioned above, the geometry and operation conditions were kept as similar as possible with the nominal application of each component; thus, the shaft should perform similarly to when in normal application. A simplified static-structural finite element analysis was performed using the ANSYS® 18 Mechanical™ software to assure that the structural integrity of the shaft is not compromised with the minor changes that were made. For conducting this analysis, the geometry of the shaft was imported and structural steel was selected as the material. The assumed properties of such a material were a density of 7850[kg/m^3], a yield stress of 250[MPa], a Young's modulus of 200[GPa] and a poison ratio of 0.3. A fine mesh dominated by hexahedral elements was defined, resulting in 24269 nodes and 7084 elements. Two fixed supports were defined at the location of the bearings. The applied loads were a rotational speed of 50000[rpm] (10% higher than the maximum allowable rotational speed), gravity, a bending force F_1 located at 76[mm] from the rear end and a force F_2 located at 210[mm] from the rear end of the shaft. The force F_1 accounts for the unbalance of the generator rotor and the

force F_2 accounts for the unbalance of the turbine rotor. The magnitude of both forces was defined assuming that a specific unbalance 15 times greater than the residual permissible specific unbalance defined in the standard ISO1940-1:2003(E) [224] is allowed. In such a standard, the balance quality grade recommended for turbochargers is G2.5, whose maximum permissible unbalance running at 50000[rpm] is e_{per}=1.5×10^{-6}[kg-m/kg]. Therefore, the resulting forces were F_1=300[N] and F_2=30[N], which consider a mass of the generator shaft m_1=0.48[kg] and a mass of an aluminium impeller m_2=0.04[kg] respectively.

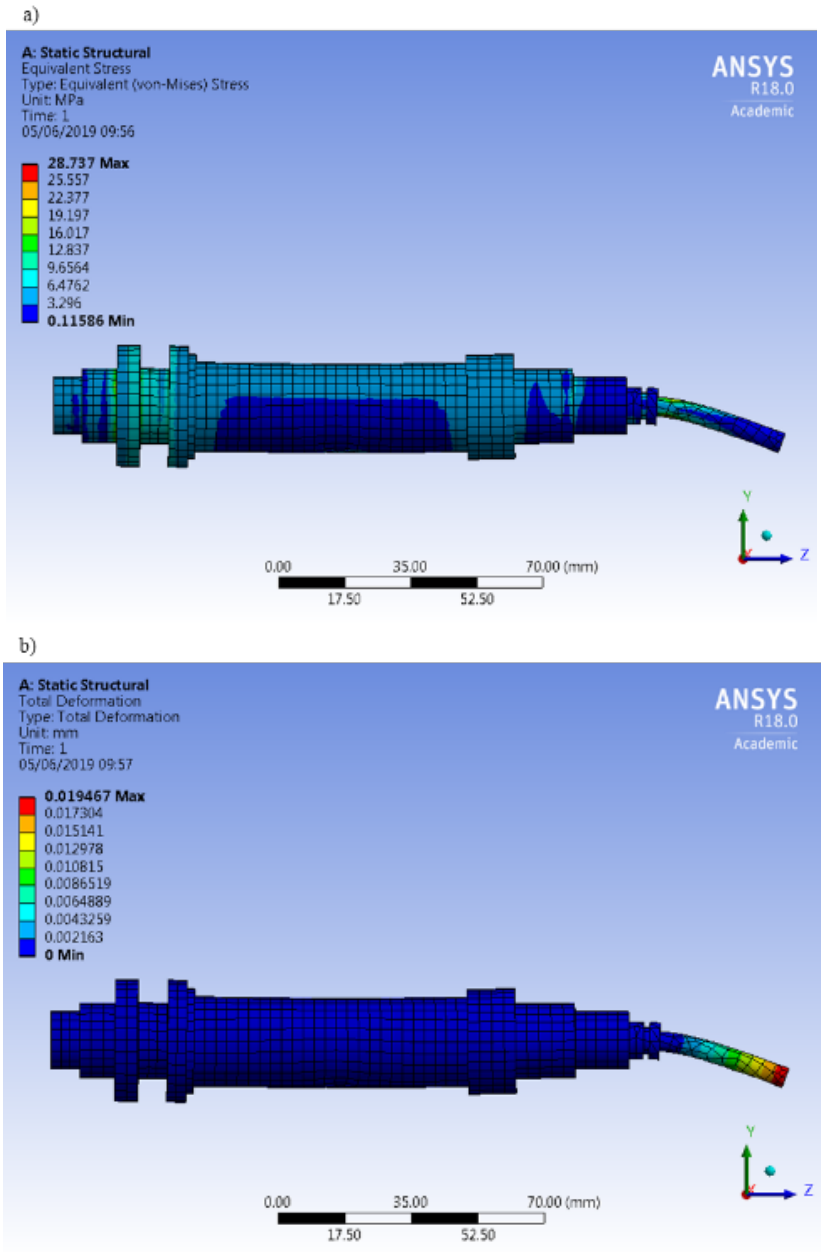


Fig. 4.6 Static structural finite element analysis of the shaft;
a) Von-Misses equivalent stress; b) Total deformation.

The results are shown in Fig. 4.6, where the maximum deformation seems to be ϵ_{max}=1.9×10^{-5}[m], which occurs in the front end of the shaft. The maximum equivalent stress is σ_{max}=28.7[MPa] and the minimum factor of safety $FoS = 8.7$, which occurs at 33[mm] from the front end of the shaft. These results show that the shaft seems to be suitable for the application as predicted earlier.

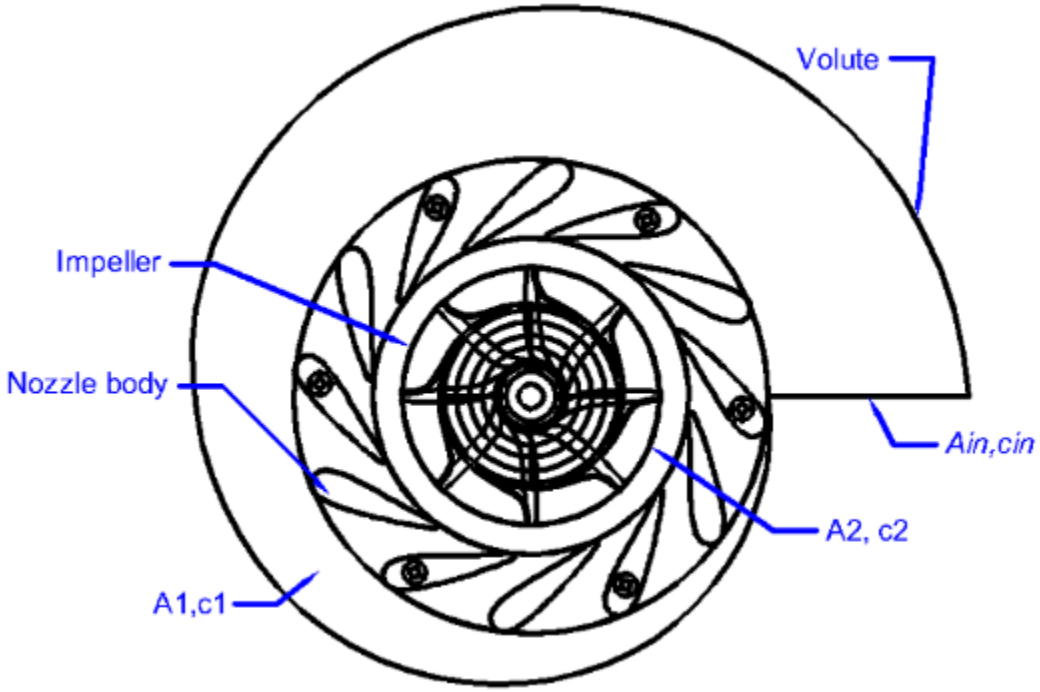
4.5.5. Selection of the inlet volute

The inlet volute of the turbine, also known as inlet scroll, can be designed using the method described by Aungier [150]. This method was conceived assuming that the angular momentum of the inlet flow is conserved as shown in Eqn.(4.3), where r is the radius of curvature of the inlet passage, c_u is the tangential speed of the flow and i represents any given point along the volute.

$$r_i c_{i,u} = constant \tag{4.3}$$

At the inlet point, the flow is totally tangential, hence, the speed c_{in} has only a component in the tangential direction and the radial component is zero, as can be seen in Fig. 4.7. Thus, when the volute is equipped with a nozzle body (Fig. 4.7a), the acceleration of the flow occurs from the point 1 to the point 2 and the flow speed at nozzle inlet, c_1, would be small. Therefore, the inlet flow speed, c_{in}, and the inlet area, A_{in}, can be calculated with c_1, and the resulting inlet area of the volute would be large. In contrast, if the volute is not equipped with a nozzle body (Fig. 4.7b), the volute becomes a nozzle itself and the speed of flow, c_{in}, and the inlet area, A_{in}, can be calculated with the flow speed at the nozzle outlet c_2, which results in an smaller volute inlet area. The design without guide vanes is simpler and more compact, as can be seen in Fig. 4.7b, but it has two shortcomings: a greater pressure loss and a narrower range of high efficiency.

a)



b)

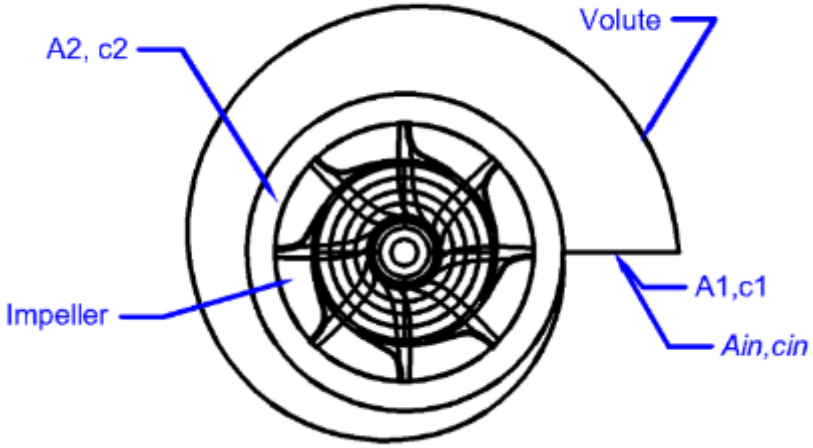


Fig. 4.7 Design of the inlet volute for a radial turbine;
a) with nozzle body; b) without a nozzle body; A_{in}: Volute inlet area, A_1: nozzle inlet area, A_2: nozzle outlet area, c_{in}: volute inlet speed, c_1: nozzle inlet speed, c_2:nozzle outlet speed.

Although the design of the inlet volute is not an extremely demanding task, its fabrication would require considerable resources because the fabrication of the volute would require metal casting and bulky machining, which are not available at the time of this investigation. Consequently, the volute of a turbocharger compressor is adapted and equipped with a nozzle body. The selected turbocharger is a GT1549s, which is equipped with a compressor volute that has an inlet diameter of 38[mm] and allocates

an impeller with the dimensions: exducer diameter of 49[mm], inducer diameter of 34.7[mm] and blade height of 3[mm]. These dimensions agree with the impeller designed in section 4.5.1.

4.6. SELECTION OF THE GENERATOR

As can be observed in the aforementioned procedure, the design of the generator may become a very intricated task that can demand a great deal of time and resources. Therefore, for the purposes of this investigation, a commercial high-speed induction motor was adapted to become a high-speed permanent magnet generator. Nevertheless, a reasonable similarity of the geometry, materials and operational conditions must be assured to conduct safe and reliable operation.

The adapted motor, shown in Fig. 4.8, is a three phase spindle motor with the following characteristics: power of 2.2[kW], voltage of 220[V], frequency range from 0.1[Hz] to 400[Hz], nominal rotational speed of 24000[rpm], nominal current of 11[A] and temperature range from 263[K] to 313[K]. The rotor is supported on an array of two paired angular ball bearings, one at 17[mm] from the rear end and the other at 122[mm] from the rear end. The stator is built with a three-phase winding array with an unspecified number of turns per phase and an unspecified cable gauge. The motor is cooled with liquid, then, the stator body has a slotted aluminium jacket to circulate the liquid coolant (water). The overall dimensions of the motor are 200[mm] length and 80[mm] outer diameter, the stator dimensions are 72[mm] active length and 32[mm] bore. The shaft diameter is 31.6[mm] and its active length is 72[mm].



Fig. 4.8 High-speed motor spindle.
image adapted from the supplier literature [225].

For this investigation, the aforementioned motor was modified to be converted into a high-speed permanent magnet generator, though most of their components and the operational conditions were preserved if possible. The stator body, for example, was not modified because it contains the cooling jacket, the stator core, the bearing housings and the electrical connections, though the front cap A11 in Fig. 4.1 was redesigned to assure the bit between the stator body and the baseplate of the turbine, component A12 in Fig. 4.1. The rotor of the generator was designed and fabricated using the shaft described in section 4.5.4, two arrays of rare earth magnets and a sleeve retainer. Each of the arrays of magnets consisted of the six pieces of neodymium magnets grade N50 that can be seen in Fig. 4.9a, three having north polarity and three having south polarity. Each of the pieces has an outer diameter of 27.2[mm] and a length of 36[mm]. The sleeve is made of stainless steel 316 with a length of 80[mm], inner diameter of 27.2[mm] and a thickness of 1.9[mm].

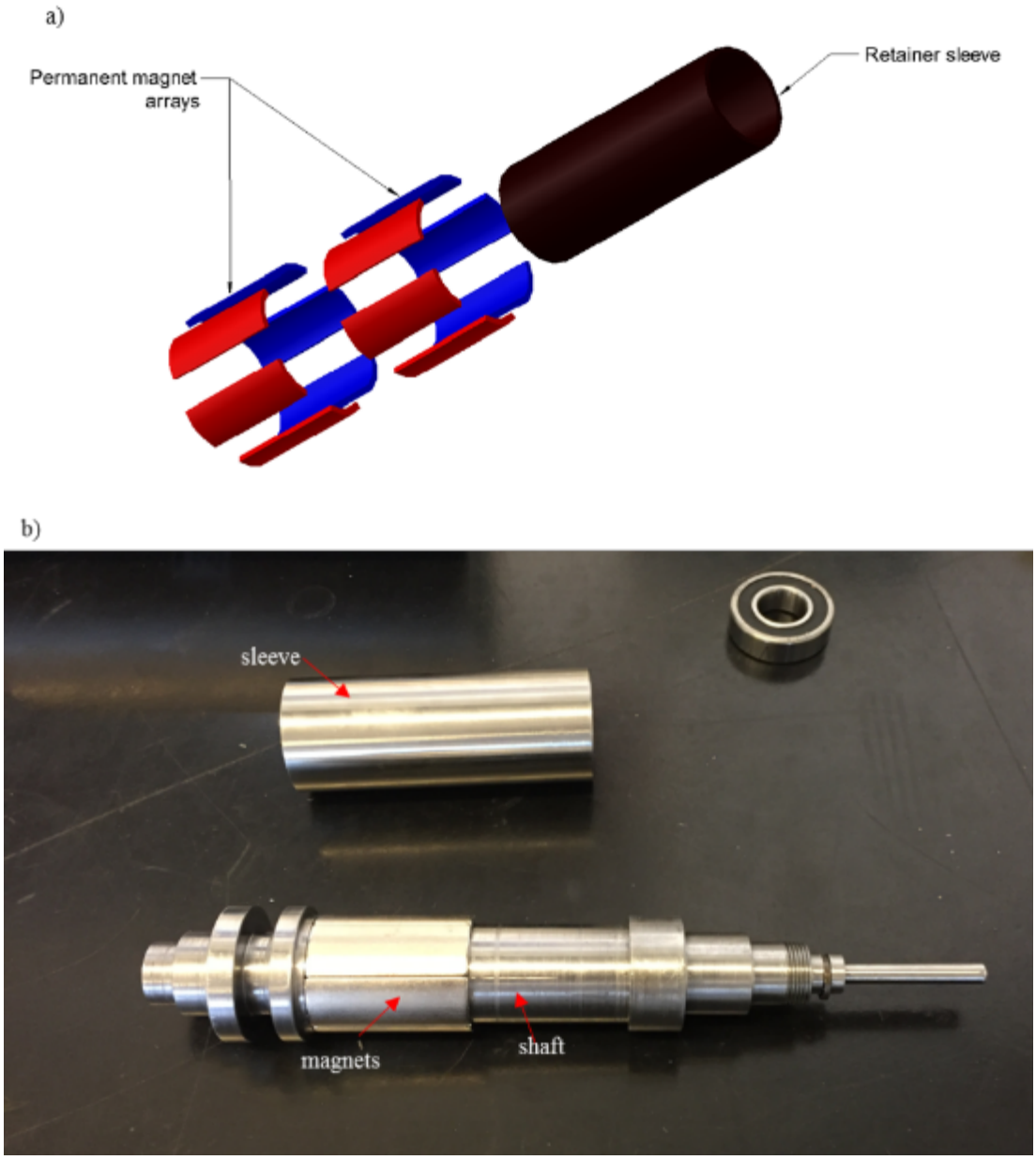


Fig. 4.9 Design of the rotor of the generator;
a) schematic of the arrays of magnets; b) actual assembly of the magnets.

The behaviour of the modified generator must be assessed to assure reliable and safe operation in the final application, even though the geometry, materials and operational conditions are similar. Thus, structural, electromagnetic and thermal assessments have to be performed alongside an examination of the selected bearings.

The expected power of the modified generator is 1.5[kW], which is considerably lower than the nominal power of the motor 2.2[kW]; however, the rotational speed was increased to 36000[rpm], which is 50% above the nominal rotational speed of the motor (24000[rpm]), which endorses the necessity of a further examination of the rotor.

The design of the shaft was presented in section 4.5.4 and is valid for rotational speeds of up to 50000[rpm], which confirms that the modified generator is suitable for the intended application. Then, only the mechanical integrity of the sleeve remains to be assessed. For that purpose, a mechanical static finite element analysis was performed. The geometry of the sleeve was made in AUTOCAD® 2014 and imported into ANSYS® 18 Mechanical™, where the analysis was made. Stainless steel was assumed as the material, whose density is 7750[kg/3], yield stress is 207[MPa], Young's modulus is 193[GPa], and poison ratio is 0.31. A fine mesh dominated by hexahedral elements was defined resulting in 30318 nodes and 5023 elements. Two fixed supports where defined at the inner edge of the ending faces. The applied loads were a rotational speed of 50000[rpm] and gravity. The magnets were bonded to the inner face and, for practicality, they were assigned to the same material as the sleeve.

The results reveal that the maximum displacement is 4.87×10^{-6}[m] (Fig. 4.10b), the maximum equivalent stress is σ_{max}=146[MPa] (Fig. 4.10a) and the minimum factor of safety is FoS=1.71, occurring at the outer face of the sleeve. As a conclusion, it can be said that, with the assumptions made, the sleeve may be near the upper limit of its structural capacity for this application, though the bonding and magnetic forces acting on the magnets might offset the centrifugal force. In any case, a stronger sleeve would be required to achieve a more conservative factor of safety, i.e., FoS=3 or superior; and would be mandatory if the rotational speed is further increased.

As described in the design of the shaft, the array of bearings consisted of two high speed angular bearings, designation 7002 whose location remained unchanged with respect to the nominal application in the motor. However, the nominal speed of rotation was increased from 24000[rpm] to 36000[rpm] and the maximum allowable speed was increased to 46000[rpm]; therefore, the type of bearings was replaced by high-speed high-precision angular contact bearings designation 7002CE/P4A from SKF. These are hybrid bearings with ceramic balls and steel rings whose specifications are: basic dynamic load rating 4.42[kN], basic static load rating 1.93[kN], attainable speed with grease lubrication 68000[rpm], contact angle 15[°] and number of balls 7. These bearings can withstand the maximum allowable speed of the MTG-ORC and the centrifugal forces due to unbalance.

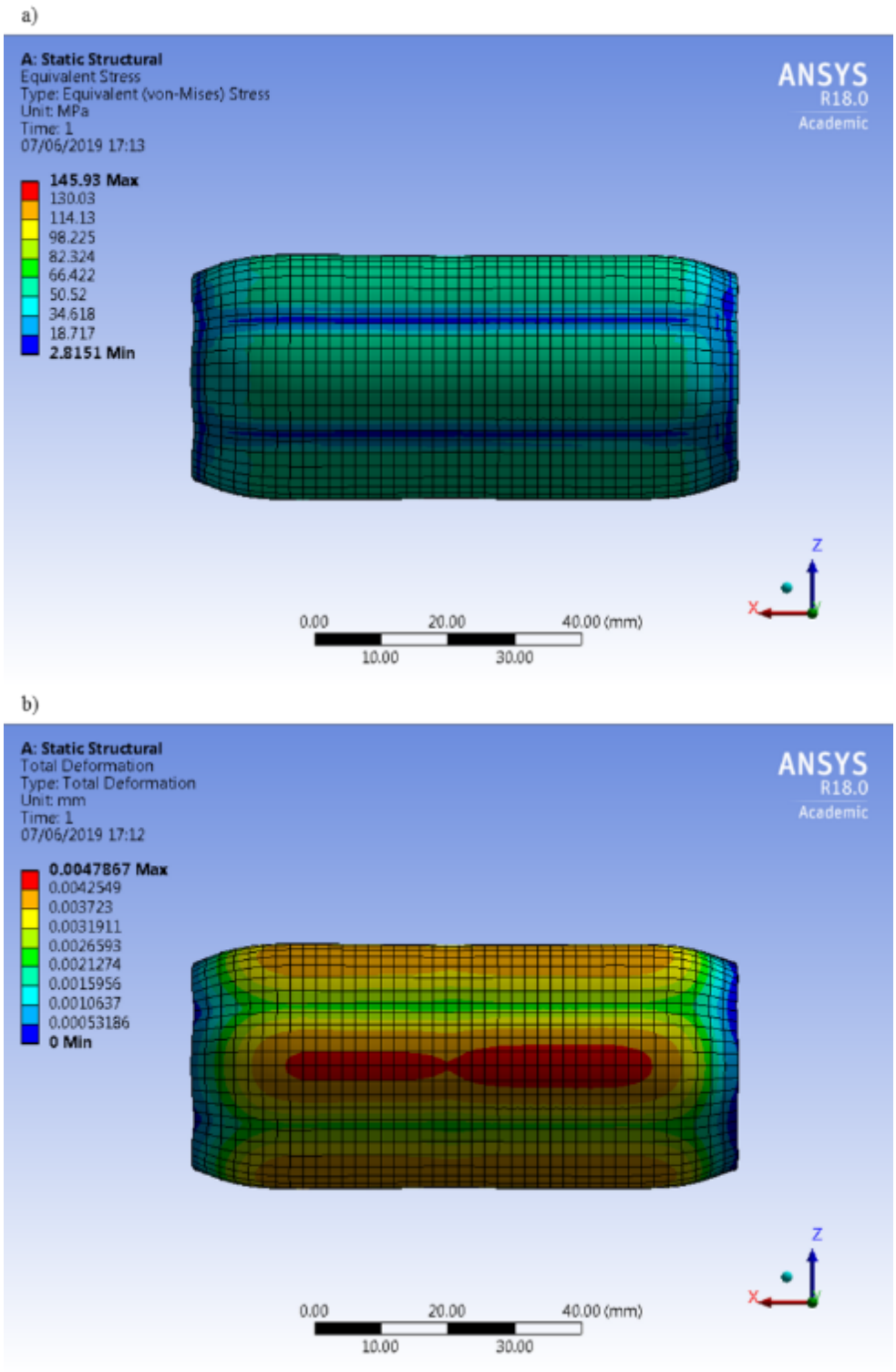


Fig. 4.10 Static structural finite element analysis of the magnets sleeve;
a) Von-Misses equivalent stress; b) Total deformation.

For the review of the electromagnetic design, the induced electromagnetic force in each of the generator coils was calculated with Eqn.(4.4), which is derived from

Faraday's law. In this equation, V_{rms} is the root mean squared voltage, n_e the number of turns in the coil, B the magnetic field, A the transversal area of the coil, ω the rotational speed and f the frequency of rotation. As can be seen in such an equation, the root mean squared voltage is proportional to the rotational speed and thus, to the frequency.

$$V_{rms} = \frac{n_e BA}{\sqrt{2}}\omega = \frac{n_e BA}{\sqrt{2}}\, 2\pi f \tag{4.4}$$

The magnets are made of Neodymium grade N50 with a minimum magnetic field strength of 1.4[T], though the stainless-steel sleeve that holds them in place and the air gap between the rotor and stator might significantly reduce the strength of the magnetic field. The number of turns and the transverse area of the windings are unknown, though the active area per phase should be 1/3 of the total active area of the stator. In consequence, the mean squared voltage cannot be known unless the parameters n, B and A of the generator are known; however, the product $n_e BA$ can be experimentally obtained if the root mean squared voltage and the frequency are measured and correlated with a linear regression.

As the stator has three phases, then the power of the motor can be calculated with Eqn.(4.5), where V_{rms} is the root mean squared voltage per phase and I_{rms} is the root mean squared current. As the nominal power of the motor is $\dot{W}_{motor}$=2.2[kW], the nominal voltage V_{rms}=220[V] and the frequency is f=400[Hz]; the nominal current per phase should be I_{rms}=5.8[A] and the product $\frac{n_e BA}{\sqrt{2}}2\pi$ of the motor should be around 0.55.

$$\dot{W}_{electric} = \sqrt{3}\, V_{rms} I_{rms} \tag{4.5}$$

The motor was electro-magnetically and thermally designed for operating with the above-mentioned conditions, therefore, for ensuring a reliable operation, the generator should not exceed an operational current of I_{rms}=5.8[A] and a product $\frac{n_e BA}{\sqrt{2}}2\pi = 0.55$. The design power of the generator is $\dot{W}_{MTG}$=1.5[kW], which is lower than the nominal

power of the motor; thus, the current per phase in the generator should be lower than the nominal current of the motor with a root mean squared voltage of 220[V].

Finally, the generator is of variable frequency; therefore, the output signal needs to be conditioned for distribution and consumption of the power. In other words, a frequency converter is needed to convert the power output into a standard alternating power (AC), i.e., a signal with a standard frequency and voltage. According to literature [226, 227], two options are available for achieving this conversion: a rectifier-inverter and a Matrix converter.

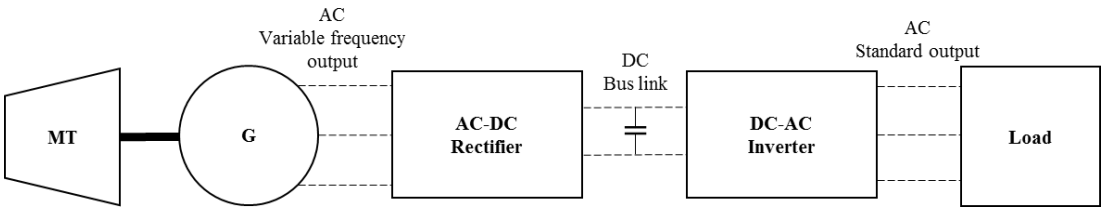


Fig. 4.11 Schematic of a rectifier-inverter for frequency conversion.

The rectifier-inverter is, arguably, the most common type of frequency converter [226, 227] because it is simple, robust and inexpensive, though it has the shortcoming of generating undesired harmonics. This device rectifies the variable frequency alternating current and converts it into a direct current that is later inverted into a standard alternating current, as illustrated in Fig. 4.11. However, the design of the power conditioning is out of the scope of this work and is left for future investigations.

4.7. SELECTION OF THE CONTROL

In this work, the opportunity of implementing a governing system using a controlled expansion is proposed. This method can be an option for allowing the rotational speed to be variable but kept under allowable limits while freely spinning. The principle of operation of such a control is explained below.

According to Eqn.(3.6) thermodynamically the output power of the MTG-ORC is a function of the mass flowrate, $\dot{m}$, the ideal specific enthalpy drop across the turbine, Δh_0, and the thermodynamic efficiency, η_{thermo}. Thus, the power can be controlled with variations of such parameters, and as they depend on the expansion ratio, the power can be controlled with a throttling valve.

On the other hand, if the pressures and the temperatures at the boundaries are constant, and the internal geometry of the turbine does not change; the output power can only change with variations of the efficiency. The efficiency can be represented as a function of two dimensionless parameters: the loading coefficient and the flow coefficient; as can be seen in Eqn.(7.1). According to the definition of these parameters, the flow coefficient is a function of the speed of the blade, u, and the radial speed of the flow at the nozzle exit, $c_{f,2}$. The loading coefficient is a function of the speed of the blade, u, and the isentropic drop of specific enthalpy, Δh_{0s}. Thus, if the expansion ratio is constant, Δh_{0s} and $c_{f,2}$ would also be constant and the efficiency would only be a function of u, which in turn, would be a function of the rotational speed, ω. In other words, the power output can be controlled with variations of the blade speed ratio, *BSR*, and, as the *BSR* is always within the range $0 \leq BSR \leq 1$, the speed of the blade cannot exceed the spouting velocity c_0. Consequently, the rotational speed of the MTG-ORC can be kept within the range $0 \leq \omega \leq \omega_{max}$ with the maximum rotational speed, ω_{max}, given by Eqn.(4.6).

$$\omega_{max} = \frac{c_0}{r_2} = \frac{\sqrt{2\Delta h_{0s}}}{r_2} \tag{4.6}$$

Depending on the array, the limited expansion control can be done with a single valve controlling the differential pressure or two independent valves controlling the upstream and downstream absolute pressures. A single valve would keep the inlet-outlet differential pressure constant, as illustrated in Fig. 3.7c, whilst bypassing the excess flow whereas two independent valves can be used, one upstream and one downstream of the turbine, to keep the inlet and outlet pressures constant. The latest type of pressure control is common in domestic refrigeration systems as regulators are used to control the pressure in the evaporator and the condenser; therefore, they can be also implemented into ORC systems.

The speed control through limited expansion can represent two important advantages: simplicity and passive actuation. The benefit of simplicity, in terms of operation and economy, may be easy to recognise but the benefit of a passive actuation can be better understood in terms of the reduced self-consumed power and a longer

lifespan of the actuators. In contrast, the limited expansion control presents two shortcomings: the rotational speed would often be near the maximum allowable limit and useful fluid power would be wasted, although both of these shortcomings can be addressed as explained below.

The rotational speed varies if the load is modified while the mass flowrate remains constant, at a given condition. This change of the rotational speed would produce a change in the efficiency until the generated power matches the power required by the new load. If this new load is too low and the flowrate is high, the rotational speed can increase and cause the blade to achieve the spouting speed, which causes the efficiency and the power to dropdown. In that situation, the MTG-ORC would be working in the range $\omega_{nominal} \leq \omega \leq \omega_{max}$. However, if the bearings are selected considering the maximum rotational speed as the design speed, the unit should withstand this condition.

Conversely, a waste of fluid power can occur if the efficiency deviates from the optimal efficiency whilst the supply of fluid power remains constant because, in such a situation, a fraction of useful power would be underutilised. This should not be a significant concern as the potential applications (WHR, geothermal and solar) of the heat supplied does not represent a fuel cost. If the heat supplied is not used, it would be wasted anyway. Moreover, in applications such as waste heat conversion and geothermal energy, a minimal perturbation of the upstream supply of heat is highly desired.

4.8. DESIGN OF THE ENCLOSURE

Two important issues must be addressed for the MTG-ORC to work safely and reliably: leaking and burst. Leaking of the working fluid is a critical issue for several reasons. Firstly, the leak of the working fluid is detrimental to the performance of the MTG-ORC because the working fluid skips the expander without producing power. Additionally, the leak can cause the ORC system to stop due to lack of fluid, which results in intermittent operation. Secondly, the leak of working fluid represents a hazard in terms of health, safety and environmental impact. And lastly, the leak of working fluid also represents a considerable cost for the replacement of the fluid and servicing.

In the refrigeration industry, the problem of working fluid leakage in compressors has been resolved with an outer hermetic enclosure, shown in Fig. 2.6. The motor and the compressor are enclosed into this welded shell that prevents leaks. However, as the shell is welded, the maintenance of hermetic compressors is difficult, and consequently, their lifespan is limited. Similarly, an outer hermetic enclosure can be implemented for the MTG-ORC to prevent leaks. The outer enclosure is a simple solution that can be fabricated and sealed much more easily than a turbine casing. Additionally, the pressure inside the shell would act on the outer surface of the turbine casing, relieving some of the stress, which may enhance its mechanical integrity. Although the leak from the interior of the turbine into this envelope may still happen and affect the performance, the critical issue of leaking to the environment is eradicated. Unfortunately, the scarce accessibility of this hermetic enclosure can result in a limited lifespan of the unit due to a lack of maintenance.

If the MTG-ORC is contained in the aforementioned enclosure, all its components would be exposed to the working fluid. Consequently, the design of the enclosure must also consider the chemical compatibility of the refrigerant with the materials used in all the components of the MTG-ORC. Moreover, this enclosure would be a pressure vessel that must be designed and fabricated in accordance with the standards: ISO 16528-1 Boilers and pressure vessels [228] and/or ASME boiler and pressure vessel code (BPVC) [229]. These standards provide guidelines for the design, material selection and fabrication of pressure vessels to withstand the specified operation conditions. According to ASME-BPVC [229], the thickness of the shell (t_s) can be calculated with Eqn.(4.7), the thickness of the heads can be calculated with Eqn.(4.8) and the thickness of nozzles can be calculated with Eqn.(4.9). In those equations, the P is the internal design pressure in psi, r is the inside radius of the shell, head and nozzle, in inches, σ_{max} is the maximum allowable stress of the material in psi; and E_j is the join factor. It must be noted that the resulting thickness t_s, t_h and t_n should be approximated to the upper closest standard thickness.

$$t_s = \frac{P \cdot r}{\sigma_{max} E_j - 0.6P} \tag{4.7}$$

$$t_h = \frac{P \cdot r}{2\sigma_{max} E_j - 0.2P} \tag{4.8}$$

$$t_n = \frac{P \cdot r}{\sigma_{max} E_j - 0.6P} \tag{4.9}$$

For this investigation, the shell to enclose the MTG-ORC was designed with the following parameters: working temperature of the shell of 353[K], which is the maximum working temperature of the cycle; design temperature of 371[K], which allows a 5% margin above the working temperature; design pressure of 1.39[MPa] (202[psi]), which allows a 15% margin above the saturation pressure at the design temperature; internal radius of the shell of 150[mm](6[in]), which is sufficiently large for allocating the volute of the turbine; maximum allowable stress of the material of S=114[MPa], which is the maximum allowable stress for carbon steel SA-516 Gr.70 for a design temperature of up to 644[K] in accordance with the ASME BPVC [229]; and a join factor of E=0.7, which corresponds to joints with visual examination without radiography. A summary of the resulting thicknesses is presented in Table 4.8.

Table 4.8 Calculation of thickness for the outer enclosure

Imperial system units		**International system units**	
T[°F]	208	T[K]	371
P[psi]	202	P[kPa]	1380
R[in]	6	R[m]	0.15
σ_{max}[psi]	16600	σ_{max}[MPa]	114.45
Ej[1]	0.7	Ej[1]	0.7
Ts[in]	1/8	Ts[mm]	3
Th[in]	1/8	Th[mm]	3
Tn[in]	1/8	Tn[mm]	3

On the other hand, a burst is a dangerous situation that is always possible in turbomachinery. Bursts can happen to a turbomachine in two situations: overspeed or overpressure. If the turbomachine experiences overspeed, a failure of rotating components can happen due to centrifugal forces .This is more likely if the rotor experiences an abrupt acceleration, for example, when the resisting load is suddenly disconnected and the supply of working fluid is maintained. The over-speeding can result in a dramatic increment of the centrifugal forces that can cause a failure of

components, ejection of debris and/or the rotor to run-away, which are very dangerous situations for personnel around the machine. The causes of overspeed are diverse though the principal can be considered an improper operation of the turbomachine and/or failure of the control system. As a consequence, measures to prevent or mitigate a burst must be implemented such as an outer enclosure, though the risk cannot be completely eliminated. In this investigation, the aforementioned outer shell can be an additional protection measure to mitigate a burst since the volute of the turbine would be the primary burst container; however, if a burst occurs, damage to the equipment cannot be avoided.

The outer shell must also be designed to contain the energy release in case of a rotor burst. The energy released in case of the entire rotor running-away can be calculated with Eqn.(4.10), which assumes the rotor as an eccentric flywheel. In such an equation, E_k is the kinetic energy stored in the rotor, I_r is the momentum of inertia of the rotor with respect to the rotation axis and ω is the rotational speed of the rotor. Additionally, the momentum of inertia of the rotor with respect to the rotation axis can be calculated with Eqn.(4.11), where I_{0r} is the momentum of inertia of the rotor with respect to its centre of mass, m_r is the mass of the rotor and e is the maximum allowable eccentricity of the rotor.

$$E_k = \frac{1}{2} I_r \omega^2 \tag{4.10}$$

$$I_r = I_{0r} + \frac{1}{2} m_r e^2 \tag{4.11}$$

For this investigation, an eccentricity of the rotor of 1[mm] was allowed and the energy stored in the rotor was calculated assuming the shaft as a uniform cylinder of steel with a density of 8000[kg/m^3], a length of 220[mm] and a diameter of 28[mm]. Additionally, an impeller made of PEEK-GF30 with a density of 1510[kg/m^3], volume of 1.12×10^{-5}[m^3] and a volume moment of inertia of 1.68×10^{-9}[m^5]. The energy stored in the shaft resulted of 780[J]; thus, the outer shell should be capable of dissipating at least this amount of energy. In accordance with the standard ISO 23125: Machine tools-

Safety-Turning machines [230], the protection against ejected fragments in turning machines must be capable of containing at least 3[kJ]. This can be achieved with a steel plate with a tensile strength of 639[MPa] and a thickness 3[mm]; this thickness should be added to the thicknesses of the outer shell reported in Table 4.8.

CHAPTER 5. ANALYSIS

In this section, three sets of analyses are performed to assess the design of the MTG-ORC: a simulation of the aerodynamic performance, a fluid-structure interaction study and a fluid-material chemical compatibility study. The results of these analyses should provide a prediction of the performance of the unit in the proposed application before it is put into a test.

5.1. PROGRAM FOR SIMULATION OF THE PERFORMANCE

The assessment of the performance is done through the analysis of two parameters: efficiency, η, and power, $\dot{W}$. A program for the simulation of the thermo-aerodynamic performance of the MTG is developed. The program follows the mean-line method, which assumes a single streamline flowing through the gas path with constant transversal properties [158] and the nomenclature defined in Fig. 4.2. Such a program is an iterative routine made in Microsoft Excel and Visual Basic Applications whose simplified flow-chart is presented in Fig. 5.1.

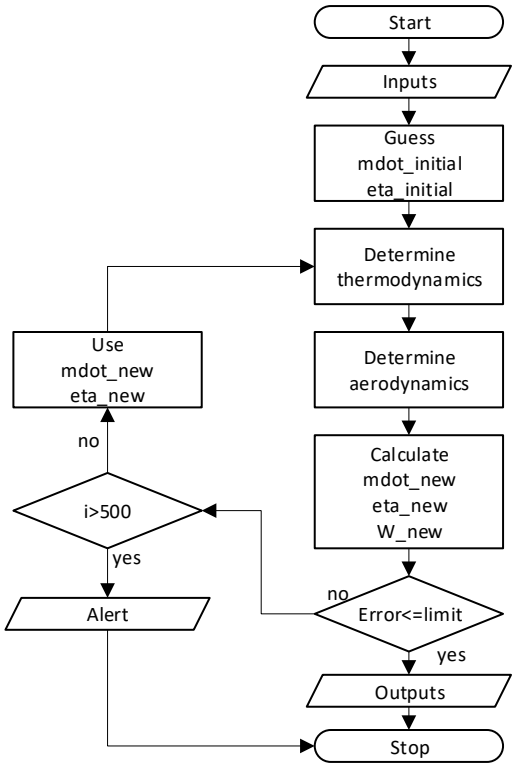


Fig. 5.1. Simplified flow-chart of the program for performance prediction;
mdot_initial: initial guess of flowrate; eta_initial: initial guess of thermo-aerodynamic efficiency; mdot_new, calculated mass flowrate; eta_new: calculated thermo-aerodynamic efficiency; Waero_new: calculated thermo-aerodynamic power; i: iteration.

The routine successively approximates the thermo-aerodynamic efficiency, mass flow and power of the turbine. It starts reading the inputs presented in Table 5.1 and gives an initial guess of the thermo-aerodynamic efficiency (eta_initial) and mass flow (mdot_initial). Then, the thermo-aerodynamic equations are resolved and the new thermo-aerodynamic efficiency (eta_new), mass flow (mdot_new) and power (W_new) are obtained and used for resolving a new iteration. The iterative cycle continues until the maximum allowed error or the maximum number of iterations are achieved; finally, the results are exported.

Table 5.1 Summary of inputs for the performance prediction program

Description	Symbol
Nozzle	
Inlet total temperature	T_{01}
Inlet total pressure	P_{01}
Absolute exit angle	α_2
Rotor	
Exit total pressure	P_{03}
Inlet diameter	D_2
inlet blade height / Inlet diameter	$\frac{b_2}{D_2}$
Outlet mean diameter / Inlet diameter	$\frac{D_3}{D_2}$
Exit blade height / Inlet diameter	$\frac{b_3}{D_2}$
Relative inlet angle	β_2
Relative outlet angle	β_3
Blade speed ratio	BSR

5.1.1. Thermo-aerodynamics

The thermodynamic analysis can be performed using the principles and equations presented in section 3.1.1. However, the program gives the option of selecting the ideal gas law or the real gas formulation from REFPROP [152] to calculate the thermophysical properties of the fluid. When the ideal gas law is selected, the specific enthalpy and density for any given state, i, are calculated using Eqn.(5.1) and Eqn. (5.2) respectively; the actual change of total specific enthalpy across the rotor, Δh_0, can be obtained with Eqn. (5.3); and the isentropic change of specific enthalpy across the rotor is calculated with Eqn.(5.4).

$$h_i = c_p T_i \tag{5.1}$$

$$\rho_i = \frac{P_i}{RT_i} \tag{5.2}$$

$$\Delta h_0 = c_p(T_{02} - T_{03}) \tag{5.3}$$

$$\Delta h_{0s} = h_{02} - h_{03s} = c_p T_{02}\left(1 - \left(\frac{P_{03}}{P_{02}}\right)^{\frac{\gamma-1}{\gamma}}\right) \tag{5.4}$$

When the real gas formulation is selected, the specific enthalpy and density for any given state, i, are calculated using Eqn.(5.5) and Eqn.(5.6), respectively; the actual change of total specific enthalpy across the rotor, Δh_0, can be obtained with Eqn.(5.7); and the isentropic change of the specific enthalpy across the rotor is calculated with Eqn.(5.8).

$$h_i = f_{REFPROP}(T_i, P_i) \tag{5.5}$$

$$\rho_i = f_{REFPROP}(T_i, P_i) \tag{5.6}$$

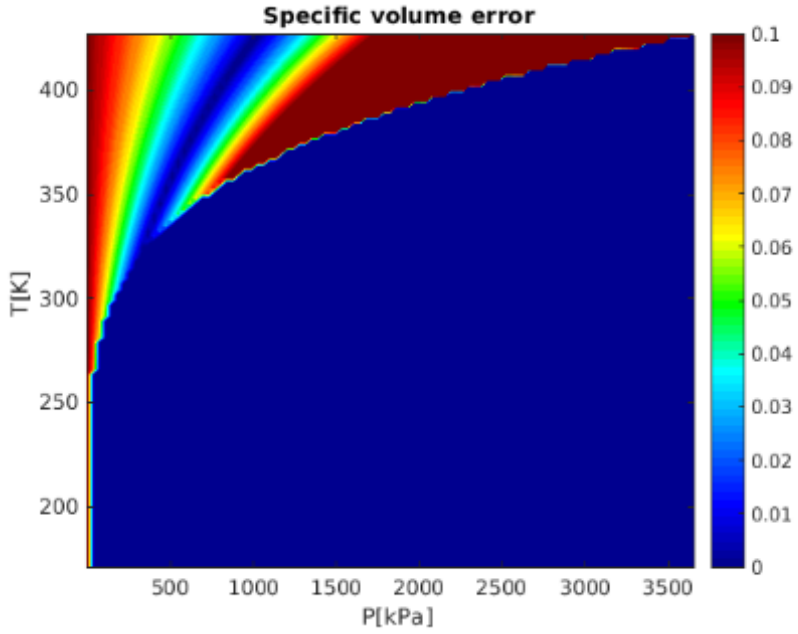
$$\Delta h_0 = h_{02}(T_2, P_2, c_2) - h_{03}(T_3, P_3, c_3) \tag{5.7}$$

$$\Delta h_{0s} = (h_{02} - h_{03s})_{@constant\ entropy} \tag{5.8}$$

The ideal gas law should predict, with a reasonable accuracy, the thermophysical properties of real gases at temperatures and pressures considerably lower than those at the critical point [231]. As the range of pressure and temperature defined in section 4.2 fulfil that condition, the ideal gas law should reasonably predict the properties with respect to the real gas formulation. This can be seen in the results presented in Fig. 5.2b, Fig. 5.3b and Fig. 5.4b, where the error of the prediction of properties, in the interval of operation, of the ideal gas equation with respect of the real gas properties from

REFPROP [152], are presented for specific volume, specific enthalpy and speed of sound.

a)



b)

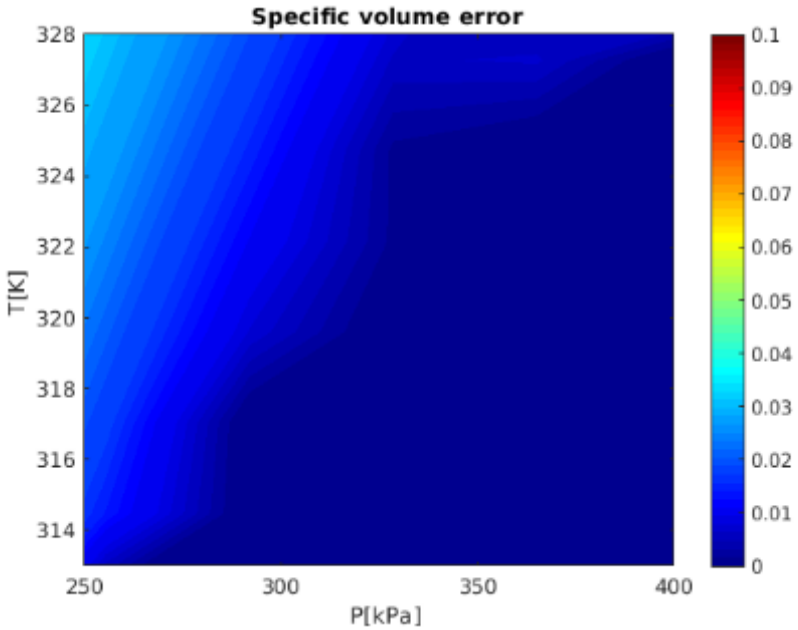
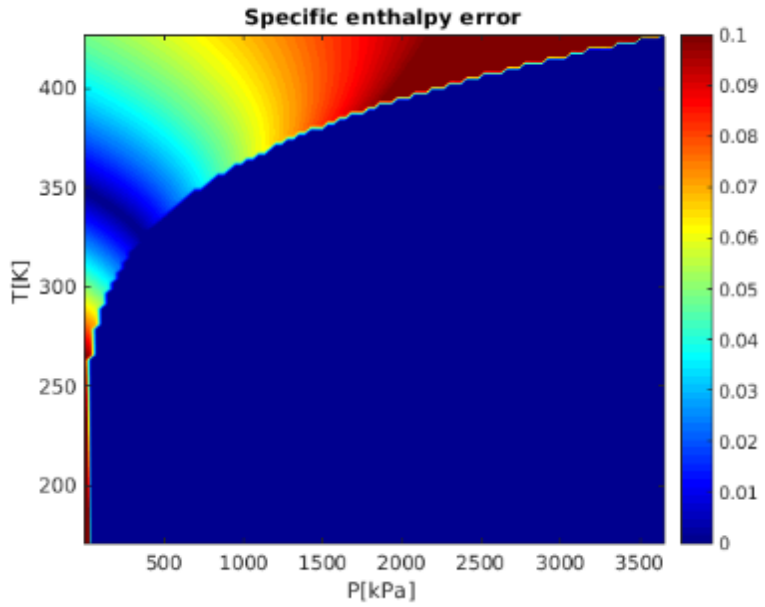


Fig. 5.2 Error of calculation of the specific volume using ideal gas;
a) full range from triple point to critical point of the substance; b)interval of interest for this investigation; error with respect to the calculated property using REFPROP[152].

a)



b)

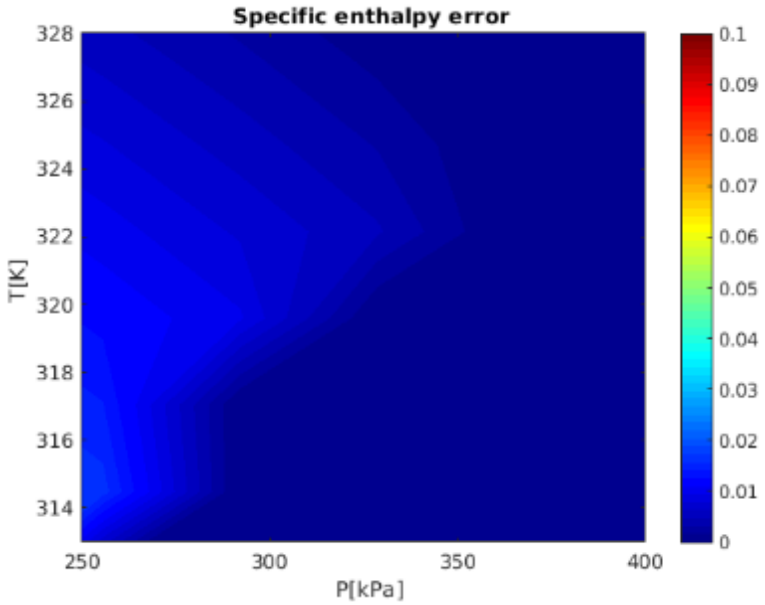
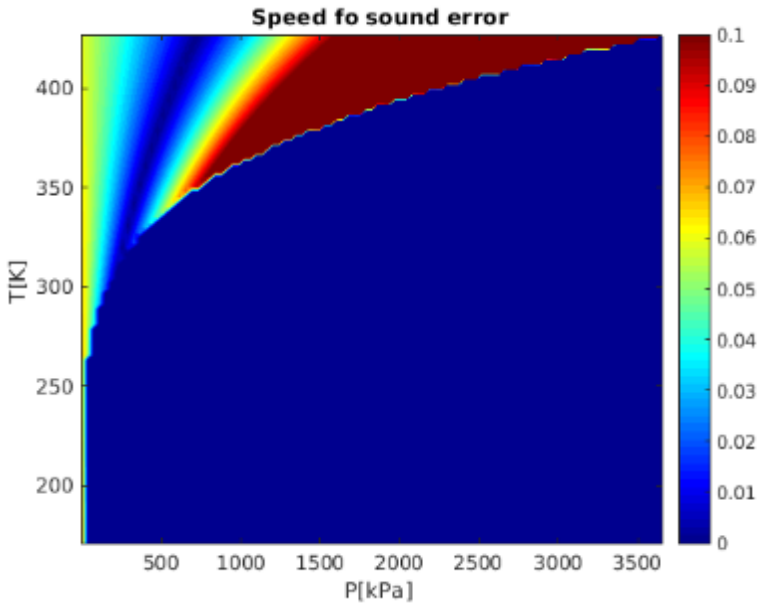


Fig. 5.3 Error of calculation of the specific enthalpy using ideal gas;
a) full range from triple point to critical point of the substance; b)interval of interest for this investigation; error with respect to the calculated property using REFPROP[152].

a)



b)

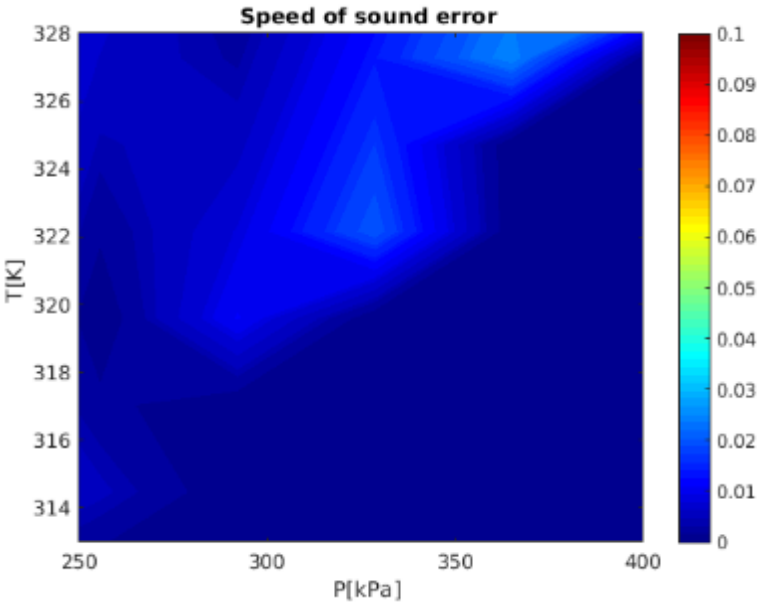


Fig. 5.4 Error of calculation of the speed of sound using ideal gas;
a) full range from triple point to critical point of the substance; b)interval of interest for this investigation; error with respect to the calculated property using REFPROP[152].

As can be seen in the aforementioned figures, the prediction of properties in the interval of interest has an error lower than 3%, with respect to the real properties. Therefore, the results of the simulation at the design point should be comparable with the results of the design tool, which relies on the ideal gas law only.

The velocity triangles are determined with the combination of the equation of continuity, the thermodynamic equations, the nozzle geometry and the rotor geometry

presented in Table 5.1, in accordance with section 3.1.1. Analogously, the efficiency, power and mass flow rate are obtained with the methods and equations described in the aforementioned section.

If the temperature at the outlet of the rotor is unknown, Eqn.(5.3) and Eqn.(5.7) cannot be used for calculating the actual drop of specific enthalpy. However, the actual enthalpy drop can be calculated using Eqn.(5.9), which is a function of the isentropic change of total specific enthalpy across the unit and the aerodynamic losses, Δh_{loss}. Thus, the thermo-aerodynamic efficiency can be calculated with Eqn.(5.10), accounting for an overall loss of specific enthalpy, Δh_{loss}.

Although the most employed models in literature for predicting aerodynamic losses in radial turbines are the models of Rohlik [78] and Whitfield-Baines [232], the aerodynamic losses are evaluated using the model proposed by Suhrmann et.al [233]. This is a compilation of loss models conceived for the application on low-capacity turbines that accounts for the loss of specific enthalpy produced by skin friction, Δh_f, secondary flow, Δh_s, incidence, Δh_i, clearance leaking, Δh_c and exiting speed, Δh_e, as illustrated in Eqn.(5.11).

$$\Delta h_0 = \Delta h_{0s} - \Delta h_{loss} \tag{5.9}$$

$$\eta_{thermo-aero} = \frac{\Delta h_{0s} - \Delta h_{loss}}{\Delta h_{0s}} \tag{5.10}$$

$$\Delta h_{loss} = \Delta h_f + \Delta h_s + \Delta h_i + \Delta h_c + \Delta h_e \tag{5.11}$$

The skin friction loss, Δh_f, is calculated with Eqn.(5.12), which is a function of the further corrected friction factor, $c'_{f,c}$; this factor can be obtained with the correlation of Musgrave [234] presented in Eqn.(5.13), which in turn, depends on the corrected friction factor, $c_{f,c}$. The corrected friction factor is calculated with Eqn.(5.14), which depends on the friction factor, c_f. Lastly, the friction factor is calculated with the correlation of Colebrook et al. [235], presented in Eqn.(5.15). In the aforementioned equations, the hydraulic diameter, D_h is the average ratio of the "wet" area of the gas

path over its diameter, the hydraulic length, L_h is the length of the main-line of the flow, the curvature radius, r_c is the average curvature radius of the mean-line, the diameter, D_2 is defined at the rotor inlet and the average relative flow-speed across the rotor, $\overline{w}_{2-3}$ is calculated with Eqn.(5.16).

The secondary flow loss, Δh_s, is calculated with Eqn.(5.17), which is a function of the rotor diameter at the inlet, D_2, the number of rotor blades, Z, the curvature radius of the blades, r_c, and the flow-speed at the rotor inlet, c_2. The clearance loss, Δh_c, is calculated with Eqn.(5.18), which is a function of the tip clearance of the blades, tc, the height of the rotor blade at the inlet, b_2, and the absolute tangential speed of the flow at the rotor inlet, $c_{2,u}$. These equations for calculating secondary and leaking losses are adopted from the work of Rodgers and Geiser [236]. The incidence loss, Δh_i, is calculated with Eqn.(5.19) proposed by Whitfield and Wallace [237], which depends on the relative tangential speed of the flow at the rotor inlet, $w_{2,u}$. Finally, the exit loss, Δh_e, produced by the speed of the exiting gas, c_3, is calculated with Eqn.(5.20). A schematic of the cross-sectional view of a radial turbine and the geometric nomenclature used for the model is presented in Fig. 5.5.

$$\Delta h_f = c'_{f,c} \frac{L_h}{D_h} (\overline{w}_{2-3})^2 \tag{5.12}$$

$$c'_{f,c} = c_{f,c} \left[\mathrm{Re} \left(\frac{D_2}{2r_c} \right)^2 \right]^{0.05} \tag{5.13}$$

$$c_{f,c} = c_f \left(1 + 0.075 \mathrm{Re}^{\frac{1}{4}} \sqrt{\frac{D_h}{2r_c}} \right) \tag{5.14}$$

$$\frac{1}{\sqrt{4c_f}} = -2 \log \left(\frac{\frac{k}{D_h}}{3.7} + \frac{2.51}{\mathrm{Re}\sqrt{4c_f}} \right) \tag{5.15}$$

$$\overline{w}_{2-3} = \frac{w_2 + w_3}{2} \tag{5.16}$$

$$\Delta h_s = \frac{D_2}{Z r_c} (c_2)^2 \tag{5.17}$$

$$\Delta h_c = 0.4 \frac{tc}{b_2} \left(c_{2,u}\right)^2 \tag{5.18}$$

$$\Delta h_i = \frac{1}{2} \left(w_{2,u}\right)^2 \tag{5.19}$$

$$\Delta h_e = \frac{1}{2} (c_3)^2 \tag{5.20}$$

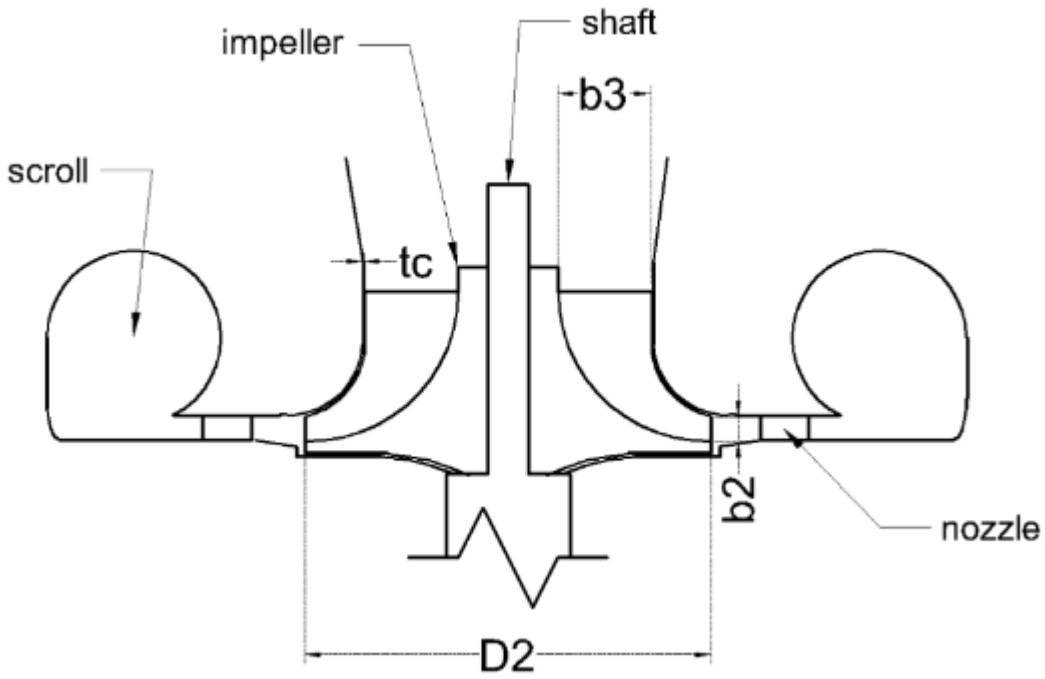


Fig. 5.5. Cross-sectional view of a radial turbine and model nomenclature; D2: rotor inlet diameter; b2: rotor inlet blade height; b3: rotor outlet blade height; tc: tip clearance.

5.1.2. Mass flow

The mass flow can be iteratively obtained by simultaneously solving the above equations and the equation of continuity for a volume of control shown in Eqn.(3.10).

$$\dot{m} = \rho_2 A_2 c_{f,2} = \rho_3 A_3 c_{f,3} \tag{5.21}$$

5.1.3. Dimensionless interpretation

Arguably, the most important parameter for assessing the performance of the MTG is the efficiency. It can be represented as a function of two dimensionless parameters: the flow coefficient ϕ and the loading coefficient, ψ, defined in Eqn.(3.11) and Eqn.(3.12), respectively. The efficiency is, thus, three-dimensional in a space $\phi - \psi - \eta_{aero}$, which is commonly presented in Smith [238] type charts. These charts show contours of the efficiency in a plane $\phi - \psi$ or, in other words, the projection of the three-dimensional efficiency in such a plane. However, for convenience, the results in this work are presented in four separate charts that are projections of the three-dimensional efficiency in different planes as described below.

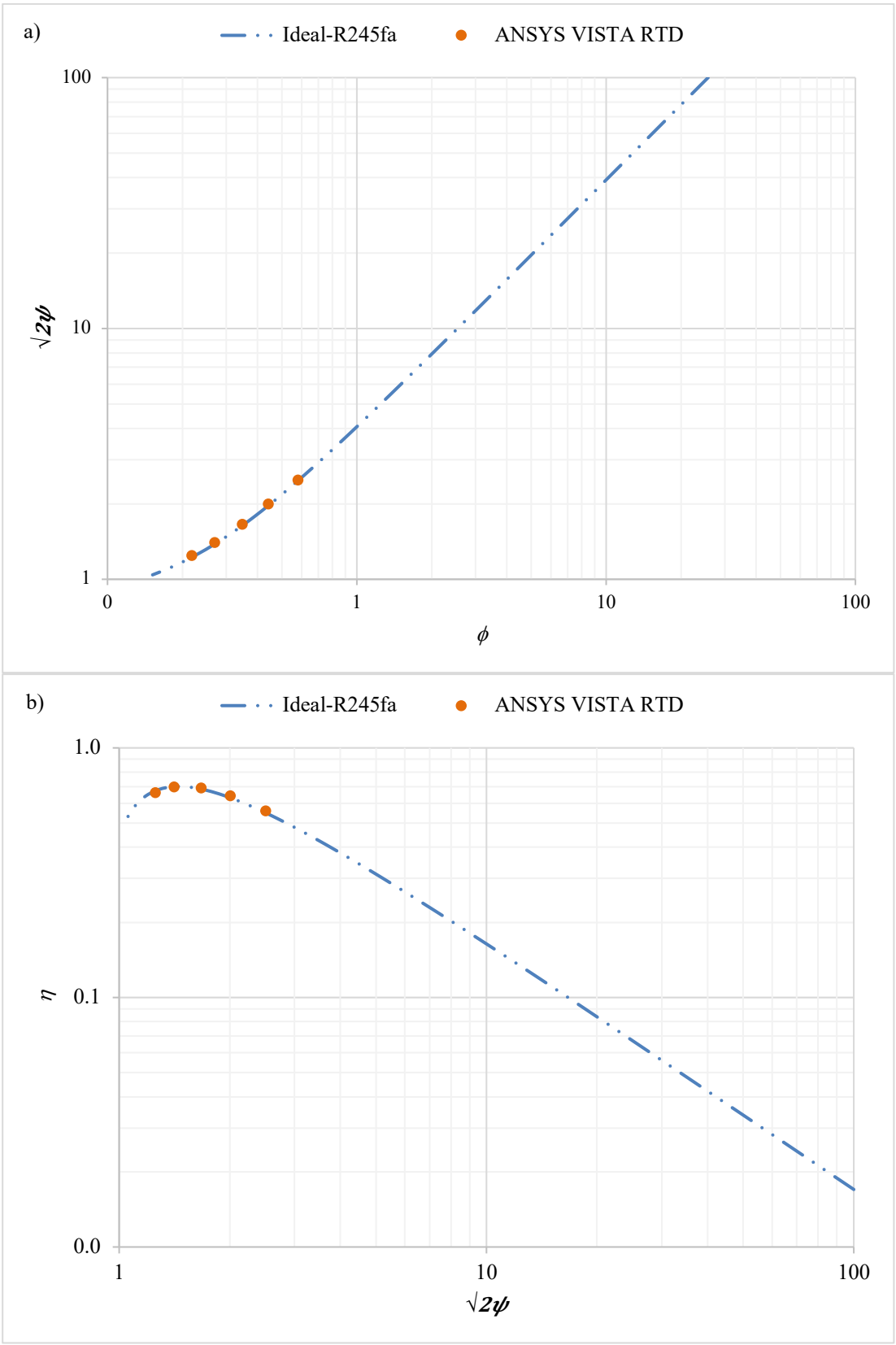
The first chart is a representation of the relationship between the flow coefficient ϕ and the loading coefficient ψ but the linearized parameter $\sqrt{2\psi}$ is used instead of ψ; this means that such a chart presents the efficiency in the plane $\phi - \sqrt{2\psi}$. This chart is analogous to the maps of radial turbines, adopted by Alshammari et al. [239] to describe the relationship between the corrected mass flow rate $\dot{m}_c$ and the expansion ratio PR. In these two charts, the mass flow rate is represented by the flow coefficient and the corrected mass flow rate, while the expansion is represented by the loading coefficient and the expansion ratio. The flow and loading coefficients are, however, more convenient when presented in a $\phi - \sqrt{2\psi}$ plane, where their relationship is described as a straight line. The second chart is a projection of the efficiency in a plane $\phi - \eta_{aero}$ and the third chart is a projection of the efficiency in a plane $\sqrt{2\psi} - \eta_{aero}$. Finally, the fourth chart is a handy representation of the efficiency that shows it in a plane $BSR - \eta_{aero}$, with BSR being the blade speed ratio presented in Eqn.(5.22). This chart is analogous to the representation in a plane of $\sqrt{2\psi} - \eta_{aero}$ because the blade speed ratio

BSR is a function of the loading coefficient ψ. However, the chart $BSR - \eta_{aero}$ is more common in specialised literature for representing the performance of radial inflow turbines [240].

$$BSR = \frac{u_2}{C_0} = \frac{1}{\sqrt{2\psi}} \tag{5.22}$$

5.1.4. Validation of the program

The program was validated using the design tool ANSYS® 16.2 VISTA RTD™, ideal-R245fa as the working fluid, and the design thermodynamic conditions given above. Several scenarios were modelled with the program in the range $0 \leq BSR \leq 1$ and five scenarios were modelled with ANSYS® 16.2 VISTA RTD™ in the range $0.4 \leq \frac{u}{C_0} \leq 0.8$. The range of BSR used for validation with the design tool had to be narrowed due to the lack of convergence of the software for values $BSR < 0.4$ and $BSR > 0.8$.


a)
Ideal-R245fa
ANSYS VISTA RTD
100
10
1
√2ψ
0
1
10
100
ϕ
b)
Ideal-R245fa
ANSYS VISTA RTD
1.0
0.1
0.0
η
1
10
100
√2ψ

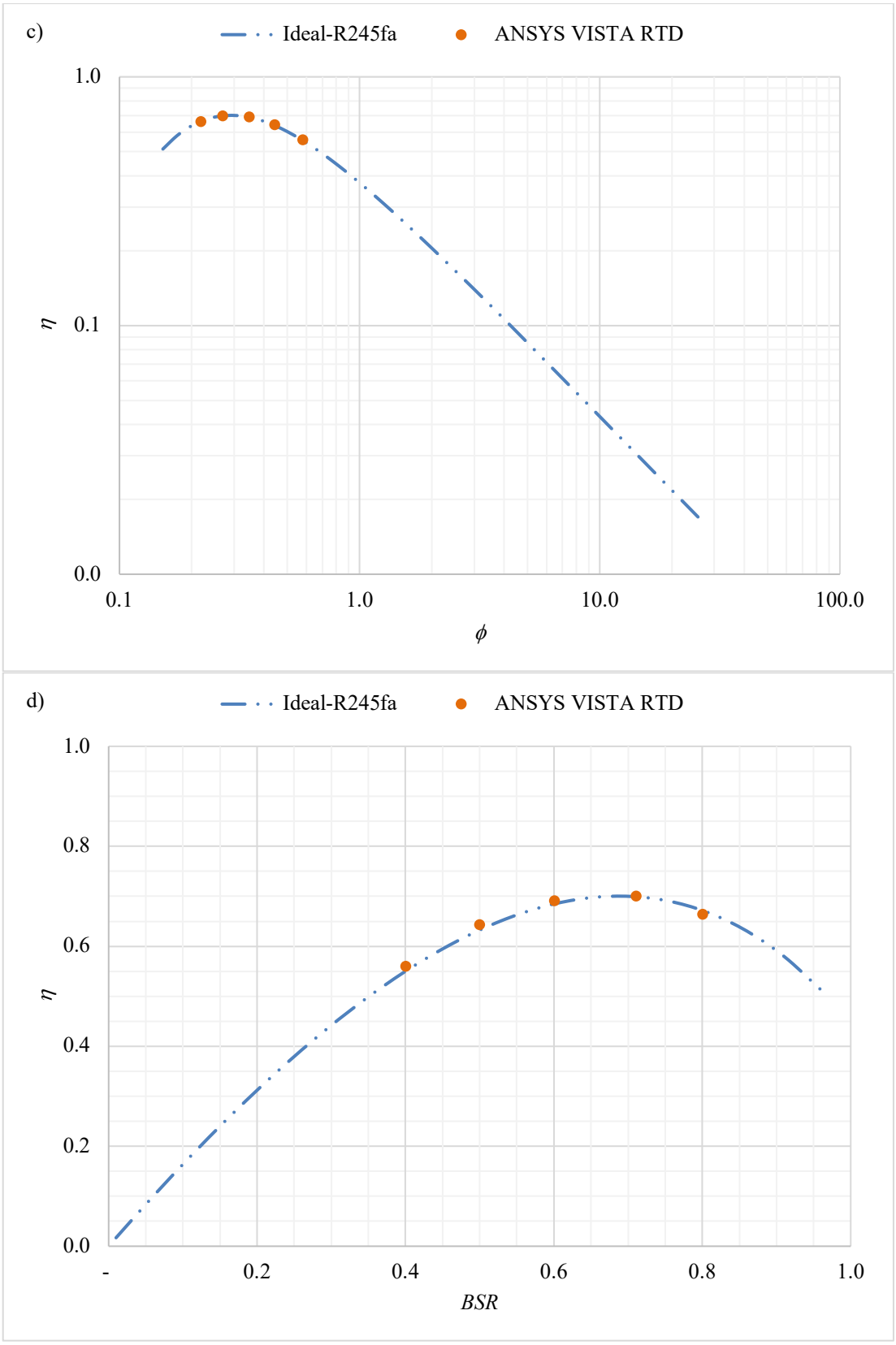


Fig. 5.6 Validation of the results using ANSYS® 16.2 VISTA RTD™.

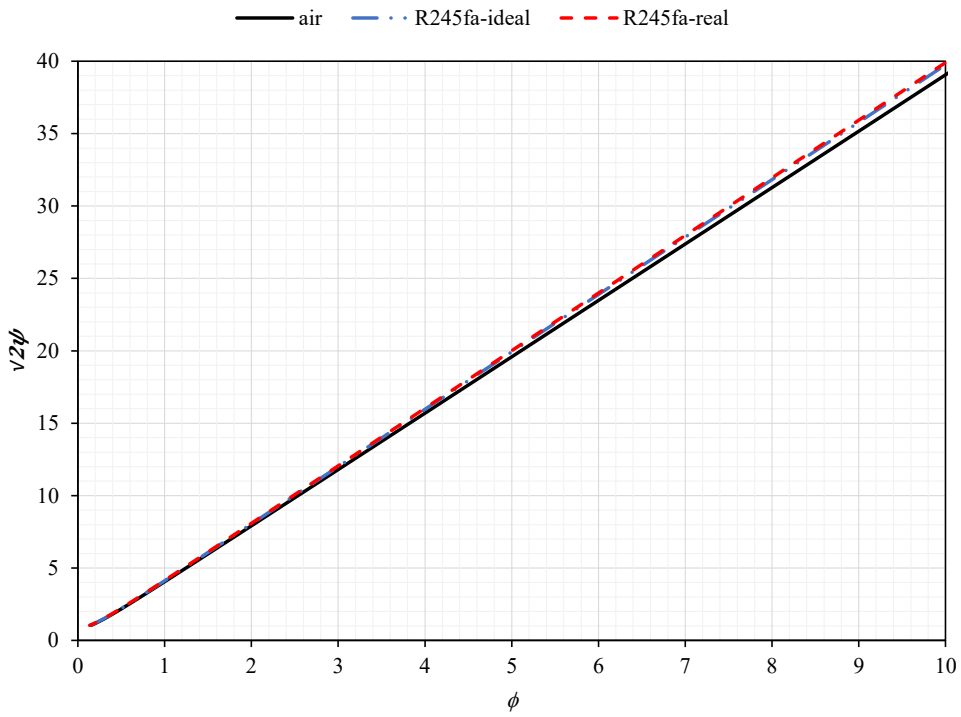
A comparison of the dimensionless results using these two methods is presented in Fig. 5.6. In this graph it is evident that the program for performance simulation has a

good agreement with the design software. The range for comparison is narrow; therefore, a logarithmic scale is used in Fig. 5.6a-c to highlight the agreement; however, a linear scale is used for similar results hereinafter. A maximum root mean squared error of 0.003 was found in the results of the simulations with respect to the results of ANSYS® 16.2 VISTA RTD^{TM}, using ideal-R245fa as the working fluid. Consequently, the program can be considered adequate for the simulation of the performance of the radial turbine of the MTG-ORC.

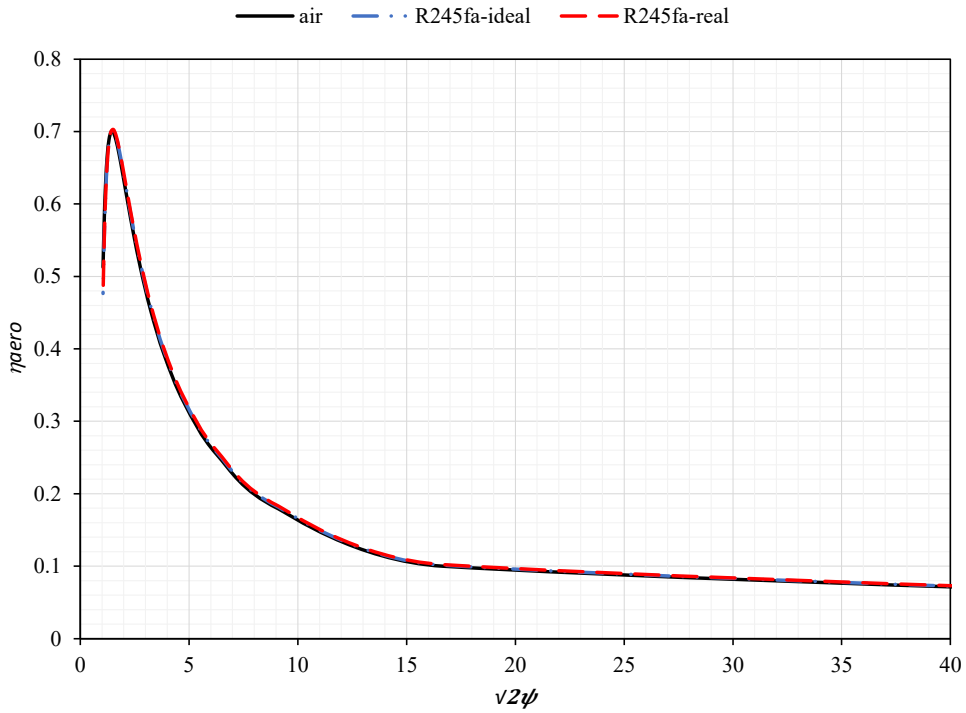
5.1.5. Results of simulations

The results of the simulations showed a strong alignment with the results of the design tool as described in section 5.1.1. Additionally, the simulations show an root mean squared error ($RMSE$) $= 0.023$ for real-R245fa and a $RMSE = 0.006$ for air with respect to ideal-R245fa, for a broad range of *BSR*. The results of the simulations with these three working fluids can be observed in Fig. 5.7,. The results in the plane $\phi - \sqrt{2\psi}$ are shown in Fig. 5.7a, where the parameter $\sqrt{2\psi}$ follows a straight line with a positive slope with respect to ϕ. This behaviour is expected for an ungoverned turbine. As can be seen in Fig. 5.7a, the deviation of the simulations for air, with respect to ideal-R245fa and real-R245fa, increase for large values of ϕ and $\sqrt{2\psi}$, though the difference remains reasonably low. The results in the planes $\phi - \eta_{aero}$ and $\sqrt{2\psi} - \eta_{aero}$ are shown in Fig. 5.7b-c, where the maximum aerodynamic efficiency of η_{aero}=0.7 occurs at the values ϕ=0.3 and $\sqrt{2\psi}$=1.5 (ψ=1.1). However, according to the White-Sayma [241], the efficiency can be higher if the flow coefficient of ϕ=0.3 and a loading coefficient ψ=0.95 were achieved. In any case, the simulated aerodynamic efficiency seems to be within the range reported in experimental literature [88, 89, 94, 95, 102-104] and hence may be considered an acceptable prediction.

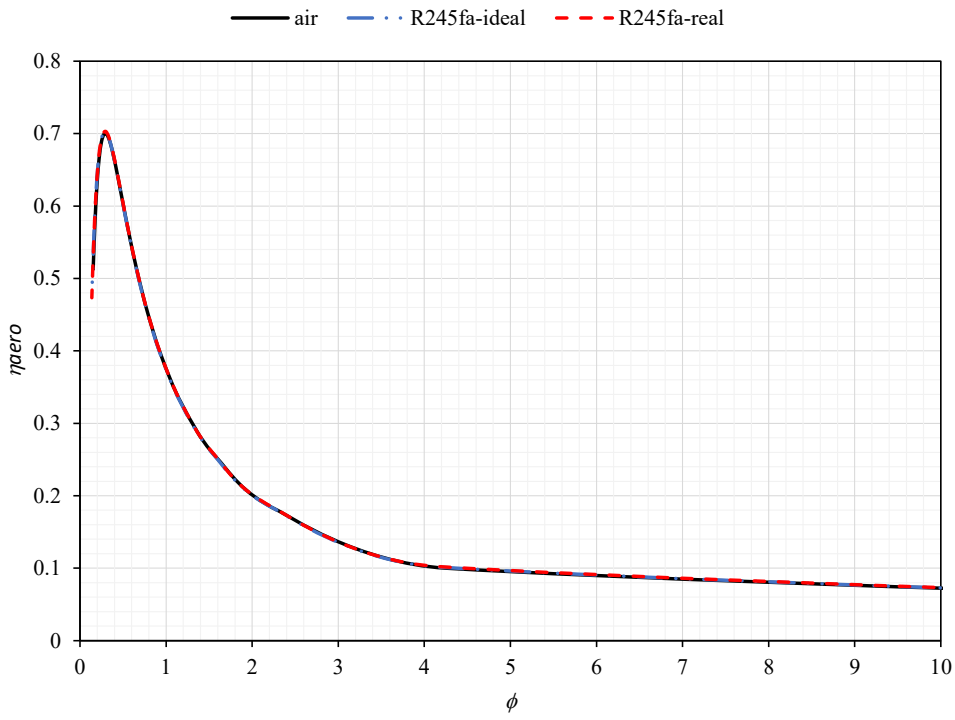
a)


air
R245fa-ideal
R245fa-real
40
35
30
25
20
15
10
5
0
0
1
2
3
4
5
6
7
8
9
10
√2ψ
ϕ

b)


air
R245fa-ideal
R245fa-real
0.8
0.7
0.6
0.5
0.4
0.3
0.2
0.1
0
0
5
10
15
20
25
30
35
40
ηaero
√2ψ

c)



d)

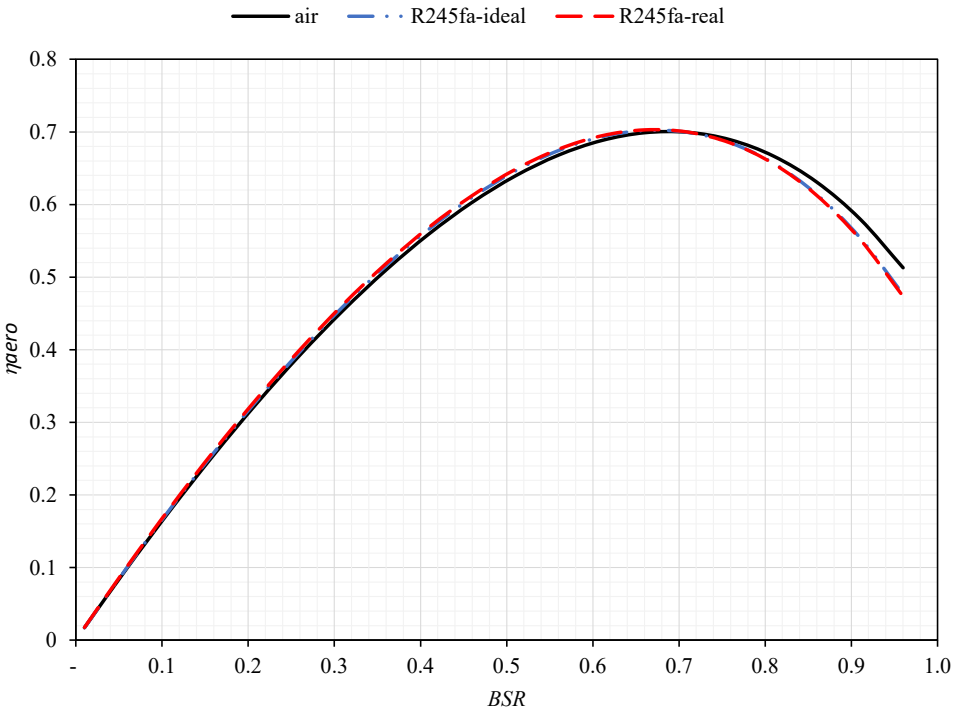


Fig. 5.7 Comparison of the simulated performance;
between air, air ±10% error, ideal-R245fa and real R245fa; a) plane $\phi - \sqrt{2\psi}$; b) plane $\sqrt{2\psi} - \eta_{aero}$; c) plane $\phi - \eta_{aero}$; d) plane $BSR - \eta_{aero}$; ϕ: flow coefficient, ψ: loading coefficient, BSR: blade speed ratio, η_{aero}: aerodynamic efficiency.

Additionally, the results in the plane $BSR - \eta_{aero}$ show a typical behaviour of a radial inflow turbine, where the maximum aerodynamic efficiency η_{aero}=0.7 corresponds to a *BSR*=0.66, as can be seen in Fig. 5.7d. Furthermore, a good agreement of the simulation with air, ideal-R245fa and real-R245fa is also evident.

In conclusion, it can be said that the simulation program gives an acceptable insight of the performance in a dimensionless interpretation. The root squared mean error of the aerodynamic efficiency is around $RMSE = 0.023$ whereas the maximum error is around 0.08 considering air, ideal-R245fa and real-R245fa as the working fluid. This conclusion suggests that the performance, in a dimensionless interpretation, may be comparable for the three studied working fluids.

5.2. FLUID STRUCTURE INTERACTION STUDY

The suitability of polymeric materials is assessed with a structural examination of the impeller under the working conditions reviewed above. The selected method is a fluid-structure interaction (FSI) analysis with one-way coupling. This method evaluates the effect of the fluid dynamics on the structural mechanics of the impeller. Consequently, the FSI analysis comprises two major stages: a computational fluid dynamics (CFD) simulation and a structural finite element analysis (FEA). The interaction lies on the fact that the conditions obtained from the fluid simulation are fed into the FEA. The CFD simulation was conducted using ANSYS®16.2 Fluent® and the FEA was conducted using ANSYS® Mechanical™. These two programs were coupled using ANSYS® Workbench™ as an interphase.

5.2.1. Studied scenarios

For the FSI study, three situations were evaluated: normal operation, rotor blocked and overspeed. In normal operation the unit is expected to work normally at full load. In the rotor blocked situation, full flow is supplied with the rotor stopped. In the overspeed condition, the maximum allowed rotational speed is achieved as defined in international standards [242, 243], which is 27% above the rated rotational speed. Each of these scenarios was studied on three materials (Aluminium, Quadrant EPP Ketron© GF30 PEEK-Extruded 30% Glass-Reinforced Polyether Ketone (PEEK-GF30), and

Acrylonitrile Butadiene Styrene (ABS) Therefore, a total of nine scenarios were studied as illustrated in Table 5.2.

Table 5.2 Scenarios for the FSI study

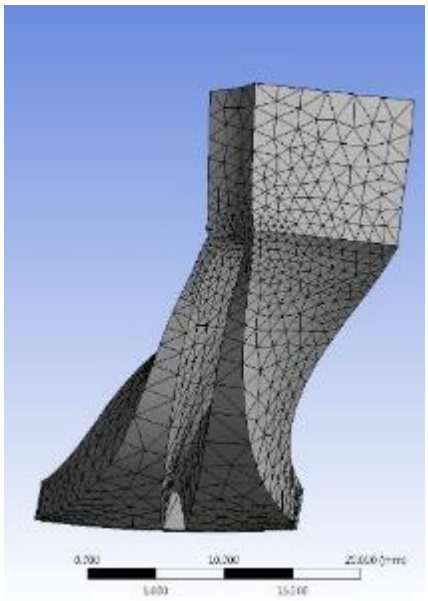
	Aluminium	PEEK-GF30	ABS
Full load	FL-AL	FL-PK	FL-AB
Rotor blocked	RB-AL	RB-PK	RB-AB
Over-speed	OS-AL	OS-PK	OS-AB

5.2.2. Computational Fluid Dynamics (CFD)

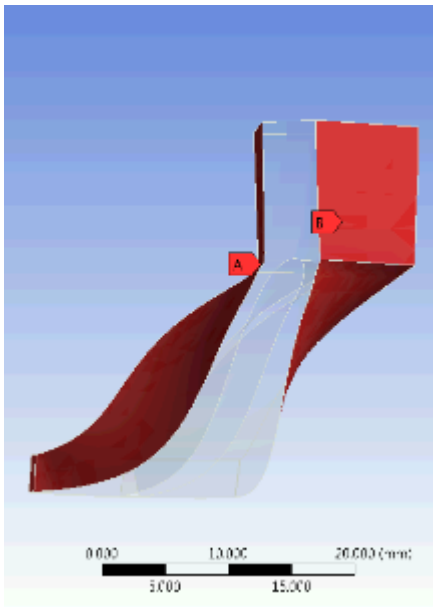
Geometry

The three-dimensional geometry of a single blade of the impeller described in section 4.5 was imported to ANSYS® Fluent®. A fluid rotational domain was then defined for the flow path of a single blade and refrigerant R245fa was selected as the material. This fluid domain was discretised with a tetrahedral mesh (Fig. 5.8a) having 3196 nodes, 14733 elements and periodic rotational symmetry. Seven surfaces were defined in the domain: periodic surface 1 (Fig. 5.8b) and periodic surface 2 (Fig. 5.8b), blade surface (Fig. 5.8c), inlet surface (Fig. 5.8c), outlet surface (Fig. 5.8c), hub surface (Fig. 5.8d), shroud surface (Fig. 5.8d). Match control was given in the periodic faces to enable the periodicity.

a)



b)



c) d)

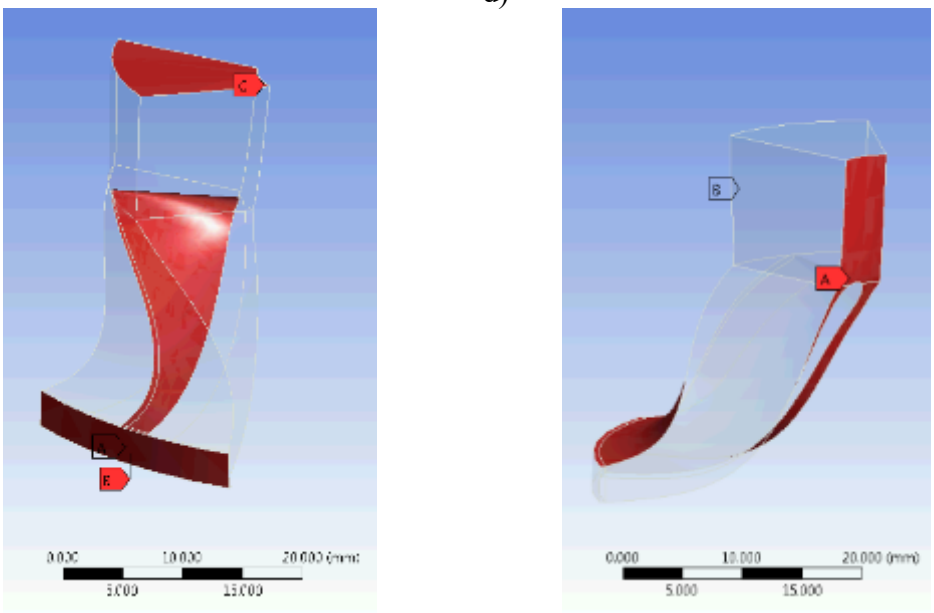


Fig. 5.8 Geometry of the rotational element of fluid;
view from the hub; a) tetrahedral mesh; b) A: periodic surface1, B: periodic surface2; c) A: blade surface, B: inlet surface, C: outlet surface; d) A: hub surface, B: shroud surface.

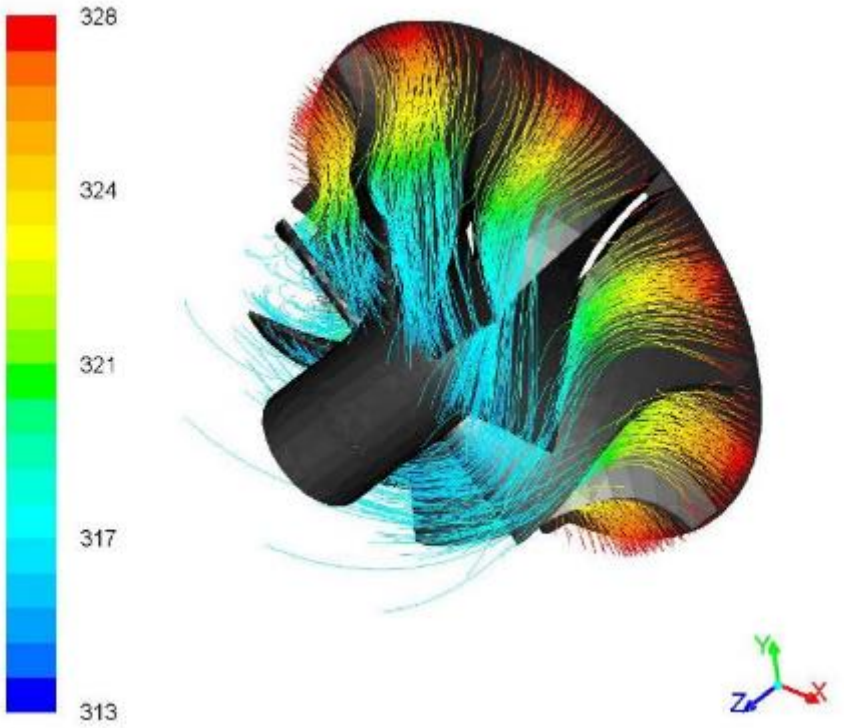
Setup

For the CFD simulation, the input parameters were loaded according to the user's manual [244], to ANSYS® Fluent®. The Reynolds-Averaged Navier-Stokes equations were solved using the standard k-omega turbulence model within a pressure-based steady-state analysis and absolute velocity formulation. The REFPROP EOS [152] were enabled within the software to model the R245fa real gas behaviour. Only one fluid rotational element, corresponding to one blade, was evaluated because the symmetry of the turbine allows for the extrapolation of the results to the entire impeller. The shroud, hub, and blade surfaces were defined as wall boundaries; the periodic faces were defined as periodic-symmetric walls; the inlet was defined as a mass-flow-inlet boundary and the outlet was set as a pressure-outlet boundary. A rotational speed was given to the rotational fluid elements, corresponding to 36000[rpm] for the full load condition, 0[rpm] for the rotor blocked condition and 45720[rpm] for the overspeed condition. The simulation was performed using the pressure-velocity coupled scheme and pseudo-transient formulation, standard discretization for the pressure and first order upwind for density, momentum, and turbulent kinetic energy.

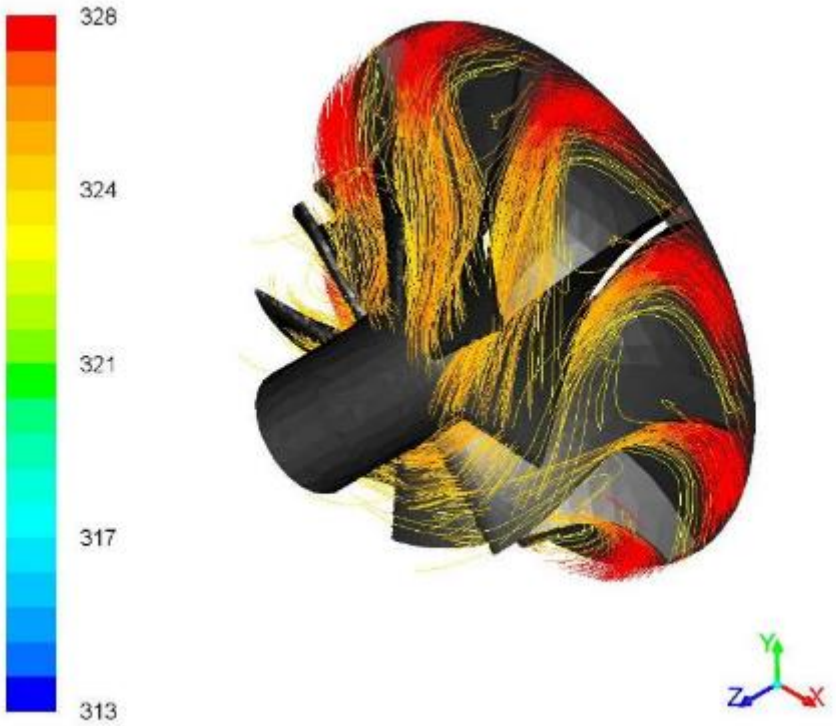
Results of the CFD simulations

In terms of thermodynamic conditions, the results of the CFD simulations are consistent with the results of the power cycle definition and the mean-line design. The streamlines coloured by temperature, for the three evaluated conditions, are shown in Fig. 5.9; in this figure a smooth flow path can be seen for the full load condition. However, clash of the streamlines against the pressure face of the blade is evident for the rotor blocked condition and against the suction face of the blade for the over-speed condition. This clash causes a bending moment that acts as a load alongside the centrifugal force, which is the principal mechanical loading. The simulated efficiency of the impeller was estimated to be 0.86, 0.0, and 0.84 for the full load, rotor blocked and over-speed situations respectively. The impeller efficiency at full load seems to be greater than the efficiency calculated with the mean-line method (0.77).This difference seems to be associated with the secondary losses, which are the greatest in the mean-line analysis, accounting for 0.19 of the efficiency, whereas the CFD simulation reveals an even flow path. Therefore, 0.76-0.86 can be considered an appropriate range for the real efficiency prediction.

a)



b)



c)

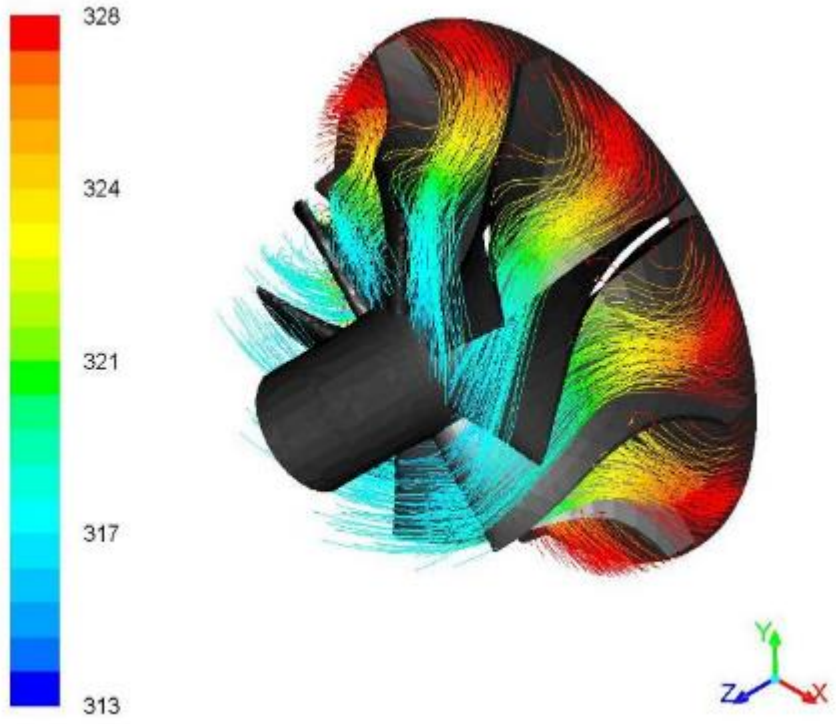


Fig. 5.9 Relative streamlines coloured by total temperature [K];
a) full load; b) rotor blocked and c) 27% over-speed.

5.2.3. Structural Finite Element Analysis (FEA)

Geometry

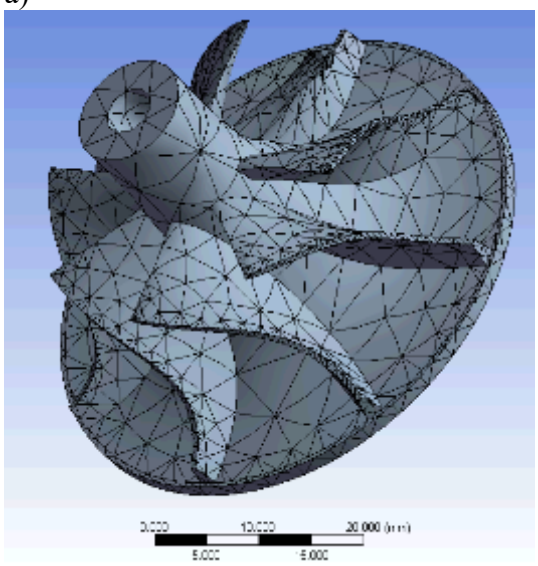
The geometry of the impeller described in section 4.5 was imported to ANSYS® Mechanical™. A tetrahedral mesh with 8977 nodes and 3998 elements (shown in Fig. 5.10a) was defined to perform the structural simulation of this impeller. The three materials mentioned were all evaluated for all scenarios, i.e., aluminium was defined for the scenarios FL-AL, RS-AL and OS-AL; PEEK-GF30 was defined for the scenarios FL-PK, RS-PK and OS-PK; and ABS was selected for the scenarios FL-AB, RS-AB and OS-AB.

Table 5.3. Summary of properties of studied materials.

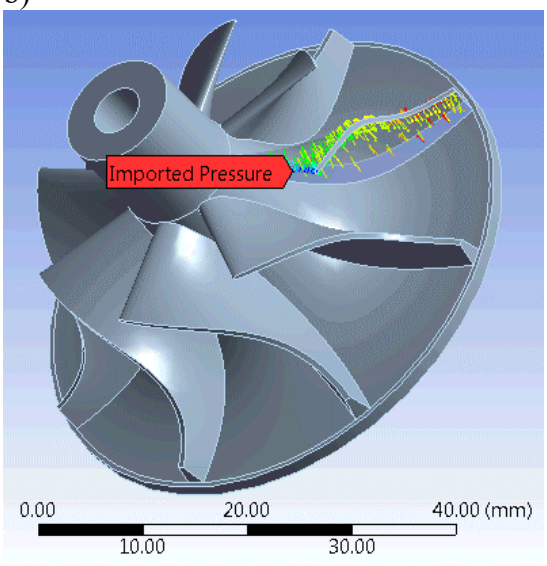
Property	Units	Aluminium	PEEK-GF30	ABS
Density	[kg/m^3]	2710	1510	1070
Yield strength	[MPa]	255	159	67.6
Elastic Modulus	[GPa]	73.1	6.89	2.35
Coefficient of thermal expansion	[m/m-K] x10^{-5}	2.09	2.16	7.87
Service temperature	[K]	523	522	362.9

The properties of the aforementioned materials were extracted from the MatWeb [221] database and imported to the ANSYS® Mechanical™; the summary of such properties is presented in Table 5.3.

a)



b)



c)

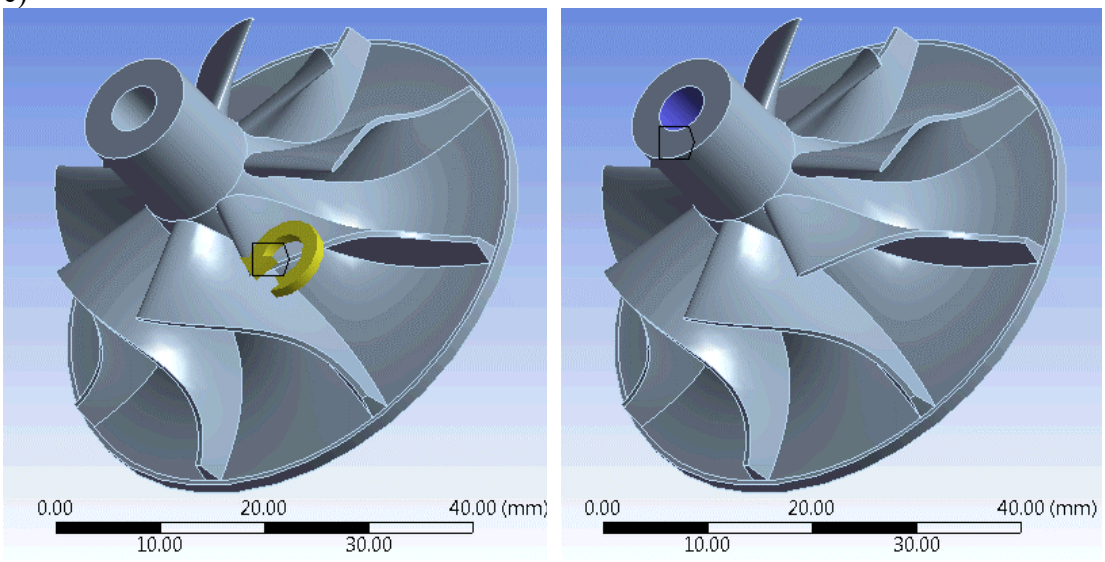


Fig. 5.10 Finite Element Analysis of the impeller;
a) mesh with tetrahedral elements; b) imported field of pressure; c) rotational speed; d) cylindrical support.

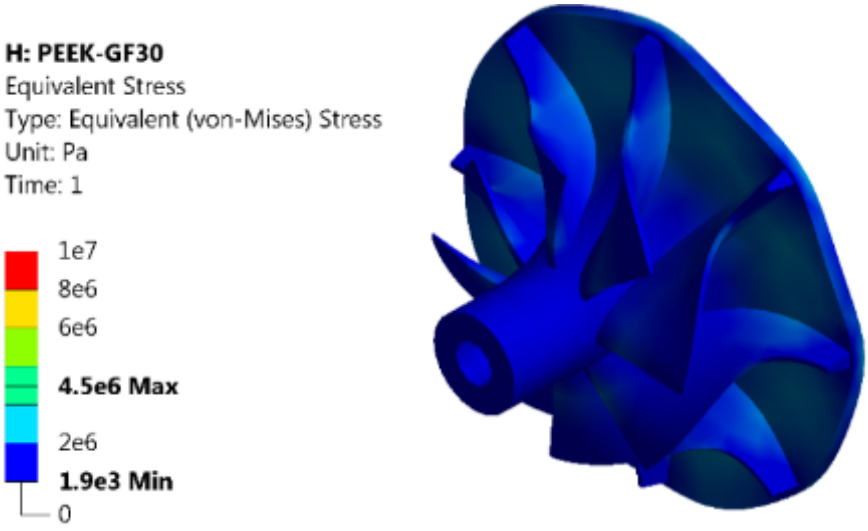
Setup

For the FEA simulation, a static structural simulation was conducted assuming isotropic linear elastic behaviour of the material. Then, the field pressure obtained from CFD was imported and set as loading (Fig. 5.10b) for one of the blades. Additionally, the rotational speed (Fig. 5.10c) was applied for the impeller for each the respective conditions, i.e., to 36000[rpm] for full load, 0[rpm] for rotor blocked and 45720[rpm] for overspeed. Finally, a cylindric support was defined in the shaft bore of the impeller (Fig. 5.10d).

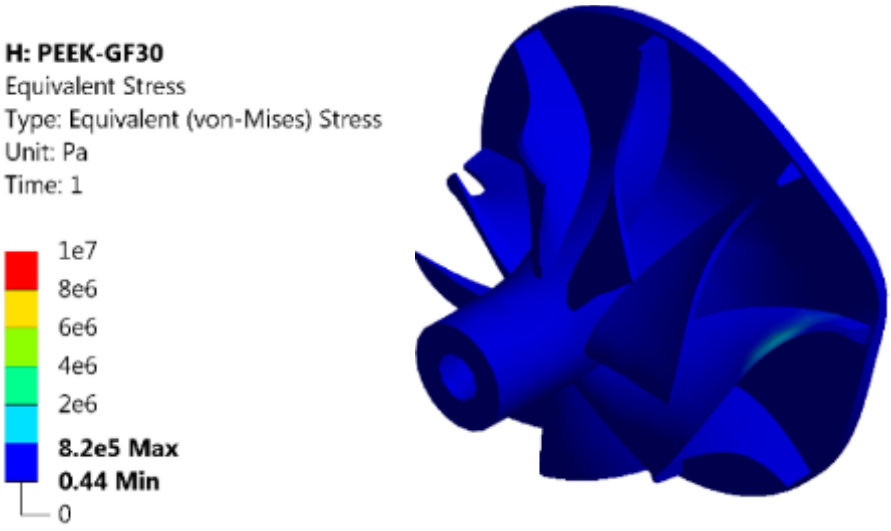
Results of the FEA

The maximum equivalent Von-Misses stress and the principal elastic strain were calculated in the simulation; however, as none of them sufficiently describe the mechanical integrity of the impeller, the factor of safety (FoS) is used as the unique dimensionless parameter for comparison purposes. The resulting Von Misses stress of for PEEK-GF30 at the three flow conditions, are presented in Fig. 5.11, where it can be seen that the pressure loading does not have a considerable effect on the impeller. The stress distribution is uniform for the full load and overspeed condition and has only a small effect on the rotor blocked condition.

a)



b)



c)

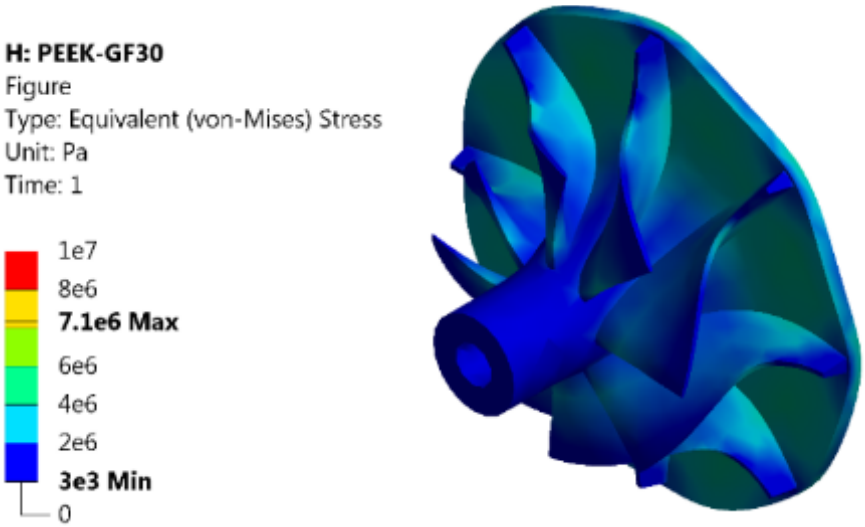


Fig. 5.11 Stress contours in Pascal for PEEK;
a) FL-PK scenario; b) RB-PK scenario; c) OS-PK scenario.

The examination of the FoS revealed that the rotational speed contributes most significantly to the stress whereas the pressure loading has a minimal influence. Consequently, the most critical condition is over-speed, where the minimum FoS of 19.92, 22.25 and 13.32 were obtained for Aluminium, PEEK-GF30 and ABS respectively. All materials have a FoS greater than 20 under the full load condition and greater than 80 under the rotor blocked condition. Although the thermal stresses were not evaluated because the clearance (0.2[mm]) should allow the impeller to grow freely. Thermal stressing at the fixing nuts may represent an issue for higher temperature applications, especially in the rotor blocked condition where the highest average temperature occurs as can be seen in Fig. 5.9.

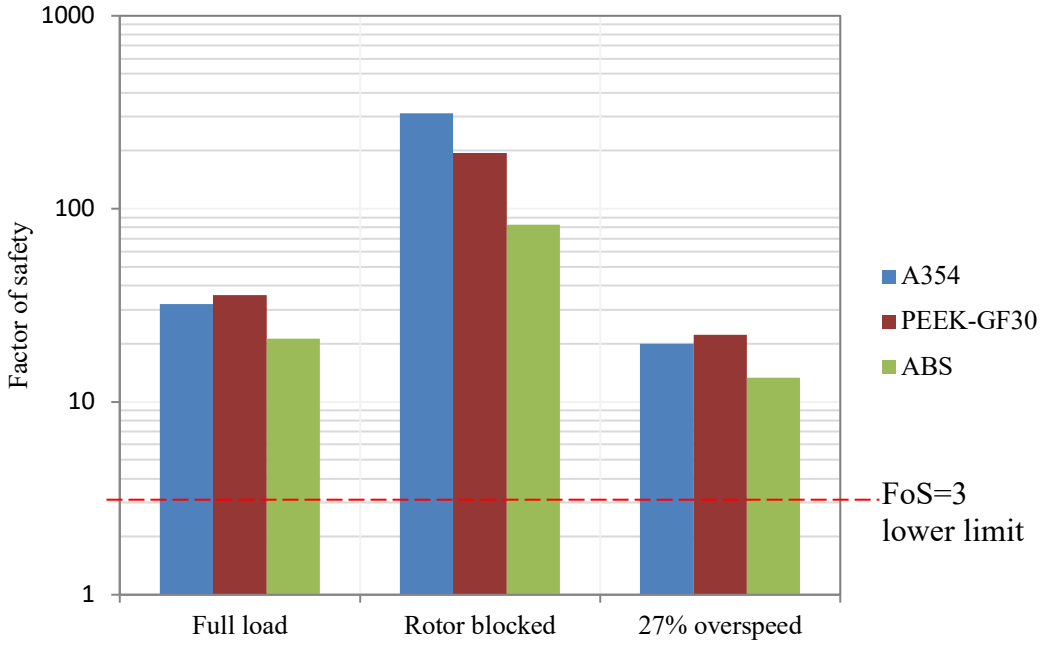


Fig. 5.12 Comparison of the results from the fluid-structure interaction study; A354: Aluminium 354; PEEK-GF30: poly-ether-ether-ketone; ABS: Acrylonitrile Butadiene Styrene; FoS: factor of safety; adapted from [25].

A review of the specialised literature [245] revealed that for small gas turbines with impellers made of unconventional materials, the minimum acceptable FoS should be 3. This FoS can be considered the lower allowable limit and can help to conclude whether a material is suitable for the application or not. This means that a FoS of 3 or greater suggest that the material can be accepted and a FoS under 3 suggest that the material must be rejected. A comparison of the FoS for the nine studied scenarios is shown in Fig. 5.12. It can be seen from this figure that PEEK-GF30 presents the best mechanical integrity of the assessed materials since it has an FoS 11% greater than Aluminium in

the worst situation. Conversely, ABS can be considered the material with the lowest mechanical integrity because its FoS is 40% lower than Aluminium. However, the three studied materials have FoS several times greater than the minimum requirement, hence both PEEK-GF30 and ABS can withstand the operating conditions and can be substituted for aluminium in this application.

Although all the selected materials are satisfactorily strong, raw ABS can be less expensive than Aluminium whereas PEEK-GF30 can be more expensive than both, which is a disadvantage despite its superior performance. However, as PEEK-GF30 is not only more resistant to centrifugal stress than aluminium but also lighter, it may represent a high-performance solution for applications where the weight/strength ratio plays a predominant role, for example in waste heat recovery of vehicles. Moreover, the production cost PEEK-GF30 impellers can be reduced by introducing mass production techniques; meaning, it has the potential to be a competitive high-performance alternative for Aluminium. Although ABS is weaker than aluminium, the raw material is considerably cheaper than any of the other studied materials which is the dominant driver.

5.3. CHEMICAL COMPATIBILITY STUDY

The replacement of metals with polymers in structural elements of the MTG-ORC may enhance its performance because this substitution represents advantages in terms of production cost, mass and resistance to corrosion. Nevertheless, the reliability, efficiency and lifespan of these elements into an ORC must not be overlooked. For example, the suitability of such polymers into a refrigerant environment must be carefully evaluated before their implementation is recommended; thus, an evaluation of the chemical interaction between polymers and working fluids has been undertaken.

This study was developed with an experimental approach, where two materials (PEEK-GF30 and PET-G) and six working fluids (R134a, R245fa, R1233zd, R1224yd, R1234yf and R1234zd) were evaluated; this means that 12 different fluid-polymer combinations were assessed. Additionally, three conditions were considered: before exposure (reference), right after exposure (wet) and dried after exposure (dry).

This analysis was performed in a collaborative investigation between the Sustainable Research Centre of the University of Nottingham and the Institute for Energy Systems of the Technical University of Munich in Germany. The study was carried out following the procedure presented by Eyerer et al. [137, 246]. This procedure is comprised of five tasks: selection of the working fluids, selection of the structural polymers, preparation of the specimens to be tested, exposure and drying of the specimens as required and the execution of the mechanical tests. The mechanical tests and measurement of properties were conducted three times: before the exposure (reference), and at wet and dry conditions.

For the first and second tasks, the six working fluids discussed in section 2.3.2 and the two polymers proposed in 4.4 were selected. For the third task, 36 specimens were fabricated at the University of Nottingham, 18 for each polymer, following the recommendations of the standard ISO 20753 [247]. A picture of a the specimens of ABS polymer is presented as example in Fig. 5.13. The preparation of specimens and the exposure to the aforementioned working fluids and the drying process was conducted at the Technical University of Munich. The exposure was performed following the general recommendations of ISO 175 [248]; however, as previously done by Eyerer et al. [137], the conditions were tailored for the specific application of this investigation.

The specimens were stored at 296[K] and 50% humidity without cleaning. Then, they were exposed for a period of 28 days at 348[K] and dried for 21 days at 298[K] under vacuum. Five properties were measured: volume, mass, hardness, tensile strength, and tensile modulus of elasticity. The volume was determined by measuring the overall dimensions of the specimen with a high accuracy caliper, the mass was measured with an analytical balance, the hardness was measured with a Shore D durometer, following the recommendations of the standard ISO 48 [249].The tensile strength and the tensile modulus of elasticity were measured with a tensile testing machine, following the recommendations of the standard ISO 37 [250].

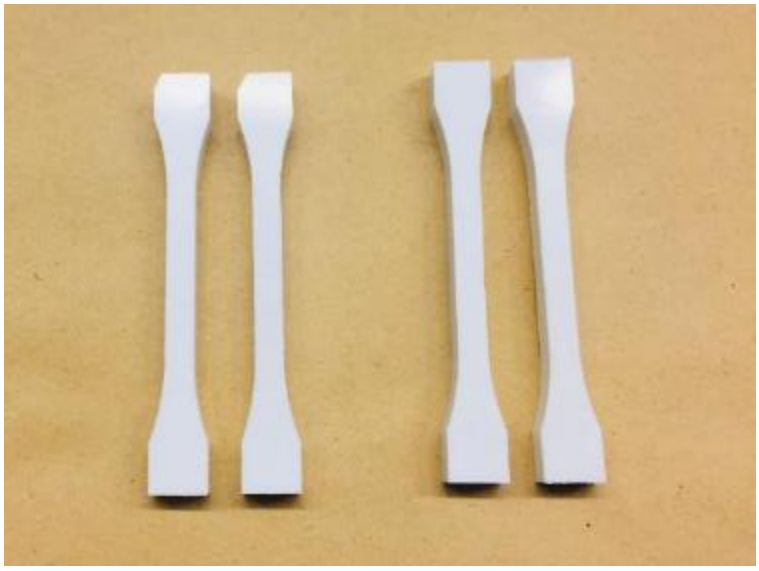


Fig. 5.13 Specimens of ABS for the chemical compatibility analysis.
Fabricated according with the standard ISO 20753 [247]

A compatibility criterion was defined to assess whether the combinations material-fluid are compatible. Although Eyerer et al. [137] suggested a tailored examination of the mechanisms of interactions for each polymer-fluid combination, a quantitative and systematic criterion [251] seems to be more adequate for performing an unbiassed evaluation of the compatibility and hence is used in this investigation. In the assessment, the measurements of the properties at the wet and dry conditions are compared with the reference and the relative changes per property are measured against the compatibility criterion. Depending on the level of relative change, the criterion defines three categories of risk in the chemical compatibility: low risk, medium risk and high risk. However, the limits of change proposed by Majurin et al. [251] seem to be specific for their application and may not be appropriate for this investigation. Therefore, the limits were amended as shown in Table 5.4.

The properties were classified into two classes: non-critical and critical. The non-critical properties are mass and hardness whereas the critical properties are volume, tensile strength and modulus of elasticity. For a non-critical property, a maximum relative change of 10% is allowed for considering low risk, a maximum of 20% for considering medium risk and above 20% is considered high risk. For a critical property, a maximum relative change of 5% is allowed for considering low risk, a maximum of 10% for considering medium risk and above 10% is considered high risk. The aforementioned 10% limit is general practice in other compatibility criteria [137]

whereas the 5% is a selected as a more restrictive for critical properties. For this investigation, a material will be considered compatible if all the critical properties and all the non-critical properties are low risk.

Table 5.4 Limits of change in properties for the chemical compatibility assessment

Category	Low risk	Medium risk	High risk
Volume	$\delta V \leq \pm 5\%$	$\delta V > \pm 5\%$ $\delta V \leq \pm 10\%$	$\delta V > 10\%$
Mass	$\delta m \leq \pm 10\%$	$\delta m > \pm 10\%$ $\delta m \leq \pm 20\%$	$\delta m > 20\%$
Hardness	$\delta H \leq \pm 10\%$	$\delta H > \pm 10\%$ $\delta H \leq \pm 20\%$	$\delta H > 20\%$
Tensile strength	$\delta \sigma \leq \pm 5\%$	$\delta \sigma > \pm 5\%$ $\delta \sigma \leq \pm 10\%$	$\delta \sigma > 10\%$
Modulus of elasticity	$\delta M_t \leq \pm 5\%$	$\delta M_t > \pm 5\%$ $\delta M_t \leq \pm 10\%$	$\delta M_t > 10\%$

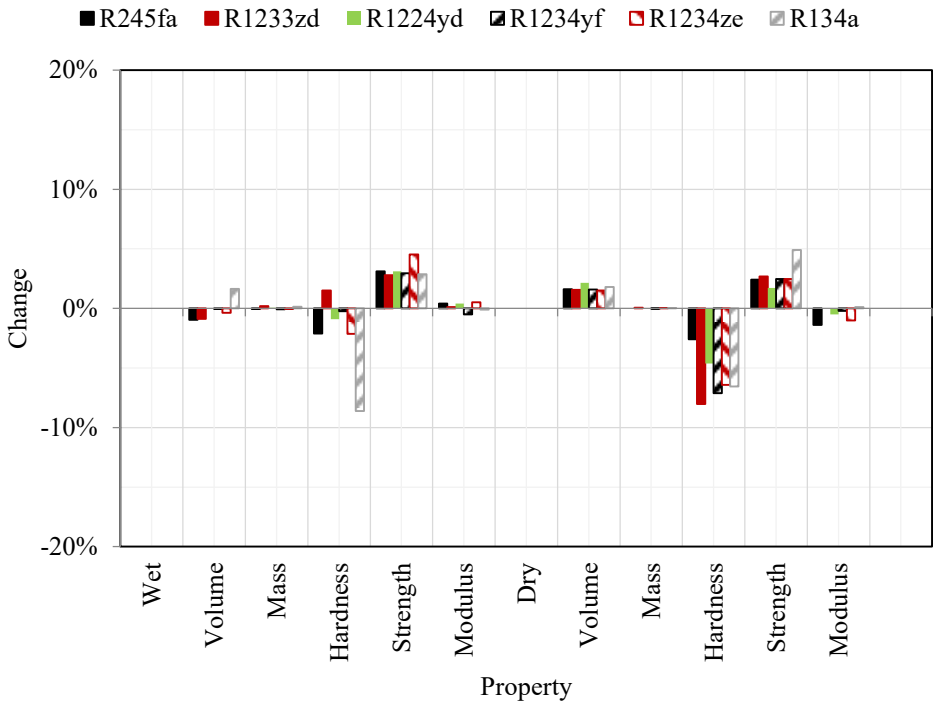
The results are shown in Fig. 5.14, where the relative changes of the five properties are presented. As can be observed in Fig. 5.14a, PEEK-GF30 presented a relative change under $\pm 10\%$ for mass and hardness and under $\pm 5\%$ for volume, strength and modulus of elasticity with all the working fluids and the two studied conditions (wet and dry). Hardness is the most affected property with a -9% relative change for R134a (wet) and -6.5% (dry), -8% for R1233zd (dry) and -7% for R1234yf (dry). The fluid most affecting performance is R134a with a volume increment of 1.6% (wet) and the aforementioned reduction in hardness.

In contrast, as can be seen in Fig. 5.14b, PET-G showed a significant relative change in most of its properties. The relative change of volume exceeded $\pm 5\%$ for all the working fluids (wet and dry) except for R34a (wet), which was 4.3%. The relative change of strength and modulus of elasticity significantly exceeded $\pm 5\%$ for all the working fluids in both conditions. The relative change of hardness exceeded $\pm 10\%$ for R1233zd (wet and dry). R245fa (dry), R1224yd (dry) and R1234yf (dry).

Therefore, PEEK-GF30 may be considered compatible with all the studied working fluids whilst PET-G seems to be compatible with none of the studied working fluids. For this reason the application of PET-G into ORC systems is not recommended if any

of these fluids is used. Alternatively, PEEK-GF30 or a working fluid compatible with PET-G from Table 4.5 can be used instead.

a)



b)

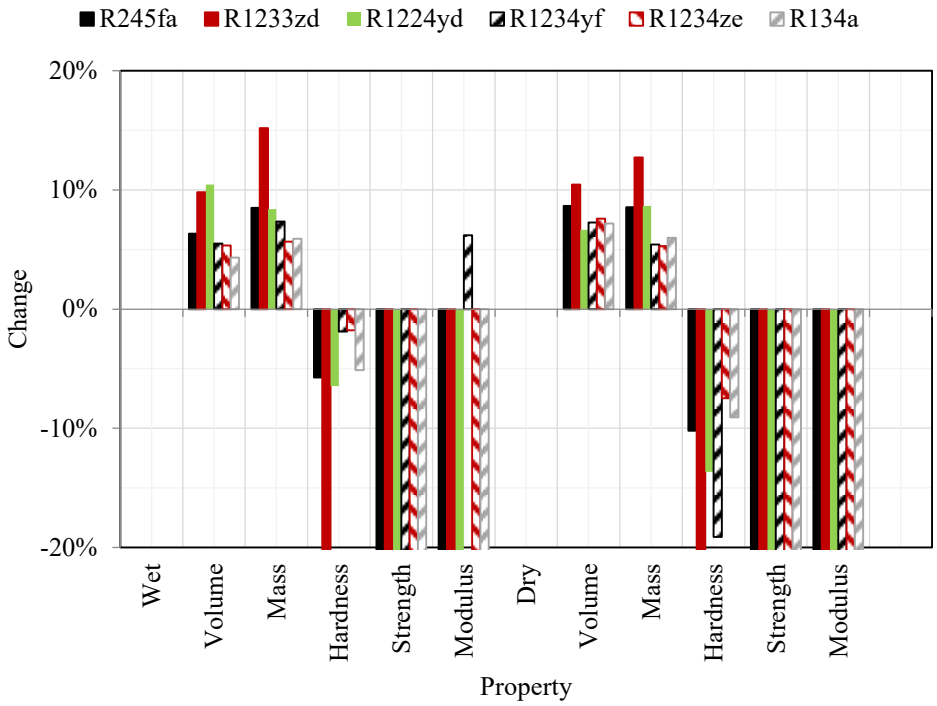


Fig. 5.14 Results of the chemical compatibility analysis for a) PEEK and b) PET.

CHAPTER 6. MANUFACTURE &TEST

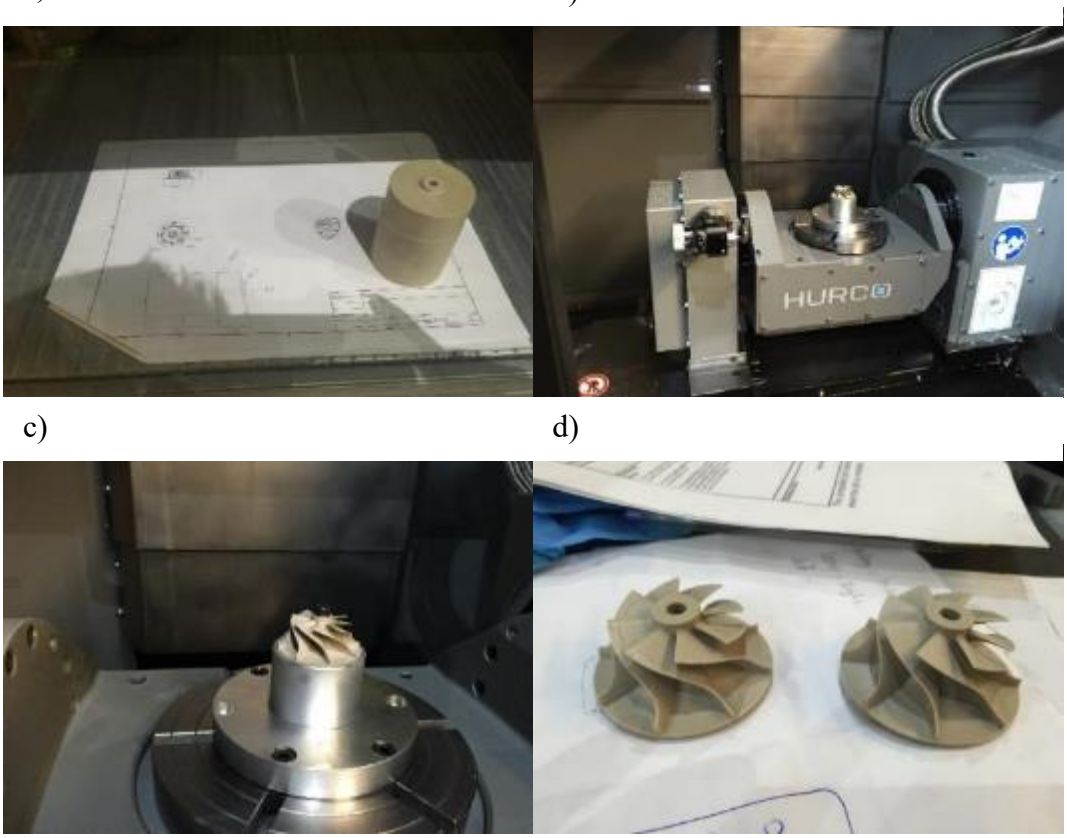
In this section, an extensive review into the manufacture of the prototype, test equipment and testing of the MTG-ORC is given.

6.1. FABRICATION

The fabrication of the MTG-ORC was made at the laboratory of the sustainable research centre of the University of Nottingham. Two type of elements were used for the fabrication: standard components and custom-made components. The standard components were purchased from vendors authorised by the university and the custom-made components were either fabricated at the university workshops or specified for the fabrication with an authorised manufacturer.

The nozzle body and the impeller were made of polymers; thus, they can be fabricated using mould injection. However, moulding demands complex and costly equipment, which is not cost-effective to make for a small number of parts. Therefore, for prototyping purposes, additive manufacturing was selected to fabricate the nozzle and computer numerical controlled (CNC) machining to fabricate the impeller. The cylindric bar of PEEK-GF30 used to make the impeller can be seen in Fig. 6.1a, the machining process into a Hurco VM10Ui five axis milling machine is illustrated in Fig. 6.1b-c and two finished impellers are shown in Fig. 6.1d.

a) b)

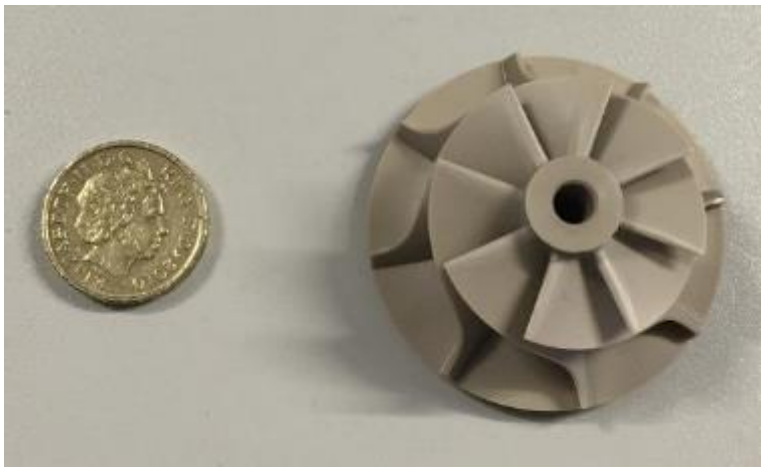


c) d)

Fig. 6.1 Fabrication of the impeller made of PEEK-GF30;
made by CNC machining; a) cylindric bar of the material; b) Hurco 5 axis milling machine and d) two finished prototypes of the impeller.

Alongside the PEEK-GF30 impeller, a number of 3D printed impellers were fabricated using the plastics PET, ABS and PLA. A comparison of the PEEK-GF30 impeller and an ABS impeller is shown in Fig. 6.2a-b. The fabrication of these alternative impellers allowed comparative testing in air. Although the FSI analysis suggested at least the ABS polymer could withstand the centrifugal loading, the anisotropic properties of 3D printed components raised the concern of potential failure of the impeller. For this reason only the PEEK-GF30 impeller was tested and the others can be tested in future investigations when the behaviour of the MTG is well known and destructive tests can be safely conducted.

a)



b)

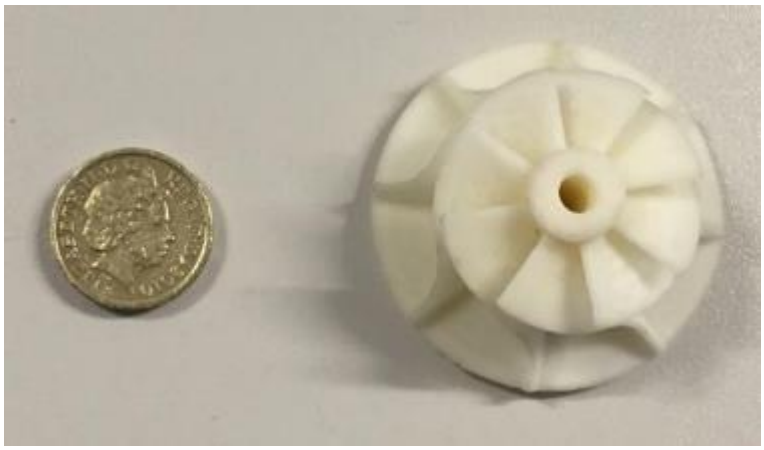


Fig. 6.2 Comparison of prototype impellers;
a) PEEK-GF30, fabricated by CNC Machining and b) ABS, 3D printed.

The nozzle body, shown in Fig. 6.3d, was fabricated using polymer fused deposition and filament of PET-G with a resolution of 0.06[mm] and 100% infill density. This nozzle body was fastened to the baseplate of the turbine casing. This was a custom-made component that acted as one of the transitions pieces to connect the turbine and the generator; therefore, it was designed and fabricated in purpose.

Two steps were followed for its fabrication; in the first step, a fast prototype of the piece shown in Fig. 6.3a-b was made with 3D printing, this part aimed to check critical dimensions. Then, the actual component made of aluminium was fabricated with CNC machining as shown in Fig. 6.3c. In total, three different transition pieces were needed to connect the turbine volute and the body of the generator stator. These transitions were made of standard grade aluminium and fabricated into a CNC lathe.

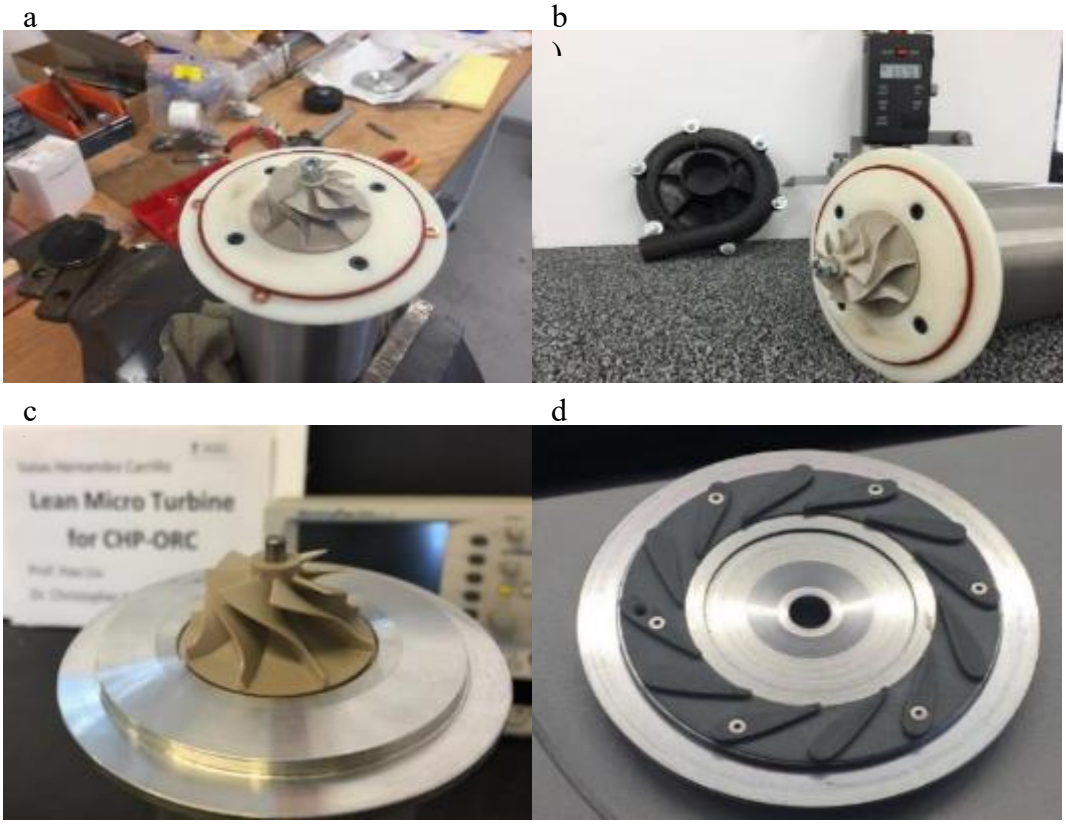


Fig. 6.3 Assembly of the MTG-ORC;
a) clearance and sealing check-up, b) preliminary assembly with polymeric prototypes of casing and baseplate, c) preliminary breakout, d) preliminar MTG subassembly.

The shaft, shown in Fig. 6.4b-d, is comprised of a main body made of mild steel and an inner insert of silver steel. This shaft was fabricated into a CNC lathe and aligned with a micrometre as illustrated in Fig. 6.4a. The shaft has dedicated slots to allocate the bearings and the permanent magnets can be seen partially assembled onto the shaft in Fig. 6.4d. A steel sleeve, shown in Fig. 6.4c, covers the magnets to keep them in place and is assembled with an interference fit and bonded to the main body of the shaft with a high strength retaining compound.

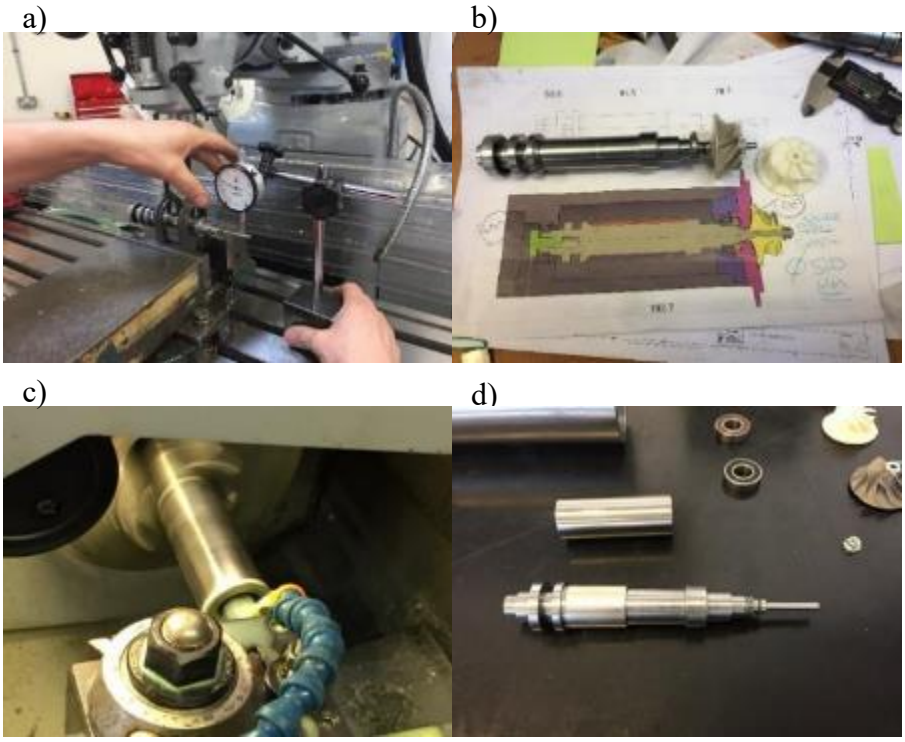
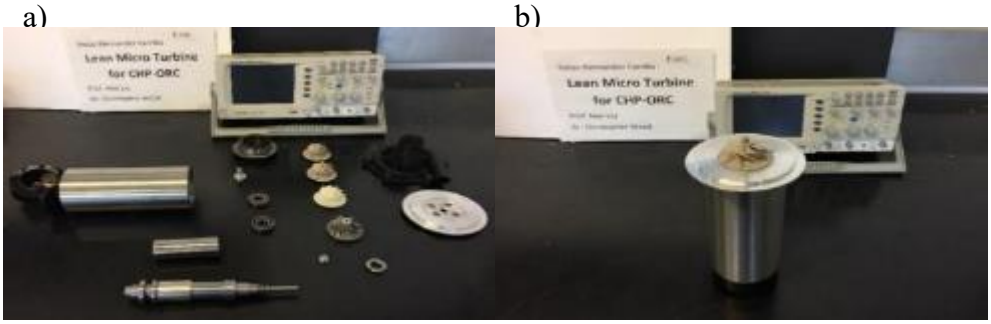


Fig. 6.4 Fabrication of the shaft;
a) alignment assurance; b) finished shaft; c) sleeve fabrication and d) magnets and sleeve assembly on the shaft.

The turbine casing, Fig. 6.5c, was adapted from a turbocharger compressor, model GT1549s, with an area/radius ratio A/R=0.42. The bearings, Fig. 6.5a, are standard high-speed hybrid-ceramic ball bearings designation 7002CE/HCP4A with wave springs for preloading. The stator of the generator, Fig. 6.5a-b, is adapted from a high-speed, 400[Hz], 80[mm] spindle motor and the magnets of the rotor are made Neodymium rare earth magnets model M5033 from the supplier “Super Magnet Man”.

a) b)



c)



Fig. 6.5 Assembly of the MTG;
a) preliminary piece breakout; b) preliminary subassembly; c) final assembly.

6.2. THE TEST RIG

The test rig is comprised of the MTG, a safety envelope, a supply system of compressed air, an electric load bank and monitoring instrumentation. The safety envelope is a 304 stainless steel tank with internal baffles for burst containment. The air supply system consists of a GX7FF compressor, a pneumatic pressure regulator, a main control valve, a shutoff valve, piping and hose connections. The load bank is a three-phase array of electric bulbs with fused switches. The schematic of the performance testing rig is shown in Fig. 6.6a and the photo of the test rig with the key equipment clearly marked is shown in Fig. 6.6b, whereas the instrumentation of the test rig is described in section 6.3.2. The MTG-ORC is anchored inside the envelope.

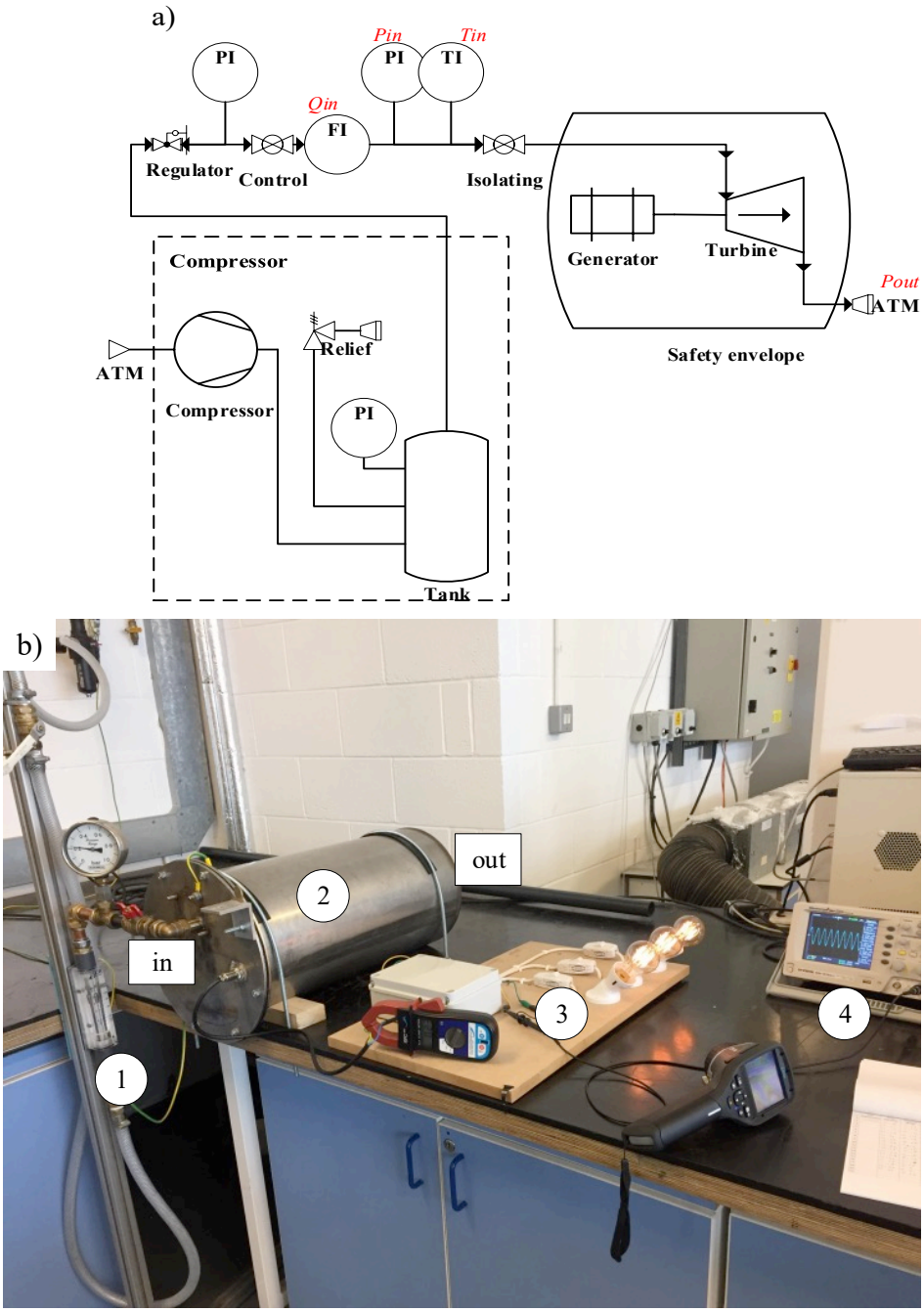


Fig. 6.6. Test rig using compressed air;

a) schematic set up; b) photo of the actual array; Q_{in}: volume flow rate at inlet; P_{in}: static pressure at inlet; T_{in}: static temperature at inlet; P_{out}: static pressure at outlet; PI: pressure indicator, TI: temperature indicator, FI: flowrate indicator; ATM: atmosphere; 1: air supply, 2: safety envelope, 3: load bank, 4: monitoring oscilloscope.

The test rig shown in Fig. 6.6a-b, is a system for evaluating the performance of the MTG-ORC with air. The compressor takes air from the atmosphere and discharges it into an air tank, which is equipped with a relief pressure valve and a pressure gauge. Then, the air is conducted to the vicinity of the rig with a distribution pipe, whose pressure is monitored with a pressure gauge. The supply pressure is controlled to avoid

burst of the piping and/or excessive speed of the MTG-ORC. An isolation valve isolates the test rig from the air supply; this isolation valve operates in open (normal operation) or closed (shut-off) position only, while an additional valve controls the pressure and flowrate being supplied. After passing through the turbine, the exhaust air is discharged into the safety envelope to cool the generator and bearings. The inlet pressure, temperature, and volume flowrate are measured at the inlet pipe with a pressure gage, a thermometer and a flow meter. The outlet temperature is measured at the outlet of the MTG-ORC with a thermometer.

6.3. PROCEDURE

A stream of compressed air is supplied to the rig at the point labelled as “in” and discharged to the atmosphere at the point labelled as “out” at the back of the rig (both “in” and “out” are indicated in Fig. 6.6b). Conventionally, the test of turbines is performed at nominal capacity (or fractions of it) and the nominal rotational speed. Additionally, the rotational speed is controlled with a governor that responds to variations of the load keeping the speed constant. In this study, however, the unit is comprised of a variable frequency MTG that is not equipped with a governor, because the control of the unit lies on a controlled expansion ratio. Consequently, the rotational speed responds to changes in the load and the conventional testing methods may not suit the requirements of this investigation. Thus, a procedure for the test, consisting of ten steps, is proposed and described below.

I. Perform preliminary checks, ensure the control valve is fully closed and the isolation valve is fully open, supply compressed air to the system.
II. Connect the first load combination.
III. Initiate a trial by opening the control valve until achieving a frequency of f=50[Hz].
IV. Let the unit settle, 10 minutes for the first trial and 5 minutes for subsequent trials, to allow bearings and lubricants to warm.
V. Let the unit settle for 2 minutes for the parameters to achieve a steady state.
VI. Register the parameters in the corresponding record sheet and number the register to record.

VII. If the control valve is fully open, proceed to step VIII, otherwise, open the control valve to increase the inlet pressure ΔP_{in}=2[kPa] and repeat from step V , starting a new record.

VIII. If the total number of loads have been tested, proceed to step IX, otherwise connect the next load and repeat from step III.

IX. If three trials have been recorded for each load, proceed to step X, otherwise, close the control valve to reset the rotational speed to *f*=50[Hz] and repeat from step IV for starting a new trial with Load1.

X. Fully close the control valve, fully close the isolation valve and suspend the supply of compressed air.

The test is performed with a rigorous monitoring of the unit while a register of the instruments readings is maintained. A set of readings for a given time is called a record, whereas a set of 8 records at 0.25, 0.37, 0.50, 0.6, 0.7, 0.8, 0.9 and 1 span of the inlet pressure is called a trial. Three different loads were tested: the load 3 consisted of three 40[W] bulb connected to the phases *a*, *b* and *c* of the generator; the load 2 consisted of two 40[W] bulbs connected to the phases *a* and *b*, and the load 1 consisted of one 40[W] bulb connected to the phase *a*. Thus, a total of 72 records are generated in the test, as shown in in Table 6.1. The records 1 to 24 correspond to the trials 1, 2 and 3; the records 25 to 48 correspond to the trails 4, 5 and 6; the records 49 to 72 correspond to the trials 7, 8 and 9. This assured repeatability of the test.

Table 6.1 Convention for numbering for the experimental test.

		Record number							
Span of P_{in}		0.25	0.37	0.5	0.6	0.70	0.8	0.9	1
Load1	Trial1	1	2	3	4	5	6	7	8
	Trial2	9	10	11	12	13	14	15	16
	Trial3	17	18	19	20	21	22	23	24
Load2	Trial4	25	26	27	28	29	30	31	32
	Trial5	33	34	35	36	37	38	39	40
	Trial6	41	42	43	44	45	46	47	48
Load3	Trial7	49	50	51	52	53	54	55	56
	Trial8	57	58	59	60	61	62	63	64
	Trial9	65	66	67	68	69	70	71	72

6.3.1. Experimental determination of the dimensionless parameters

The experimental parameters have to be compared with the theoretical parameters generated in the simulation. Although the procedure given in section 5.1 is still valid for the experiment, the inputs of the simulation are not the same as the inputs of the experiment; thus, the aforementioned procedure cannot be directly applied and a few adjustments are needed to obtain the experimental parameters.

Thermodynamic efficiency

The experiment was carried out using compressed air as the working fluid, which can confidently be considered an ideal gas. Additionally, the experiment is performed at near-ambient temperature; thus, the heat losses should be negligible and the total specific enthalpy along the inlet and the outlet can be considered constant. As a consequence, the thermo-aerodynamic analysis of section 5.1 should also be valid for the boundary conditions "in" and "out" defined in this procedure. Then, the thermodynamic efficiency can be obtained with Eqn.(3.7), Eqn.(5.3) and Eqn.(5.4) if the subscripts 2 and 3 are replaced with "in" and "out" respectively.

Aerodynamic efficiency

In conventional applications, the mechanical and electrical losses are a negligible fraction of the aerodynamic power and the aerodynamic efficiency is approximately equal to the electromechanical efficiency measured at the brake. For this reason, the electromechanical efficiency can be reasonably extrapolated through dynamic similarity of the flow. In this study, however, the mechanical and electrical losses account for a considerable fraction of the aerodynamic power and consequently, they must be accounted in the test and considered for the determination of the aerodynamic efficiency.

The aerodynamic efficiency, η_{aero}, can be then experimentally obtained from Eqn.(6.1), which is a function of the power consumed in the load bank, $\dot{W}_{bank}$, the mechanical losses, $\dot{W}_m$, and the electrical losses, $\dot{W}_e$. Thus, the Eqn.(3.7) and Eqn.(6.1) can be used for the comparison of analytical and experimental results. Moreover, if the

heat losses are negligible, the aerodynamic efficiency and the thermodynamic efficiency should be equal and Eqn.(5.10) should be comparable with Eqn.(3.7) and Eqn.(6.1).

$$\eta_{aero} = \frac{\dot{W}_{aero}}{\dot{m}\Delta h_{0s}} = \left(\frac{\dot{W}_{bank} + \dot{W}_{loss}}{\dot{m}\Delta h_{0s}}\right) \tag{6.1}$$

The power measured at the load bank $\dot{W}_{bank}$ can be calculated with Eqn.(6.2), which is a function of the root mean square voltage V_{rms} and current I_{rms} in the windings. It should be pointed out that the voltage V_{rms} is uniform in all the phases, whereas the current I_{rms} is the average value among the three phases a, b and c of the generator, in accordance with Eqn.(6.3).

$$\dot{W}_{bank} = \sqrt{3} V_{rms} I_{rms} \tag{6.2}$$

$$I_{rms} = \frac{I^a_{rms} + I^b_{rms} + I^c_{rms}}{3} \tag{6.3}$$

The power losses, $\dot{W}_{losses}$, are a combination of mechanical, $\dot{W}_m$, and electrical losses, $\dot{W}_e$, as can be seen in Eqn.(6.4). The mechanical losses can be split in bearing losses, $\dot{W}_{bearing}$, and windage losses, $\dot{W}_{windage}$, see Eqn.(6.5). In this investigation, the mechanical losses are expected to mainly be friction in the bearings. Although windage exists [252] it should be small compared to the mechanical loses and is hence neglected.

The bearing losses can be obtained from Eqn.(6.6), which is a function of the rotational speed, ω, and the frictional moment, τ_m. This is a very small dynamic moment that is difficult to measure because it requires sophisticated equipment, which is unavailable at the time of testing. Consequently, the frictional moment was estimated with the mathematical model provided by the manufacturer [253].

The windage loss of the turbine has been considered already in the aerodynamic losses and the windage loss of the generator can be estimated with Eqn.(6.7) [252]. This is a function of the coefficient of friction of the rotor, c_f, the density of the working

fluid, ρ, the rotational speed, ω, the outer radius of the generator rotor, r_g, and the active length of the generator rotor L_g.

$$\dot{W}_{loss} = \dot{W}_m + \dot{W}_e \tag{6.4}$$

$$\dot{W}_m = \dot{W}_{bearings} + \dot{W}_{windage} \tag{6.5}$$

$$\dot{W}_{bearings} = \omega \tau_m \tag{6.6}$$

$$\dot{W}_{windage} = \pi c_f \rho \omega^3 r_g^4 L_g \tag{6.7}$$

The electrical losses, $\dot{W}_e$, can be split in joule effect losses in the windings, $\dot{W}_{joule}$, and parasitic losses in the core, $\dot{W}_{core}$; as can be seen in Eqn.(6.8). Both of these electrical losses are expected to be small in this investigation and can be hence neglected. In any case, the joule effect losses can be calculated with Eqn.(6.9), which is a function of the mean root square current in the windings, I_{rms}, and the internal resistance per phase R_w. The core losses can be estimated with Eqn.(6.10) [254], where C_m, α_e, and β_e are empirical constants, and B_m is the magnetic peak flux density.

$$\dot{W}_e = \dot{W}_{joule} + \dot{W}_{core} \tag{6.8}$$

$$\dot{W}_{joule} = \sqrt{3} I_{rms}^2 R_w \tag{6.9}$$

$$\dot{W}_{core} = C_m f^{\alpha_e} B_m^{\beta_e} \tag{6.10}$$

Flow and loading coefficients

With careful examination of the thermo-aerodynamic analysis it can be seen that the flow and loading coefficients, described in section 3.1.1, can be experimentally determined if the eighteen parameters presented in Table 6.2 are known. These

parameters can be classified as 'variable' or 'constant' throughout the test. Variable are those parameters that change and must be continuously monitored whereas constant are those parameters that are not expected to change and can be measured once throughout the test or assumed as a constant referenced value.

Table 6.2 Experimental parameters

#	Parameter	Symbol	Type	Source
1	Current, root mean squared phase a	I_{rms}^{a}	Variable	Measured
2	Current, root mean squared phase b	I_{rms}^{b}	Variable	Measured
3	Current, root mean squared phase c	I_{rms}^{c}	Variable	Measured
4	Frequency	f	Variable	Measured
5	Pressure, static inlet	P_{in}	Variable	Measured
6	Temperature, static inlet	T_{in}	Variable	Measured
7	Temperature, static outlet	T_{out}	Variable	Measured
8	Voltage, root mean squared	V_{rms}	Variable	Measured
9	Volume flow rate, inlet	Q_{in}	Variable	Measured
10	Diameter, inlet	D_{in}	Constant	Measured
11	Diameter, outlet	D_{out}	Constant	Measured
12	Diameter, rotor-inlet	D_2	Constant	Measured
13	Height, blade rotor-inlet	b_2	Constant	Measured
14	Resistance, generator windings resistance per phase	R_w	Constant	Measured
15	Angle, nozzle exit	α_2	Constant	Referenced
16	Coefficient, heat capacity at constant pressure	c_p	Constant	Referenced
17	Coefficient, isentropic expansion	γ	Constant	Referenced
18	Pressure, static outlet	P_{out}	Constant	Referenced

6.3.2. Instruments

The experimental parameters are defined and/or measured as explained below. The nozzle exit angle is extracted from the design of this investigation. The gas heat capacity Cp=1005[J/kgK] and the coefficient of isentropic expansion γ=1.4 are assumed constant and taken from the specialised literature [255]. The outlet pressure P_{out}=102[kPa] is assumed constant and equal to the average atmospheric pressure recorded in September 2018 at the UK East Midlands weather station [256]. The root mean squared electric current per phase, I_{rms}^{a}, I_{rms}^{b} and I_{rms}^{c}, are measured with a clamp ammeter. The frequency, f, and the root mean squared voltage, V_{rms}, are measured with a two-channel oscilloscope. The inlet static pressure, P_{in}, is measured with a pressure gauge. The inlet static temperature, T_{in}, and outlet static temperature, T_{out}, are measured with an electronic thermometer. The inlet volume flowrate, Q_{in}, is measured

with a variable area flowmeter (rotameter). The inlet, outlet and rotor inlet diameters, D_{in}, D_{out}, D_2, and the blade height, b_2, are measured with a digital caliper. The electrical resistance, R_w, of the generator windings is measured with an ohmmeter. Table 6.3 presents details of all the instruments used during the test.

Table 6.3 Instruments used for the measurement of the parameters

Parameter	Quantity	Units	Instrument	Range	Accuracy
I_{rms}^{a}	Current	[A]	Ammeter	0 to 2	0.01
I_{rms}^{b}	Current	[A]	Ammeter	0 to 2	0.01
I_{rms}^{c}	Current	[A]	Ammeter	0 to 2	0.01
f	Frequency	[Hz]	Oscilloscope	10 to $7x10^{6}$	2% of reading
P_{in}	Gauge pressure	[kPa]	Manometer	0 to 100	1.6
T_{in}	Temperature	[K]	Electronic thermometer	173 to 1,473	2.5
T_{out}	Temperature	[K]	Electronic thermometer	173 to 1,473	2.5
V_{rms}	Electric potential difference	[V]	Oscilloscope	0 to 600	2% reading
Q_{in}	Flow rate	[m^3/s]	Rotameter	0 to $2.4x10^{-2}$	$7.2x10^{-4}$
D_{in}	Length	[m]	Calliper	0 to 0.2	$1x10^{-5}$
D_{out}	Length	[m]	Calliper	0 to 0.2	$1x10^{-5}$
D_2	Length	[m]	Calliper	0 to 0.2	$1x10^{-5}$
b_2	Length	[m]	Calliper	0 to 0.2	$1x10^{-5}$
R_w	Resistance	[Ω]	Ohmmeter	0-200	0.8% of reading

6.4. RESULTS OF THE TEST

In this section, an assessment of the performance of the MTG-ORC proposed in this investigation is conducted alongside a comparison with the performance of a state-of-the-art MTG-ORC of similar characteristics, i.e., the MTG-ORC equipped with components made of aluminium instead of polymers. Lastly, an assessment of the potential improvement of micro-turbines for ORC derived from this work is given.

6.4.1. Performance assessment

The performance assessment is comprised of six tasks: analysis of simulations of the thermo-aerodynamic performance, examination of the results of the air test, examination of the results of the enhanced air test, analysis of the uncertainty and

propagation of error, prediction of the performance in ORC conditions and analysis of the structural integrity.

In the first task, the results of the simulations with air, ideal-R245fa and real-R245fa are compared aiming to validate the assumption that the thermo-aerodynamic performance may be comparable, in a dimensionless interpretation, regardless of the working fluid used. In the second task, the results of the test were compared with the results of the aforementioned simulations; this analysis sought to validate whether the simulations agree with an experiment and, additionally, served to identify major sources of inefficiency and propagation of error. In the third task, a few enhancements of the test described in section 6.4.3 were conducted, the test was repeated and the results were compared with the simulations. This analysis aimed a better agreement between the test and the simulations. In the fourth task, the error propagation in the enhanced test was calculated to determine the degree of inaccuracy in the determination of the dimensionless parameters and the validity of the experimental results. In the fifth task, a prediction of the performance of the unit in the actual application, i.e., ORC conditions, was performed. Finally, in the sixth task, the analysis of the structural integrity of the polymeric components is performed to conclude whether they can withstand the ORC operational conditions.

6.4.2. Results of the air test

The unit exhibited a stable behaviour during the test while operating at a broad range of conditions. Although the design point could not be reached due to limitations on the air supply system, the off-design results provided enough information to conclude about its performance. The experimental parameters were recorded and presented in a reduced form in Fig. 6.7, which encompasses the total of 72 records described in Table 6.1. The thermodynamic parameters are shown in Fig. 6.7a and the electric parameters are shown in Fig. 6.7b. In these figures, a dimensionless form is used to represent a parameter referred to its maximum and minimum limits in the experiment. The calculation of the reduced frequency f^r is presented as an example in Eqn.(6.11), where the reduced form is denoted with the superscript r and its maximum and minimum limits are denoted with the subscripts max and min respectively; all the parameters are reduced analogously.

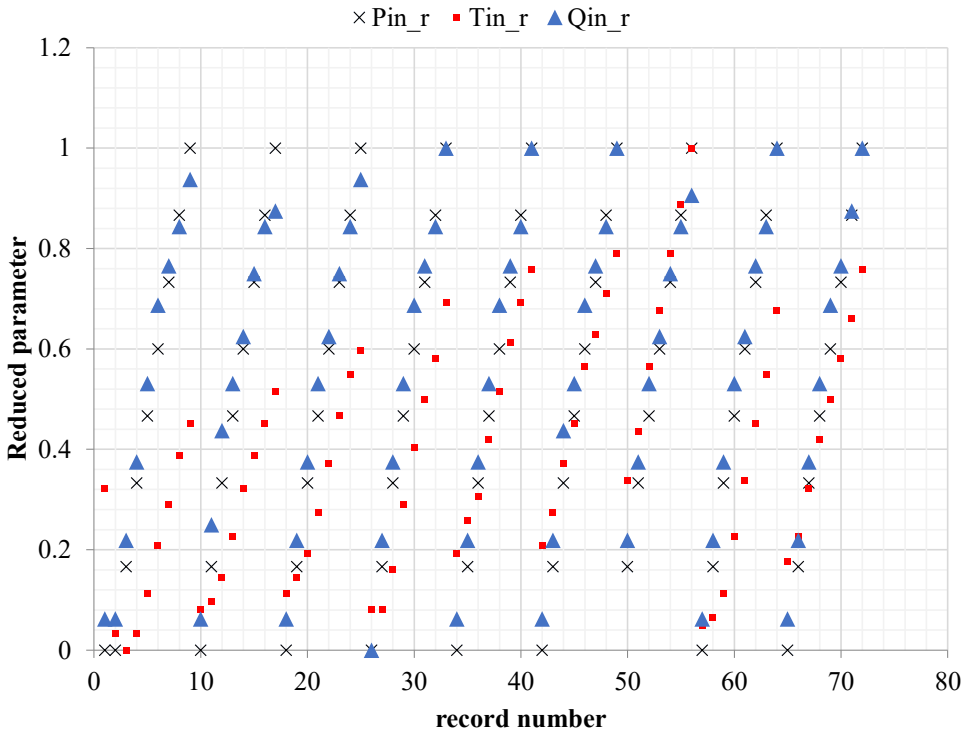
$$f^r = \frac{f - f_{min}}{f_{max} - f_{min}} \tag{6.11}$$

The main experimental parameter is the inlet pressure and, as it varies with the aperture of the control valve, the inlet pressure is expected to rise uniformly in each of the trials. As expected, the inlet pressure showed this behaviour throughout the test.

Air is throttled from a storage tank to the inlet of the unit and, as the temperature and pressure in the tank should be constant, the turbine inlet temperature is related to the temperature in the storage tank. The inlet temperature is, thus, expected to mimic the behaviour of the inlet pressure and their curves should overlap in Fig. 6.7a. Unfortunately, unlike the pressure, the temperature at the tank is not precisely controlled because the tank is cooled with surrounding air, whose temperature varied during the test. Consequently, some difference is found between the behaviour of the inlet temperature and the inlet pressure as can be observed in Fig. 6.7a.

The inlet volume flowrate is driven by the inlet to outlet pressure difference and the hydraulic resistance of the rig. As the hydraulic resistance and the outlet pressure do not change throughout the test, the volume flowrate should mimic the behaviour of the inlet pressure as well. As expected, a good correlation between the behaviour of the inlet volume flow rate and the inlet pressure can be seen in Fig. 6.7a.

a)



b)

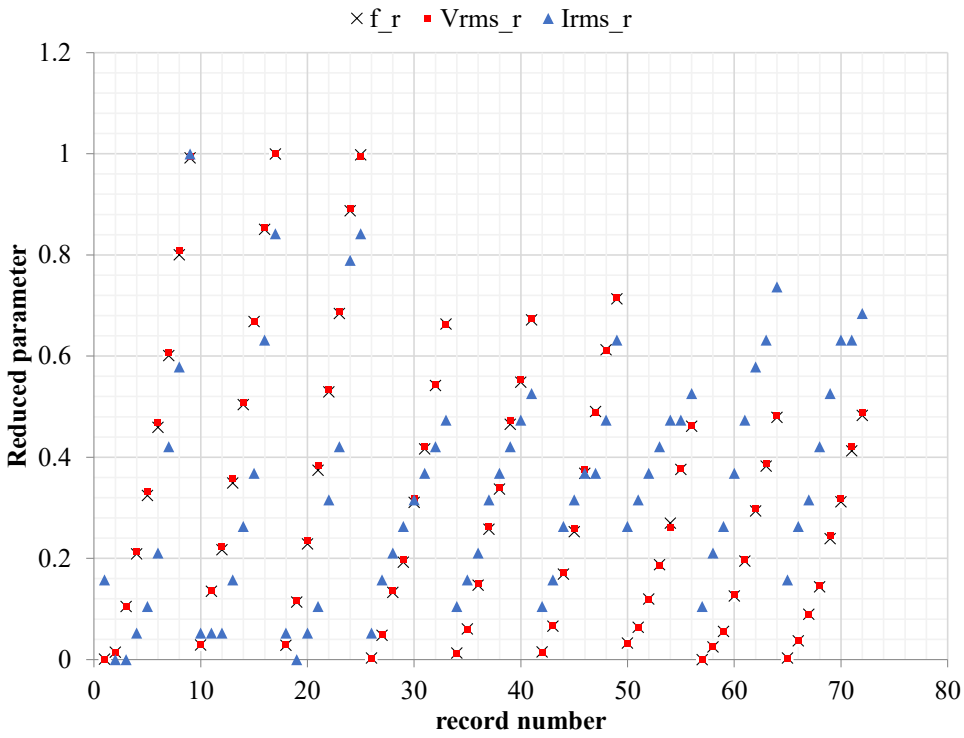


Fig. 6.7. Parameters of the test presented in a reduced form;
a) thermodynamic parameters; b) electric parameters; Pinr: reduced inlet pressure, min 5[kPa], max 20[kPa]; Tinr: reduced inlet temperature, min 288.9[K], max 295.1[K]; Qinr: reduced inlet volume flowrate, min 0.011[m^3/s], max 0.019[m^3/s]; fr: reduced frequency, min 17.8[Hz], max 534[Hz]; Vrmsr: reduced root mean squared voltage, min 6.8[V], max 200[V]; Irmsr: reduced root mean squared current, min 0[A], max 0.19[A].

The frequency is an indirect indicator of the rotational speed and therefore, the rotational speed can be known by reading the frequency, which simplifies the setup of the experiment. The rotational speed responds to changes of the inlet pressure and the load, because it is governed by the expansion ratio and the electromagnetic brake. Thus, for a given exhaust pressure and load, the frequency is a function of the inlet pressure. As predicted, during the test, the frequency presented a good correlation with the inlet pressure, though a different span is identified for each of the loads, as can be seen in Fig. 6.7b. The maximum reported frequency was $f = 559[\text{Hz}]$, which corresponds to a rotational speed $\omega = 33540[\text{rpm}]$. Nevertheless, a greater frequency of $f = 675[\text{Hz}]$ corresponding to $\omega = 40500[\text{rpm}]$ was achieved but not stabilised due to intermittent operation of the air supply system under the highest air flow condition.

The root mean squared voltage is expected to have a linear correlation with the frequency in accordance with the Faraday law. As shown in Fig. 6.8, during the test, the root mean squared voltage and the frequency had a good linear correlation; the slope of this line may proportional to the product $n_e BA$ of the generator windings in accordance with Eqn.(4.4). If this is the case then in Fig. 6.7b, the voltage, V_{rms}, and the frequency, f, should overlap.

The root mean squared current, I_{rms}, has a complex relationship with the inlet pressure as it depends proportionally on the available power and inversely on the load. This means that the current, like the frequency, is expected to mimic the behaviour of the inlet pressure but with a different span for each of the loads.

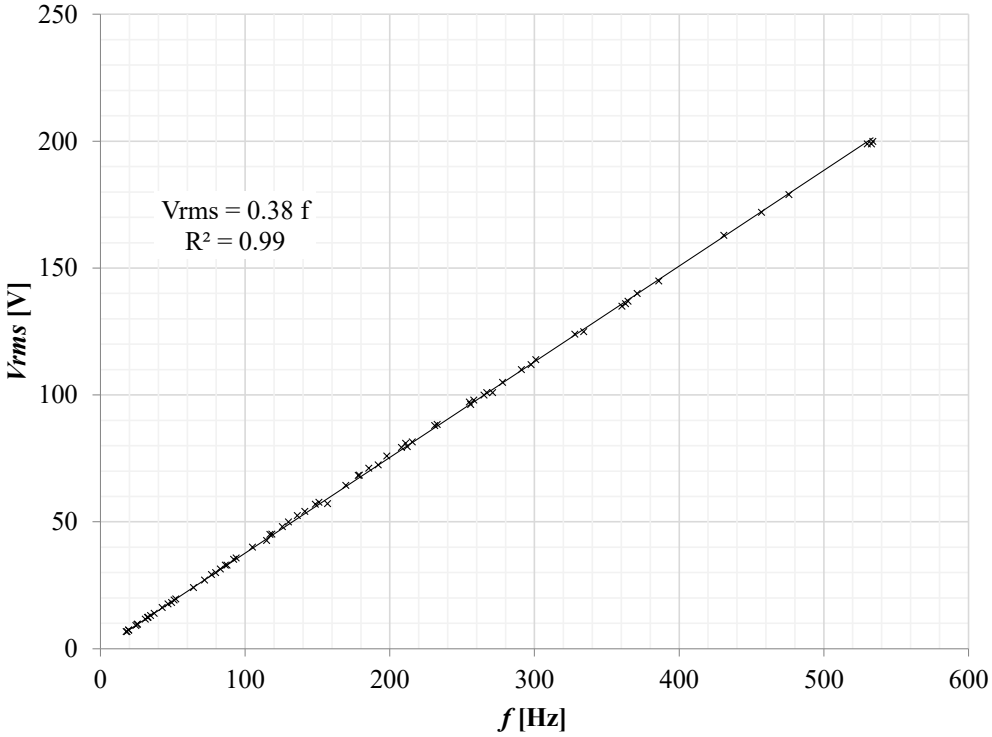


Fig. 6.8. Electric output of the MTG;
***Vrms*: voltage; *f*: frequency.**

The mechanical loss is estimated and presented in Fig. 6.9. Although these results mimic the behaviour of the frictional moment reported in the literature of the manufacturer [253], the accuracy of these results should be experimentally confirmed for the specific application. Lastly, the electrical losses are found negligible during the test as the power loss in the windings is determined to be under 0.2% of the aerodynamic power.

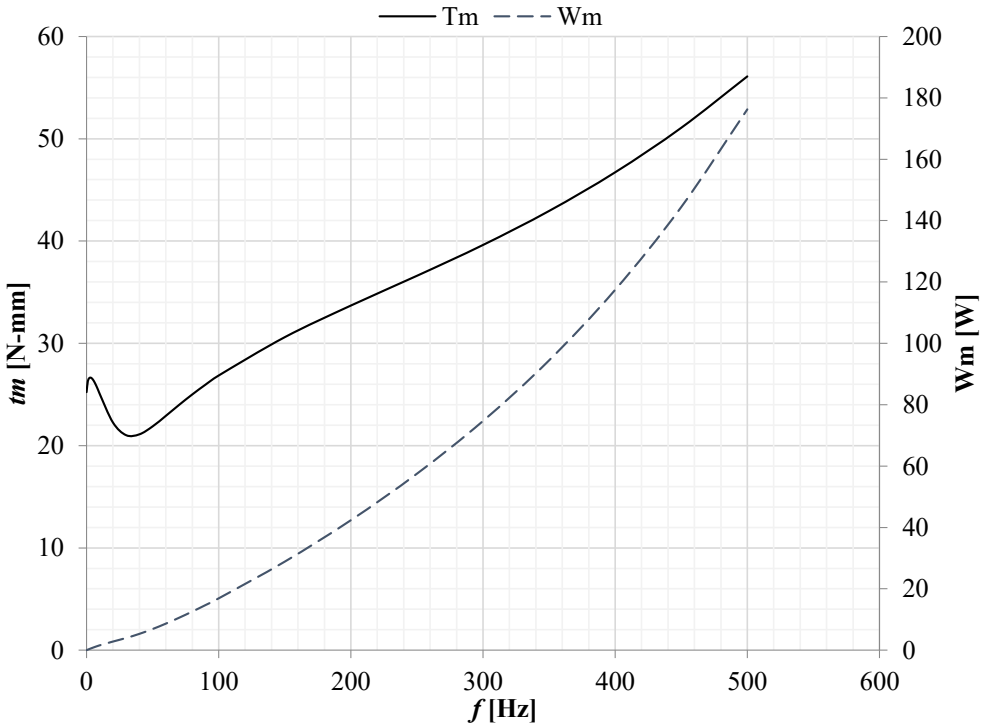


Fig. 6.9. Model for the estimation of mechanical loss;
f: frequency; t_m: frictional moment; Wm: mechanical power loss.

The error produced by typical thermocouples ($\pm 2.5[\mathrm{K}]$) was thought to have led to a wrong determination of the thermodynamic efficiency. The problem arises from the fact that the accuracy of the temperature drop across the turbine would be $\pm 3.53[\mathrm{K}]$. This would be a significant fraction of the actual temperature drop across the turbine, which can be in the range $0[\mathrm{K}]$ to $10[\mathrm{K}]$. Thus, only the aerodynamic efficiency was considered during the testing and compared with the thermo-aerodynamic efficiency of the simulation and the power at the load bank and the aerodynamic efficiency were calculated as described in Section 5.1.

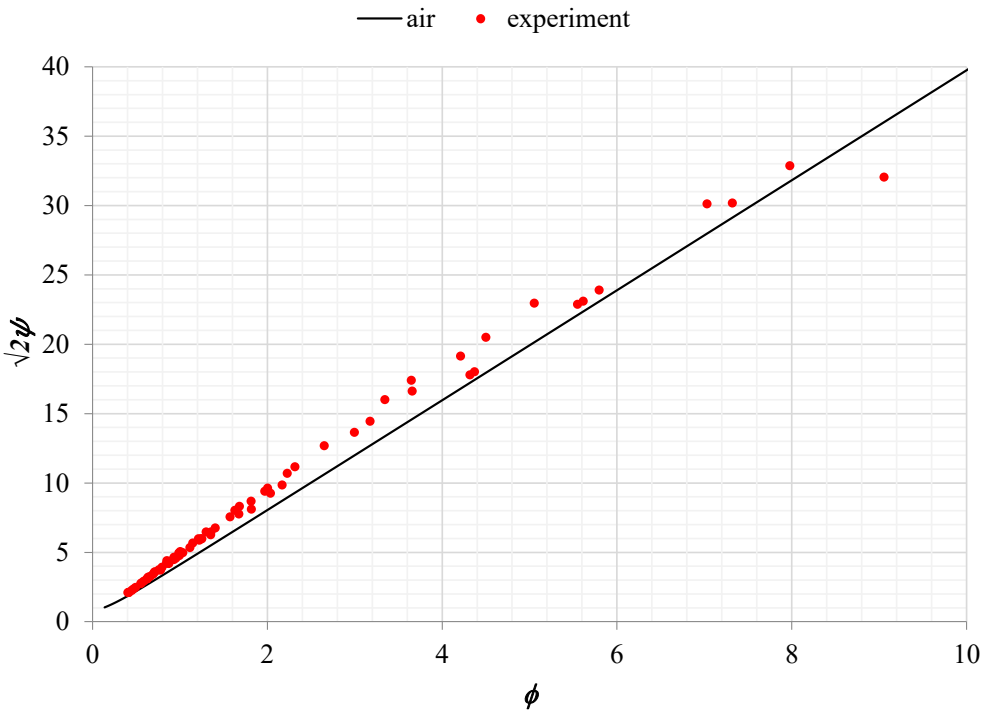
A comparison of the results of the test and the simulation with air, in the plane $\phi - \sqrt{2\psi}$, are shown in Fig. 6.10a, where the expected linear behaviour for an ungoverned turbine can be clearly identified. Additionally, the correlation of the simulation, with respect to the experiment, seems to have a reasonable error for a wide range of ϕ and $\sqrt{2\psi}$. In contrast, Fig. 6.10b and Fig. 6.10c show this comparison in the planes $\sqrt{2\psi} - \eta_{aero}$ and $\phi - \eta_{aero,}$ respectively. In some regions of these figures the simulation seems to have a great error with respect to the test but, in general, they show a similar behaviour.

The simulation appears to overestimate the aerodynamic efficiency with respect to the test at high values of the flow coefficient ϕ and $\sqrt{2\psi}$, however the results have a better agreement near the point of maximum aerodynamic efficiency. This difference could suggest greater losses than estimated in the simulation. Although the causes that generate this issue may be diverse, an inaccurate estimation of the mechanical losses can be the principal reason as explained later in this section. Additionally, the comparison, in the plane $BSR - \eta_{aero}$, is presented in Fig. 6.10d, where the absence of data of the test can be seen for values of *BSR* greater than 0.5. This situation is caused for the lack of available fluid power during the test, which suggests the design point and hence the maximum efficiency were not achieved.

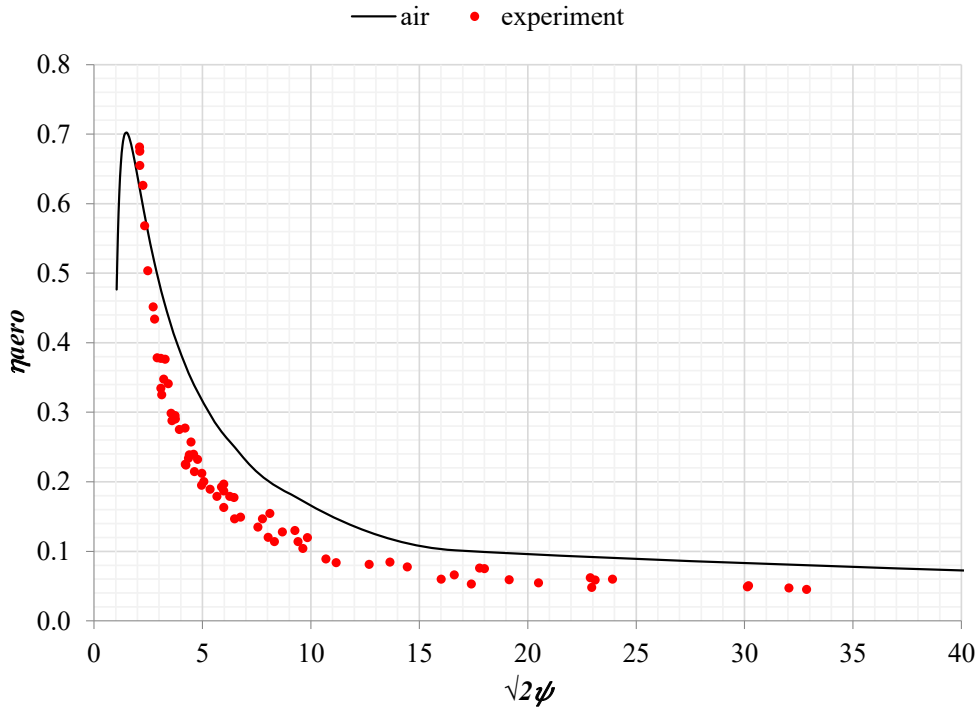
It should be noted that the aforementioned problem, of deviation of experimental results with respect to simulations, does not necessarily mean that the simulations are wrong because slight deviations of theoretical and experimental data are common. This issue can also be observed, for example, in the investigation performed by Kang [257], where variations of the turbine efficiency of around 0.3 are reported. However, a larger error can be hiding a systematic deviation of the simulation with respect to the test and, for that reason, further validation should be considered in future investigations with a reduction of sources of error.

Four major sources of error were explored: inaccuracy of the estimation of the mechanical loss, imprecise fabrication of the prototype, poor control of the inlet temperature and intermittent operation of the air supply system.

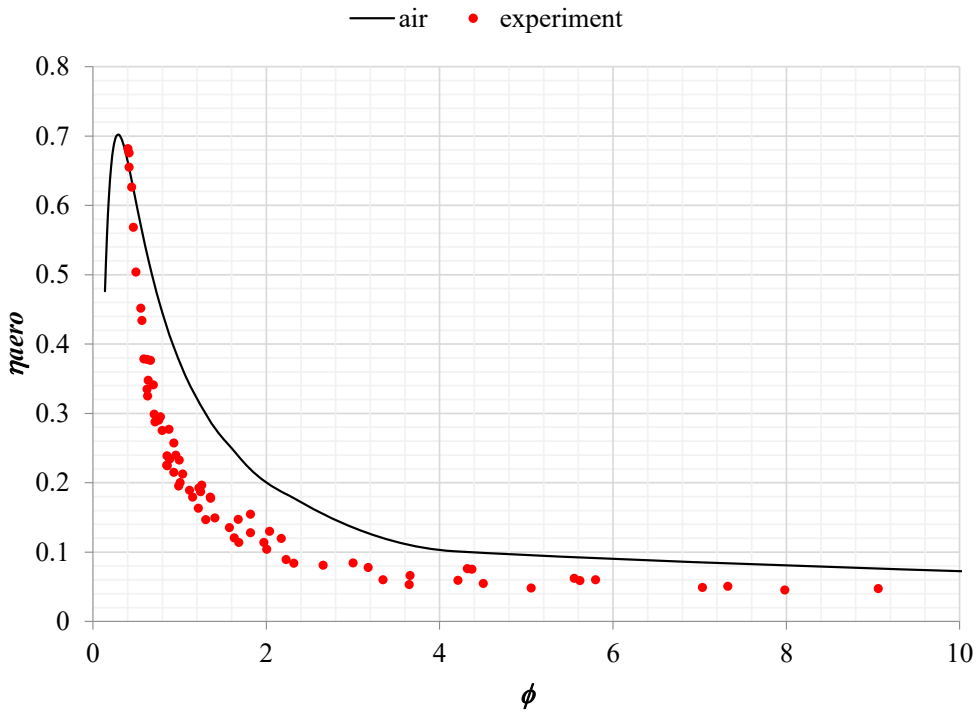
a)


air
experiment
40
35
30
25
20
15
10
5
0
0
2
4
6
8
10
√2ψ
ϕ

b)


air
experiment
0.8
0.7
0.6
0.5
0.4
0.3
0.2
0.1
0.0
0
5
10
15
20
25
30
35
40
ηaero
√2ψ

c)



d)

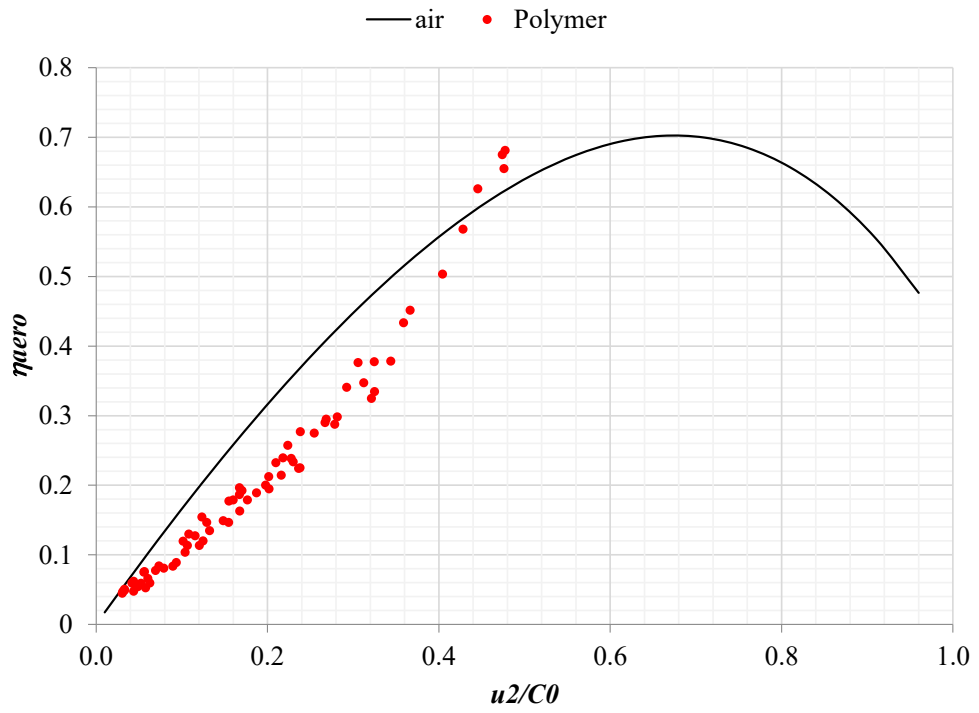


Fig. 6.10. Comparison of the performance of the test for PEEK-GF30;
Simulation with air and test with air; a) plane $\phi - \sqrt{2\psi}$; b) plane $\eta_{aero} - \sqrt{2\psi}$; c) plane $\phi - \eta_{aero}$ and d) plane $BSR - \eta_{aero}$; ϕ: flow coefficient, ψ: loading coefficient, BSR: blade speed ratio, η_{aero}: aerodynamic efficiency.

The inaccuracy of the estimation of the mechanical loss was found to be the principal contributor to deviation with respect of the simulation. The mechanical loss at the bearings consumes a significant fraction of the aerodynamic power, thus, an inaccuracy in its determination has a major impact on the estimation of the overall efficiency. Furthermore, a strong influence of the mechanical loss on the aerodynamic efficiency can be observed in Fig. 6.10d, where the lower edge of the cloud of points shows similar behaviour to the mechanical loss shown in Fig. 6.9. This great impact of the mechanical loss on the aerodynamic efficiency can be minimised by increasing the aerodynamic power. For example, if the aerodynamic power is considerably greater than the mechanical loss, which can be achieved using a denser fluid, the aerodynamic efficiency would be barely affected by the mechanical loss. If the aforementioned condition is met, the rotational speed might not be limited by the lack of fluid power, which could allow the experiment to cover a greater range of blade speed ratio *BSR* in Fig. 6.10d and consequently, the point of maximum efficiency may be achieved.

An imprecise manufacturing of the prototype turbine was found as another source of error because, to simplify the fabrication of the unit, conventional fabrication methods were used, which do not provide a high precision. These defects in fabrication can cause greater clearances and lower tolerances. Greater clearances generate clearance losses (leaks); thus, the aerodynamic efficiency in the test can result lower than predicted in the simulation.

The obvious solution for this problem is the use of a high precision fabrication method to control clearances. However, high precision fabrication requires high precision equipment and specialised labour, which contradicts the philosophy of this investigation in terms of the simplification of the fabrication the MTG-ORC. Consequently, when possible, the clearances can be minimised with gaskets otherwise some leaking must be accepted.

The lack of control of the inlet temperature resulted in the dispersion of the experimental aerodynamic efficiency. This problem originated in the utility room where the compressor is located, which is poorly ventilated and heats-up during operation. Although this problem can be resolved with an additional control of the temperature, a

later analysis revealed that the maximum difference of the inlet temperature in comparable records 2.1[K], which may not be significant.

The intermittent operation of the air supply system resulted in repeated and unpredictable hydraulic transient effects. The hydraulic transience is an important source of inaccuracy in the experimental results as it prevents steady state readings from being reached. Two practical solutions can be implemented to reduce their impact on the experiment: the first is to replace the existing compressor with a larger flow capacity compressor and the second is to significantly increase the storage capacity of the current system. Both solutions should be considered in the future when the required resources become available.

The deviation of the simulation is not negligible with respect to the experimental results but the simulation program is still valid as described by the reasons given below. Firstly, as presented in section 5.1.1, the simulation presents a good agreement with ANSYS® 16.2 VISTA RTD^{TM}. Secondly, the simulation and the experimental results show a good agreement in the plane $\phi - \sqrt{2\psi}$. Thirdly, the maximum simulated aerodynamic efficiency agrees with the efficiency reported in specialised literature of section 2.3.2. Finally, the experimental results are close to the simulation near the maximum efficiency point. Therefore, the program can be used to predict the performance of the turbine using a refrigerant as the working fluid, with some deviation being acknowledged.

6.4.3. Enhanced air test

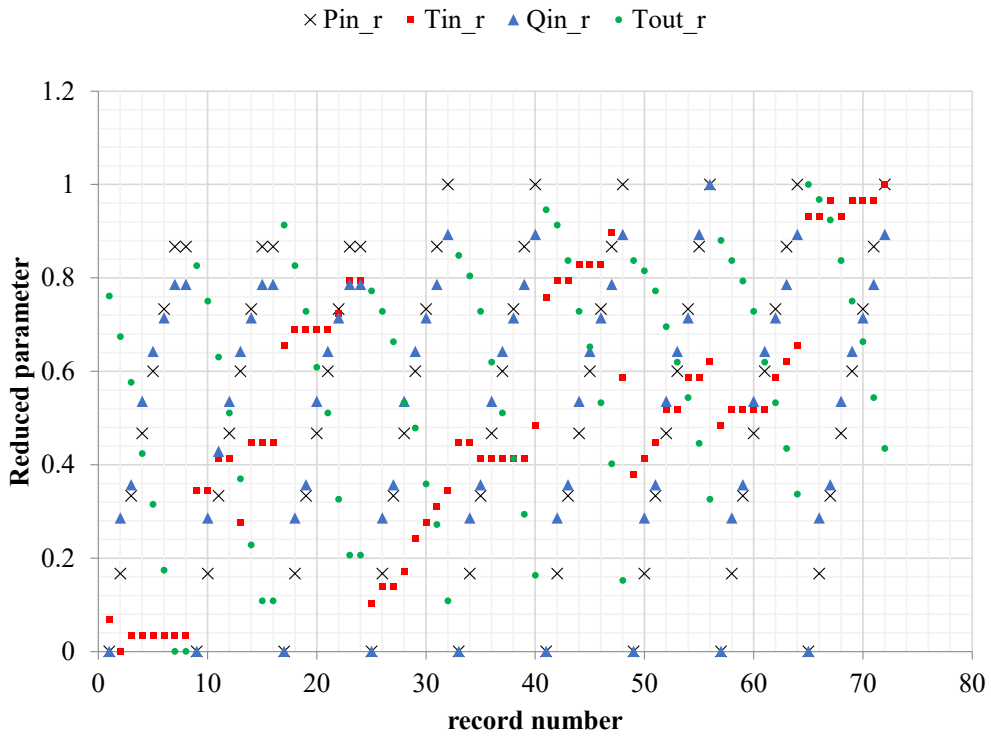
A later examination revealed that the pressure drop across the inlet piping [174] was underestimated and so the aerodynamical losses and hence the experimental efficiency was under estimated. The windage loss, the joule loss, and the core loss were also considered negligible, which can be causing deviation of the results and, combined with the possible inaccuracy of the mechanical loss, was introducing errors in the prediction. Consequently, some enhancements were made to the rig and the test was repeated as described in this section.

Table 6.4 Certificate of calibration

Instrument	Electronic temperature indicator
Model	RS Pro Model 1314
Serial #	180508028
Certificate #	1575716
Date	16 April 2019
Type	UKAS
Input 1, type K accuracy	$\pm\mathbf{0.41[K]}$
Input 2, type K accuracy	$\pm\mathbf{0.42[K]}$

The sealing of the unit was enhanced to prevent leaks and a calibrated digital thermometer was implemented onto the rig to reduce the error of measurement in the temperature; the details of such a thermometer are presented in Table 6.4. Then, the experiment was carried out again. The results are shown in Fig. 6.11, where the history of the enhanced test can be seen. In this figure, the introduction of the outlet temperature can be seen. This allowed the determination, the thermodynamic efficiency and the aerodynamic efficiency separately.

a)



b)

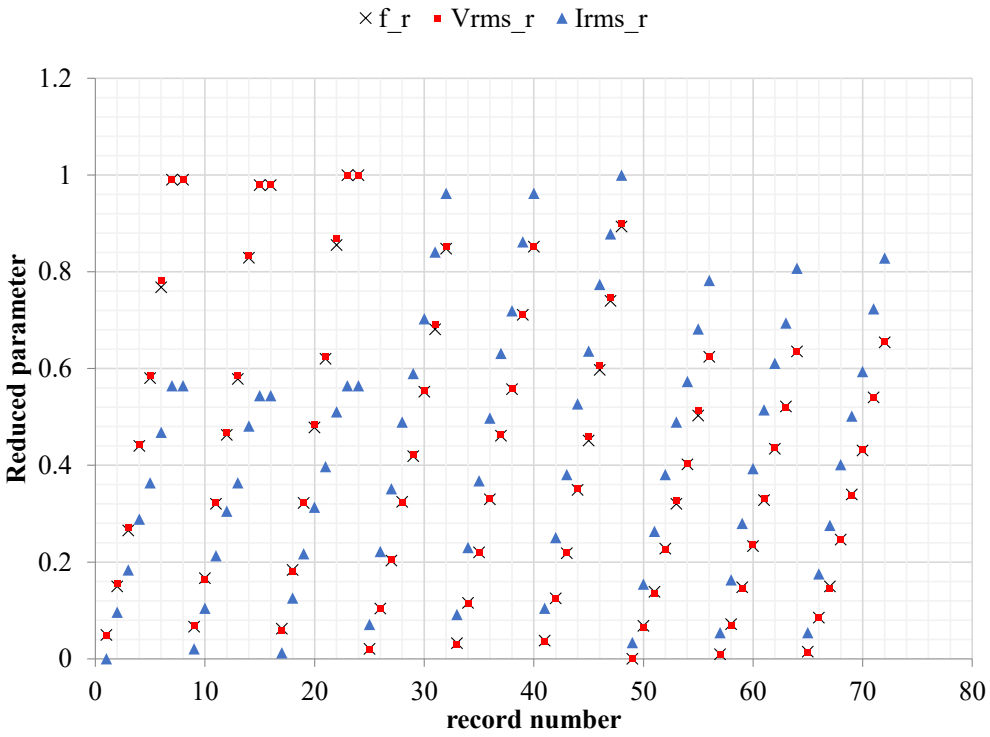


Fig. 6.11 Parameters of the enhanced test presented in a reduced form;
a) thermodynamic parameters; b) electric parameters; Pinr: reduced inlet pressure, min 5[kPa], max 20[kPa]; Tinr: reduced inlet temperature, min 283.6[K], max 296.5[K]; Qinr: reduced inlet volume flowrate, min 0.008[m^3/s], 0.015[m^3/s]; Toutr: reduced outlet temperature, min 286.8[K], max 296[K]; fr: reduced frequency, min 32[Hz], max 559[Hz]; Vrmsr: reduced root mean squared voltage, min 12.3[V], max 210[V]; Irmsr: reduced root mean squared current, min 0.05[A], max 0.284[A].

The pressure drop across the inlet piping was found to have a considerable impact on the experimental performance and so it was included into the analysis for the determination of the experimental parameters as described below.

Estimation of the inlet pressure drop

The pressure loss across the inlet can be experimentally estimated with Eqn.(6.12) if air is supplied through the inlet piping and the inlet pressure, $P_{0,in}$, and nozzle inlet pressure, P_{01}, are measured.

$$\Delta P_{loss} = P_{0,in} - P_{01} \tag{6.12}$$

$$\Delta P_{loss}(Q_{in}) = a_Q Q_{in}^2 + b_Q Q_{in} \tag{6.13}$$

Although the pressure loss has a complex relationship with the flowrate, it is proportional to the inlet flowrate and can be approximated with the second order polynomial regression shown in Eqn.(6.13), whose constants are given in Table 6.5.

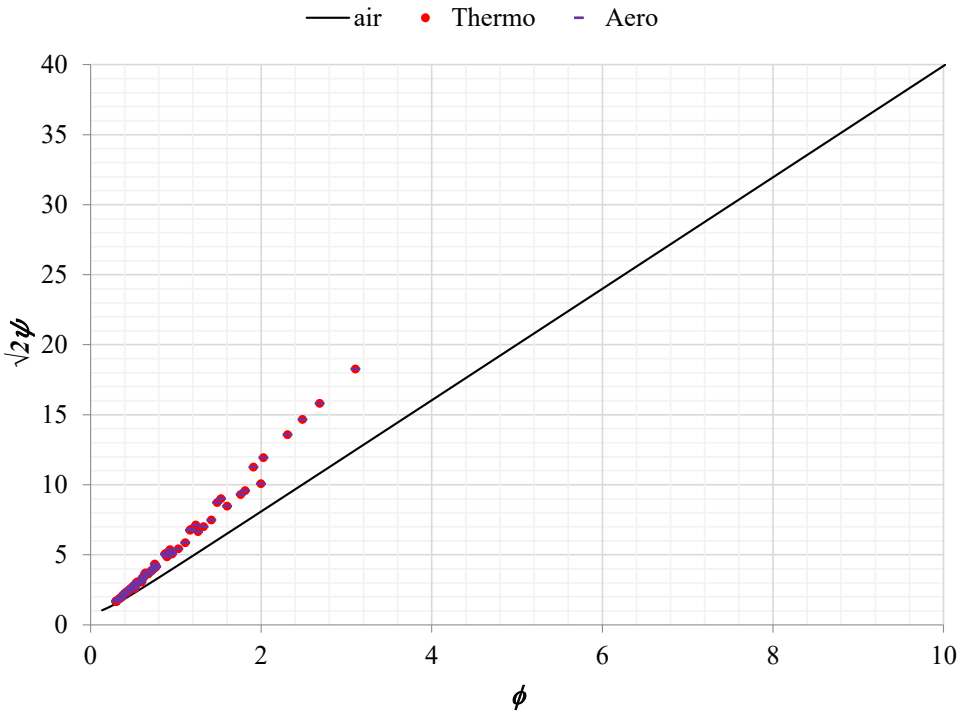
Table 6.5 Values of the constants for the regression of inlet pressure drop, ΔP.

Constant	Value	Units
a_Q	0.0148	[kg/m^7]
b_Q	-0.258	[kg/m^4-s]
R^2	0.998	-

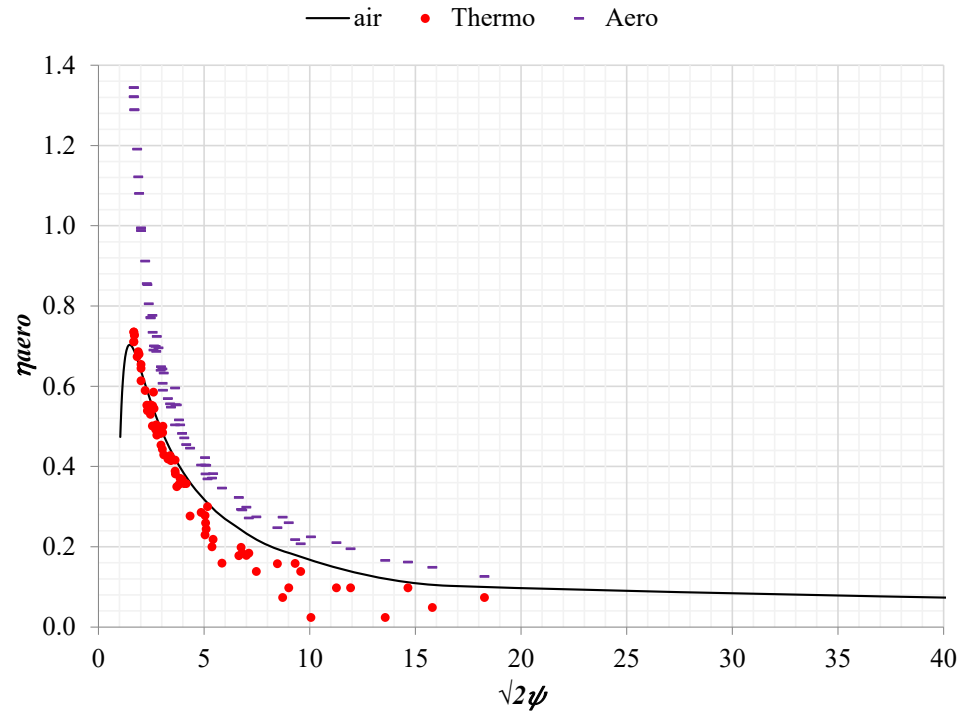
The updated thermodynamic efficiency and the aerodynamic efficiency were calculated and compared with the simulation; the results of this comparison is shown in Fig. 6.12. It appears that after the enhancement of the test, the efficiency of the unit was improved significantly, which can be noted when the results of the thermodynamic efficiency are observed. However, a significant disagreement is now found between aerodynamic efficiency, shown in purple in Fig. 6.12, and the simulated thermo-aerodynamic efficiency. The aerodynamic efficiency shows results over 1, which is unrealistic; this fact suggests that the mechanical losses are overestimated with the manufacturer's model of frictional moment [253]. Therefore, the estimation of mechanical losses was revised and the determination of the aerodynamic efficiency updated.

In contrast the thermodynamic efficiency, shown in red in Fig. 6.12, presents a very good agreement with the simulation; thus, it can be used to revise the estimation of mechanical losses.

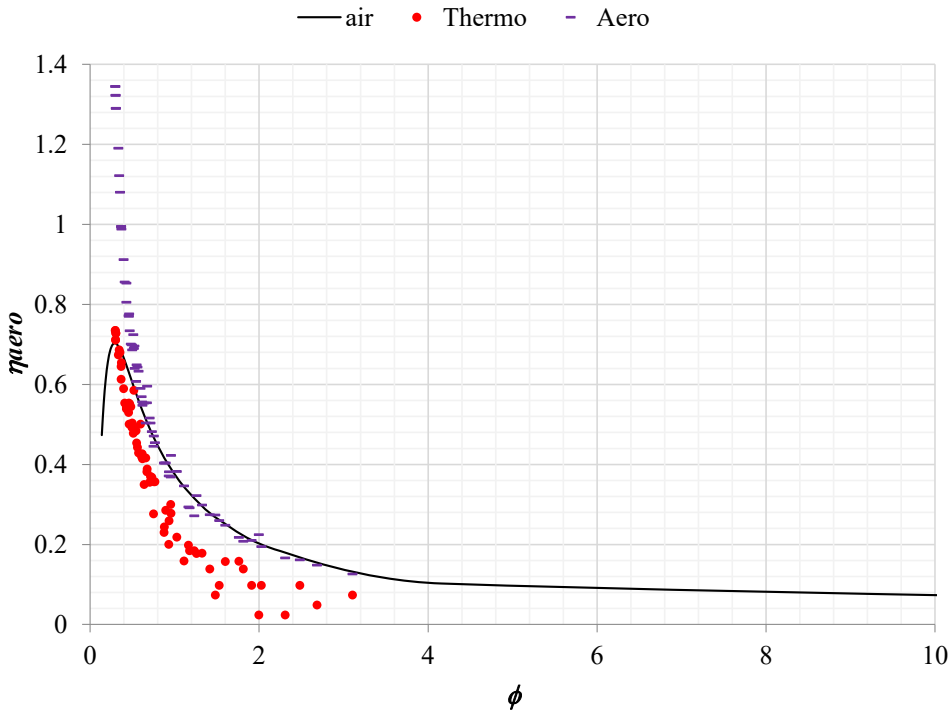
a)


air
Thermo
Aero
40
35
30
25
20
15
10
5
0
√2ψ
0
2
4
6
8
10
ϕ

b)


air
Thermo
Aero
1.4
1.2
1.0
0.8
0.6
0.4
0.2
0.0
ηaero
0
5
10
15
20
25
30
35
40
√2ψ

c)



d)

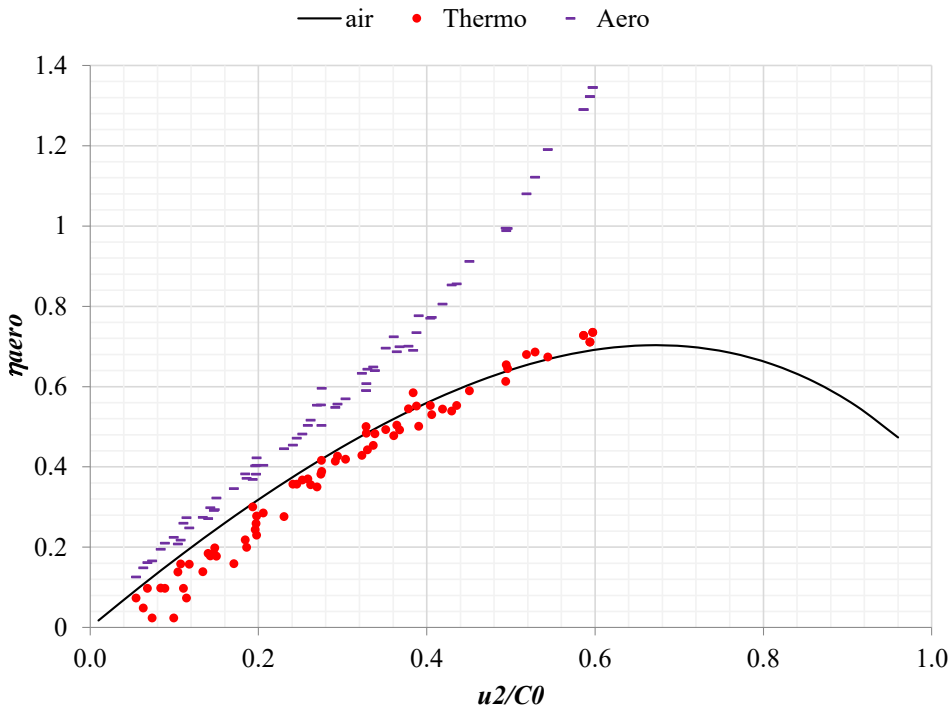


Fig. 6.12 Comparison of the performance of the enhanced air test for PEEK-GF30;

after correction of pressure drop, simulation with air and test with air; a) plane $\phi - \sqrt{2\psi}$; b) plane $\eta_{aero} - \sqrt{2\psi}$; c) plane $\phi - \eta_{aero}$ and d) plane $BSR - \eta_{aero}$; ϕ: flow coefficient, ψ: loading coefficient, BSR: blade speed ratio, η_{aero}: aerodynamic efficiency.

Revised estimation of losses

An alternative model for the estimation of all the losses is given in this section, which includes mechanical and electrical losses. This new model is based on the results of the thermodynamic efficiency and thus, the adiabatic condition must be fulfilled for the model to be valid.

Bearing loss, windage loss and core loss are a function of the frequency, *f*, as can be seen in Eqn.(6.6), Eqn.(6.7) and Eqn.(6.10). Thus, they can be evaluated together with a single function $L(f)$ dependant on the frequency as shown in Eqn.(6.14). Additionally, if the adiabatic condition is reasonably achieved, the thermodynamic power should be equal to the aerodynamic power. Thus, in accordance with Eqn.(6.1) and the aforementioned equations, the losses can be experimentally obtained with Eqn.(6.15) using the results of the thermodynamic power, the power at the load bank and the joule losses.

$$\dot{W}_{bearings} + \dot{W}_{windage} + \dot{W}_{core} = L(f) \tag{6.14}$$

$$L(f) = \dot{W}_{thermo} - \dot{W}_{bank} - \dot{W}_{joule} \tag{6.15}$$

$$L(f) = a_L f^2 + b_L f \tag{6.16}$$

Additionally, $L(f)$ can be empirically obtained with the second order polynomial regression shown in Eqn.(6.16), whose constants are given in Table 6.6.

Table 6.6 Values of the constants for the polynomial regression of the losses.

Constant	Value	Units
a_L	1.45x10^{-4}	[kg-m^2/s]
b_L	0.102	[kg-m^2/s^2]
R^2	0.977	-

A comparison of the estimation of losses with the aforementioned regression and the manufacturer model [253] is shown in Fig. 6.13. In this figure, the overestimation of mechanical losses is evident. Thus, the new model was implemented and the experimental aerodynamic efficiency updated.

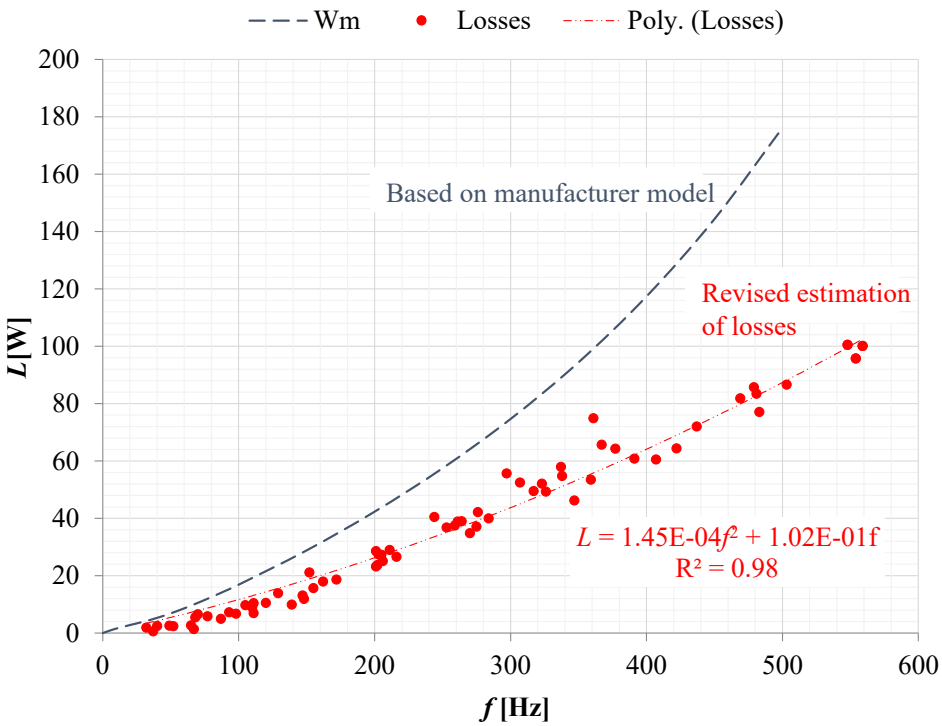
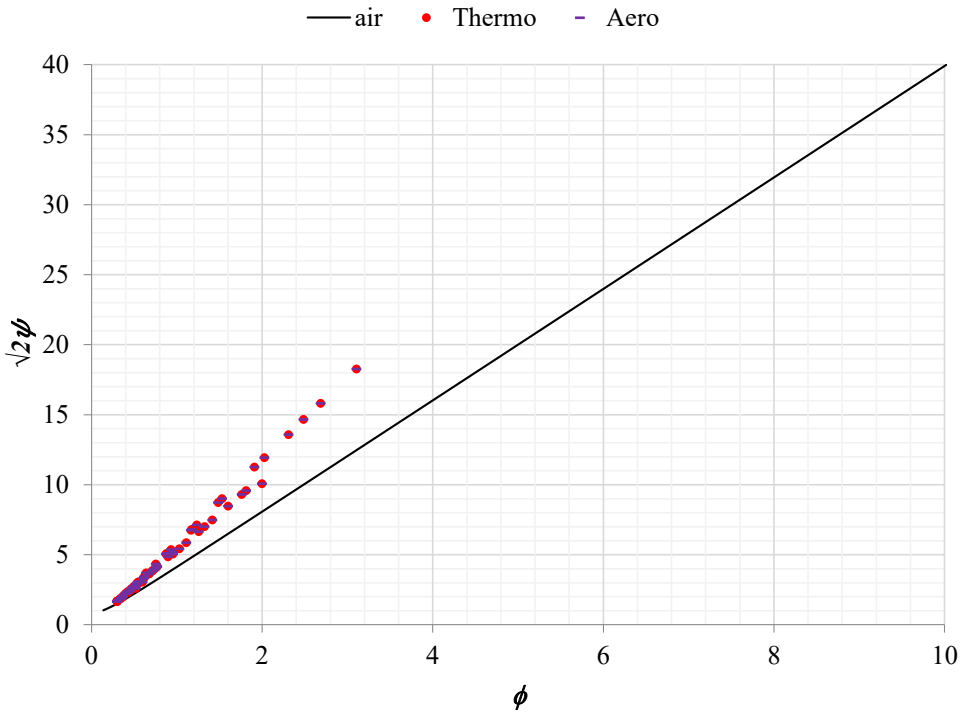


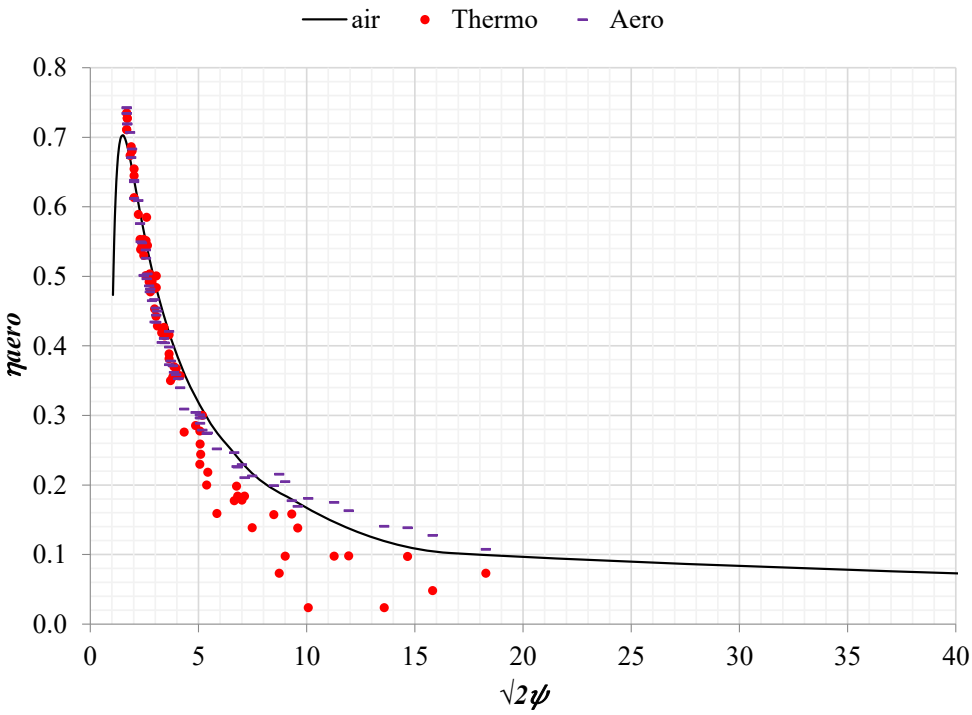
Fig. 6.13 Enhanced polynomial model for the estimation of losses;
comparison with manufacturer model for the estimation of the mechanical losses; f: frequency; Wm_dot: mechanical power loss.

The further updated results of the enhanced experiment are shown in Fig. 6.14, where a much better agreement of the experimental aerodynamic efficiency, the experimental thermodynamic efficiency and the simulated thermo-aerodynamic efficiency is evident. The root mean squared error of the experimental thermodynamic efficiency is $RMSE = 0.083$ whereas the root mean squared error of the aerodynamic efficiency is $RMSE = 0.232$, both with respect to the simulated thermo-aerodynamic efficiency.

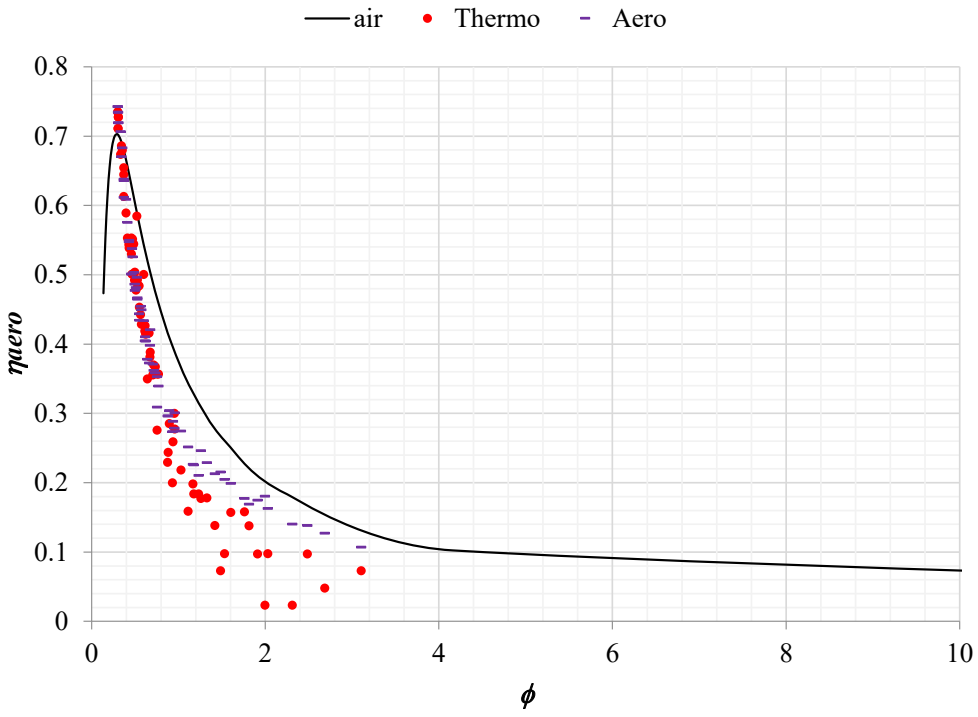
a)


air
Thermo
Aero
40
35
30
25
20
15
10
5
0
0
2
4
6
8
10
√2ψ
ϕ

b)


air
Thermo
Aero
0.8
0.7
0.6
0.5
0.4
0.3
0.2
0.1
0.0
0
5
10
15
20
25
30
35
40
ηaero
√2ψ

c)



d)

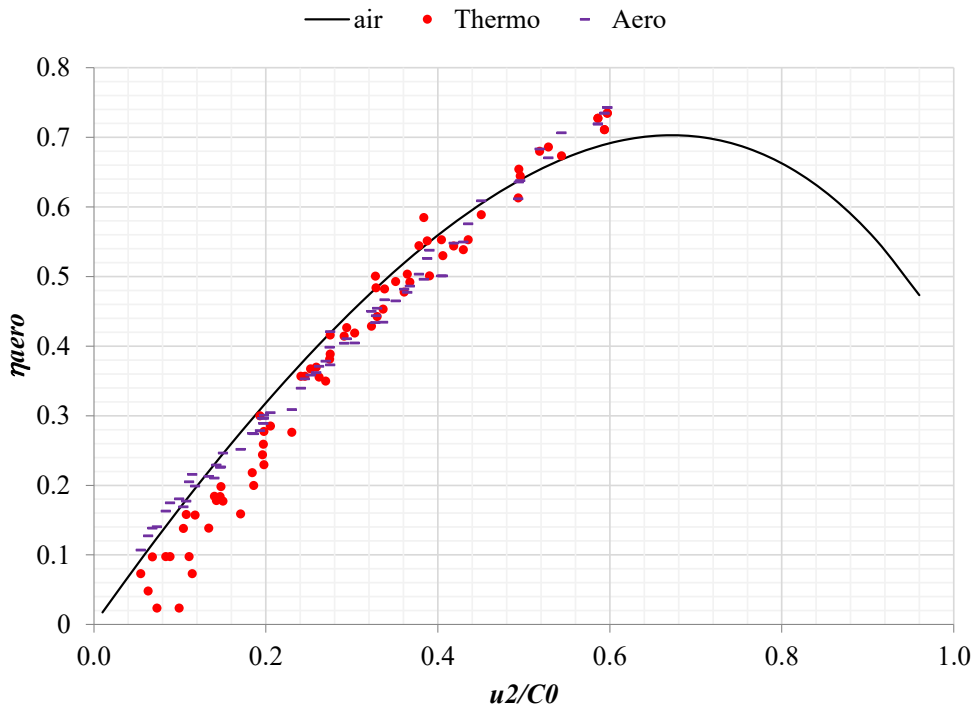


Fig. 6.14 Comparison of the performance of the enhanced air test for PEEK-GF30 with the empirical loss model;

simulation with air and test with air; a) plane $\phi - \sqrt{2}\psi$; b) plane $\eta_{aero} - \sqrt{2}\psi$; c) plane $\phi - \eta_{aero}$ and d) plane $BSR - \eta_{aero}$; ϕ: flow coefficient, ψ: loading coefficient, BSR: blade speed ratio, η_{aero}: aerodynamic efficiency.

6.4.4. Uncertainty and error propagation

The dimensionless parameters of interest are not measured but calculated with the experimental parameters presented in Table 6.3. Thus, an analysis of propagation of error must be performed to assess how the inaccuracy of the measurement of those parameters affects the determination of the dimensionless parameters η_{thermo}, η_{aero}, ϕ and $\sqrt{2\psi}$.

As an example a generic function of efficiency that has a central value η and an associated error $\delta\eta$ can be considered. This function may depend on a number of variables $x_1, x_2, \dots x_n$; however, each variable would have a central value x_n and a corresponding error δx_n as presented in Eqn.(6.17). The central value of the efficiency function depends on the central value of each variable, as shown in Eqn.(6.18), and its associated error depends not only on the central values but also on the associated errors as presented in Eqn.(6.19) [258].

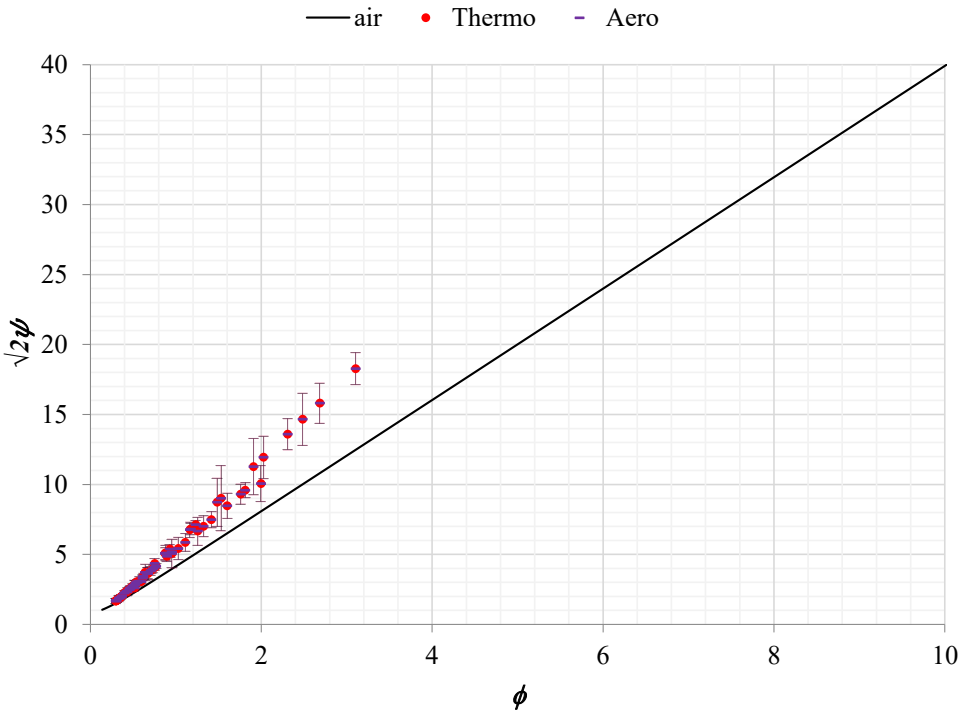
$$\eta \pm \delta\eta = \eta(x_1 \pm \delta x_1, x_2 \pm \delta x_2, \dots, x_n \pm \delta x_n) \tag{6.17}$$

$$\eta = \eta(x_1, x_2, \dots, x_n) \tag{6.18}$$

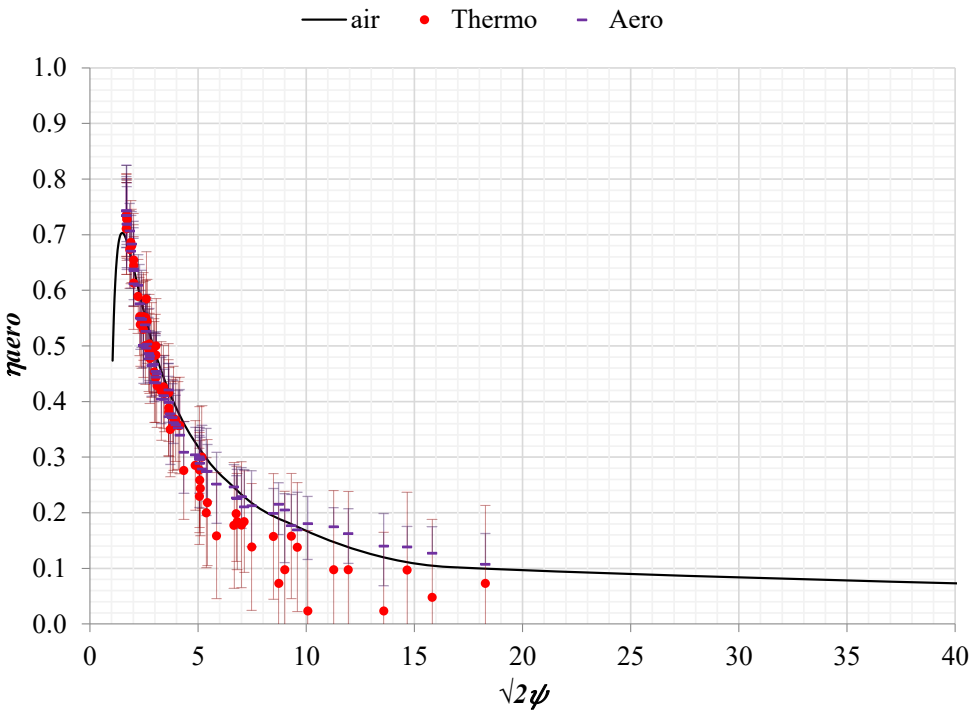
$$\delta\eta = \sqrt{\left(\frac{\partial\eta}{\partial x_1}\delta x_1\right)^2 + \left(\frac{\partial\eta}{\partial x_2}\delta x_2\right)^2 + \cdots + \left(\frac{\partial\eta}{\partial x_n}\delta x_n\right)^2} \tag{6.19}$$

The above analysis grows in complexity with the number of equations, their complexity and the number variables involved; therefore, such an analysis was made using the software Maple™-2017. In this analysis, the errors of the n experimental parameters were combined with the equations of the thermo-aerodynamic analysis for each of the i records of the test. The code used for such an analysis is presented in Appendix A and the results are shown in Fig. 6.15. Additionally, a summary is presented in Table 6.7, where the *RMSE* of the error for the 72 records is included.

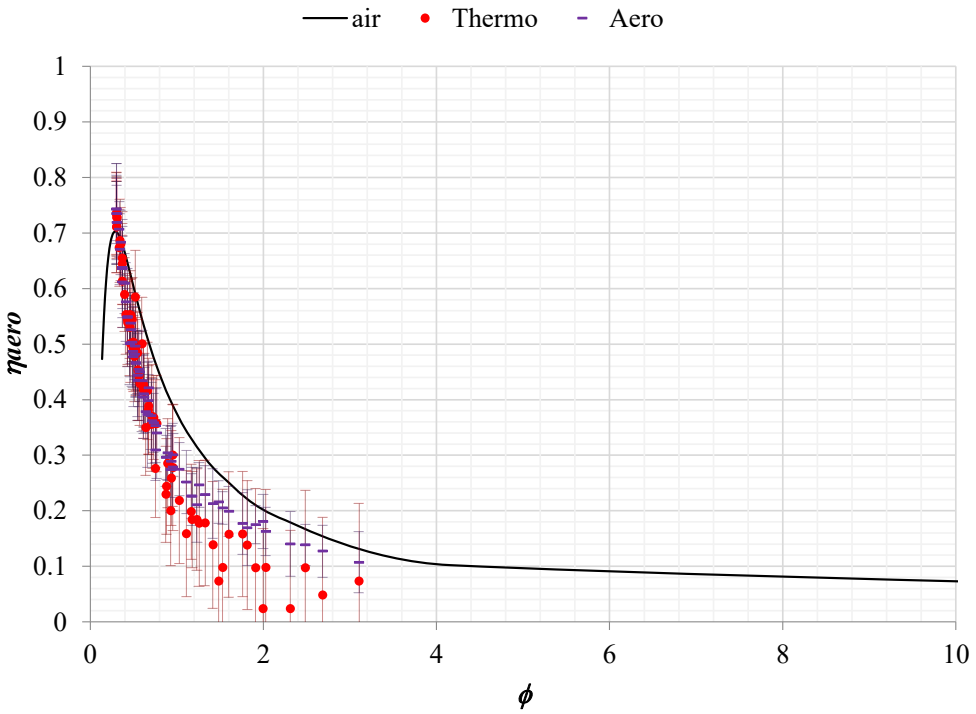
a)


air
Thermo
Aero
40
35
30
25
20
15
10
5
0
√2ψ
0
2
4
6
8
10
ϕ

b)


air
Thermo
Aero
1.0
0.9
0.8
0.7
0.6
0.5
0.4
0.3
0.2
0.1
0.0
ηaero
0
5
10
15
20
25
30
35
40
√2ψ

c)



d)

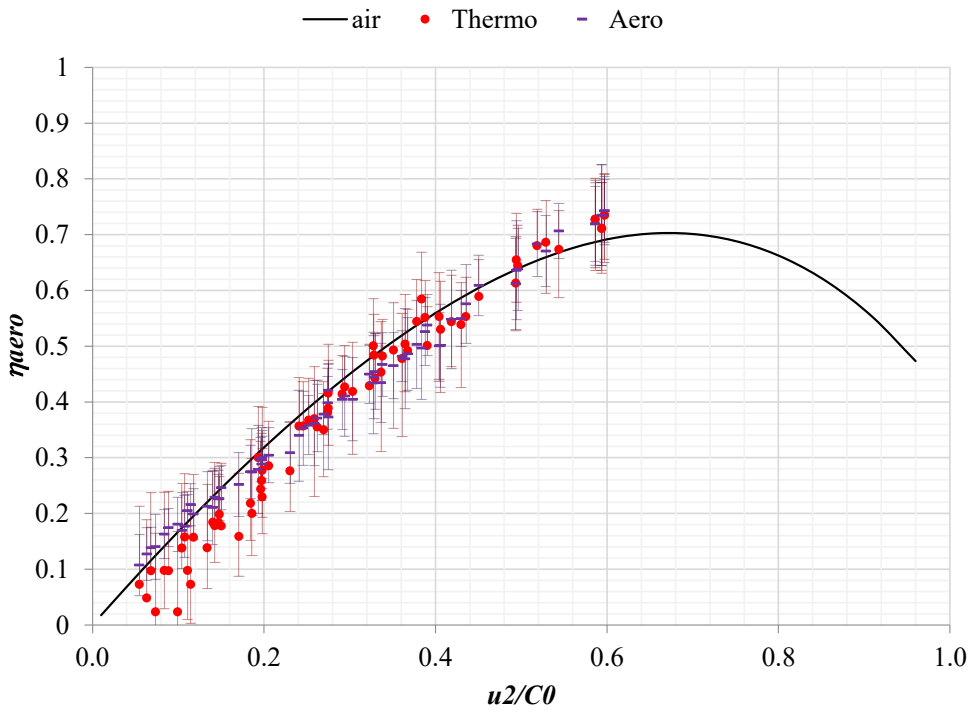


Fig. 6.15 Comparison of the performance of the enhanced air test for PEEK-GF30 with the empirical loss model and including propagation of error;
simulation with air and test with air; a) plane $\phi - \sqrt{2\psi}$; b) plane $\eta_{aero} - \sqrt{2\psi}$; c) plane $\phi - \eta_{aero}$ and d) plane $BSR - \eta_{aero}$; ϕ: flow coefficient, ψ: loading coefficient, BSR: blade speed ratio, η_{aero}: aerodynamic efficiency.

These results show that the thermodynamic efficiency can be obtained with a mean uncertainty of 0.09, the aerodynamic efficiency can be obtained with a mean uncertainty of 0.06, the flow coefficient with a mean uncertainty of 0.1 and $\sqrt{2\psi}$ with a mean uncertainty of 0.69. The examination of these results revealed that, although a calibrated thermometer was used, the inaccuracy of the temperature measurement still has an important contribution to the error of the dimensionless parameters because the drop of temperature across the turbine is small.

Table 6.7 Summary of the results of the analysis of propagation of error

Parameter	Mean Uncertainty
η_{thermo}	0.09
η_{aero}	0.06
ϕ	0.1
$\sqrt{2\psi}$	0.69

6.4.5. Structural integrity

The structural integrity of the rotor is critically governed by the centrifugal force on the blades [259] and the bending forces are not significant. Therefore, the structural capacity of the rotor to withstand the required rotational speed must be verified to assure that the impeller can operate with the speed rated for the ORC application.

The structural integrity of the impeller was assessed with the FSI analysis presented in section 5.1.5. This analysis [25] showed that the impeller made of PEEK-GF30 can have a better structural performance than aluminium in the most demanding condition, which is over-speeding. Moreover, although PEEK-GF30 is not stronger than aluminium in the other studied conditions, it is still suitable. Therefore, structurally, the impeller made of PEEK-GF30 may be considered a good substitute for an aluminium impeller at low-temperatures.

6.5. COMPARISON WITH ALUMINIUM COMPONENTS

A comparative evaluation is conducted to understand how the polymeric components perform with respect to state-of-the-art components. In this study, the performance of metal components was tested and compared with the performance of the polymeric components studied in this work.

6.5.1. The aluminium impeller and nozzle body

The MTG-ORC was equipped with an equivalent impeller and a nozzle body, shown in Fig. 6.16, made of a standard-grade aluminium, which has a yield strength of 255[MPa]. These components were designed, fabricated, assembled and tested following the methods and procedures used for their polymeric counterparts but the material was replaced with Aluminium.

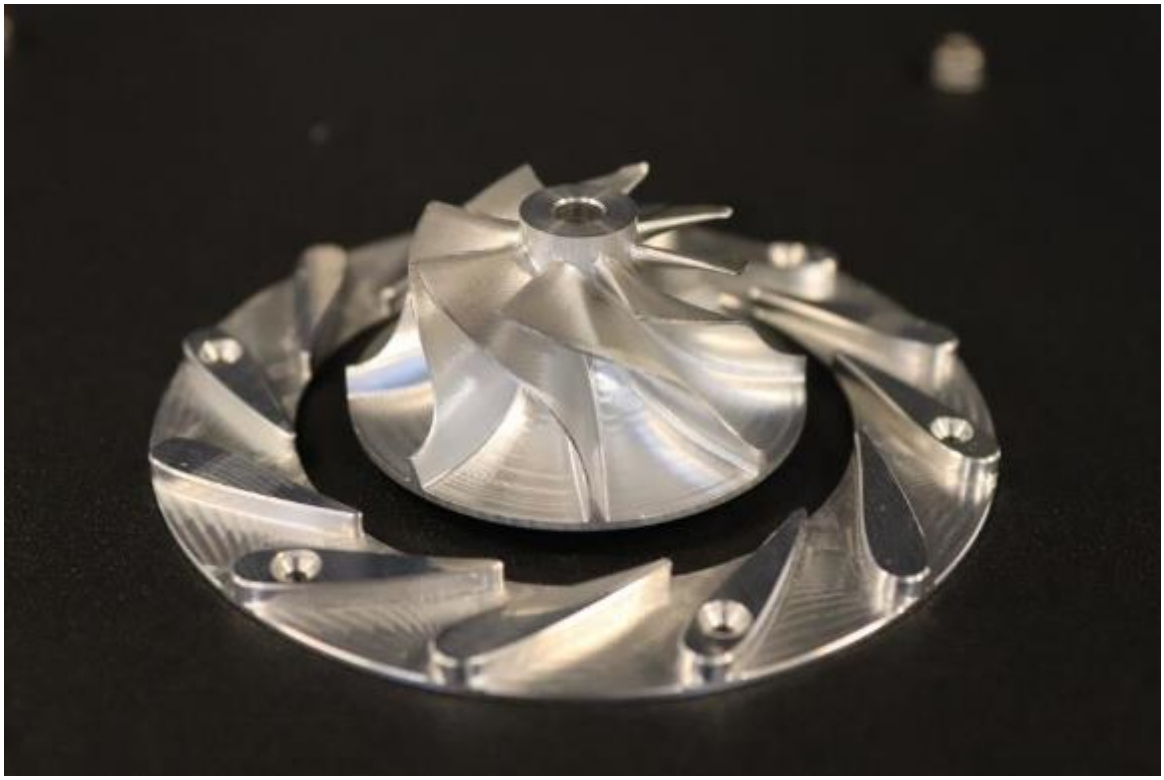
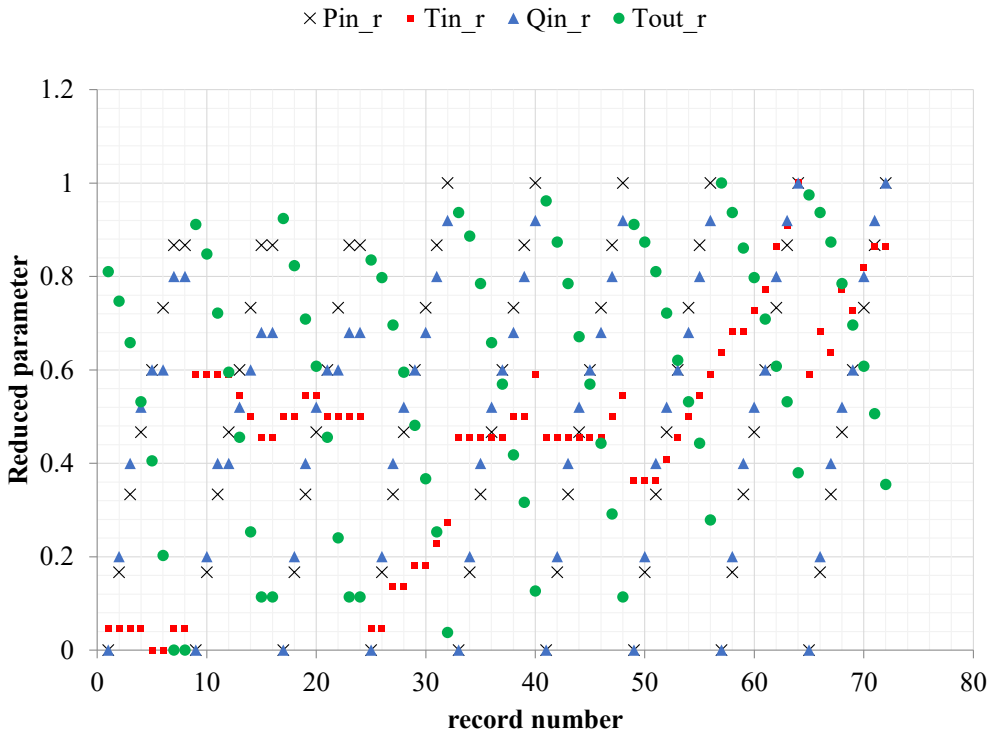


Fig. 6.16. Impeller and nozzle body made of Aluminium.

6.5.2. Results of testing with aluminium components

As can be seen in Fig. 6.17, the results with the aluminium components seem consistent with the results of the polymeric components of Fig. 6.11; which is an early insight of their performance being comparable.

a)



b)

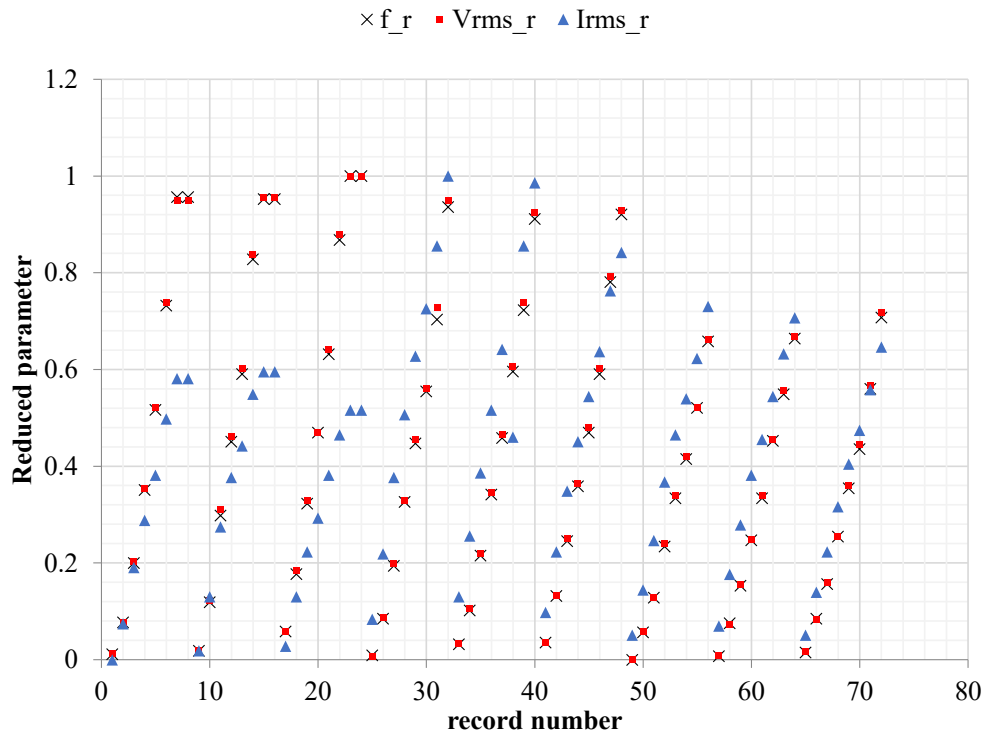


Fig. 6.17 Parameters of the aluminium test presented in a reduced form;
a) thermodynamic parameters; b) electric parameters; Pinr: reduced inlet pressure, min 5[kPa], max 20[kPa]; Tinr: reduced inlet temperature, min 292.9[K], max 295.1[K]; Qinr: reduced inlet volume flowrate, min 0.009[m^3/s], max 0.015[m^3/s]; Toutr: reduced outlet temperature, min 286.5[K], max 294.4[K]; fr: reduced frequency, min 33[Hz], max 563[Hz]; Vrmsr: reduced root mean squared voltage, min 12.5[V], max 211[V]; Irmsr: reduced root mean squared current, min 0.033[A], max .248[A].

Additionally, the estimation of the mechanical losses with the polynomial regression presented in Fig. 6.18 also seems to be consistent with the estimation of losses of Fig. 6.13; although, they not necessarily have to be equal because the tribological properties of PEEK-GF30 and Aluminium are not the same.

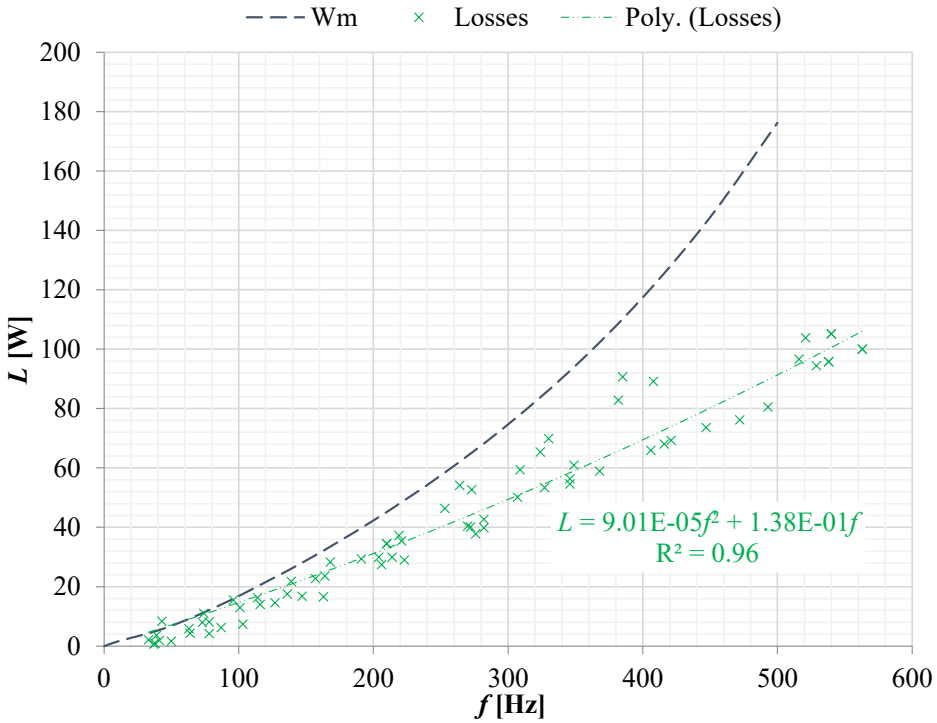
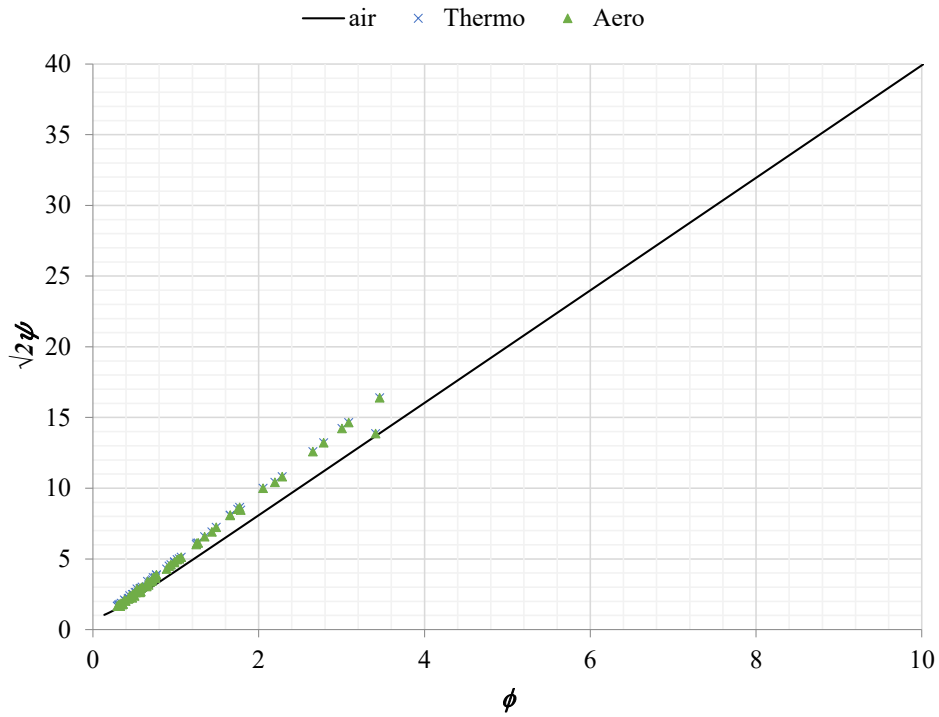


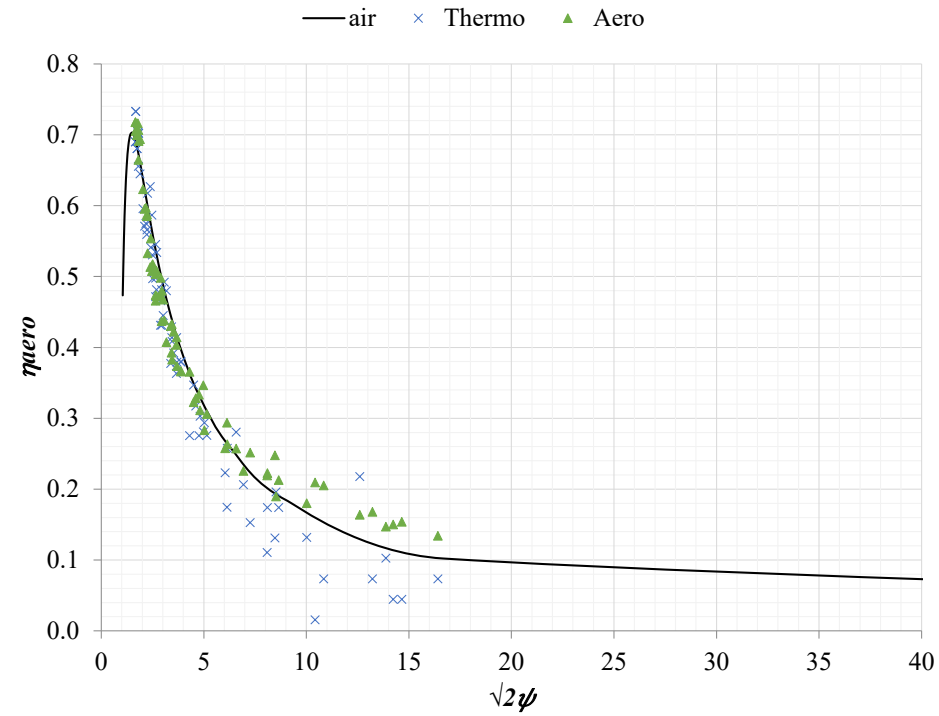
Fig. 6.18 Polynomial model for Aluminium for the estimation of losses; comparison with the manufacturer model for the estimation of the mechanical losses; f: frequency; Wm_dot: mechanical power loss.

Finally, the dimensionless results of the test with the aluminium components, in the planes $\phi - \sqrt{2\psi}$, $\eta_{aero} - \sqrt{2\psi}$, $\phi - \eta_{aero}$ and $BSR - \eta_{aero}$, are presented in Fig. 6.19. These results seem to be similar to the results of the test with polymeric components of Fig. 6.14, which is further evidence that their performance can be comparable.

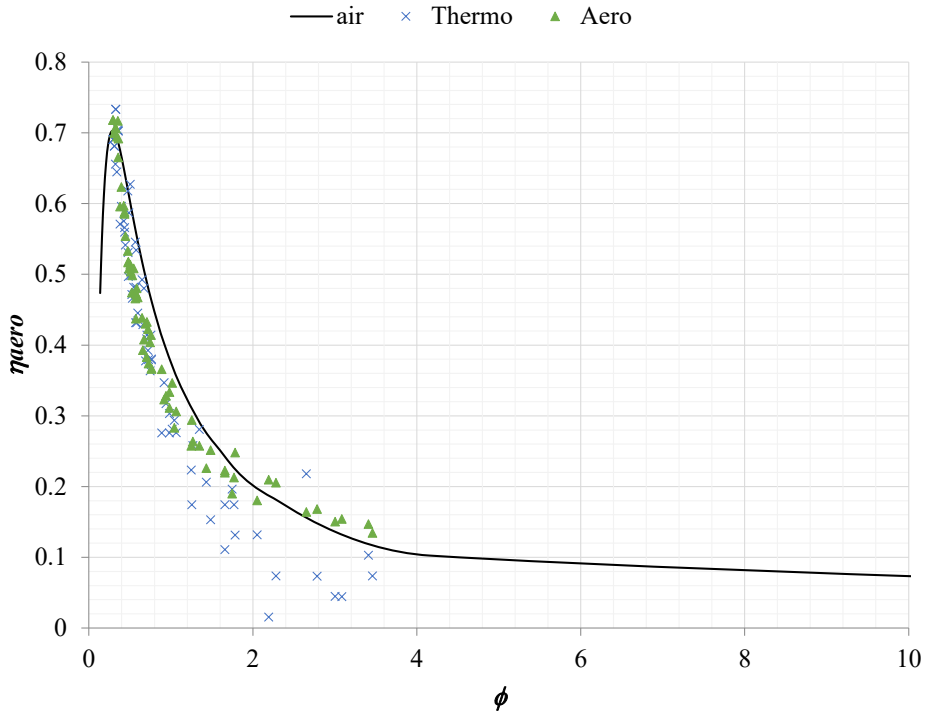
a)


air
Thermo
Aero
40
35
30
25
20
15
10
5
0
0
2
4
6
8
10
√2ψ
ϕ

b)


air
Thermo
Aero
0.8
0.7
0.6
0.5
0.4
0.3
0.2
0.1
0.0
0
5
10
15
20
25
30
35
40
ηaero
√2ψ

c)



d)

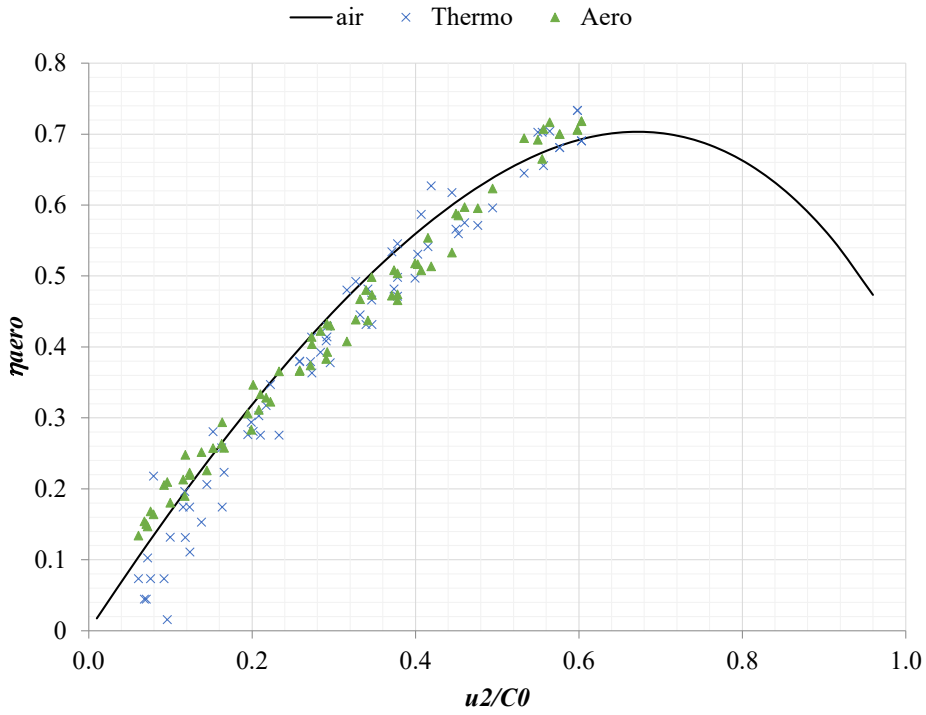


Fig. 6.19 Comparison of the performance of the enhanced air test for Aluminium with the empirical loss model;

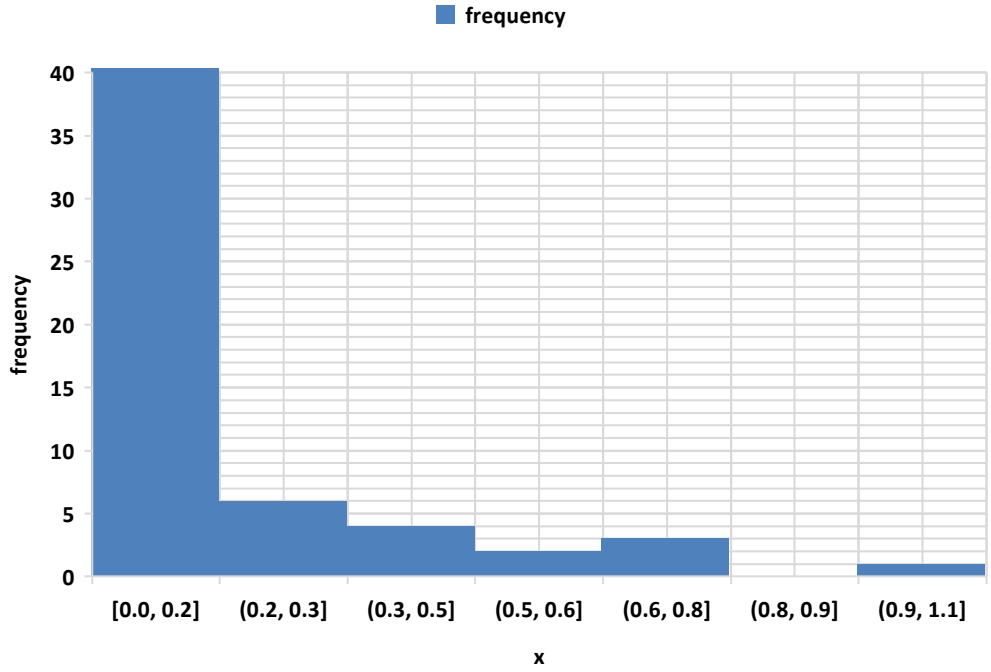
simulation with air and test with air; a) plane $\phi - \sqrt{2\psi}$; b) plane $\eta_{aero} - \sqrt{2\psi}$; c) plane $\phi - \eta_{aero}$ and d) plane $BSR - \eta_{aero}$; ϕ: flow coefficient, ψ: loading coefficient, BSR: blade speed ratio, η_{aero}: aerodynamic efficiency.

6.5.3. Statistical comparison

The performance of the polymeric components appears to be comparable. Nevertheless, to quantitatively evaluate whether the performance of the MTG-ORC with polymeric components is any different with respect to the MTG-ORC with aluminium components, a statistical analysis is conducted with a test of that hypothesis.

The error, x, is defined to assess the deviation of the thermodynamic efficiency with respect to the simulated thermo-aerodynamic efficiency. Then, the error is calculated with Eqn.(6.20) for the 72 records of two samples: the thermodynamic efficiency with polymeric components and the thermodynamic efficiency with aluminium components. These should result in two random samples of the variable x, which can be statistically analysed. Nevertheless, x is a biased variable, as can be observed in Fig. 6.20, because the absolute value of the numerator in Eqn.(6.20) always makes the error non-negative. Thus, the samples cannot be treated normally.

a)



b)

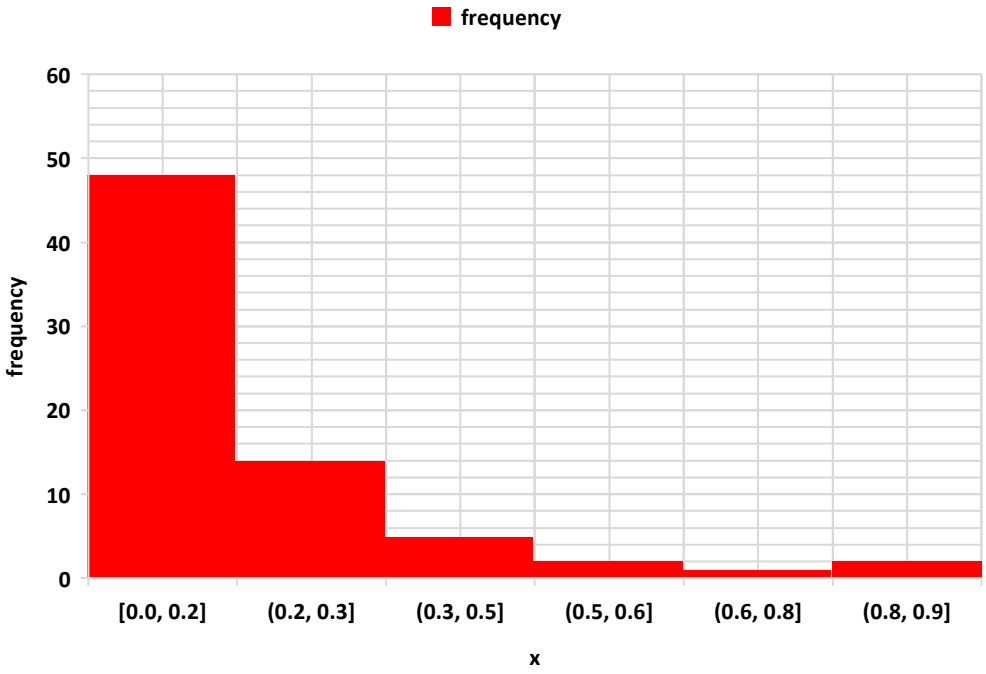


Fig. 6.20 Histogram of the error, *x*, for the experimental thermodynamic efficiency;
with respect to the simulated thermo-aerodynamical efficiency; a) Aluminium; b) Polymer PEEK-GF30.

$$x_i = \frac{\left|\eta_i^{test} - \eta_i^{sim}\right|}{\eta_i^{sim}} \tag{6.20}$$

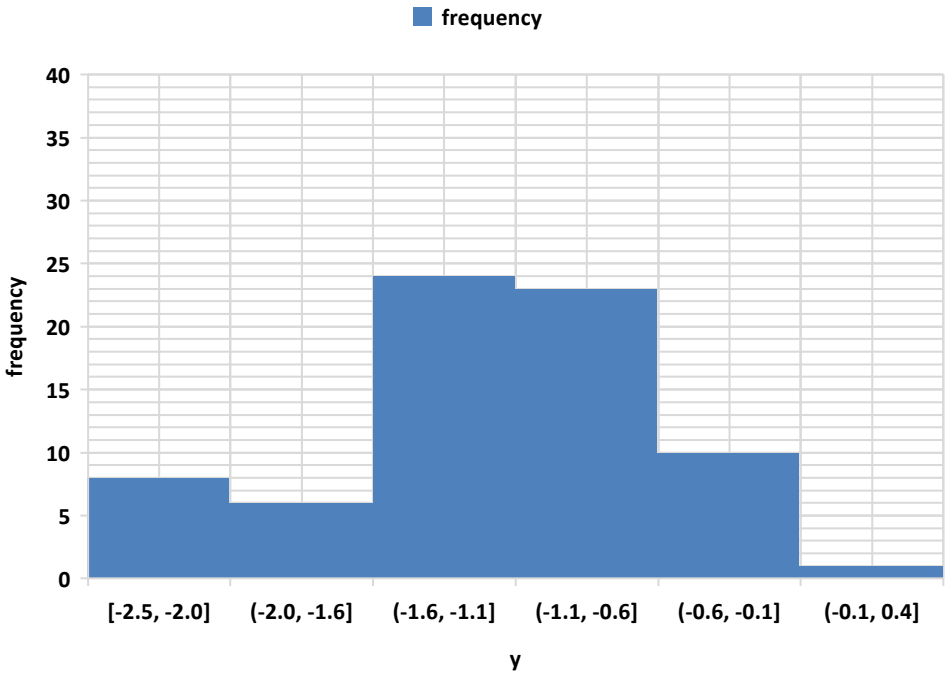
$$y_i = \log_{10} x_i \tag{6.21}$$

$$\bar{y} = \frac{\sum_{i=1}^{n} y_i}{n} \tag{6.22}$$

$$S_y = \sqrt{\frac{1}{n-1}\sum_{i=1}^{n}(y_i - \bar{y})^2} \tag{6.23}$$

Consequently, the samples must be normalised, using with Eqn.(6.21), to transform their distributions into normal alike distributions. With this transformation, the samples of the transformed error, y_i, can be treated as normal distributions that have a mean and a standard deviation, defined in Eqn.(6.22) and Eqn.(6.23) respectively. The histogram of the two normalised samples are presented in Fig. 6.21, where normal alike distributions can be seen.

a)



b)

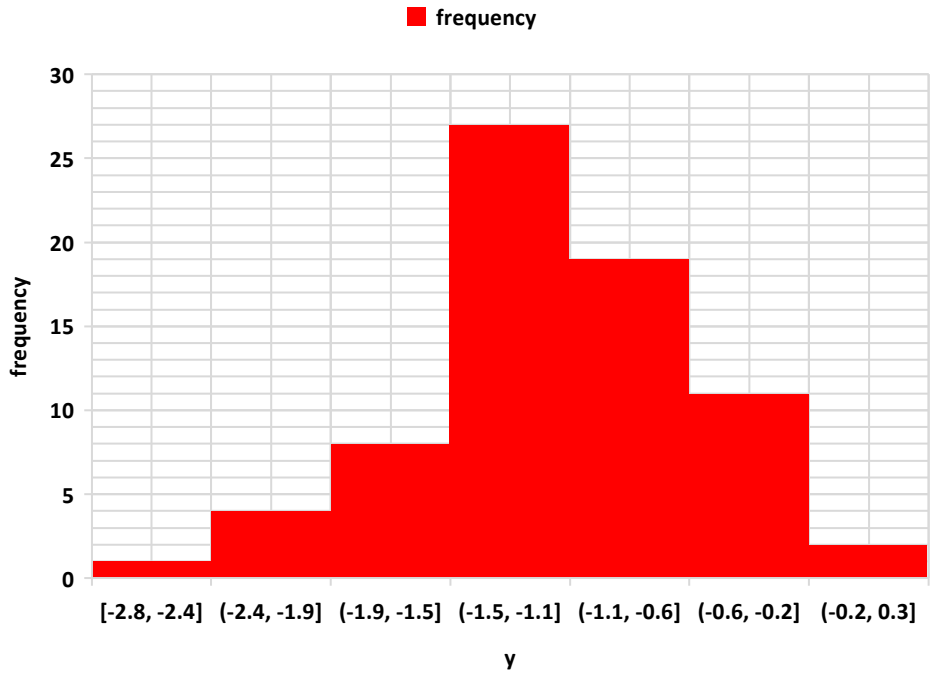


Fig. 6.21 Histogram of the normalised error, *y*, for the experimental thermodynamic efficiency;
with respect to the simulated thermo-aerodynamic efficiency; a) Aluminium; b) Polymer PEEK-GF30.

A summary of the descriptive statistics of these two samples is presented in Table 6.8, where the means and standard deviations of the two samples appear to be similar.

Their skewness seem very similar as well, though the negative sign reveals a slight skewness to positive values.

Table 6.8 Descriptive statistics of the normalised error of the two samples

Sample	Aluminium	Polymer
Mean	-1.16	-1.08
Standard Error	0.07	0.06
Median	-1.12	-1.10
Mode	-2.52	-1.51
Standard Deviation	0.57	0.53
Sample Variance	0.33	0.28
Kurtosis	0.36	0.77
Skewness	-0.58	-0.53
Range	2.48	2.75
Minimum	-2.52	-2.82
Maximum	-0.04	-0.07
Sum	-83.52	-77.83
Count	72	72

After normalization, the samples appear to be alike; however, the normality must be checked to assure that a normal statistical analysis is valid. Thus, a normality test using the Kolmogorov–Smirnov test (K-S test) [260] is performed. In this test, the cumulative probability function of the sample, FC, is compared with the corresponding theoretical cumulative probability of a normal distribution, FC_0, both having identical mean $\bar{y}$ and standard deviation S_y. Then the test difference, d, given by Eqn.(6.24), is compared with the critical difference, $d_{critical}$, given by Eqn.(6.25). If the test difference is lower or equal than the critical difference, Eqn.(6.26), the samples may be treated as normal, otherwise, they should not.

$$d = Max|FC(y) - FC_0(y)| \tag{6.24}$$

$$d_{critical}|@\alpha = 0.05, n > 35 \ = \frac{13.6}{\sqrt{n}} \tag{6.25}$$

$$d \leq d_{critical} \tag{6.26}$$

The results of the K-S a test are presented in Table 6.9 and Fig. 6.22, where it can be seen that both samples can be acceptably treated as normal distributions.

Table 6.9 Results of the K-S test of normality for the samples

	Aluminium	Polymer
d	0.102	0.072
$d_{critical}$	0.16	0.16
Normality	TRUE	TRUE

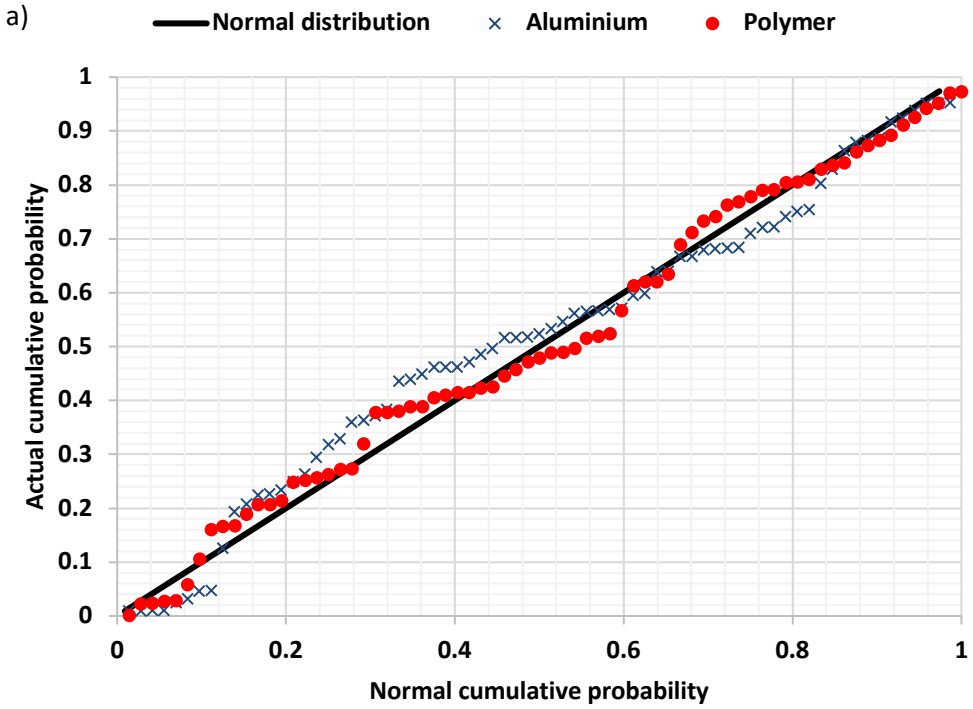


Fig. 6.22 Graphical comparison of the normalised error, y, and the normal standard distribution for the Kolmogorov–Smirnov [260] test of normality.

To assess whether the two samples can be considered statistically similar, two tests of hypothesis were performed: the test of means and the test of variances. These tests are performed with a statistical significance $\alpha = 0.05$.

In the test of means, the null hypothesis is that the mean of the normalised error with polymer components, $\bar{y}_{Poly}$, is statistically equal to the mean of the normalised error with aluminium components, $\bar{y}_{Al}$, as shown in Eqn.(6.27). Thus, the alternative hypothesis is that they are not equal, Eqn.(6.28). A two-tailed test was performed and, as the sample size is greater than 30, the normal standard distribution [261] is used. The test value, Z_n, is calculated with Eqn.(6.29) and the critical limits of the test, $Z_{n,min}$ and

$Z_{n,max}$, are given by Eqn.(6.30). The null hypothesis will be rejected if the condition defined in Eqn.(6.31) is not met.

$$Hypothesis_0: \bar{y}_{Poly} = \bar{y}_{Al} \tag{6.27}$$

$$Hypothesis_1: \bar{y}_{Poly} \neq \bar{y}_{Al} \tag{6.28}$$

$$Z_n = \frac{\bar{y}_{Poly} - \bar{y}_{Al}}{\sqrt{\frac{S^2_{y,Poly}}{n_{Poly}} + \frac{S^2_{y,Al}}{n_{Al}}}} \tag{6.29}$$

$$\begin{aligned} Z_{n,min} &= Norm.Standard.Inv.\left(\frac{\alpha}{2}\right) \\ Z_{n,max} &= Norm.Standard.Inv.\left(1 - \frac{\alpha}{2}\right) \end{aligned} \tag{6.30}$$

$$Z_{n,min} \leq \mathrm{Z} \leq Z_{n,max} \tag{6.31}$$

In the test of variances, the null hypothesis is that the ratio of variances of the normalised error with polymer components, $S^2_{y,Poly}$, over the variance of the normalised error with aluminium components, $S^2_{y,Al}$, is equal to the unity, Eqn.(6.32). The alternative hypothesis is thus that their ratio is different to the unity, Eqn.(6.33). A two-tailed test is performed and the Fisher distribution [261] is used. The test value, F, is given by Eqn.(6.34) and the critical limits of the test, F_{min} and F_{max}, are given by Eqn.(6.35). The null hypothesis will be rejected if the condition defined in Eqn.(6.36) is not met.

$$Hypothesis_0: \frac{S^2_{y,Poly}}{S^2_{y,Al}} = 1 \tag{6.32}$$

$$Hypothesis_1: \frac{S_{y,Poly}^2}{S_{y,Al}^2} \neq 1 \tag{6.33}$$

$$F = \frac{S_{y,Poly}^2}{S_{y,Al}^2} \tag{6.34}$$

$$\begin{aligned} F_{min} &= Fisher\left(\frac{\alpha}{2}, n_{Poly}, n_{Al}\right) \\ F_{max} &= Fisher\left(\frac{\alpha}{2}, n_{Poly}, n_{Al}\right) \end{aligned} \tag{6.35}$$

$$F_{min} \leq F \leq F_{max} \tag{6.36}$$

The results of the two test are presented in Table 6.10, which did not provide sufficient statistical evidence to reject the null hypotheses of the two tests, with a significance of $\alpha = 0.05$. Consequently, the thermo-aerodynamic performance of the polymeric components cannot be assumed different than the performance of the aluminium components.

Table 6.10 Results of the statistical comparison

Test	Mean	Test	Variance
α	0.05	α	0.05
Z_n	0.85	F	0.84
$Z_{n,min}$	-1.96	F_{min}	0.63
$Z_{n,max}$	1.96	F_{min}	1.12
H_0	TRUE	H_0	TRUE
H_1	FALSE	H_1	FALSE

CHAPTER 7. DISCUSSION

7.1. PREDICTION OF THE PERFORMANCE FOR AN ORC

Once a better agreement of the simulation program and the test had been achieved, the performance of the MTG working with the refrigerant R245fa can be predicted. The performance of turbomachines may be similar if they have geometric and dynamic similarity; as explained by Dixon and Hall [240] and implemented by Zhang et.al [262] and White and Sayma [196]. In this investigation, the geometry of the turbine does not change; thus, the flow can be considered dynamically similar for identical values of the flow coefficient ϕ and $\sqrt{2\psi}$. Accordingly, as shown in Eqn.(7.1), the aerodynamic efficiency should be comparable in different scenarios, working with, for example, different working fluid if the flow coefficient ϕ and $\sqrt{2\psi}$ are identical. Consequently, the rotational speed, the mass flow rate and the power can be derived from the dimensionless parameters and the geometry of the unit if dynamic similarity is achieved.

$$\eta_{aero}^{real-R245fa} \cong \eta_{aero}^{ideal-R245fa} \cong \eta_{aero}^{air} = f(\phi, \sqrt{2\psi}) \tag{7.1}$$

A prediction of the performance with a refrigerant can be achieved through simulations. However, the validation shows that in some cases the mean error between the test and the simulation can be as large as 8%. In these cases, the confidence of the prediction may be increased if an equivalent experimental prediction is given. Accordingly, two predictions of the performance with refrigerant are given; the first based on the simulation program and the second based on the air test**.**

In accordance with the simulation program, the maximum thermo-aerodynamic efficiency can be achieved with a flow coefficient $\phi = 0.3$ and squared loading coefficient $\sqrt{2\psi} = 1.52$. The MTG operating with R245fa in dynamic similarity should achieve identical values for those parameters. For example, for a specific enthalpy drop of Δh_{0s}=8.4[kJ/kg] as proposed by Hernandez-Carrillo et al. [25], the rotational speed would be $\omega = 33200$[rpm], the mass flowrate $\dot{m}$=0.22[kg/s], the aerodynamic efficiency $\eta_{aero} = 0.7$ and the aerodynamic power $\dot{W}_{aero}$=1.3[kW].

According to the test, the maximum thermodynamic efficiency corresponds to a flow coefficient $\phi = 0.3$ and a squared loading coefficient $\sqrt{2\psi} = 1.67$. Therefore, for a specific enthalpy drop of Δh_{0s}=8.4[kJ/kg], the unit would achieve the aforementioned parameters with a rotational speed of $\omega = 30100[\text{rpm}]$, a mass flow rate of $\dot{m}$=0.2[kg/s] and an aerodynamic power of $\dot{W}_{aero}$=1.2[kW].

7.2. ASSESSMENT OF THE IMPROVEMENT

In this investigation, the MTG-ORC showed the ability to operate, in a safe manner, at the high rotational speed required for the proposed application and with sufficient power to satisfy, the demand of an average single-family household. Its maximum thermo-aerodynamic efficiency appears to be around 0.7, which is within the range of efficiency (0.35-0.8) reported by other investigations [263] with similar capacities and applications. Therefore, such a device can be a good option of expander for domestic ORC cogeneration systems. However, the polymeric components of this prototype are yet to be tested with refrigerant to confirm their capabilities in terms of reliability and performance.

7.2.1. Feasibility of features

Additionally, this investigation, helped to assess the feasibility of several of the features proposed for the MTG-ORC as described below.

The impeller

The polymeric impeller withstood rotational speeds of up to $\omega = 40500[\text{rpm}]$. This is 13% above the nominal rotational speed of $\omega = 36000[\text{rpm}]$ [25] but is 11% lower than the maximum allowed rotational speed $\omega = 45720[\text{rpm}]$, which was defined as 127% of the rated rotational speed with reference on the standard ISO10437 [243]. Although the maximum rotational speed has not been tested yet, the MTG-ORC appears to be capable to withstand such a rotational speed with the polymeric impeller as demonstrated by simulations and calculations.

In section 4.4., the maximum service temperature and the glass transition temperature of PEEK-GF30 are reported to be $T_s = 522[\text{K}]$ and $T_g = 425[\text{K}]$ respectively. However, it should be noted that the maximum service temperature is

higher than the glass transition temperature. Additionally, considering that the material changes from a hard and brittle structure to a rubbery structure at the glass transition temperature, an undesired change which could affect the integrity of the impellor. Then, the maximum operational temperature of the impeller must remain under the glass transition temperature of the polymer.

The bending moment on the impeller blades is driven by the differential pressure between the pressure face and the suction face of the blade. This differential pressure is expected to be greater for the actual application than it is in the experiment with air. However, for a given power, the torque is considerably lower if the rotational speed is high; thus, the bending moment may not have a critical influence on the stress of the blades [25]. Then, a reasonably greater differential pressure should not compromise the structural integrity of the impeller.

Additionally, according to section 5.3, PEEK-GF30 appears to be chemically compatible with R245fa and the alternative refrigerants R134a, R1233zd, R1224yd, R1234yf and R12324ze. Thus, chemically, the impeller made of PEEK-GF30 seems to be suitable for the application discussed in this work, though the design should be reconfirmed if any of the other working fluids is selected.

Until now, the impeller has performed acceptably from the thermodynamic, aerodynamic, structural and chemical perspective. Therefore, the evidence to this point suggests that PEEK-GF30 can be considered a suitable candidate for replacing aluminium and can be used to fabricate the impeller of the MTG-ORC. Nevertheless, important aspects such as fatigue of the blades must be addressed before absolute confirmation can be given.

The nozzles body

The nozzle body, made of 3-D printed PET-G, performed well whilst tested with air and the finishing of the surface formed an adequate flow pattern, which allowed the MTG-ORC to achieve a good efficiency. However, the nozzle body is a static element whose principal mechanical load is the differential pressure across itself. Then, when exposed to a greater expansion or a fluid with a higher molecular weight, such as a refrigerant, the stress on the blades can be considerably higher, which may have a

considerable influence on the structural integrity of the nozzle body. Furthermore, the study of chemical compatibility, section 5.3, revealed a clear incompatibility of PET-G with the studied working fluids, even though Table 4.5 suggested that PET-G should be compatible with R134a, R1234yf and R1234ze. Moreover, the unresolved issues of the impeller in terms of fatigue should also be addressed for the nozzle body. Consequently, a comprehensive study to examine the ability of the PET-G to withstand the real conditions must be performed in further investigations or, alternatively, the nozzle body can be fabricated with PEEK-GF30 or another material with a comparable mechanical performance.

The two above-mentioned elements were fabricated with traditional machining and 3-D printing but in high volume production, they would be more effectively fabricated with plastic injection. This technique would allow changing the raw material with minimal differences in the fabrication process. Therefore, the components of the MTG-ORC can be made of a wide variety of polymers, for instance, PPS, Nylon, Polycarbonate and their composite derivates. This flexibility on the fabrication could make the use of polymers effective and customizable. Additionally, the 3-D printing technique can promote the fast optimization of components, which in the case of the rotor, can result in the minimization of centrifugal forces if the mass can be further reduced, by for example making hollow rotors.

The generator

The adapted generator performed well at high speeds. The expected voltage per phase, at the design frequency $f = 600$[Hz], was $V_{rms} = 224$[V], which is comparable with the three-phase domestic utility voltage of several countries. However, as the frequency is unconventional and variable, a power converter is needed for standardising the frequency. The maximum current was estimated to be 25% lower than the nominal current of the windings, which can reduce the electrical losses and hence the cooling needs.

The control

According to the analysis presented in section 4.7 and the experience gained during the test, the limited expansion control should be feasible if appropriate hardware is

implemented. However, such a control could not be experimentally validated due to several technical difficulties with the valve used for the test as described below.

For the test, the preliminary array of the inlet pressure regulation shown in Fig. 7.1 was installed upstream of the MTG-ORC inlet. Unfortunately, the sensitivity of the valve used, which is a turbocharger wastegate, did not allow a precise control of the pressure. This became problematic because although the activation pressure of the valve is adjustable, the lowest activation pressure was found to be 50[kPa], which is higher than the range of inlet pressures in the test (0[kPa] to 20[kPa]). Then, the wastegate was latterly disabled and a conventional air pressure regulator had to be used to control the inlet pressure during the test, which disturbed the upstream conditions. Therefore, the feasibility of the limited expansion control of the speed is yet to be validated at the laboratory.

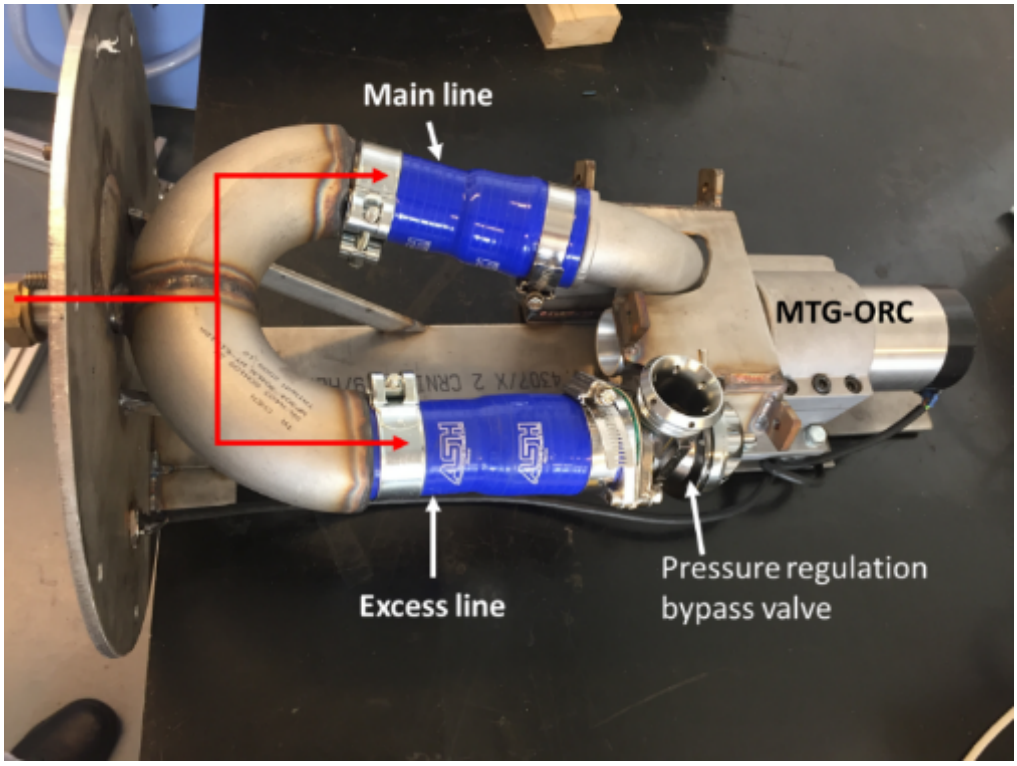


Fig. 7.1 Schematic of the proposed speed control with a bypass valve.

The outer enclosure

The outer enclosure described in section 4.8 had two purposes: leak prevention and burst containment, however, neither of these functionalities were experimentally validated. Leak prevention was not validated because the test was performed with the

outer enclosure at atmospheric pressure; thus, no differential pressure existed and hence no leaks.

Burst protection was not validated because bursting of the MTG-ORC would be a destructive test that could potentially destroy the prototype, which would have been unacceptable at this time of the research. However, the testing of the two above-mentioned functionalities is required for assessing their feasibility, advantages and shortcomings, though a number of destructive and non-destructive tests can be required, which can be conducted when more time and resources become available.

7.2.2. Technical improvement

This study proposes the use of plastic components into an MTG-ORC and several technical advantages arise from this advancement, namely, the potential of production cost reduction, the adoption of alternative manufacturing techniques and the deployment of a large-scale production. The replacement of metals with polymers can contribute to improving the MTG-ORC in terms of chemical resistance, minimising unbalance, reducing shaft fatigue and protection against impeller burst as explained below.

The reduction in weight is arguably the most important as it is an attractive feature in dynamic elements. In the case of the impeller, the implementation of a low-density material promotes an agile response of the rotor and reduces the centrifugal forces in the wheel. The reduction of centrifugal forces also benefits the structural integrity, which can extend the lifespan of the blades. Additionally, the adoption of a low-density material may also reduce the unbalance due to manufacturing defects.

A light impeller also reduces the requirements of protection against burst of the rotor. The protection against burst is important but it becomes critical for domestic applications, where safety is paramount. Moreover, a low inertia rotor could also mean longer lifespan of bearings, which are also vital components of the MTG-ORC.

Furthermore, further benefits can be obtained from the implementation of polymeric components because they can be fabricated with a good dimensional stability, tight tolerances, reduced unbalance, and low post-processing needs.

On the other hand, potential limitations of the plastic components with respect of their metal counterparts must also be recognised. These may include a shorter lifespan and erosion. The latter can happen when the components are exposed to a high-speed stream containing impurities. Additionally a narrower range of application may also be a limitation because most polymers have a limited service temperature, though PEEK-GF30 and Aluminium have comparable service temperature.

7.2.3. Economic improvement

Another attractive characteristic of the adoption of polymers is the potential reduction of the production cost of components. The production of metal components is costly, time-consuming and often labour intensive. Therefore, if polymers can effectively replace metals, the cost production of several components can be significantly reduced as experienced in other industries [19] where reductions of 20-50% have taken place.

The impeller, for example, would ordinarily be machined from a piece of metal, which would take considerable time, labour and sophisticated equipment. In contrast, the production of a polymeric impeller through moulding can be a fast process and can drive a reduction of cost. While is true that raw polymers can be more expensive than raw metals, the reduced cost of a polymeric impeller may lie on the reduced labour, energy and time during manufacturing. If polymeric impellers can be fabricated with moulding, a number of advantages can be achieved, namely, cost, tight tolerances, good finishing, and reduced fabrication time. All of these characteristics are beneficial for the assurance of quality and, specifically, tight tolerances drive a reduction of post-processing, which makes the fabrication process leaner.

Several other components of the MTG-ORC, apart from the impeller and the nozzle body, can be made of structural polymers. These elements can include the turbine volute, the outer enclosure, the generator body, transition pieces, seals, nuts and bolts amongst others. If metals are replaced with polymers in these components, a compact and easy to fabricate MTG-ORC may be achieved.

A compact and easy to fabricate MTG-ORC would be particularly attractive in applications where a reduced footprint and/or portability are driving requirements. The

domestic cogeneration and the power conversion from waste heat of combustion engines are good examples of this, with the latter requiring portable and cost-effective ORC systems to convert waste heat to useful power.

The real impact on the economy of the production of the MTG-ORC is difficult to quantify precisely at this early stage of the development. This is because only one prototype has been fabricated so far and large scale production has not been achieved. However, to provide an early insight, the direct cost to fabricate the prototype was estimated and a prediction of the probable costs of future production is given based on the experience curve of the fabrication of such a prototype.

The estimated direct production cost of the prototype is 3,100[£], of which 58% consisted of outsourced components, 14% labour, 6% raw materials, 16% equipment, and 6% assembly. Evidently, a major fraction of the cost was dedicated to outsourced components because the unit was conceived to allocate several standard components. In terms of internal elements, the direct cost encompassed 37% for the turbine, 15% for the generator, 6% for the enclosure, 6% for consumables, 9% for piping and valves, 2% for other consumables and 24% for the control. Clearly, the turbine is the most expensive element because it includes turbine components as well as the bearings and the shaft, which are also components of the generator.

The prediction of the future direct costs of production was made using the direct cost of the prototype, per component, and an experience curve [264] per component. An experience curve assumes that the cost of performing a specific task, in this case, the fabrication of individual components, decreases in a fixed rate every time the accumulative production is doubled. Thus, the future direct cost per component, C_i^f, can be calculated with Eqn.(7.2), which is a function of the current direct cost of production per component, C_i^0, the future cumulative production per component, P_i^f, the current cumulative production per component, P_i^0, and the constant of elasticity of the direct cost per component a_i. Since the cost per component would experience a fairly constant reduction of cost, r_{cs}, every time the cumulative production is doubled, the constant of elasticity of cost per component would be given by Eqn.(7.3) and the total future direct cost per unit, C_u, would be given by Eqn.(7.4).

$$C_i^f = C_i^0 \left(\frac{P_i^f}{P_i^0} \right)^{-a_i} \tag{7.2}$$

$$a = \frac{Ln(1 - r_{cs})}{Ln(2)} \tag{7.3}$$

$$C_u = \sum_i C_i^f \tag{7.4}$$

In this prediction, the cost reduction rates per component were assumed: turbine 20%, generator 20%, control 5%, enclosure 20%, consumables 10%, P&I 15% and others 5%. To select these rates, the author assumed 20% as the baseline and considered, qualitatively, a degree of uncertainty in the direct cost of components to reduce the rates. This means that a lower rate was given if a great uncertainty of the direct cost is identified. However, these rates can be updated in future investigations to improve the accuracy of the projections. The results are shown in Fig. 7.2, where it can be observed that the direct cost could drop under 1,000[£] per unit when the cumulative production reaches 200 units; however, a production of over 1,000,000 would be needed to reduce the direct cost to 350[£] per unit, which may be a reasonable goal for commercial purposes.

The aforementioned prediction considers only the direct costs with the indirect cost yet to be considered. Additionally, the prediction assumes that the fabrication methods and materials are similar regardless of cumulative production. However, CNC machining and 3D printing were used for the fabrication of the prototype, which are considerably more expensive than plastic moulding, which would be used on a full-scale production. Thus, the actual direct production cost per unit can be lower than predicted, though a more accurate prediction cannot be made at this stage of the investigation. Furthermore, in a full-scale production, the fraction of outsourced components can be reduced as in-house fabricated components can be considerably cheaper, the production cost can be even lower.

According to literature [15, 17, 39, 265], to be economically attractive, the capital cost of an ORC plant should be in the range 2000[£/kW]-3000[£/kW] and, according to section 1.1 of this thesis, the expander may account for 40%-70% of this. Therefore if the direct cost of the expander is considered in the range 30%-50% of the total capital cost of the ORC, the marginal direct cost of the MTG-ORC would be in the range 240[£/kW]-1050[£/kW], which can be compared with a current benchmark cost of micro-capacity turbines. According to Fig. 7.2, the upper limit is achievable with the production of a few hundred units but the lower limit would require the cumulative production to be as large as 50 million units, which for domestic waste heat recovery in the United Kingdom is not realistic. In any case, this early economic evaluation still has a significant degree uncertainty; thus, to confidently predict the economical enhancement of the MTG-ORC proposed in this work, a more precise estimation of costs should be performed when accurate information becomes available.

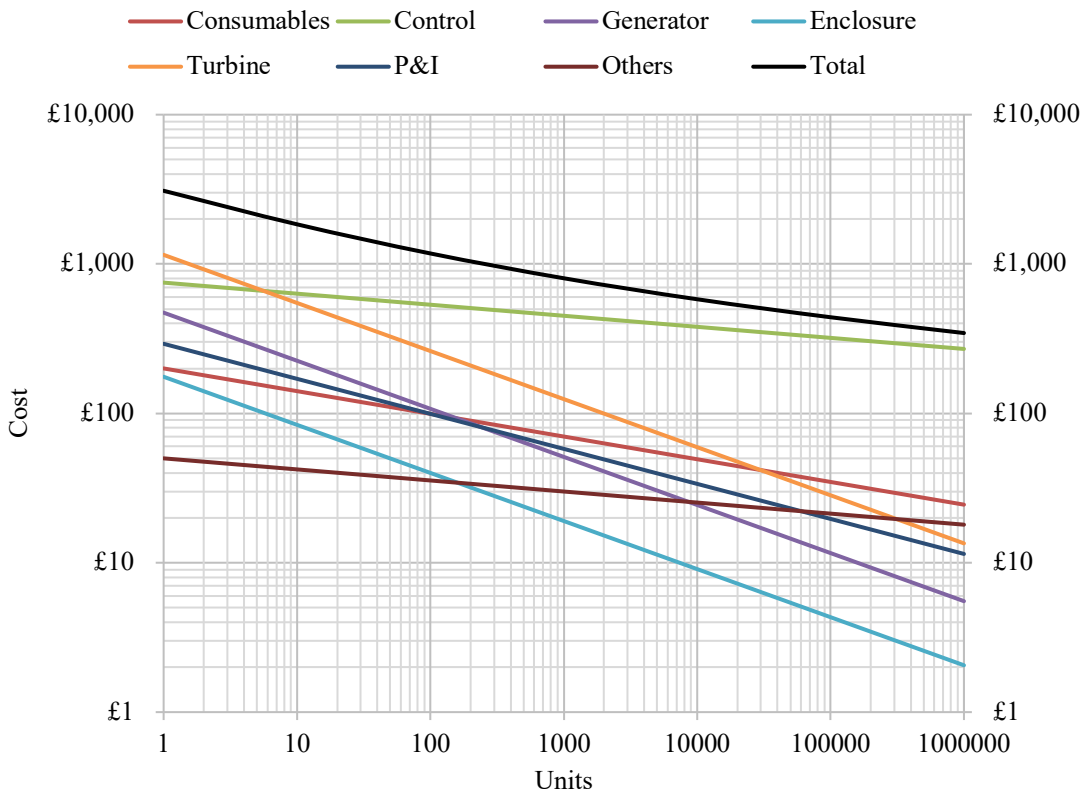


Fig. 7.2 Prediction of the production cost per unit.

7.2.4. Structural polymers beyond the MTG-ORC

Elastomers and fluoropolymers are common materials in the ORC and refrigeration industries, which are typically used for sealing and gasketing. However, even though they have a huge potential, the application of polymers for structural purposes is scarce. The polymeric components proposed in this investigation have shown suitability for a low temperature MTG-ORC. This can break the paradigm of exclusiveness of metals in these components and other elements, as structural polymers can be adopted in diverse elements such as piping, vessels, valves, pumps, heat exchangers and compressors.

In the chemical industry, structural polymers are considered state-of -the-art materials for piping, vessels and pumps since several thermoplastics and thermosets are employed [266-269]. Specifically, in refrigeration [270-272], some thermoplastics such as PEEK and PET have been successfully tested for conveyance lines and other piping for the conduction of refrigerants (R12, R134a and R22). In valves for the natural gas and chemical industries, structural polymers are commonly employed to make bodies, bonnets, and O-rings, though their application in refrigeration and ORC is scarcely documented. Heat exchangers made of polymers such as PEEK and PET, have showed a performance comparable with their metal counterparts in refrigeration [273, 274] and ORC [275] applications.

Conversely, the use of structural polymers in dynamic components such as compressors and expanders seems to be less common and only a small number of works can be found in literature. The most common use of structural polymers seems to be in bearings [276-281], due to the good tribological properties of polymers like PTFE and PEEK, though polymeric seals [282, 283], seem to become popular.

In fact, structural polymers can be used in a number of components of expanders and compressors such as impellers and volutes. In turbomachinery, centrifugal compressors made of PEEK and Epoxy resin have been proposed for refrigeration [284, 285] and have a long history for other compression applications such as turbocharging of combustion engines [286], other gas compression [215] and steam turbines [287]. Furthermore, PEEK and other polymers have been proposed for the volutes of scroll compressors [288], though their performance may not be comparable with their metal counterpart. Lastly, recent investigations reveal an increasing interest of the scientific

community in adopting additive manufacturing for the development of functional prototypes of turbomachinery using polymeric components [25, 173, 174, 289]. This may have an enormous impact in the agility of the deployment of new technology in areas like energy, aerospace, automotive, ORC systems and refrigeration.

7.3. CONTRIBUTION TO THE KNOWLEDGE RESEARCH IN THE FIELD.

This work can provide a contribution to the development of a new generation of low-capacity ORC expanders as the findings arising in this work may have an impact on the technical performance and economy of expanders as explained below.

7.3.1. Technical relevance

The successful implementation of structural polymers may set a milestone in the evolution of low-capacity ORC expanders as it may disrupt the exclusiveness of metals in this field. Although polymers are common in ORC for sealing and gasketing, for structural purposes their application is scarce even though they have a significant potential. The characteristic low temperature of ORC enables the implementation of structural polymers, which represents some technical and economic advantages such as lightness and simplicity of production. Among the technical advances of implementing structural polymers, reduction in weight is probably the most important as low mass is a very attractive feature. In fact, light, compact, and easy to manufacture components are particularly attractive in applications where a reduced footprint and/or portability are strong requirements. The low capacity power systems are a good example of this because they demand not only reliable and cost-effective components but also compact.

Turbomachinery is one of the technological options where structural polymers can be successfully implemented. Turbomachines do not have wear contact between moving and static components (other than the bearings); thus, polymers may be suitable for turbomachinery and might not be suitable for other type of expander unless strongly wear resistant polymers are used. Unlike most of the volumetric expanders, turbines can handle a broad range of expansion ratios with high efficiency. This is of particular interest for the exploitation of low-temperature resources, where a narrow temperature difference results in a small expansion ratio, though the capacity can be increased with an increment of the flow rate.

Turbines can be controlled by regulating the expansion of the fluid, which would eliminate the need for a governor and makes the control considerably simpler. Standard elements from the refrigeration industry can be adopted to achieve control of the expansion; this can reduce the cost and the development timeline.

7.3.2. Economic relevance

A reduction in the production cost of expanders, without a significant reduction on their technical performance, could have a direct impact on the economy of distributed power systems of the ORC type. The levelised cost of energy is very sensitive to changes on the upfront cost of the plant in applications of waste heat and renewable energy where the fuel cost is not significant. Thus, a techno-economically enhanced micro-turbine may produce a reduction in the cost of the ORC plant, which would directly benefit the levelised cost of the energy. However, although a reduction of cost is an attractive feature, the reliability, performance and lifespan must not be overlooked and the suitability of polymers, for structural purposes, into ORC elements must be carefully evaluated before their implementation is recommended. An exhaustive evaluation of the thermo-dynamical, mechanical, and chemical response of proposed polymers under the relevant environment is critical.

7.3.3. Beyond the organic Rankine cycle

The advances presented in this work, in regards of the use of structural polymers, may attract industrial interest in the adoption of polymers in other various elements of ORC and refrigeration systems of comparable capacity. The elements where polymers can be adopted include tanks, pipes, heat exchangers, pumps, and valves, among others.

CHAPTER 8. CONCLUSIONS AND FUTURE WORK

The aim of this investigation was to address the key research question 'How can the overall performance of a micro-capacity ORC expander be improved?'. A number of specific research tasks, including thorough literature review, analysis of theory and methods, design, analysis, fabrication and testing and discussion were carried out to achieve this research aim.

8.1. CONCLUSIONS

The following conclusions can be drawn from the investigation:

1. The literature review revealed the points given below.
   1.1. The organic Rankine cycle (ORC) is advantageous for converting low-grade heat.
   1.2. Although the selection of the working fluid is critical, lack of general agreement exists on this subject in the academic community.
   1.3. R245fa and R134a are the most popular working fluids in experimental works, R1224yd, R1233zd, R1234yf and R1234ze are modern alternatives.
   1.4. Volumetric expanders dominate the micro-capacity range despite microturbines are advantageous. Research is needed to confirm micro-turbines as a valid option.
   1.5. Experimental work is scarce in this field, mainly because the equipment and facilities required are expensive. Experimentally, efficiency of 0.7 and rotational speeds of up to 200,000[rpm] are achievable with moderate resources.
   1.6. Traditional methods for studying turbines cannot be generalized. However, a preliminary design can be achieved if the working fluid can be reasonably idealised in the interval of interest.
   1.7. Polymers can be a valid option of material for structural components in ORC turbines (nozzles and blades) but further investigation is urgently needed to conclude about their applicability.
2. The study of the theory revealed the points below.
   2.1. The theory of turbines is of general applicability and the traditional methods can be adapted to consider the change of working fluids.

2.2. The principle of dynamic similarity is of general applicability if the thermophysical properties of substances are accurate.

2.3. The product design method can be used to develop human-made artefacts because is methodologically analogous to the scientific method.

2.4. The most critical task to address the research question is the exploration of the problem (need).

3. The conclusions arising from the design are given below.

3.1. The implementation of polymers in structural components of the micro-scale ORCs is the major advancement in this research. Several polymers can be used. PEEK-GF30 and PET are convenient and hence selected.

3.2. The mean-line approach allows a fast preliminary design of a turbine. ANSYS® Vista RTDTM 16.2 provided a reasonably efficient design, but this may have not be the case if the working fluid could not be idealised.

3.3. The performance in off-design conditions cannot be predicted with the aforementioned software. Thus, a custom-made software is necessary.

3.4. Software for the three-dimensional design is necessary for prototyping purposes. ANSYS® BladeModeler™ performs well for this.

3.5. A standard shaft from a spindle motor did not meet the requirements. Thus, a custom shaft was required. A simple shaft can work for basic testing but a robust shaft is needed for intensive testing.

3.6. A standard volute can be adopted from a turbocharger to save time and resources but leaking must be resolved. The use of a nozzle-less volute is possible with a narrow range of high efficiency.

3.7. A basic high-speed permanent magnet generator can be designed and built from an adapted motor spindle. This device can work for basic testing but a standard high speed generator is needed for intensive testing.

3.8. Theoretically, the unit can be controlled with limited expansion but this function must be experimentally validated.

3.9. Semi-automatic control is acceptable for basic testing but automatic control of the unit is required for intensive testing. This control must include an over-speed trip and loading-speed control.

3.10. The outer enclosure can eliminate leaks and act as a barrier against burst. This feature must be validated experimentally.

4. The analysis of the unit highlighted the below conclusions.
   4.1. The accuracy of the developed program to predict the performance is reasonable.
   4.2. The dimensionless results of the simulations with air, ideal-R245fa and R245fa can be considered with a difference of the efficiency under 10%. Therefore, the dynamic similarity can be achieved.
   4.3. The principal mechanical loading in the impeller is the centrifugal force; PEEK-GF30 and ABS adequately withstand this mechanical loading. In fact, PEEK-GF30 can be stronger than Aluminium, which is the reference material.
   4.4. PEEK-GF30 is compatible with R134a, R245fa, R1233zd, R1224yd, R1234yf and R1234z whereas PET-G is compatible with none of them. This latter conclusion seems to disagree with the literature that suggests that PET can be compatible with R134a, R1234yf and R1234ze. The reason for this disagreement can be the glycol modification of PET.
5. The Manufacture and test provided the following conclusions.
   5.1. The fabrication of an MTG is possible with conventional tools, and skilled technicians if several standard components are adopted from turbochargers and/or high-speed motors.
   5.2. A polymeric nozzle body can be made of 3D printed PET-G, though it should be made of PEEK-GF30 or another chemically compatible material. The impeller of PEEK-GF30 can be made with CNC machining.
   5.3. The configuration of test rig and the procedures for the air test were simple and effective, though hermeticity must be ensured if refrigerant is used.
   5.4. The accuracy of the used instruments is acceptable for basic testing but it should be enhanced for intensive testing. Special observance should be given to the accuracy of the thermometers and the flowmeter as they are important contributor to error.
   5.5. The impeller, made of PEEK-GF30, withstood the centrifugal forces at a rotational speed of 32040[rpm] and a peak rotational speed of 40500[rpm], which is an indicator of good structural integrity. The 3-D printed nozzle body had an acceptable surface finishing and allowed the achieved thermo-aerodynamic efficiency of 0.7.

5.6. The generator achieved a maximum voltage of 200[V] at 534[Hz], however, a power converter is required to covert the output signal to a standard frequency.

5.7. The results of the air test have good agreement with the simulations after the main sources of deviation were addressed (determination of mechanical losses and leaking).

5.8. The thermodynamic efficiency showed an agreement with the simulation with an $RMSE \leq 0.1$.

5.9. The prediction was made with two methods. The first, based on the simulation program, estimated an efficiency of 0.7 and a power of 1.3[kW]. The second, based on the air test, showed an efficiency of 0.71 and an aerodynamic power of 1.2[kW]. Both are in agreement

5.10. The performance of the MTG with polymeric components was compared with the unit with aluminium components. The results did not reveal a difference with a statistical significance of p=0.05.

6. The discussion provided the below conclusions.
   6.1. The adoption of polymers into an MTG is a feasible and a noticeable improvement is foreseen in terms of weight and economy, though the lifespan is an issue to be addressed.
   6.2. The components that can be made of polymers include nozzle body and the impeller as well as casing, bearings, body and generator; and other elements of ORC and refrigeration systems, e.g. pumps, valves, piping, etc.
   6.3. The fabrication of polymeric components can be simpler and faster with respect to their metal counterparts, which could result in a cheaper full-scale production. Their performance can be comparable with their aluminium counterparts.
   6.4. An accurate economic assessment cannot be done at this stage of the research.

Finally, with the evidence to date it can be concluded that, the MTG developed in this investigation can be a feasible option of expander into an ORC type WHP system , though further research and development is needed to bring the concept to a greater technology readiness level.

8.2. FUTURE WORK

The investigation presented in this thesis, developed the concept of a simplified MTG-ORC from the concept to the preliminary laboratory test in simulated conditions. Although the results of this investigation suggest that the proposed MTG-OC can be a feasible option of expander for distributed power systems of the ORC type, the maturity of the technology is still low. Therefore, further stages of this research should be conducted to bring the technology to a greater maturity. The specific recommended tasks are given below.

- **Test of the components in real conditions.** The two components proposed in this work were tested using air, which is a simulated working fluid. However, to validate the feasibility of the implementation of these components, the test should be performed with the relevant working fluid, which is R245fa. If this test is accomplished and the full operation conditions of the MTG-ORC are reached, the feasibility of the proposed components would be validated and hence recommended for further development or production.
- **Experimental validation of the outer enclosure.** The outer enclosure represents an important component of the MTG-ORC in terms of performance and safety. However, for the particular characteristics of this investigation, this component was implemented but could not be fully tested. Therefore, a full test of the outer enclosure should be conducted, which should include a hermeticity test, a hydrostatic test and a burst containment test. The latter of these tests would be destructive and hence might require considerable resources to be expended.
- **Experimental validation of the limited expansion control.** The control of the unit is a critical aspect to be addressed and, although the limited expansion control seems to be advantageous, it is not strictly needed as other type of control can be used. Nevertheless, if possible, the experimental validation of the limited expansion control is recommended because it has the potential to considerably simplify the control system and hence the production and operation costs of the MTG-ORC.

- **Long-lasting test.** The air test aimed to assess the thermo-aerodynamic performance and the structural integrity of the unit with an experimental approach. However, as this was a short test (less than 2 hours per trial), the test did not provide evidence to conclude the resistance to fatigue or the potential lifespan of the unit. For these purposes, a long-lasting test should be performed, in which a long period of testing allows the identification of the effect of cyclic stresses as well as the lifespan of the bearings and polymeric components.
- **Research on bearings.** In this investigation, high speed hybrid ball bearings were used, which were lubricated with high speed grease to avoid the need of an additional lubrication system. However, the lifespan of the bearings is limited due to such a high speed and limited lubrication. Although this was not an issue for a short test, in a longer lasting test and the actual application, the limited life of the bearings may become a considerable issue that can be addressed beforehand. At this stage of the research it cannot be concluded whether the life of the proposed bearings would be sufficient for the actual application until a long-lasting test is conducted.
- **Pilot production**. If the aforementioned research is conducted with successful results, the production of a small batch of components would allow for a much more accurate prediction of the costs of larger scale production proposed in this work.

REFERENCES

1. Forman, C., et al., *Estimating the global waste heat potential*. Renewable and Sustainable Energy Reviews, 2016. **57**: p. 1568-1579.

2. Laboratory;, L.L.N. and D.o. Energy;, *Estimated U.S Energy Consumption in 2017: 97.7 Quads*. 2017, Lawrence Livermore National Laboratory: USA.

3. Liu, H., Y. Shao, and J. Li, *A biomass-fired micro-scale CHP system with organic Rankine cycle (ORC) – Thermodynamic modelling studies*. Biomass and Bioenergy, 2011. **35**(9): p. 3985-3994.

4. Moharamian, A., et al., *Thermodynamic analysis of a wall mounted gas boiler with an organic Rankine cycle and hydrogen production unit*. Energy & Environment, 2017. **28**(7): p. 725-743.

5. Macchi, E. and M. Astolfi, *18.1 Requirements and Main Features of Domestic Organic Rankine Cycle Systems*, in *Organic Rankine Cycle (ORC) Power Systems - Technologies and Applications*. Elsevier.

6. Vélez, F., et al., *A technical, economical and market review of organic Rankine cycles for the conversion of low-grade heat for power generation*. Renewable and Sustainable Energy Reviews, 2012. **16**(6): p. 4175-4189.

7. Tchanche, B.F., et al., *Low-grade heat conversion into power using organic Rankine cycles – A review of various applications*. Renewable and Sustainable Energy Reviews, 2011. **15**(8): p. 3963-3979.

8. Dai, C. and V. Chen. *Classification of shallow and deep geothermal energy*. in *Geothermal Resources Council Annual Meeting 2008: "Geothermal - Gaining Steam"*. 2008. Reno, NV.

9. Stefansson, V. *World geothermal assessment*. in *Proceedings world geothermal congress*. 2005.

10. Waring, G.A., R.R. revised by Blankenship, and R. Bentall, *Thermal springs of the United States and other countries of the world; a summary*, in *Professional Paper*. 1965.

11. Heimiller, D., *Solar Resources by Class and Country*, National Renewable Energy Laboratory, Editor. 2014, U.S. Departament of Energy: United States.

12. Pepermans, G., et al., *Distributed generation: definition, benefits and issues*. Energy Policy, 2005. **33**(6): p. 787-798.

13. Ackermann, T., G. Andersson, and L. Söder, *Distributed generation: a definition1In addition to this paper, a working paper entitled 'Distributed power generation in a deregulated market environment' is available. The aim of this working paper is to start a discussion regarding different aspects of distributed generation. This working paper can be obtained from one of the authors, Thomas Ackermann.1*. Electric Power Systems Research, 2001. **57**(3): p. 195-204.

14. Bracco, R., et al., *18 - Micro-Organic Rankine Cycle systems for domestic cogeneration*, in *Organic Rankine Cycle (ORC) Power Systems*, E. Macchi and M. Astolfi, Editors. 2017, Woodhead Publishing. p. 637-668.

15. Preißinger, M. and D. Brüggemann, *Thermoeconomic Evaluation of Modular Organic Rankine Cycles for Waste Heat Recovery over a Broad Range of Heat Source Temperatures and Capacities*. Energies, 2017. **10**(3): p. 269.

16. Nguyen, V.M., P.S. Doherty, and S.B. Riffat, *Development of a prototype low-temperature Rankine cycle electricity generation system*. Applied Thermal Engineering, 2001. **21**(2): p. 169-181.

17. Quoilin, S., et al., *Thermo-economic optimization of waste heat recovery Organic Rankine Cycles*. Applied Thermal Engineering, 2011. **31**(14): p. 2885-2893.

18. Lukawski, M., *Design and optimization of standardized organic Rankine cycle power plant for European conditions*, in *School for Renewable Energy Science*. 2010, University of Iceland;University of Akureyri. p. 77.

19. Crawford, M. *Metal to Plastic: Design Flexibility*. 2013.

20. Thombare, D.G. and S.K. Verma, *Technological development in the Stirling cycle engines*. Renewable and Sustainable Energy Reviews, 2008. **12**(1): p. 1-38.

21. Wang, K., et al., *Stirling cycle engines for recovering low and moderate temperature heat: A review*. Renewable and Sustainable Energy Reviews, 2016. **62**: p. 89-108.

22. Jouhara, H., et al., *Waste heat recovery technologies and applications*. Thermal Science and Engineering Progress, 2018. **6**: p. 268-289.

23. Madhawa Hettiarachchi, H.D., et al., *The Performance of the Kalina Cycle System 11(KCS-11) With Low-Temperature Heat Sources*. Journal of Energy Resources Technology, 2007. **129**(3): p. 243-247.

24. Colonna, P., et al., *Organic Rankine cycle power systems: from the concept to current technology, applications, and an outlook to the future*. Journal of Engineering for Gas Turbines and Power, 2015. **137**(10): p. 100801.

25. Hernandez-Carrillo, I., C.J. Wood, and H. Liu, *Advanced materials for the impeller in an ORC radial microturbine*. Energy Procedia, 2017. **129**: p. 1047-1054.

26. Kaplan, U., *Organic Rankine Cycle Configurations*, in *Proceedings European Geothermal Congress* 2007: Unterhaching, Germany. p. 5.

27. Ho, T., S.S. Mao, and R. Greif, *Increased power production through enhancements to the Organic Flash Cycle (OFC)*. Energy, 2012. **45**(1): p. 686-695.

28. Mondal, S., S. Alam, and S. De, *Performance assessment of a low grade waste heat driven organic flash cycle (OFC) with ejector*. Energy, 2018. **163**: p. 849-862.

29. Ho, T., S.S. Mao, and R. Greif, *Comparison of the Organic Flash Cycle (OFC) to other advanced vapor cycles for intermediate and high temperature waste heat reclamation and solar thermal energy*. Energy, 2012. **42**(1): p. 213-223.

30. Karellas, S. and A. Schuster, *Supercritical fluid parameters in organic Rankine cycle applications*. International Journal of Thermodynamics, 2008. **11**(3): p. 101-108.

31. Gao, H., et al., *Performance Analysis and Working Fluid Selection of a Supercritical Organic Rankine Cycle for Low Grade Waste Heat Recovery*. Energies, 2012. **5**(9): p. 3233.

32. Saleh, B., et al., *Working fluids for low-temperature organic Rankine cycles*. Energy, 2007. **32**(7): p. 1210-1221.

33. Sarkar, J., *Review and future trends of supercritical CO2 Rankine cycle for low-grade heat conversion*. Renewable and Sustainable Energy Reviews, 2015. **48**: p. 434-451.

34. Imran, M., et al., *Recent research trends in organic Rankine cycle technology: A bibliometric approach*. Renewable and Sustainable Energy Reviews, 2018. **81**: p. 552-562.

35. Rahbar, K., et al., *Review of organic Rankine cycle for small-scale applications*. Energy Conversion and Management, 2017. **134**(Supplement C): p. 135-155.

36. Schubert, D., *MEMS-concept using micro turbines for satellite power supply*. 2012: INTECH Open Access Publisher.

37. Fu, B.-R., et al., *Statistical analysis of patent data relating to the organic Rankine cycle*. Renewable and Sustainable Energy Reviews, 2014. **39**: p. 986-994.

38. Zywica, G., T.Z. Kaczmarczyk, and E. Ihnatowicz, *A review of expanders for power generation in small-scale organic Rankine cycle systems: Performance and operational aspects*. Proceedings of the Institution of Mechanical Engineers, Part A: Journal of Power and Energy, 2016: p. 0957650916661465.

39. Qiu, G., H. Liu, and S. Riffat, *Expanders for micro-CHP systems with organic Rankine cycle*. Applied Thermal Engineering, 2011. **31**(16): p. 3301-3307.

40. Imgur. *Scroll compressor*. [cited 2019; Available from: http://i.imgur.com/BMrLku2.jpg.

41. Song, P., et al., *A review of scroll expanders for organic Rankine cycle systems*. Applied Thermal Engineering, 2015. **75**: p. 54-64.

42. Imran, M., et al., *Volumetric expanders for low grade heat and waste heat recovery applications*. Renewable and Sustainable Energy Reviews, 2016. **57**: p. 1090-1109.

43. Rahbar, K., et al., *Review of organic Rankine cycle for small-scale applications*. Energy Conversion and Management, 2017. **134**: p. 135-155.

44. *Screw Compressor*.

45. PSIAUTOMATION. *Safety Silencers*. [cited 2019 14/05/19]; Available from: http://www.psiautomation.com/test-pictures.htm.

46. Inc.;, U.D. *Equipment for Engineering Education*. 2003 [cited 2019 14/05/2019]; Available from: http://www.usdidactic.com/teaching-lab-equipment/i4429_Foto_Totale.htm.

47. Quoilin, S., et al., *Techno-economic survey of Organic Rankine Cycle (ORC) systems*. Renewable and Sustainable Energy Reviews, 2013. **22**: p. 168-186.

48. Bronicki, L. and Z.T. Harry, *Vapor turbines*, I.S.P. Office, Editor. 1962, Google Patents: US. p. 4.

49. Marcuccilli, F. and S. Zouaghi, *Radial inflow turbines for Kalina and organic Rankine cycles*. system, 2007. **2**: p. 1.

50. Bao, J. and L. Zhao, *A review of working fluid and expander selections for organic Rankine cycle*. Renewable and Sustainable Energy Reviews, 2013. **24**: p. 325-342.

51. Saidur, R., et al., *Technologies to recover exhaust heat from internal combustion engines*. Renewable and Sustainable Energy Reviews, 2012. **16**(8): p. 5649-5659.

52. Barber-Nichols Inc. *Design & Manufacture of Specialty Turbomachinery*. 2015 [cited 2019 22/01/18]; Barber-Nichols is a proven supply chain partner that can move your prototype to production. We're committed to quality and reliability and customers who work with us once keep coming back.]. Available from: http://www.barber-nichols.com/.

53. Celeroton AG. *Celeroton, Ultra High Speed Electrical Drive Systems*. 2008 [cited 2019 22/01/2019]; Available from: https://www.celeroton.com/en.html.

54. Dyson, J.E. and B.W. Darvell, *Torque, power and efficiency characterization of dental air turbine handpieces*. Journal of Dentistry, 1999. **27**(8): p. 573-586.

55. Khelladi, S., et al., *Flow Study in the Impeller–Diffuser Interface of a Vaned Centrifugal Fan*. Journal of Fluids Engineering, 2005. **127**(3): p. 495-502.

56. Li, P., et al. *Study on the steady and unsteady aerodynamic performance of a radial inflow turbine with small partial admission in a miniature ORC system*. in *ASME 2011 Power Conference collocated with JSME ICOPE 2011*. 2011. American Society of Mechanical Engineers.

57. Li, J., et al., *Evaluation of external heat loss from a small-scale expander used in organic Rankine cycle*. Applied Thermal Engineering, 2011. **31**(14–15): p. 2694-2701.

58. Klonowicz, P., et al., *Significance of loss correlations in performance prediction of small scale, highly loaded turbine stages working in Organic Rankine Cycles*. Energy, 2014. **72**: p. 322-330.

59. Weiß, A.P. *Volumetric expander versus turbine–which is the better choice for small ORC plants?* in *ASME-ORC2015*. 2015. Brussels, Belgium: ASME.

60. Da Lio, L., G. Manente, and A. Lazzaretto, *Predicting the optimum design of single stage axial expanders in ORC systems: Is there a single efficiency map for different working fluids?* Applied Energy, 2016. **167**: p. 44-58.

61. Da Lio, L., G. Manente, and A. Lazzaretto, *New efficiency charts for the optimum design of axial flow turbines for organic Rankine cycles*. Energy, 2014. **77**: p. 447-459.

62. Klonowicz, P., et al., *Design and performance measurements of an organic vapour turbine*. Applied Thermal Engineering, 2014. **63**(1): p. 297-303.

63. Astolfi, M. and E. Macchi. *Efficiency correlations for axial flow turbines working with non-conventional fluids*. in *Proceedings of the 3rd International Seminar on ORC Power Systems, Brussels, Belgium*. 2015.

64. Craig, H. and H. Cox, *Performance estimation of axial flow turbines*. Proceedings of the Institution of Mechanical Engineers, 1970. **185**(1): p. 407-424.

65. Uusitalo, A., et al., *Combined Thermodynamic and Turbine Design Analysis of Small Capacity Waste Heat Recovery ORC*. Proceedings of the ASME ORC, 2015.

66. Capata, R. and G. Hernandez, *Preliminary Design and Simulation of a Turbo Expander for Small Rated Power Organic Rankine Cycle (ORC)*. Energies, 2014. **7**(11): p. 7067.

67. Capata, R. and G. Hernandez. *Proposal Design Procedure and Preliminary Simulation of Turbo Expander for Small Size (2–10 kW) Organic Rankine Cycle (ORC)*. in *ASME 2014 International Mechanical Engineering Congress and Exposition*. 2014. American Society of Mechanical Engineers.

68. Lopez Sanz, E., *Study on a radial turbine stage with inlet guide vanes for an orc process with an electrical output of 3, 5 kw*. 2013.

69. Ssebabi, B., R.T. Dobson, and A.B. Sebitosi, *Characterising a turbine for application in an organic Rankine cycle*. Energy, 2015. **93, Part 2**: p. 1617-1632.

70. Arifin, M. and A. Pasek. *Design of Radial Turbo-Expanders for Small Organic Rankine Cycle System*. in *IOP Conference Series: Materials Science and Engineering*. 2015. IOP Publishing.

71. Demierre, J., A. Rubino, and J. Schiffmann, *Modeling and Experimental Investigation of an Oil-Free Microcompressor-Turbine Unit for an Organic Rankine Cycle Driven Heat Pump*. Journal of Engineering for Gas Turbines and Power, 2015. **137**(3): p. 032602.

72. Rahbar, K., S. Mahmoud, and R.K. Al-Dadah. *OPTIMIZED EFFICIENCY MAPS AND NEW CORRELATION FOR PERFORMANCE PREDICTION OF ORC BASED ON RADIAL TURBINE FOR SMALL-SCALE APPLICATIONS*. 2015.

73. Rahbar, K., S. Mahmoud, and R.K. Al-Dadah, *Mean-line modeling and CFD analysis of a miniature radial turbine for distributed power generation systems*. International Journal of Low-Carbon Technologies, 2016. **11**(2): p. 157-168.

74. White, M. and A.I. Sayma, *System and component modelling and optimisation for an efficient 10 kWe low-temperature organic Rankine cycle utilising a radial inflow expander*. Proceedings of the Institution of Mechanical Engineers, Part A: Journal of Power and Energy, 2015: p. 0957650915574211.

75. Suhrmann, J.F., et al. *Validation and development of loss models for small size radial turbines*. in *ASME Turbo Expo 2010: Power for Land, Sea, and Air*. 2010. American Society of Mechanical Engineers.

76. Li, Y. and X.-d. Ren, *Investigation of the organic Rankine cycle (ORC) system and the radial-inflow turbine design*. Applied Thermal Engineering, 2016. **96**: p. 547-554.

77. Baines, N. *Radial turbines: An integrated design approach*. in *Concepts NREC, 6th European Turbomachinery Conference-Fluid Dynamics and Thermodynamics, Lille, France*. 2005.

78. Rohlik, H.E., *Analytical determination of radial inflow turbine design geometry for maximum efficiency*. 1968.

79. Al Jubori, A.M., R. Al-Dadah, and S. Mahmoud, *New performance maps for selecting suitable small-scale turbine configuration for low-power organic Rankine cycle applications*. Journal of Cleaner Production, 2017. **161**: p. 931-946.

80. Song, J., C.W. Gu, and X.S. Li, *Performance estimation of Tesla turbine applied in small scale Organic Rankine Cycle (ORC) system*. Applied Thermal Engineering, 2017. **110**: p. 318-326.

81. Song, J. and C.W. Gu. *1-D model analysis of Tesla Turbine for small scale Organic Rankine Cycle (ORC) system*. in *ASME Turbo Expo 2017: Turbomachinery Technical Conference and Exposition, GT 2017*. 2017. American Society of Mechanical Engineers (ASME).

82. Rahbar, K., et al., *Parametric analysis and optimization of a small-scale radial turbine for Organic Rankine Cycle*. Energy, 2015. **83**: p. 696-711.

83. Kosowski, K., et al. *Design and Investigations of a micro-turbine flow part*. in *ASME Turbo Expo 2012: Turbine Technical Conference and Exposition*. 2012. American Society of Mechanical Engineers.

84. Harinck, J., et al., *Performance improvement of a radial organic Rankine cycle turbine by means of automated computational fluid dynamic design*. Proceedings of the Institution of Mechanical Engineers, Part A: Journal of Power and Energy, 2013. **227**(6): p. 637-645.

85. Cho, S.-Y., C.-H. Cho, and S.-K. Choi, *Experiment and cycle analysis on a partially admitted axial-type turbine used in the organic Rankine cycle*. Energy, 2015. **90, Part 1**: p. 643-651.

86. Kaczmarczyk, T.Z., G. Ywica, and E. Ihnatowicz, *Measurements and vibration analysis of a five-stage axial-flow microturbine operating in an ORC cycle*. Diagnostyka, 2017. **18**(2): p. 51-58.

87. Klonowicz, P., et al. *A turbine based domestic micro ORC system*. in *4th International Seminar on Organic Rankine Cycle (ORC) Power Systems, ORC 2017*. 2017. Elsevier Ltd.

88. Yamamoto, T., et al., *Design and testing of the Organic Rankine Cycle*. Energy, 2001. **26**(3): p. 239-251.

89. Pei, G., et al., *Construction and dynamic test of a small-scale organic rankine cycle*. Energy, 2011. **36**(5): p. 3215-3223.

90. Zywica, G., et al. *Prototype of the domestic CHP ORC system: construction and experimental research*. in *ASME-ORC2015*. 2015. Brussels, Belgium: University of Liège and Ghent University.

91. Kaczmarczyk, T.Z., G. Żywica, and E. Ihnatowicz, *The impact of changes in the geometry of a radial microturbine stage on the efficiency of the micro CHP plant based on ORC*. Energy, 2017. **137**: p. 530-543.

92. Wong, C.S., D. Meyer, and S. Krumdieck, *Selection and conversion of turbocharger as turbo-expander for organic rankine cycle (ORC)*. 2013.

93. Deligant, M., Q. Danel, and F. Bakir, *Performance assessment of a standard radial turbine as turbo expander for an adapted solar concentration ORC*. Energy Procedia, 2017. **129**: p. 1085-1092.

94. Shao, L., et al., *Experimental study of an organic Rankine cycle system with radial inflow turbine and R123*. Applied Thermal Engineering, 2017. **124**: p. 940-947.

95. Shao, L., et al., *Design and experimental study of a small-sized organic Rankine cycle system under various cooling conditions*. Energy, 2017. **130**: p. 236-245.

96. Ma, X., et al., *Design and performance study of radial inflow turbine used on organic Rankine cycle waste heat power generation system*. Zhongguo Dianji Gongcheng Xuebao/Proceedings of the Chinese Society of Electrical Engineering, 2014. **34**(14): p. 2289-2296.

97. Chen, Y., H. Ying, and W. Ya, *Experimental Study of Low-temperature Organic Rankine Cycle with Axial Flow Turbine*. Energy Procedia, 2015. **75**: p. 1583-1589.

98. Li, M., et al. *Performance evaluation of a turbine used in a regenerative organic rankine cycle*. in *ASME Turbo Expo 2012: Turbine Technical Conference and Exposition*. 2012. American Society of Mechanical Engineers.

99. Borsukiewicz-Gozdur, A., *Experimental investigation of R227ea applied as working fluid in the ORC power plant with hermetic turbogenerator*. Applied Thermal Engineering, 2013. **56**(1–2): p. 126-133.

100. Kunte, H.S. and J.R. Seume. *EXPERIMENTAL SETUP OF A SMALL SUPERSONIC TURBINE FOR AN AUTOMOTIVE ORC APPLICATION RUNNING WITH ETHANOL*. in *ASME-ORC2015*. 2015. Brussels, Belgium: University of Liège and Ghent University.

101. Guillaume, L., et al., *Performance of a radial-inflow turbine integrated in an ORC system and designed for a WHR on truck application: An experimental comparison between R245fa and R1233zd*. Applied Energy, 2016.

102. Li, L., et al., *Experimental investigations into power generation with low grade waste heat and R245fa Organic Rankine Cycles (ORCs)*. Applied Thermal Engineering, 2017. **115**: p. 815-824.

103. Pu, W., et al., *Experimental study on Organic Rankine cycle for low grade thermal energy recovery*. Applied Thermal Engineering, 2016. **94**: p. 221-227.

104. Yagoub, W., P. Doherty, and S.B. Riffat, *Solar energy-gas driven micro-CHP system for an office building*. Applied Thermal Engineering, 2006. **26**(14): p. 1604-1610.

105. Enogia SAS. *Enogia, The Small ORC Company*. 2015 [cited 2016 03/05/2016]; Available from: http://www.enogia.com/product.html.

106. Nguyen, V., P. Doherty, and S. Riffat, *Development of a prototype low-temperature Rankine cycle electricity generation system*. Applied Thermal Engineering, 2001. **21**(2): p. 169-181.

107. Li, J., et al., *Energetic and exergetic investigation of an organic Rankine cycle at different heat source temperatures*. Energy, 2012. **38**(1): p. 85-95.

108. Kicinski, J. and G. Zywica, *Prototype of the domestic CHP ORC energy system*. Bulletin of the Polish Academy of Sciences-Technical Sciences, 2016. **64**(2): p. 417-424.

109. Kaczmarczyk, T.Z., G. Żywica, and E. Ihnatowicz, *Experimental investigation of radial microturbine in organic Rankine cycle system with HFE7100 as working fluid*. 2015.

110. Kaczmarczyk, T.Z., et al. *Initial experimental investigation of the ORC system in a cogenerative domestic power plant with a microturbine*. in *8th World Conference on Experimental Heat Transfer, Fluid Mechanics, and Thermodynamics*. 2013.

111. Kozanecki, Z., et al. *Theoretical and experimental investigations of oil-free bearings and their application in diagnostics of high-speed turbomachinery*. in *Key Engineering Materials*. 2014. Trans Tech Publ.

112. Bagiński, P., A. Andrearczyk, and G. Zywica, *Experimental investigation of ceramic ball bearings for microturbines*. Diagnostyka, 2017. **18**(1): p. 51-58.

113. Bleuler, H., et al., *Magnetic bearings: theory, design, and application to rotating machinery*. 2009: Springer Science & Business Media.

114. Gazet, C., et al. *OPERATIONAL EXPERIENCE ON ORC USE FOR WASTE HEAT VALORIZATION IN BIOGAS POWER PLANT*. in *ASME-ORC2015*. 2015. Brussels, Belgium: University of Liège and Ghent University.

115. Uusitalo, A., et al., *Siloxanes as Working Fluids for Mini-ORC Systems Based on High-Speed Turbogenerator Technology*. Journal of Engineering for Gas Turbines and Power, 2013. **135**(4): p. 042305-042305.

116. Zuccato Energia. *Zuccato Energia Srl*. 2016 [cited 2016 08/09/2016]; Available from: http://www.zuccatoenergia.it/index.php/en/.

117. Calnetix. *Calnetix Technologies*. 2016 [cited 2016 08/09/2016]; Available from: https://www.calnetix.com/.

118. Verdicorp. *Verdicorp, Environmental Technologies*. 2012 [cited 2016 08/09/2016]; Available from: http://www.verdicorp.com/contact.html.

119. Kaczmarczyk, T., et al. *Experimental investigation of the ORC system in a cogenerative domestic power plant with a microturbine and an expansion valve*. in *ASME ORC 2013, 2nd International Seminar on ORC Power System*. 2013.

120. Macchi, E. and M. Astolfi, *Organic Rankine Cycle (ORC) Power Systems: Technologies and Applications*., ed. W. Publishing. 2016, Kidlington, UK: Woodhead Publishing. 698.

121. Turboden. *Turboden: Organic Rankine Cycle - Description*. 2015 [cited 2015 5 Nov]; Available from: http://www.turboden.eu/en/rankine/rankine-history.php.

122. Cleveland, C.J. and C.G. Morris, *Handbook of Energy : Chronologies, Top Ten Lists, and Word Clouds*. 2013, Elsevier Science: Saint Louis.

123. Li, H., et al., *Hydrocarbon working fluids for a Rankine cycle powered vapor compression refrigeration system using low-grade thermal energy*. Energy and Buildings, 2013. **65**: p. 167-172.

124. Pezzuolo, A., et al., *The ORC-PD: A versatile tool for fluid selection and Organic Rankine Cycle unit design*. Energy, 2016. **102**: p. 605-620.

125. Badr, O., S. Probert, and P. O'callaghan, *Selecting a working fluid for a Rankine-cycle engine*. Applied Energy, 1985. **21**(1): p. 1-42.

126. Quoilin, S., et al. *Working fluid selection and operating maps for Organic Rankine Cycle expansion machines*. in *Proceedings of the 21st international compressor conference at Purdue*. 2012.

127. Darvish, K., et al., *Selection of Optimum Working Fluid for Organic Rankine Cycles by Exergy and Exergy-Economic Analyses*. Sustainability, 2015. **7**(11): p. 15362-15383.

128. Wang, E.H., et al., *Study of working fluid selection of organic Rankine cycle (ORC) for engine waste heat recovery*. Energy, 2011. **36**(5): p. 3406-3418.

129. Klonowicz, P., et al., *Design and numerical study of turbines operating with MDM as working fluid*. Open Engineering, 2015. **5**(1).

130. Mendoza-Ramirez, M., *Seleccion del Fluido de Trabajo para el Ciclo Binario de Evaporacion Instantanea CBEI*, in *Facultad de Ingenieria*. 2016, Universidad Nacional Autonoma de Mexico: Ciudad Universitaria, Mexico.

131. Qiu, G., *Selection of working fluids for micro-CHP systems with ORC*. Renewable Energy, 2012. **48**: p. 565-570.

132. Nouman, J., *Comparative Studies and Analyses of Working Fluids for Organic Rankine Cycles—ORC*. Master of Science Thesis EGI-2012-086MSC, 2012.

133. Drescher, U. and D. Brüggemann, *Fluid selection for the Organic Rankine Cycle (ORC) in biomass power and heat plants*. Applied Thermal Engineering, 2007. **27**(1): p. 223-228.

134. Hærvig, J., K. Sørensen, and T.J. Condra, *Guidelines for optimal selection of working fluid for an organic Rankine cycle in relation to waste heat recovery*. Energy, 2016. **96**: p. 592-602.

135. Park, B.S., et al., *Review of Organic Rankine Cycle experimental data trends*. Energy Conversion and Management, 2018. **173**: p. 679-691.

136. Lemmon, E.W., M.O. McLinden, and D.G. Friend, *"Thermophysical Properties of Fluid Systems" en NIST Chemistry WebBook, NIST Standard Reference Database Number 69*. 20899, ed. N.I.o.S.a.T. Eds. P.J. Linstrom and W.G. Mallard, Gaithersburg MD. Vol. 2019. 2018, United States of America: National Institute of Standards and Technology,.

137. Eyerer, S., et al., *Theoretical analysis and experimental investigation of material compatibility between refrigerants and polymers*. Energy, 2018. **163**: p. 782-799.

138. Honeywell International, *Genetron R245fa* H. International, Editor. 2010: Germany.

139. Zyhowski, G., M. Spatz, and S.Y. Motta, *An Overview of the Properties and Applications of HFC-245fa*. 2002.

140. ACG Chemicals, *Technical Information -AMOLEA 1224yd*, ACG Chemicals, Editor. 2018: Japan.

141. Arkema, *Forane FBA 1233zd Blowing Agent Technical Profile*, Arkema, Editor. 2017, Arkema: France.

142. Honeywell, *Storage, Handling and Use Guidelines for Solstice zd Refrigerant*, Honeywell, Editor. 2014, Honeywell: Belgium.

143. Chemours, *Freon™ 134a-Refrigerant (R-134a)-Properties, Uses, Storage, and Handling*, Chemours, Editor. 2016.

144. Honeywell, *Solstice yf Properties and Materials Compatibility*, Honeywell, Editor. 2015, Honeywell: USA.

145. Linde, *R1234yf – Opteon® YF. Automotive refrigerant with low global warming potential*, Linde, Editor.: Germany.

146. Honeywell, *Solstice ze Refrigerant (HFO-1234ze)*, Honeywell, Editor. 2015, Honeywell: Belgium.

147. Ge, Y.T., et al., *Performance evaluation of a low-grade power generation system with CO2 transcritical power cycles*. Applied Energy, 2017.

148. Colonna, P., et al. *Real-gas effects in ORC turbine flow simulations: influence of thermodynamic models on flow fields and performance parameters*. in *ECCOMAS CFD 2006: Proceedings of the European Conference on Computational Fluid Dynamics, Egmond aan Zee, The Netherlands, September 5-8, 2006*. 2006. Delft University of Technology; European Community on Computational Methods in Applied Sciences (ECCOMAS).

149. Redlich, O. and J.N.S. Kwong, *On the Thermodynamics of Solutions. V. An Equation of State. Fugacities of Gaseous Solutions*. Chemical Reviews, 1949. **44**(1): p. 233-244.

150. Aungier, R.H., *Turbine aerodynamics : axial-flow and radial-inflow turbine design and analysis / Ronald H. Aungier*. 2006, New York: New York : ASME Press.

151. Peng, D.-Y. and D.B. Robinson, *A New Two-Constant Equation of State*. Industrial & Engineering Chemistry Fundamentals, 1976. **15**(1): p. 59-64.

152. Lemmon, E.W., M.L. Huber, and M.O. McLinden, *NIST Standard Reference Database 23: Reference Fluid Thermodynamic and Transport Properties-REFPROP*. 2013, National Institute of Standards and Technology: Standard Reference Data Program, Gaithersburg.

153. Bell, I.H., et al., *Pure and Pseudo-pure Fluid Thermophysical Property Evaluation and the Open-Source Thermophysical Property Library CoolProp*. Industrial & Engineering Chemistry Research, 2014. **53**(6): p. 2498-2508.

154. Colonna, P. and T. Van der Stelt, *FluidProp: a program for the estimation of thermo physical properties of fluids*. Energy Technology Section, Delft University of Technology, Delft, The Netherlands, http://www. FluidProp. com, 2004.

155. White, M. and A. Sayma, *The one-dimensional meanline design of radial turbines for small scale low temperature organic rankine cycles*. ASME Paper No. GT2015-44133, 2015.

156. Erbaş, M. and A. Bıyıkoğlu, *Design and multi-objective optimization of organic Rankine turbine*. International Journal of Hydrogen Energy, 2015. **40**(44): p. 15343-15351.

157. Erbas, M., et al. *Design and optimization of a low temperature organic Rankine cycle and turbine*. in *ASME 2013 International Mechanical Engineering Congress and Exposition*. 2013. American Society of Mechanical Engineers.

158. Rahbar, K., et al., *Modelling and optimization of organic Rankine cycle based on a small-scale radial inflow turbine*. Energy Conversion and Management, 2015. **91**: p. 186-198.

159. Colonna, P., et al., *Real-gas effects in organic Rankine cycle turbine nozzles*. Journal of Propulsion and Power, 2008. **24**(2): p. 282-294.

160. Hoffren, J., et al., *Numerical simulation of real-gas flow in a supersonic turbine nozzle ring*. Journal of engineering for gas turbines and power, 2002. **124**(2): p. 395-403.

161. Spinelli, A., et al., *EXPERIMENTAL OBSERVATION OF NON-IDEAL NOZZLE FLOW OF SILOXANE VAPOR MDM*.

162. Uusitalo, A., et al. *Design and Flow Analysis of a Supersonic Small Scale ORC Turbine Stator With High Molecular Complexity Working Fluid*. in *ASME Turbo Expo 2014: Turbine Technical Conference and Exposition*. 2014. American Society of Mechanical Engineers.

163. Pasquale, D., A. Ghidoni, and S. Rebay, *Shape Optimization of an Organic Rankine Cycle Radial Turbine Nozzle*. Journal of Engineering for Gas Turbines and Power, 2013. **135**(4): p. 042308-042308.

164. Harinck, J., et al., *Computational Study of a High-Expansion Ratio Radial Organic Rankine Cycle Turbine Stator*. Journal of Engineering for Gas Turbines and Power, 2010. **132**(5): p. 054501-054501.

165. Vitale, S., et al. *Fluid dynamic design and analysis of a highly loaded Centrifugal rotor for mini orc power systems*. in *3rd International Seminar on ORC Power Systems, Brussels, Belgium, 12-14 October 2015*. 2015. ASME.

166. Sauret, E. and Y. Gu, *Three-dimensional off-design numerical analysis of an organic Rankine cycle radial-inflow turbine*. Applied Energy, 2014. **135**: p. 202-211.

167. Persico, G., et al., *Aerodynamics of Centrifugal Turbine Cascades*. Journal of Engineering for Gas Turbines and Power, 2015. **137**(11): p. 112602-112602.

168. Rinaldi, E., R. Pecnik, and P. Colonna, *Unsteady Operation of a Highly Supersonic Organic Rankine Cycle Turbine*. Journal of Turbomachinery, 2016. **138**(12): p. 121010-121010.

169. Sciacovelli, L. and P. Cinnella. *Numerical investigation of dense gas flows through transcritical multistage axial Organic Rankine Cycle turbines*. in *Congrès français de mécanique (21; 2013; Bordeaux (Gironde)*. 2013.

170. Sciacovelli, L. and P. Cinnella, *Numerical study of multistage transcritical organic Rankine cycle axial turbines*. Journal of Engineering for Gas Turbines and Power, 2014. **136**(8): p. 082604.

171. Rahbar, K., et al., *Development and experimental study of a small-scale compressed air radial inflow turbine for distributed power generation*. Applied Thermal Engineering, 2017. **116**(2017): p. 549 - 583.

172. Novotný, V., et al., *3D Printed Parts for Power Industry*, in *Technological forum 2018*. 2018, Czech Technical University: Prague, Czech Republic. p. 8.

173. Zywica, G., et al., *Design and Manufacturing of Micro-Turbomachinery Components with Application of Heat Resistant Plastics*. Mechanics and Mechanical Engineering, 2018. **Vol. 22**(No. 2): p. 649–660.

174. Hernandez-Carrillo, I., C. Wood, and H. Liu, *Development of a 1000 W organic Rankine cycle micro-turbine-generator using polymeric structural materials and its performance test with compressed air*. Energy Conversion and Management, 2019. **190**: p. 105-120.

175. Novotny, V., et al., *3D Printing in Turbomachinery: Overview of Technologies, Applications and Possibilities for Industry 4.0*, in *Proceedings of ASME Turbo Expo 2019: Turbomachinery Technical Conference and Exposition*, ASME, Editor. 2019, ASME: Phoenix, Arizona, USA. p. 9.

176. Weiß, A.P., et al., *Customized small-scale orc*

turbogenerators–combining a 1D-design tool, a

micro-turbine-generator–construction kit and potentials of 3D-printing, in *5th International Seminar on ORC Power Systems*, E.K. Sotirios Karellas, Editor. 2019, The National Technical University of Athens (NTUA): Athens, Greece.

177. Zywica, G., et al., *Application*

of a heat resistant plastic in a high-speed microturbine designed for the

domestic ORC system, in *5th International Seminar on ORC Power Systems*, E.K. Sotirios Karellas, Editor. 2019, The National Technical University of Athens (NTUA): Athens, Greece.

178. Cerce, M.A. and V.P. Patel, *Selecting Steam Turbines for Pump Drives*. 2003.

179. Moroz, L., et al. *Axial turbine flow path design for an organic Rankine cycle using R-245fa*. in *ASME Turbo Expo 2013: Turbine Technical Conference and Exposition*. 2013. American Society of Mechanical Engineers.

180. Japikse, D., et al. *Development of a 300 kWe Integrated Axial Turbine and Generator for ORC Applications*. in *2nd International Seminar on ORC Power Systems*. 2013. Brussels, Belgium.

181. Nasir, P., et al., *Utilization of turbine waste heat to generate electric power at Neptune plant*. Ormat. com, 2004.

182. Bini, R. and F. Viscuso. *High efficience ORC for power only generation mode in range -3 MW*. in *First International Seminar on ORC Power Systems*. 2011. Delft, Netherlands: ASME.

183. Pini, M., et al., *Preliminary design of a centrifugal turbine for organic rankine cycle applications*. Journal of Engineering for Gas turbines and power, 2013. **135**(4): p. 042312.

184. Šarboh, S., *The patents of Nikola Tesla*. World Patent Information, 2010. **32**(4): p. 335-339.

185. Dixon, S.L., *Fluid mechanics and thermodynamics of turbomachinery [electronic resource] / S.L. Dixon, C.A. Hall*. 6th ed. ed, ed. C.A. Hall and Knovel. 2010, Burlington, MA: Burlington, MA : Butterworth-Heinemann/Elsevier.

186. Wei, Z., *MEANLINE ANALYSIS OF RADIAL INFLOW TURBINES AT DESIGN AND OFF-DESIGN CONDITIONS*. 2014, Carleton University Ottawa.

187. Soderberg, C.R., *Unpublished note*, G.T. Laboratory, Editor. 1949, Massachusetts Institute of Technology.

188. Ainley, D. and G. Mathieson, *A method of performance estimation for axial-flow turbines*. 1951: Citeseer.

189. Balje, O. and R. Binsley, *Axial Turbine Performance Evaluation. Part A—Loss-Geometry Relationships*. Journal of Engineering for Power, 1968. **90**(4): p. 341-348.

190. Traupel, W., *Thermische Turbomaschinen—Zweiter Band, Genderte Betriebsbedingungen, Regelung, Mechanische Probleme, Temperaturprobleme*. 1982, Springer-Verlag Berlin Heidelberg New York.

191. Denton, J.D. *Loss mechanisms in turbomachines*. in *ASME 1993 International Gas Turbine and Aeroengine Congress and Exposition*. 1993. American Society of Mechanical Engineers.

192. Dunham, J. and P. Came, *Improvements to the Ainley-Mathieson method of turbine performance prediction*. Journal of Engineering for Power, 1970. **92**(3): p. 252-256.

193. Kacker, S.C. and U. Okapuu, *A Mean Line Prediction Method for Axial Flow Turbine Efficiency*. Journal of Engineering for Power, 1982. **104**(1): p. 111-119.

194. Moustapha, H., et al., *Axial and radial turbines*. Vol. 2. 2003: Concepts NREC White River Junction, VT.

195. Nichols, K.E., *How to select turbomachinery for your application*, in *Barber-Nichols Inc*. 2012. p. 5-6.

196. White, M. and A.I. Sayma, *The Application of Similitude Theory for the Performance Prediction of Radial Turbines Within Small-Scale Low-Temperature Organic Rankine Cycles*. Journal of Engineering for Gas Turbines and Power, 2015. **137**(12): p. 122605-122605-10.

197. Wong, C.S. and S. Krumdieck, *Scaling of Gas Turbine From Air to Refrigerants for Organic Rankine Cycle Using Similarity Concept*. Journal of Engineering for Gas Turbines and Power, 2015. **138**(6): p. 061701-061701.

198. Wong, C.S. and S. Krumdieck, *Scaling of Gas Turbine From Air to Refrigerants for Organic Rankine Cycle Using Similarity Concept*. Journal of Engineering for Gas Turbines and Power, 2016. **138**(6): p. 061701.

199. Chen, T., et al. *Similarity Based Performance Prediction of Organic Rankine Cycle Turbine Using Air Condition Data*. in *ASME/JSME/KSME 2015 Joint Fluids Engineering Conference*. 2015. American Society of Mechanical Engineers.

200. Smith, S. *A simple correlation of turbine efficiency*. in *Von Karman Inst. for Fluid Dyn. Proc. of the Seminar on Adv. Probl. in Turbomachinery, Pt. 1 24 p(SEE N 79-21053 12-07)*. 1965.

201. Persico, G. and S. Rebay, *A penalty formulation for the throughflow modeling of turbomachinery*. Computers & Fluids, 2012. **60**: p. 86-98.

202. Costall, A.W., et al., *Design methodology for radial turbo expanders in mobile organic Rankine cycle applications*. Applied Energy, 2015. **157**: p. 729-743.

203. Arkkio, A., T. Jokinen, and E. Lantto. *Induction and permanent-magnet synchronous machines for high-speed applications*. in *2005 International Conference on Electrical Machines and Systems*. 2005. IEEE.

204. Jachens, W., *Steam Turbines-Their Construction, Selection and Operation*. Proc. The South African Sugar Technologist's Association, 1769: p. 113-131.

205. Capstone, *Capstone C200 Microturbine Technical Reference*. 2009, Capstone Turbine Corporation 21211 Nordhoff Street, Chatsworth, CA, USA.

206. Dieter, G.E. and L.C. Schmidt, *Engineering design*. 5th ed ed. 2013, New York: McGraw-Hill.

207. Kurowski, P.M. and G.K. Knopf *Educating engineers about product design methodology*. in *Canadian Design Engineering Network*. 2006. Toronto, Canada: Canadian Engineering Education Association.

208. Gme, *BS ISO 20816-1:2016 - Mechanical vibration. Measurement and evaluation of machine vibration. General guidelines*. <germanTitle/>. 2016.

209. University of Nottingham, S.O., *Piped compressed gas systems attached to gas cylinders and stand-alone compressed gas cylinder installations*. 2012, University of Nottingham: Nottingham, UK.

210. University of Nottingham, S.O., *University Code of Practice for Electrical Safety*. 2015, University of Nottingham: Nottingham, UK.

211. Mark, J.E., *Polymer data handbook*. 2009: Oxford university press.

212. Materials, A. *Polyether Ether Ketone (PEEK) Recycling*. 2000 [cited 2019; Available from: https://www.azom.com/article.aspx?ArticleID=7989.

213. Safety, C.L. *PEEK Chemical Compatibility*. 2019 [cited 2019; Available from: https://www.calpaclab.com/polyetherether-ketone-peek-chemical-compatibility-chart/.

214. Small, G., *Outstanding physical properties make PEEK ideal for sealing applications*. Sealing Technology, 2014. **2014**(4): p. 9-12.

215. Mallick, V., *Thermoplastic composite based processing technologies for high performance turbomachinery components*. Composites Part A: Applied Science and Manufacturing, 2001. **32**(8): p. 1167-1173.

216. McLauchlin, A.R., O.R. Ghita, and L. Savage, *Studies on the reprocessability of poly(ether ether ketone) (PEEK)*. Journal of Materials Processing Technology, 2014. **214**(1): p. 75-80.

217. Ji, L.N. *Study on preparation process and properties of polyethylene terephthalate (PET)*. in *Applied Mechanics and Materials*. 2013. Trans Tech Publ.

218. Padhan, R.K. and A.A. Gupta, *Polyethylene Terephthalate-Based Blends: Thermoplastic and Thermoset*, in *Poly (Ethylene Terephthalate) Based Blends, Composites and Nanocomposites*. 2015, Elsevier. p. 65-73.

219. Garbassi, F. and R. Po, *Engineering thermoplastics, overview*. Encyclopedia of Polymer Science and Technology, 2002. **2**.

220. Pohekar, S.D. and M. Ramachandran, *Application of multi-criteria decision making to sustainable energy planning—A review*. Renewable and Sustainable Energy Reviews, 2004. **8**(4): p. 365-381.

221. MatWeb, L. *Material property data*. 2019 [cited 2019 03/06/2019]; Available from: http://www.matweb.com/index.aspx.

222. American Petroleum Institute, *Recommended Practice for Design and Installation of Offshore Production Platform Piping Systems*, in *API Rrecomended practice 14E (RP 14E)* 1991, American Petroleum Institute: Washington D.C.

223. ANSYS, *ANSYS Turbo System User's Guide*, A. Inc., Editor. 2013, ANSYS: Canonsburg, Pennsylvania, USA. p. 338.

224. ISO, *Mechanical vibration—balance quality requirements for rotors in a constant (rigid) state, Part 1: Specification and verification of balance tolerances*. 2003.

225. Amazon. *CNCShop Spindle Motor CNC Spindle Motor 2.2kw Water Cooled Spindle Motor*. 2019; Available from: https://www.amazon.com/CNCShop-Spindle-Motor-Cooled-Collet/dp/B012A8U95A.

226. Khaburi, D.A. and A. Nazempour, *Design and simulation of a PWM rectifier connected to a PM generator of micro turbine unit*. Scientia Iranica, 2012. **19**(3): p. 820-828.

227. Staunton, R. and B. Ozpineci, *Microturbine power conversion technology review*. 2003: United States. Department of Energy.

228. Pve, *BS ISO 16528-1:2007 - Boilers and pressure vessels. Performance requirements*. Dampfkessel und Druckbehälter. Festigkeitsanforderungen. 2008.

229. American Society of Mechanical Engineers, Q.S.o.M.E., *2015 ASME boiler & pressure vessel code : an international code. Section VIII, Rules for construction of pressure vessels ASME Boiler and Pressure Vessel Committee on Pressure Vessels*. 2015 ed. ed. ASME boiler & pressure vessel code, ed. E. American Society of Mechanical, A. Boiler, and V. Pressure Vessel Committee. Subcommittee on Pressure. 2015, New York: New York : American Society of Mechanical Engineers.

230. Mte, *BS EN ISO 23125:2010+A1:2012 - Machine tools. Safety. Turning machines*. Werkzeugmaschinen. Sicherheit. Drehmaschinen. 2010.

231. Luján, J.M., et al., *Model of the expansion process for R245fa in an Organic Rankine Cycle (ORC)*. Applied Thermal Engineering, 2012. **40**: p. 248-257.

232. Whitfield, A. and N.C. Baines, *Design of radial turbomachines*. 1990, Harlow, Essex, England.

233. Suhrmann, J.F., et al., *Validation and Development of Loss Models for Small Size Radial Turbines*. 2010(44021): p. 1937-1949.

234. Musgrave, D. *The prediction of design and off-design efficiency for centrifugal compressor impellers*. in *Performance Prediction of Centrifugal Pumps and Compressors*. 1980. New Orleans: ASME.

235. Colebrook, C.F., et al., *Correspondence. Turbulent flow in pipes, with particular reference to the transition region between the smooth and rough pipe laws. (Includes plates)*. Journal of the Institution of Civil Engineers, 1939. **12**(8): p. 393-422.

236. Rodgers, C. and R. Geiser, *Performance of a High-Efficiency Radial/Axial Turbine*. Journal of Turbomachinery, 1987. **109**(2): p. 151-154.

237. Whitfield, A. and F. Wallace. *Study of incidence loss models in radial and mixed-flow turbomachinery*. in *Conference on Heat and Fluid Flow in Steam and Gas Turbine Plant, Coventry, England*. 1973.

238. Smith, S.F., *A Simple Correlation of Turbine Efficiency*. The Journal of the Royal Aeronautical Society, 1965. **69**(655): p. 467-470.

239. Alshammari, F., et al., *Off-design performance prediction of radial turbines operating with ideal and real working fluids*. Energy Conversion and Management, 2018. **171**: p. 1430-1439.

240. Dixon, S.L. and C. Hall, *Fluid Mechanics and Thermodynamics of Turbomachinery (Sixth Edition)*. 6 ed. 2010, Burlington, MA: Butterworth-Heinemann/Elsevier Science. 477.

241. White, M.T. and A.I. Sayma, *A Generalised Assessment of Working Fluids and Radial Turbines for Non-Recuperated Subcritical Organic Rankine Cycles*. Energies, 2018. **11**(4): p. 800.

242. American Petroleum Institute, *API Standard 612*, in *Petroleum, Petrochemical, and Natural Gas Industries—Steam Turbines—Special-purpose Applications*. 2014, American Petroleum Institute,.

243. Standardization, I.O.f., *ISO 10437:2003*, in *Petroleum, petrochemical and natural gas industries - Steam turbines - Special-purpose applications*. 2003, International Organization for Standardization.

244. Fluent, A., *12.0 User's guide*. Ansys Inc, 2009. **6**.

245. McLean, A.F. *The Application of Ceramics to the Small Gas Turbine*. in *ASME 1970 International Gas Turbine Conference and Products Show*. 1970. American Society of Mechanical Engineers.

246. Eyerer, S., et al., *Material compatibility of ORC working fluids with polymers*. Energy Procedia, 2017. **129**: p. 137-144.

247. British Standards Institution, *BS EN ISO 20753:2014 - Plastics. Test specimens*. 2008.

248. Institution, B.S., *BS EN ISO 175:2010 - Plastics. Methods of test for the determination of the effects of immersion in liquid chemicals*. Kunststoffe. Prüfverfahren zur Bestimmung des Verhaltens gegen flüssige Chemikalien. 2010.

249. Institution, B.S., *BS ISO 48:2010 - Rubber, vulcanized or thermoplastic. Determination of hardness (hardness between 10 IRHD and 100 IRHD)*. Elastomere und thermoplastische Elastomere. Bestimmung der Härte (Härte zwischen 10 IRHD und 100 IRHD). 2010.

250. Institution, B.S., *BS ISO 37:2017 - Rubber, vulcanized or thermoplastic. Determination of tensile stress-strain properties*. <germanTitle/>. 2017.

251. Majurin, J.A., W. Gilles, and S.J. Staats, *Materials compatibility of HVACR system materials with low GWP refrigerants*. 2014.

252. Burnand, G., et al. *Validation by measurements of a windage losses model for very-high-speed machines*. in *2017 20th International Conference on Electrical Machines and Systems (ICEMS)*. 2017.

253. SKF, *The SKF model for calculating the frictional moment*, SKF, Editor. p. 1-15.

254. Zwyssig, C., S.D. Round, and J.W. Kolar. *Analytical and Experimental Investigation of a Low Torque, Ultra-High Speed Drive System*. in *Conference Record of the 2006 IEEE Industry Applications Conference Forty-First IAS Annual Meeting*. 2006.

255. Moran, M.J., *Fundamentals of engineering thermodynamics / Michael J. Moran, Howard N. Shapiro*. 5th ed. ed, ed. H.N. Shapiro. 2004, Hoboken, N.J.: Hoboken, N.J. : John Wiley & Sons.

256. The Weather Company. *Weather Underground*. 2019 [cited 2019 29/01/2016]; Available from: https://www.wunderground.com/history/monthly/EGNX/date/2018-9?req_city=East%20Midlands&req_state=LEC&req_statename=United%20Kingdom&reqdb.zip=00000&reqdb.magic=77&reqdb.wmo=03418.

257. Kang, S.H., *Design and experimental study of ORC (organic Rankine cycle) and radial turbine using R245fa working fluid*. Energy, 2012. **41**(1): p. 514-524.

258. Hughes, I. and T. Hase, *Measurements and their uncertainties: a practical guide to modern error analysis*. 2010: Oxford University Press.

259. Verstraete, T., Z. Alsalihi, and R.A. Van den Braembussche, *Multidisciplinary Optimization of a Radial Compressor for Microgas Turbine Applications*. Journal of Turbomachinery, 2010. **132**(3): p. 031004-031004-7.

260. Massey Jr, F.J., *The Kolmogorov-Smirnov test for goodness of fit*. Journal of the American statistical Association, 1951. **46**(253): p. 68-78.

261. Freund, R.J., *Statistical methods / Rudolph J. Freund, William J. Wilson, Donna L. Mohr*. 3rd ed. ed, ed. D.L. Mohr and W.J. Wilson. 2010, Burlington, Mass.

London: Burlington, Mass.

London : Academic Press.

262. Zhang, L., et al., *Similarity Theory Based Radial Turbine Performance and Loss Mechanism Comparison between R245fa and Air for Heavy-Duty Diesel Engine Organic Rankine Cycles*. Entropy, 2017. **19**(1): p. 25.

263. Park, B.-S., et al., *Review of Organic Rankine Cycle experimental data trends*. Energy Conversion and Management, 2018. **173**: p. 679-691.

264. Hax, A.C. and N.S. Majluf, *Competitive Cost Dynamics: The Experience Curve*. Interfaces, 1982. **12**(5): p. 50-61.

265. Chacartegui, R., et al., *Alternative ORC bottoming cycles FOR combined cycle power plants*. Applied Energy, 2009. **86**(10): p. 2162-2170.

266. Ebnesajjad, S. and P.R. Khaladkar, *Fluoropolymer Applications in the Chemical Processing Industries: The Definitive User's Guide and Handbook*. 2017: William Andrew.

267. McGuire, J., *Pumps for Chemical Processing*. 1990: CRC Press.

268. Besic, D., *Give thermoplastic pumps a spin*. Chemical engineering progress, 2000. **96**(5): p. 61-68.

269. Commerford, K. and A. Bould, *The significance of thermoplastic pumps for pumping corrosive chemicals*. World Pumps, 2001. **2001**(413): p. 50-54.

270. Trexler, H.E., *RESISTANCE OF POLYMERS TO PERMEATION BY AIR CONDITIONING REFRIGERANTS AND WATER*. Rubber Chemistry and Technology, 1983. **56**(1): p. 105-112.

271. Ramaswamy, S., C. Schorsch, and M. Kolar, *Polymer Air-Conditioning Conveyance Lines for Automotive HVAC*. Symposium on International Automotive Technology, SIAT 2017, 2017. **2017-January**(January).

272. Yu, Y., *Generic approach of refrigerant HFC-134a emission modes from mobile air conditioning (MAC) systems*. 2008, École Nationale Supérieure des Mines de Paris.

273. T'Joen, C., et al., *A review on polymer heat exchangers for HVAC&R applications*. International Journal of Refrigeration, 2009. **32**(5): p. 763-779.

274. Hesse, U. and T. Weimer, *Polymer material heat exchangers application in refrigerant cycles*. 2012.

275. Gómez Aláez, S.L., et al., *Evaluation of ORC modules performance adopting commercial plastic heat exchangers*. Applied Energy, 2015. **154**: p. 882-890.

276. Akram, M.W., J.L. Meyer, and A.A. Polycarpou, *Tribological interactions of advanced polymeric coatings with polyalkylene glycol lubricant and r1234yf refrigerant*. Tribology International, 2016. **97**: p. 200-211.

277. Nunez, E.E., et al., *Tribological study of high bearing blended polymer-based coatings for air-conditioning and refrigeration compressors*. Surface and Coatings Technology, 2011. **205**(8): p. 2994-3005.

278. Nunez, E.E. and A.A. Polycarpou. *Tribological performance of polymer coatings in carbon dioxide refrigerant environment*. in *2009 ASME/STLE International Joint Tribology Conference, IJTC2009*. 2010. Memphis, TN.

279. Yeo, S.M., E.E. Nunez, and A.A. Polycarpou. *Tribological performance of polymer-based coatings for oilless piston-type compressor applications*. in *STLE/ASME 2010 International Joint Tribology Conference, IJTC2010*. 2010. San Francisco, CA.

280. Demas, N.G. and A.A. Polycarpou, *Tribological performance of PTFE-based coatings for air-conditioning compressors*. Surface and Coatings Technology, 2008. **203**(3-4): p. 307-316.

281. Sheiretov, T., W. Van Glabbeek, and C. Cusano, *Evaluation of the tribological properties of polyimide and poly(amide-imide) polymers in a refrigerant environment*. Tribology Transactions, 1995. **38**(4): p. 914-922.

282. Whalen, J.K. and J.R. Dugas. *Upgrading Centrifugal Compressors With Polymer Seals In An Ethylene Plant-A Case History*. in *Proceedings of the 29th Turbomachinery Symposium*. 2000. Texas A&M University. Turbomachinery Laboratories.

283. Whalen, J., et al. *POLYMER SEAL USE IN CENTRIFUGAL COMPRESSORS–TWO USERS'EXPERIENCES OVER 15 YEARS*. in *Middle East Turbomachinery Symposia. 2013 Proceedings*. 2013. Turbomachinery Laboratory, Texas A&M Engineering Experiment Station.

284. Bodmer, U., P. Hain, and V. Mallick, *Compressor*, U.S.P. Office, Editor. 1997: US. p. 5.

285. Albring, P., et al., *Turbo-compressor impeller for coolant*. 1995, Google Patents.

286. Fukizawa, T. and I. Sato, *Centrifugal impeller*. 2007, Google Patents.

287. Vipin, V. and A.P.J. PP, *Analysis of turbine blade made of composite materials used in steam turbines*. Int J Innova Eng Technol, 2015. **5**(4): p. 167-179.

288. Shaffer, B.R. and E.A. Groll, *Performance of the use of plastics in oil-free scroll compressors*. 2012.

289. Novotný, V., et al., *3D Printed Parts for Power Industry*.

APPENDICES

A. SUMMARY OF PROPERTIES OF THE STUDIED POLYMERS

Table 0.1 Summary of the properties of the evaluated polymers.
ν: specific volume, S_t: ultimate tensile strength, ME_t: tensile modulus of elasticity, S_{ty}: tensile yield strength, S_f: ultimate flexural strength, ME_f: flexural modulus of elasticity, S_{fy}: flexural yield strength, T_g: glass transition temperature, T_s: service temperature, T_d: deflexion temperature @ 1.8×10^3 kPa.

Name	Acronym	$\nu \frac{\mathrm{m}^3}{\mathrm{kg}}$	S_t kPa	M_t kPa	S_{ty} kPa	S_f kPa	M_f kPa	S_{fy} kPa	T_g K	T_s K	T_d K	Reference
Cyclic olefin copolymer	COP	9.6E-04	-	-	3.8E+04	-	-	4.8E+04	343	-	361	http://www.matweb.com/search/DataSheet.aspx?MatGUID=39f899c8c07641e9a8230d7dc15dca94
Syndiotactic polystyrene	SPS	8.3E-04	5.0E+04	4.2E+06	-	-	-	-	373	-	503	http://www.matweb.com/search/DataSheet.aspx?MatGUID=16d70a57c03448b59fa356d1bdb0db1f
Polyoxymethylene	POM	7.1E-04	6.6E+04	2.8E+06	-	8.3E+04	2.8E+06	-	471	355	377	http://www.matweb.com/search/DataSheet.aspx?MatGUID=82d9106dc7fd4bdfa635b03873b85737
Poly (ethylene terephthalate)	PET	7.1E-04	8.6E+04	3.2E+06	-	1.2E+05	3.4E+06	-	365	372	389	http://www.matweb.com/search/DataSheet.aspx?MatGUID=281e3a595e624a06bf49d9c6138092e5
Poly (butylene terephthalate)	PBT	7.8E-04	5.8E+04	2.5E+06	-	-	-	-	318	-	333	http://www.matweb.com/search/DataSheet.aspx?MatGUID=67ed78677a8e4437b81d1eca59410d56
Poly (ethylene naphthalate)	PEN	7.4E-04	2.0E+05	5.3E+06	-	-	-	-	665	428	-	http://www.matweb.com/search/DataSheet.aspx?MatGUID=60dc5dfcf5ba48f9bb4fe2fc7d7dd4bf
Polyarylate	PAR	8.3E-04	6.9E+04	-	-	8.4E+04	2.1E+06	-	-	-	448	http://www.matweb.com/search/DataSheet.aspx?MatGUID=0ac8bb4042a64e6b8aca21f8b1491766
Liquid crystal line polymer	LCP	5.9E-04	6.9E+04	2.5E+07	-	1.3E+05	1.3E+07	-	-	-	543	http://www.matweb.com/search/DataSheet.aspx?MatGUID=0f4816e0e8744073a087fa8870f0a1d0
Poly (phenylene ether)	PPE	9.3E-04	5.7E+04	2.5E+06	-	8.9E+04	2.7E+06	-	413	366	400	http://www.matweb.com/search/DataSheet.aspx?MatGUID=5fff94be5f6449e4989a70aa062f09c2
Polycarbonate	PC	8.3E-04	7.2E+04	2.2E+06	-	9.0E+04	2.4E+06	-	418	394	416	http://www.matweb.com/search/DataSheet.aspx?MatGUID=12a48ce5b6e04fc6a75f17515f4f19a9

Aliphatic polyketone	PK	8.1E-04	6.2E+04	1.7E+06	-	-	1.6E+06	5.5E+04	-	-	366	http://www.matweb.com/search/DataSheet.aspx?MatGUID=67a5b42e67d945f69b2e37cf729d52df
Poly (ether ether ketone)	PEEK	7.6E-04	1.1E+05	4.3E+06	-	1.7E+05	4.1E+06	-	425	522	433	http://www.matweb.com/search/DataSheet.aspx?MatGUID=53b9159c018544a599a06726922c9b8e
Poly (ether ketone)	PEK	7.7E-04	-	4.2E+06	1.1E+05	1.9E+05	4.1E+06	-	426	-	440	http://www.matweb.com/search/DataSheet.aspx?MatGUID=6c77a0bc3cbe4db2b82c63704e897cac
Poly (ether ketone ketone)	PEKK	7.6E-04	1.1E+05	4.4E+06	-	-	4.6E+06	1.9E+05	433	533	448	http://www.matweb.com/search/DataSheet.aspx?MatGUID=1bdfd4b5a72143c680ba1e94390ac844
Poly (ether ketone ether ketone ketone)	PEKEKK	7.7E-04	-	4.2E+06	1.2E+05	1.9E+05	4.0E+06	-	435	-	445	http://www.matweb.com/search/DataSheet.aspx?MatGUID=23f93a4432c249298af3215ccca70d6b
Poly (methyl methacrylate)	PMMA	8.4E-04	4.8E+04	3.2E+06	-	9.7E+04	3.2E+06	-	384	368	-	http://www.matweb.com/search/DataSheet.aspx?MatGUID=2d753e087ebf414cbf5bf248378b0ae5
Poly (phenylene sulfide)	PPS	5.2E-04	9.0E+03	2.6E+06	-	1.7E+04	2.1E+06	-	358	533	377	http://www.matweb.com/search/DataSheet.aspx?MatGUID=7135b8c9bcdb4151ac4d6a2f3d53568d
Polysulfone	PSU	8.1E-04	7.0E+04	2.7E+06	-	1.0E+05	2.8E+06	-	-	422	444	http://www.matweb.com/search/DataSheet.aspx?MatGUID=60d3b7679af4483e8c8a85146609a3c8
Poly (ether sulfone)	PES	7.3E-04	9.0E+04	2.7E+06	-	-	-	-	495	473	473	http://www.matweb.com/search/DataSheet.aspx?MatGUID=62d72c45fb1b4c3d883c48f9141633c4
Poly (aryl sulfone)	PAS	7.3E-04	8.3E+04	2.7E+06	-	1.1E+05	2.8E+06	-	-	-	477	http://www.matweb.com/search/DataSheet.aspx?MatGUID=b909e0f5b60a49e291b9bc2fb43a12b8
Acrylonitrile butadiene styrene	ABS	8.3E-04	3.8E+04	-	-	6.6E+04	2.2E+06	-	-	-	350	http://www.matweb.com/search/DataSheet.aspx?MatGUID=5421ac32fa11419a885194aab55514d9
Styrene acrylonitrile	SAN	9.3E-04	7.4E+04	-	-	-	3.4E+06	1.3E+05	376	-	-	http://www.matweb.com/search/DataSheet.aspx?MatGUID=e3ccf3f9eda14a119242ddeb25a3e1ca
Styrene maleic anhydride	SMA	9.3E-04	2.9E+04	2.0E+06	3.0E+04	5.7E+04	2.0E+06	-	-	-	363	http://www.matweb.com/search/DataSheet.aspx?MatGUID=f554c7083f3d445d99f87f1a6930f090
Poly (hexamethylene adipamide)/Nylon 66	PA6,6	8.6E-04	8.6E+04	3.3E+06	-	1.2E+05	3.2E+06	-	325	377	366	http://www.matweb.com/search/DataSheet.aspx?MatGUID=cc9f3ba248e448608ca328203d599132
Poly (hexamethylene	PA6,10	9.3E-04	7.0E+04	2.4E+06	-	1.0E+05	1.9E+06	-	340	-	328	http://www.matweb.com/search/DataSheet.aspx?MatGUID=0739ca0c590640279c8159145aad57c0

sebacamide)/Nylon 610												
Poly (hexamethylene dodecanediamide)/ Nylon 612	PA6,12	9.1E-04	7.2E+04	2.9E+06	-	8.8E+04	2.8E+06	-	319	-	-	http://www.matweb.com/search/DataSheet.aspx?MatGUID=542431d19ccb4d018605397572 9aee4f
Poly (hexamethylene succinamide)/Nylon 46	PA4,6	8.4E-04	1.0E+05	3.2E+06	-	1.2E+05	3.1E+06	-	-	422	433	http://www.matweb.com/search/DataSheet.aspx?MatGUID=b25383d7445b4225aa7776687c fdc60d
Poly(caprolactam)/ Nylon 6	PA6	8.6E-04	8.6E+04	3.3E+06	-	1.2E+05	3.2E+06	-	325	377	366	http://www.matweb.com/search/DataSheet.aspx?MatGUID=cc9f3ba248e448608ca328203d5 99132
Polyundecanolactam/Nylon 11	PA11	9.7E-04	-	1.3E+06	4.2E+04	-	-	-	315	-	328	http://www.matweb.com/search/DataSheet.aspx?MatGUID=877f54274b0e4bb49406db5027 c40233
Polylauryllactam/Nylon 12	PA12	9.9E-04	-	1.2E+06	3.8E+04	-	-	-	328	-	-	http://www.matweb.com/search/DataSheet.aspx?MatGUID=657d039f75d64ddf9be1be418d3 b6b97
poly (p-phenylene terephthalamide)/Kevlar 49	Kevlar 49	6.9E-04	3.0E+06	1.1E+08	-	-	-	-	698	-	-	http://www.matweb.com/search/DataSheet.aspx?MatGUID=77b5205f0dcc43bb8cbe6fee7d3 6cbb5
Polyimide	PI	7.3E-04	1.2E+05	3.7E+06	-	1.7E+05	3.8E+06	-	622	533	627	http://www.matweb.com/search/DataSheet.aspx?MatGUID=552501ea513b4ae99dc1611e33a 7406c
Polyamide imide	PAI	6.4E-04	4.4E+04	9.1E+06	-	7.5E+04	9.8E+06	-	549	-	-	http://www.matweb.com/search/DataSheet.aspx?MatGUID=88b46b953ef34d10b91d132d44 481982
Polyphthalamide	PPA	6.4E-04	4.4E+04	9.1E+06	-	7.5E+04	9.8E+06	-	-	-	-	http://www.matweb.com/search/DataSheet.aspx?MatGUID=88b46b953ef34d10b91d132d44 481982
Polyetherimide	PEI	7.1E-04	6.2E+04	5.9E+06	-	8.3E+04	5.9E+06	-	483	443	483	http://www.matweb.com/search/DataSheet.aspx?MatGUID=e8f4028ca7f54206a54ee0852c3 c0878
Poly(tetrafluoroethylene)	PTFE	5.2E-04	9.0E+03	2.6E+06	-	1.7E+04	2.1E+06	-	-	533	377	http://www.matweb.com/search/DataSheet.aspx?MatGUID=7135b8c9bcdb4151ac4d6a2f3d5 3568d
Ethylene–tetrafluoroethylene	ETFE	6.0E-04	3.1E+04	1.7E+06	-	4.8E+04	1.7E+06	-	-	422	350	http://www.matweb.com/search/DataSheet.aspx?MatGUID=7b30296896cf436ab8bc7e80a68 4b32b
Fluorinated ethylene–propylene	FEP	4.7E-04	2.7E+04	-	-	-	5.9E+05	-	-	477	321	http://www.matweb.com/search/DataSheet.aspx?MatGUID=3dbaaa8dbb114c57996acd6738a 7efc1
Perfluorovinylether–tetrafluoroethylene	PFA	4.7E-04	2.1E+04	6.9E+05	-	1.7E+04	5.9E+05	-	-	533	353	http://www.matweb.com/search/DataSheet.aspx?MatGUID=ab2a0930685f4f67b5ba6d7755b 8bec5

B. WEIGHTED SIGNIFICANCE OF PROPERTIES FOR MATERIAL SELECTION

Table 0.2 Weighted significance of properties for material selection

Property	Symbol	Weight
specific volume	ν	0.15
ultimate tensile strength	S_t	0.1
tensile modulus	M_t	0.075
yield tensile strength	S_{ty}	0.15
ultimate flexural strength	S_f	0.1
flexural modulus	M_f	0.075
yield flexural strength	S_{fy}	0.1
glass transition temperature	T_g	0.05
maximum service temperature	T_s	0.1
deflection temperature at 1.8[MPa]	T_d	0.1

C. CODE FOR THE UNCERTAINTY AND ERROR PROPAGATION ANALYSIS.

```
restart;
with(ScientificErrorAnalysis);
A := Matrix(72, 9, [[0.50e-1, 20.600, 20.700, 17.500, 58.000, 22.000, 0.45e-1, 0.45e-1,
0.6e-2], [0.75e-1, 20.400, 19.900, 21.500, 111.000, 43.000, 0.68e-1, 0.67e-1, 0.4e-2],
[.100, 20.500, 19.000, 22.500, 172.000, 66.000, 0.89e-1, 0.88e-1, 0.4e-2], [.120, 20.500,
17.600, 25.000, 264.000, 100.000, .114, .113, 0.4e-2], [.140, 20.500, 16.600, 26.500,
338.000, 128.000, .132, .130, 0.4e-2], [.160, 20.500, 15.300, 27.500, 437.000, 167.000,
.157, .157, 0.4e-2], [.180, 20.500, 13.700, 28.500, 554.000, 208.000, .180, .180, 0.4e-2],
[.180, 20.500, 13.700, 28.500, 554.000, 208.000, .180, .180, 0.4e-2], [0.50e-1, 20.700,
20.800, 17.500, 43.000, 16.300, 0.62e-1, 0.37e-1, 0.35e-1], [0.75e-1, 20.800, 20.400,
21.500, 87.000, 33.000, 0.98e-1, 0.58e-1, 0.55e-1], [.100, 20.800, 19.800, 22.500,
139.000, 53.000, .129, 0.76e-1, 0.72e-1], [.120, 20.900, 18.600, 25.000, 203.000, 76.000,
.162, 0.95e-1, 0.91e-1], [.140, 21.100, 18.100, 26.500, 253.000, 96.000, .186, .108, .102],
[.160, 21.200, 17.000, 27.500, 323.000, 122.000, .213, .125, .119], [.180, 21.300, 16.200,
28.500, 391.000, 149.000, .246, .146, .140], [.200, 21.400, 14.700, 30.000, 479.000,
181.000, .275, .162, .156], [0.50e-1, 21.500, 21.400, 17.500, 32.000, 12.300, 0.53e-1,
0.52e-1, 0.50e-1], [0.75e-1, 21.600, 21.200, 21.500, 68.000, 25.000, 0.82e-1, 0.82e-1,
0.79e-1], [.100, 21.700, 20.800, 22.500, 105.000, 39.000, .108, .108, .105], [.120, 21.900,
20.100, 25.000, 152.000, 57.000, .136, .138, .134], [.140, 21.900, 19.400, 26.500,
201.000, 77.000, .162, .163, .158], [.160, 22.100, 18.700, 27.500, 244.000, 92.000, .182,
.185, .181], [.180, 22.100, 17.800, 30.000, 297.000, 114.000, .208, .212, .206], [.200,
22.200, 16.700, 31.500, 361.000, 136.000, .232, .238, .232], [0.50e-1, 21.400, 21.300,
17.500, 67.000, 26.000, 0.50e-1, 0.50e-1, 0.7e-2], [0.75e-1, 21.400, 20.600, 21.500,
120.000, 45.000, 0.70e-1, 0.70e-1, 0.4e-2], [.100, 21.600, 19.500, 23.500, 201.000,
76.000, 0.96e-1, 0.95e-1, 0.96e-1], [.120, 21.600, 18.400, 25.000, 276.000, 105.000, .118,
.117, 0.8e-2], [.140, 21.200, 17.100, 26.500, 337.000, 128.000, .132, .131, 0.5e-2], [.160,
21.700, 15.800, 27.500, 469.000, 177.000, .160, .159, 0.5e-2], [.180, 21.700, 14.700,
28.500, 548.000, 206.000, .175, .175, 0.5e-2], [.180, 21.700, 14.700, 28.500, 548.000,
206.000, .175, .175, 0.5e-2], [0.50e-1, 21.700, 21.500, 17.500, 49.000, 18.400, 0.67e-1,
0.39e-1, 0.37e-1], [0.75e-1, 21.700, 21.100, 21.500, 93.000, 35.000, .100, 0.59e-1, 0.55e-
1], [.100, 21.600, 20.400, 22.500, 148.000, 56.000, .133, 0.79e-1, 0.74e-1], [.120, 21.600,
19.400, 25.000, 206.000, 78.000, .164, 0.96e-1, 0.92e-1], [.140, 21.600, 18.400, 26.500,
275.000, 104.000, .196, .114, .107], [.160, 21.600, 17.500, 27.500, 326.000, 123.000,
.217, .128, .121], [.180, 21.600, 16.400, 28.500, 407.000, 153.000, .251, .148, .142],
[.200, 21.800, 15.200, 30.000, 481.000, 181.000, .275, .163, .155], [0.50e-1, 21.800,
21.800, 17.500, 37.000, 14.000, 0.58e-1, 0.58e-1, 0.56e-1], [0.75e-1, 21.900, 21.400,
21.500, 70.000, 26.000, 0.84e-1, 0.85e-1, 0.83e-1], [.100, 21.900, 21.000, 22.500,
110.000, 41.000, .112, .114, .111], [.120, 21.900, 20.400, 25.000, 155.000, 59.000, .139,
.141, .135], [.140, 21.900, 19.400, 26.500, 205.000, 78.000, .168, .171, .165], [.160,
22.100, 18.600, 27.500, 261.000, 98.800, .191, .192, .186], [.180, 22.200, 17.700, 28.500,
307.000, 115.000, .211, .215, .211], [.200, 22.300, 16.800, 30.000, 367.000, 138.000,
.238, .244, .233], [0.50e-1, 22.300, 22.100, 17.500, 65.000, 24.000, 0.48e-1, 0.48e-1,
0.5e-2], [0.75e-1, 22.400, 21.300, 21.500, 129.000, 48.000, 0.75e-1, 0.74e-1, 0.3e-2],
[.100, 22.400, 20.400, 22.500, 202.000, 76.000, 0.97e-1, 0.97e-1, 0.3e-2], [.120, 22.400,
19.300, 25.000, 284.000, 108.000, .120, .121, 0.3e-2], [.140, 22.400, 18.400, 26.500,
359.000, 136.000, .140, .140, 0.3e-2], [.160, 22.500, 16.700, 27.500, 483.000, 184.000,
.167, .167, 0.3e-2], [.180, 22.700, 15.600, 28.500, 559.000, 210.000, .180, .180, 0.3e-2],
```

```
[.180, 22.700, 15.600, 28.500, 559.000, 210.000, .180, .180, 0.3e-2], [0.50e-1, 22.600,
22.400, 17.500, 52.000, 19.500, 0.70e-1, 0.40e-1, 0.38e-1], [0.75e-1, 22.700, 22.100,
21.500, 98.000, 37.000, .105, 0.62e-1, 0.58e-1], [.100, 22.700, 21.400, 22.500, 147.000,
56.000, .136, 0.80e-1, 0.75e-1], [.120, 22.800, 20.400, 25.000, 216.000, 82.000, .171,
.100, 0.96e-1], [.140, 22.800, 19.700, 26.500, 270.000, 103.000, .197, .117, .111], [.160,
22.800, 18.600, 27.500, 347.000, 132.000, .230, .135, .128], [.180, 23.000, 17.400,
28.500, 422.000, 160.000, .255, .150, .147], [.200, 22.100, 15.100, 30.000, 503.000,
190.000, .284, .165, .160], [0.50e-1, 23.100, 22.900, 17.500, 40.000, 15.000, 0.58e-1,
0.59e-1, 0.58e-1], [0.75e-1, 23.100, 22.600, 21.500, 77.000, 29.000, 0.87e-1, 0.88e-1,
0.85e-1], [.100, 23.200, 22.200, 22.500, 111.000, 41.000, .111, .113, .110], [.120, 23.100,
21.400, 25.000, 162.000, 61.000, .141, .143, .139], [.140, 23.200, 20.600, 26.500,
211.000, 79.000, .165, .167, .161], [.160, 23.200, 19.800, 27.500, 259.000, 98.000, .187,
.190, .184], [.180, 23.200, 18.700, 28.500, 317.000, 119.000, .218, .221, .214], [.200,
23.300, 17.700, 30.000, 377.000, 142.000, .243, .249, .240]]);
for n to 72 do
"-----------------------------------Inputs-----------------------------------------";
"Variable";
PM__in := Quantity(A(n, 1), 0.1e-1);
TM__in := Quantity(A(n, 2), 0.41);
TM__out := Quantity(A(n, 3), 0.42);
QM__in := Quantity(A(n, 4), 1.5);
fM := Quantity(A(n, 5), 0.2e-1, 'relative');
VM__rms := Quantity(A(n, 6), 0.2e-1, 'relative');
IM__a := Quantity(A(n, 7), 0.9e-2);
IM__b := Quantity(A(n, 8), 0.9e-2);
IM__c := Quantity(A(n, 9), 0.9e-2);
"Constant";
k := 1.4;
cp := 1005;
R := cp*(1-1/k);
DM__in := Quantity(0.22e-1, 0.1e-4);
DM__out := Quantity(0.35e-1, 0.1e-4);
DM__1 := Quantity(0.28e-1, 0.1e-4);
DM__2 := Quantity(0.49e-1, 0.1e-4);
bM__2 := Quantity(0.3e-2, 0.1e-4);
RM__w := Quantity(2.5, 0.8e-1, 'relative');
PM__out := 101900;
"-----------------------------------Initialization--------------------------";
rho__in := 1.2;
T__in := 293;
P__in := 101900;
c__in := 1;
rho__out := 1.2;
T__out := 293;
P__out := 101900;
c__out := 1;
rho__1 := 1.2;
T__1 := 293;
P__1 := 101900;
```

```
c__1 := 1;
rho__2 := 1.2;
T__2 := 293;
P__2 := 101900;
c__2 := 1;
rho__3 := 1.2;
T__3 := 293;
P__3 := 101900;
c__3 := 1;
for i to 5 do
"----------------------------------------------In-----------------------------------";
D__in := combine(DM__in, errors);
A__in := combine((3.1416*(1/4))*D__in^2, errors);
Q__in := combine(0.4719474e-
3*QM__in*sqrt(1.2/rho__in)*sqrt((1/101325)*P__in*(294.4/T__in)), errors);
T__in := combine(TM__in+273.15, errors);
P__in := combine(100000*PM__in+PM__out, errors);
T0__in := combine(T__in+c__in^2/(2*cp), errors);
P0__in := combine(P__in+(1/2)*rho__in*c__in^2, errors);
rho__in := combine(P__in/(R*T__in), errors);
c__in := combine(Q__in/A__in, errors);
"-----------------------------------------(1)----------------------------------";
`dP__in-1` := combine((0.1477e-1*QM__in^2-.25356*QM__in-0.7148e-1)*1000,
errors);
alpha__1 := 0;
D__1 := combine(DM__1, errors);
A__1 := combine((3.1416*(1/4))*D__1^2, errors);
T__1 := combine(T0__1-c__1^2/(2*cp), errors);
P__1 := combine(P__in-`dP__in-1`, errors);
T0__1 := combine(T0__in, errors);
P0__1 := combine(P__1+(1/2)*rho__1*c__1^2, errors);
Q__1 := combine(rho__in*Q__in/rho__1, errors);
c__1 := combine(Q__1/(A__1*cos(alpha__1)), errors);
rho__1 := combine(P__1/(R*T__1), errors);
"-----------------------------------------(2)----------------------------------";
alpha__2 := combine(70*((1/360)*(2*3.1416)), errors);
b__2 := combine(bM__2, errors);
D__2 := combine(DM__2, errors);
A__2 := combine(3.1416*D__2*b__2, errors);
Q__2 := combine(rho__in*Q__in/rho__2, errors);
T__2 := combine(T0__2-c__2^2/(2*cp), errors);
P__2 := combine(P0__2-(1/2)*rho__2*c__2^2, errors);
T0__2 := combine(T0__1, errors);
P0__2 := combine(P0__1, errors);
c__2 := combine(Q__2/(A__2*cos(alpha__2)), errors);
rho__2 := combine(P__2/(R*T__2), errors);
"-----------------------------------------(3)----------------------------------";
D__3 := combine(DM__out, errors);
A__3 := combine((3.141592*(1/4))*D__3^2, errors);
```

```
Q__3 := combine(rho__2*Q__2/rho__3, errors);
T__3 := combine(T__out, errors);
P__3 := combine(P__out, errors);
c__3 := combine(Q__3/A__3, errors);
P0__3 := combine(P__3+(1/2)*rho__3*c__3^2, errors);
T0__3 := combine(T__3+c__3^2/(2*cp), errors);
T0__3s := combine(T0__1*(P0__3/P0__1)^((k-1)/k), errors);
rho__3 := combine(P__3/(R*T__3), errors);
"-------------------------------------Out-------------------------------------";
D__out := combine(DM__out, errors);
A__out := combine((3.141592*(1/4))*D__out^2, errors);
Q__out := combine(rho__in*Q__in/rho__out, errors);
T__out := combine(TM__out+273.15, errors);
P__out := combine(PM__out, errors);
c__out := combine(Q__out/A__out, errors);
T0__out := combine(T0__in*(P0__out/P0__in)^((k-1)/k), errors);
P0__out := combine(P__out+(1/2)*rho__out*c__out^2, errors);
rho__out := combine(P__out/(R*T__out), errors);
"-----------------------------------------------Calcs-----------------------------";
f := combine(fM, errors);
R__w := combine(RM__w, errors);
V__rms := combine(VM__rms, errors);
I__a := combine(IM__a, errors);
I__b := combine(IM__b, errors);
I__c := combine(IM__c, errors);
I__rms := combine((I__a+I__b+I__c)*(1/3), errors);
W__b := combine(3^.5*I__rms*V__rms, errors);
W__m := combine(0.144902407639e-3*f^2+.103907788970966*f, errors);
W__e := combine(3^.5*I__rms^2*R__w, errors);
dH__0S := combine(cp*(T0__1-T0__3s), errors);
u := combine((1/2)*(2*3.1416)*f*D__2, errors);
eta__aero := combine((W__b+W__m+W__e)/(dH__0S*rho__in*Q__in), errors);
eta__thermo := combine((T0__1-T0__3)/(T0__1-T0__3s), errors);
phi := combine(c__2*cos(alpha__2)/u, errors);
psi := combine(dH__0S/u^2, errors);
psi__sq2 := combine((2*psi)^.5, errors)
end do;
B[n, 1] := GetValue(eta__aero);
B[n, 2] := GetError(eta__aero);
B[n, 3] := GetValue(eta__thermo);
B[n, 4] := GetError(eta__thermo);
B[n, 5] := GetValue(phi);
B[n, 6] := GetError(phi);
B[n, 7] := GetValue(psi__sq2);
B[n, 8] := GetError(psi__sq2)
end do;
w := proc (l, m) options operator, arrow; B[l, m] end proc; MA := Matrix(72, 8, w);
ExportMatrix("D:/0 Thesis/Supporting materials/uncertainity.csv", MA);
```

D. RESULTS OF THE DESIGN OF THE NOZZLE BODY.

Layer: Span: 0.0000
  Layer Parameters (using M vs R*T system)
    LE Pitch = 23.5619
    TE Pitch (S) = 15.708
    Centroid:Z = 3
    Centroid:R = 37.593
    Centroid:T = -61.7
    Centroid:Mp = 0.179843
    Centroid:M = 7.40694
    Airfoil Area = 104.169
  Blade & Layer Parameters (using M vs T-Prime system)
    3D Meanline Length = 27.1211
    Camber Length = 27.1214
    Cord Length (C) = 26.8056
    Meridional Length (M) = 15
    Stagger Angle = -56.0
    Solidity (C/S) = 1.7065
    Pitch Cord Ratio (S/C) = 0.585995
Layer: Span: 1.0000
  Layer Parameters (using M vs R*T system)
    LE Pitch = 23.5619
    TE Pitch (S) = 15.708
    Centroid:Z = -3.60777e-023
    Centroid:R = 37.593
    Centroid:T = -61.7
    Centroid:Mp = 0.179843
    Centroid:M = 7.40694
    Airfoil Area = 104.169
Blade & Layer Parameters (using M vs T-Prime system)
    3D Meanline Length = 27.1211
    Camber Length = 27.1214
    Cord Length (C) = 26.8056
    Meridional Length (M) = 15
    Stagger Angle = -56.0
    Solidity (C/S) = 1.7065
    Pitch Cord Ratio (S/C) = 0.585995